ISSN 1349-0087
SPring-8 Document D2013-010

SPring-8 Research Frontiers

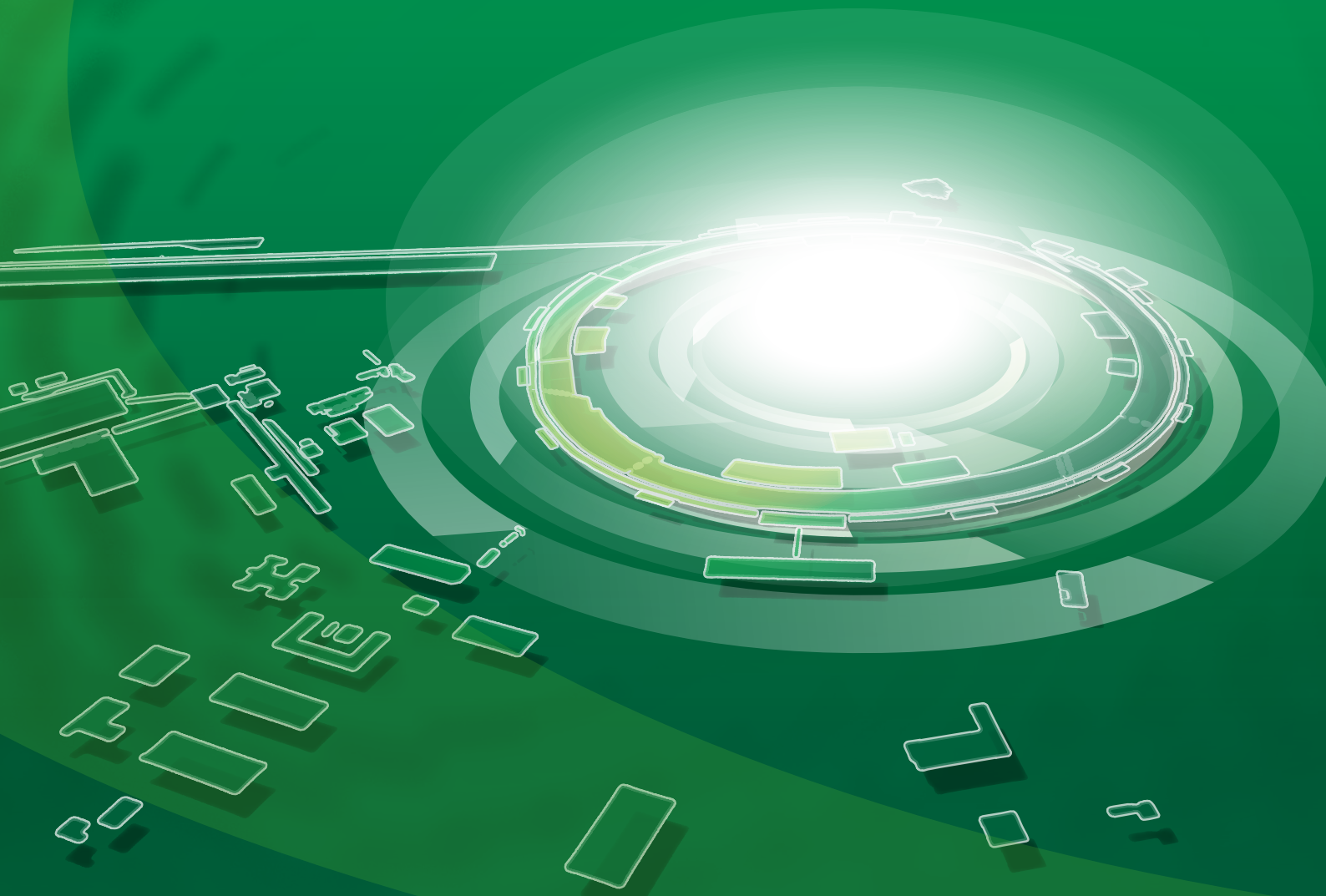

2012

SPring-8
Research Frontiers
2012

CONTENTS
2012

Note: The principal publication(s) concerning each article is indicated with all author's names in italics in the list of references.

Preface

After 15 years of public use of the SPring-8 synchrotron radiation facility from 1997, the SACLA X-ray free electron laser facility has been completed, and user operation was launched in March 2012. The SPring-8 campus operates both SPring-8 and SACLA facilities and offers a unique environment where the two can be used synergistically.

In 2012, the SPring-8 facility was used by numerous scientists and engineers in basic and applied research, including life science, materials science, chemical science, earth and planetary science, environmental science, industrial applications, and instrumentation and methodology. Collaborations between academia and industry at SPring-8 have been performed successfully in the fields of materials science and life science. In addition, nurturing of young researchers and graduate students at the SPring-8 campus was carried out for future growth of the SR user society.

A number of SPring-8 users have been awarded prizes in 2012 for their achievements in science and technology. Professor Keiichi Namba (Osaka University) was awarded the Imperial Prize and Japan Academy Prize for his research on structure and functional analyses of biological macromolecular nanomachines. The Medal of Honor with Purple Ribbon was awarded to Dr. Tetsuya Ishikawa (RIKEN) for his contribution to X-ray engineering, particularly for the development of X-ray optics for 3rd generation synchrotron radiation. Professor Nobuo Kamiya (Osaka City University) and Professor Jian-Ren Shen (Okayama University) were awarded the Asahi Prize for their scientific achievement of clarifying the molecular structure of the oxygen-evolving center of Photosystem II. Professor Hideo Hosono (Tokyo Institute of Technology) was awarded the Nishina Memorial Prize for his discovery of iron pnictide superconductors.

On June 2013, I succeeded Mr. Tetsuhisa Shirakawa, the former president of JASRI. I wish to contribute to further development of broad user-oriented facilities for various users from universities, research institutions, and industrial companies. I am very grateful to the many authors and experts who contributed their papers to this 2012 volume. Special thanks are due to Dr. Hideo Ohno and the members of the editorial board for their constant efforts.

土肥 義治

Yoshiharu Doi
President
SPring-8/JASRI

Editor's Note

SPring-8 Research Frontiers 2012 covers advances achieved during the last two consecutive research periods, the second half of 2011 (2011B) and the first half of 2012 (2012A). Remarkable scientific achievements at SPring-8 in various fields of basic and applied science including industrial applications, are described, as well as the development of accelerators, beamlines and experimental apparatus, and the present status of the SPring-8 facility. In addition, topics concerning the use of SACLA are introduced.

SACLA successfully completed its initial commissioning by the end of 2011. In this early period, exciting and useful information on radiation properties of XFEL have been obtained by utilizing instruments and methods newly developed for SACLA. Some of these findings, which indicate the novelties of SACLA, are reported in this volume. Following the commissioning, SACLA started user operation in March 2012. Stable XFEL light has been routinely provided to users without serious downtime. SACLA is now exploring the frontiers of optical science and technologies.

Two new beamlines were opened to users: BL28XU, the so-called "Kyoto University RISING-BL," named after the Research & Development Initiative for Scientific Innovation of New Generation Batteries (RISING) project, was developed to investigate the simultaneous valence and structure changes during battery charge/discharge cycles in time and space for safety, improvement and innovation of the present and future lithium batteries. BL36XU "Catalytic Reactions Dynamics for Fuel Cells" was constructed by The University of Electro-Communications under a New Energy and Industrial Technology Development Organization (NEDO) program, and is dedicated to the structural and electronic analyses of the dynamic events on polymer electrolyte fuel cell (PEFC) cathode catalysts for the development of next-generation PEFCs by high time- and spatially resolved XAFS methods.
A new facility, LEPS2 Experimental Building, for quark nuclear physics utilizing backward Compton scattered photons, has been constructed at the long straight section beamline BL31LEP (Research Center for Nuclear Physics, Osaka University). The beamline provides intense high energy polarized γ-rays with small angular divergence to allow most advanced experiments on a variety of strangeness channels with targets in a restricted space inset in a large-scale solenoid detector located outside the experimental hall. This new beamline will be opened to users in autumn 2013.

Dr. M. Takata left the editorial board and the editor in chief would like to express his sincere gratitude to him for his long-lasting contribution to Research Frontiers publications.

In the layout of Research Frontiers, photographs of flowers growing on the SPring-8 campus and at Harima Science Garden City have been inserted. These photographs taken by Mr. S. Tsujimoto and Mr. K. Shinbe are greatly appreciated.

Copies of SPring-8 Research Frontiers will be sent on request. The full text is also available on the SPring-8 website (http://www.spring8.or.jp/). For the list of publications produced by SPring-8 users and staff, please visit the publication database at http://www.spring8.or.jp/en/science/publication_database/.

We extend our appreciation to those who have recommended excellent research results suitable for publication in SPring-8 Research Frontiers. We would also like to express our sincere gratitude to the users and staff of SPring-8 for contributing their reports to this issue.

Editorial Board

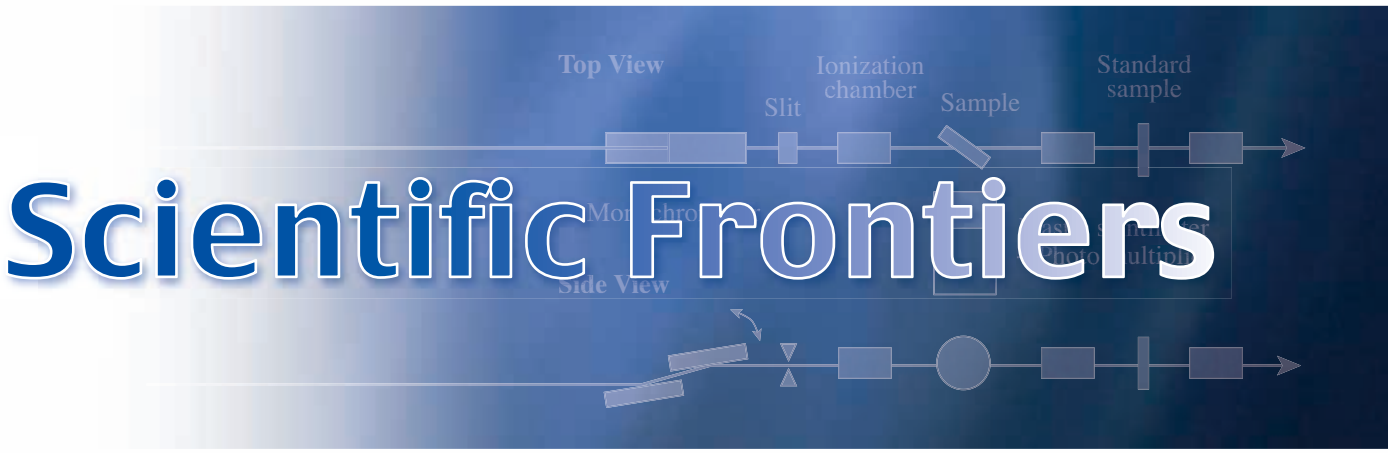

Scientific Frontiers

Life Science:

Structural biology deals with the minutest hierarchy, composed of atoms and molecules, in biological organization. Through the 3D visualization of biomacromolecules, it reveals biomolecular functions and mechanisms as a consequence of their structural features. Among the methods of visualization, X-ray crystallography is the most powerful method, but requires good quality of macromolecular crystals. To analyze structures from ill-diffracting crystals or diverse aspects of molecular structures, synchrotron beamlines have been progressively developed. As a recent achievement of the developments at SPring-8, a micro-focus beamline BL32XU has been constructed as part of a national project, the 'Target Protein Research Program' (TPRP) and is dedicated to the analysis of protein microcrystals. We can introduce the first results gained through the use of BL32XU in this issue of Research Frontiers 2012, since beamline was established in mid-2010. The next project, the 'Platform for Drug Design, Discovery and Development,' was started in 2012. BL41XU will be upgraded by installing new optical components to produce a high-flux microbeam and a new X-ray detector for ultrafast data collection. This improvement is expected to improve the efficiency of the beamline. Overall, in the field, developments in photon and quantum beam technology are expanding structure determinations of bionanomolecules. In particular, the compact X-ray free electron laser facility, SACLA, will be establishing experimental environments for determining the structures of very tiny crystals, such as those of membrane proteins, or single particles of supramolecular complexes and organelles. Sooner than later, we will be faced with the problem of proper use of these facilities.

Within the above backdrop, many outstanding results have been reported in 2012, as summarized briefly below. Among them, those on several types of membrane transport proteins stand out. This membrane protein family is involved in the movement of ions, small molecules, or macromolecules across cell membranes. Kato *et al*. revealed the structure of channelrhodopsin. This protein is well applied to neuroscience research owing its proton-transfer function in response to light. Its molecular mechanism driven by the

Structural Biology

photoisomerization of chromophore was revealed, and it will be applied to improving this protein tool for used in research. Fujiwara *et al*. analyzed another proton channel relevant to bacterial killing by immune cells. The assembly of its membrane-transport domains, regulated by the association/dissociation of its intracellular domains that sense fever heat, induces the proton transfer that leads to the production of reactive oxygen species to kill the pest. Conversely to the two passive transport proteins, a proton pump acts actively against the concentration gradient of the portage, using chemical energy. Some of the pumps found in plants use the energy supplied from pyrophosphate instead of ATP. Lin *et al*. determined the structure of a pyrophosphate-energized proton pump and revealed unique features of this protein family. Next, two active transporters move small molecules. Sugar is a major energy source for living organisms. Sun *et al*. determined the structure of a sugar transporter strongly related to diabetes, revealing a unique mechanism of substrate recognition and opening up the possibility of drug design for the protein. Efflux transporters have been discovered in multidrug-resistant bacteria and pass out toxic antibiotics from cells. Nakashima *et al*. determined a new structure in which both large and small drug molecules are bound to two rooms of its pocket. The new findings on the efflux mechanism resembling a peristaltic pump should facilitate drug discovery to pathogenic bacteria.

Five important biological molecules in other categories were selected. Alzheimer's disease (AD) is caused by the accumulation of a certain peptide into cells, induced by a mutation of a membrane protease, preseniline. Dang *et al*. solved the structure of its homolog and showed the unique architecture of the protein family. This is an important clue in resolving the mechanism of AD. Next, Mizushima *et al*. unraveled the structure of a bacterial toxin that weakens the host cell response to a dysentery bacterium. Its structural analysis showed the presence of a protease-like active center, resulting in revealing the mechanism behind the suppression of the host's response. Dynein is a motor protein that walks on the cellular skeleton to transport large molecules. The high-resolution structural analysis of dynein by Kon *et al*. unveiled the molecular mechanism of protein walking. Histone is essential to package and order DNA, whereas CENP proteins appear in the unique kinetochore structure during cell division and repackaging of DNA into daughter cells. Nishino *et al*. determined the structures of CENP protein complexes and showed unique DNA binding modes even in structures similar to those of histones. An RNA fragment, piRNA, bound to Piwi proteins maintains genome integrity in germ line cells, but the mechanism of its production remains unknown. Nishimatsu *et al*. proposed a new model of piRNA biogenesis by determining the structure of an RNase, Zuc.

Takashi Kumasaka

"Tsutsuji"- Azalea

Crystal structure of channelrhodopsin light-gated cation channel

Channelrhodopsin (ChR) is a light-gated cation channel that conducts cations in a light-dependent manner. Because the inward flow of cations triggers neuron firing, neurons expressing ChRs can be optically controlled, even within freely moving mammals. Although ChR has now been broadly applied to neuroscience research, little is known about its molecular mechanisms. We determined the crystal structure of chimeric ChR at 2.3 Å resolution and revealed its molecular architecture, especially the cation-conducting pathway. The integration of structural and electrophysiological analyses provided insight into the molecular basis of the extraordinary function of ChR, and paved the way for the principled design of ChR variants with novel properties.

Organisms from bacteria to humans perceive light and use the information for visual and non-visual functions, including ATP synthesis and circadian rhythm. In most cases, light perception is mediated by proteins from the rhodopsin family, which consist of seven-transmembrane (7-TM) domains and covalently linked retinal chromophores. The first rhodopsin family protein was discovered in 1876 in frog retina by Franz Boll. Since that discovery, more and more rhodopsin family proteins have been isolated not only from animal eyes, but also from marine bacteria and even archaea living under extreme environmental conditions. So far, on the basis of their functions, the large number of rhodopsin family proteins can be divided into four distinct classes: photoisomerases, signal transducers, ion pumps, and the most recently discovered class, ion channels.

Channelrhodopsin (ChR) was originally isolated from tiny green algae, *Chlamydomonas Reinhardtii*, and identified as a light-gated cation channel in 2002 [1]. Beginning in 2005, it was found that ChRs could be expressed in mammalian neurons to mediate precise control of action potential firing in response to light pulses. ChRs have now been used to control neuronal activity in a wide range of animals, but little is known about the molecular mechanism of ChR. Although a rough helical arrangement was visible in the recently published electron microscopic (EM) structure of ChR at 6 Å resolution [2], amino acid positioning and insights into channel function remained completely lacking. High-resolution structure would be of enormous value, not only to enhance the understanding of the mechanism of this new class of rhodopsin family proteins, but also to guide the design of ChR variants with novel functions related to their spectrum, selectivity, and kinetics.

To solve the crystal structure of ChR, we expressed a chimeric ChR between ChR1 and ChR2 in Sf9 insect cells. The crystals were obtained in the lipidic mesophase, and the data set was collected at **BL32XU** beamline. A complete data set could be collected from a single tiny crystal (~50 μm) owing to the use of a 1-μm-wide, 15-μm-high microbeam and the helical data collection strategy [3]. The phase was determined by the multiple anomalous dispersion (MAD) method using mercury-derivatized crystals. As far as we know, this is the first example of the phase determination by MAD for a crystal obtained in the lipidic mesophase. We finally determined the crystal structure of ChR in the closed state at 2.3 Å resolution.

ChR is composed of an N-terminal extracellular domain, 7-TM domains connected by three cytoplasmic and extracellular loops, and a C-terminal intracellular domain (Fig. 1). Of particular note is that, as previously predicted from EM [2], ChR is tightly associated into a dimer via interfacial interactions between the N-domain, ECL1, TM3, and TM4 of each molecule. This result is somewhat of a surprise because all other known microbial rhodopsins form trimers or tetramers. This is the first example of microbial rhodopsin that forms a dimer conformation.

To further understand the ChR structure, we compared our ChR with the most well-studied microbial rhodopsin, bacteriorhodopsin (BR). Although

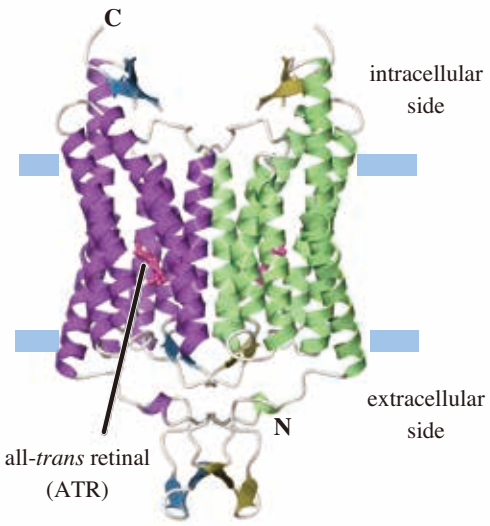

Fig. 1. Overall structure of chimeric ChR. Each protomer is shown in a ribbon representation (green and magenta) and retinal molecules are depicted by a stick model (pink). Blue lines represent the cell membrane.

the primary sequence identity between ChR and BR is as low as 15%, the overall structure of ChR is well superimposed on that of BR. TM3-6 are very similar, and the position of retinal is well conserved, whereas there are two distinct features between ChR and BR. First, ChR has an additional N-terminal and a C-terminal domain, and more importantly, the extracellular sides of TM1 and TM2 are tilted compared with those of BR. Because of this tilt, ChR has larger pores formed by TM1, 2, 3, and 7. The calculated electrostatic surface potential reveals that such a pore is strongly electronegative, so we assume that this pore act as the cation-conducting pathway in ChR (Fig. 2). To verify this hypothesis, we expressed the mutants of the pore-lining residues in HEK293 cells and recorded photocurrents in response to blue light pulses. Most mutants showed altered properties, including photoconductance, kinetics, and ion preference. Therefore, we suggest that this pore actually functions as the cation-conducting pathway.

While this putative cation-conducting pathway is opened toward the extracellular side, the cytoplasmic side of this pathway is occluded by Glu129 (Fig. 3). Although the calculated pKa of Glu129 suggests that this residue is protonated in the closed state, the E129Q mutant shows a strongly decreased photocurrent. Thus, we assume that Glu129 acts as the putative channel gate and the gating is regulated by the protonation change of Glu129 during the photocycle. The results of a recent FT-IR study also support our idea [4].

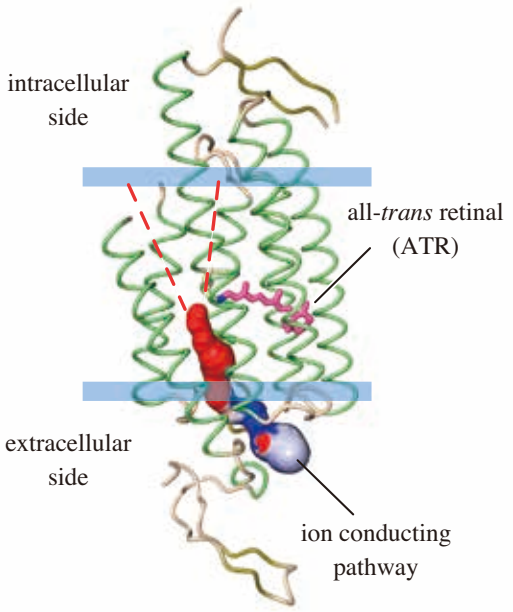

Fig. 2. Solvent accessible surface of the putative ion-conducting pathway. Blue and red indicate the positive and negative potentials, respectively. Putative intracellular vestibule is shown by red dashed line.

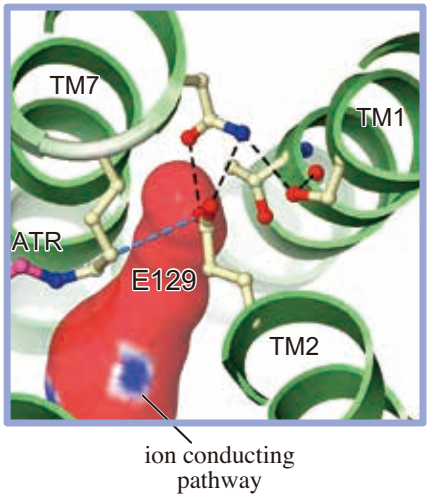

Fig. 3. Possible channel gate. Hydrogen bonds are shown as black dashed lines.

In the present study [5], we determined the first crystal structure of a light-gated cation channel, in the closed/dark state at 2.3 Å resolution, and provided insight into ChR dimerization, retinal binding, and cation conductance. In the field of ChR, there are two hypotheses about the cation-conducting pathway. One is that the pathway comprises helices from a single ChR molecule, and the other is that the ChR dimer assembles to form the conducting pathway using elements from each of the two ChRs. The results of this study strongly supports the former hypothesis and will accelerate the basic mechanistic understanding of this remarkable photoreceptor protein. This high-resolution information, along with electrophysiological analyses, will also guide the design of ChR variants with ideal properties.

Hideaki E. Kato*, Ryuichiro Ishitani and Osamu Nureki

Graduate School of Science, The University of Tokyo

*Email: emekato@biochem.s.u-tokyo.ac.jp

References

[1] G. Nagel *et al.*: Science **296** (2002) 2395.
[2] M. Müller *et al.*: J. Mol. Biol. **414** (2011) 86.
[3] K. Hirata *et al.*: AIP Conference Proc. **1234** (2010) 893.
[4] K. Eisenhauer *et al.*: J. Biol. Chem. **287** (2012) 6904.
[5] *H.E. Kato, F. Zhang, O. Yizhar, C. Ramakrishnan, T. Nishizawa, K. Hirata, J. Ito, Y. Aita, T. Tsukazaki, S. Hayashi, P. Hegemann, A.D. Maturana, R. Ishitani, K. Deisseroth and O. Nureki: Nature* ***482*** *(2012) 369.*

Structure and function of dimeric assembly in voltage-gated H^+ channel

VSOP/Hv1 is a voltage-gated H^+ channel (Hv channel) that is expressed in immunocytes and is involved in countervailing invading bacteria. VSOP/Hv1 has four-transmembrane segments that correspond to the voltage sensor domain (S1-S4) of other voltage-gated channels [1,2]. The composition of the functional unit is uniquely a dimer. Most types of ion channels show oligomeric architecture in the 3-5mer, forming a permeation pathway in the assembly center. In the Hv channel, by contrast, only one subunit of the dimeric unit is sufficient for its channel activity. Thus, the functional role of an assembly that lies outside the forming of the permeation pathway remains unknown.

To identify the assembly domain, we focused on the cytoplasmic C-terminus of mouse Hv1/VSOP (mVSOP/Hv1). Deletion of the C-terminal domain markedly reduced the dimer fraction in a cross-linking western blot. Sedimentation equilibrium for the purified C-terminal protein showed a twofold molecular weight of the monomer, suggesting the assembly domain. Structural analysis of the C-terminal domain was carried out using beamline **BL44XU**. The overall structure was a parallel left-handed, two-stranded coiled-coil (Fig. 1(a)) [3]. The coiled-coil core consists of well-packed hydrophobic residues, showing an I/L core packing pattern, in which Ile/Leu residues are situated and are periodically observed along the entire length of the coiled-coil (layers 1/2, 5/6, and 9/10). Mutation to the I/I or L/L pattern altered the coiled-coil structure to the trimeric one, while the L/I pattern resulted in the tetrameric structure (Fig. 1(b)) [4]. Despite this background, hydrophilic Asn (N231), instead of hydrophobic residues, comprise the core at layer-3 (Fig. 1(c)). They are asymmetrically packed, and notably, the neighboring residues are hydrophobic (I230 and I232) in an irregular gement; suggesting that this layer could be a weakness of core packing. The thermal stability of the mHv1/VSOP coiled-coil was lower (apparent Tm = ~40°C) than those of other naturally occurring coiled-coil proteins (Tm > 65°C), and the unfolding was irreversible (Fig. 1(d)). Thus, the mVSOP/Hv1 assembles into a dimer using a cytoplasmic coiled-coil architecture that is well folded and thermally labile.

The functional significance of the dimeric coiled-coil assembly in mVSOP/Hv1 was assessed using whole-cell patch clamp recordings. Deletion of the C-terminal coiled-coil domain (ΔC) accelerated the channel's activation kinetics (Fig. 2(a)). Given that the assembly of the coiled-coil was thermally labile, the relationship between temperature and activation kinetics was further analyzed. Deletion of the coiled-coil domain shifted the thermosensitivity relationship by 15°C without changing the slope (Fig. 2(b)). We also tested the effects of introducing mutations. The "4R" mutation, where bulky hydrophilic Arg is introduced into the hydrophobic core layers to disrupt the coiled-coil, shifted the thermosensitivity relationship by ~8°C in the direction of the ΔC phenotype (Fig. 2(c)). Assembly was suppressed in the 4R mutant, as shown by size exclusion chromatography. On the other hand, the NIN mutation, where an inverse mutation in hydrophobicity, NIN, is introduced into the lyer-3 to stabilize the coiled-coil, shifted the thermosensitivity relationship by ~5°C away from the ΔC phenotype (Fig. 2(c)). Using the CD spectrum of the coiled-coil protein, the coiled-coil assembly was stabilized by the NIN mutation (Fig. 1(d)). Thus, the stability of the C-terminal domain

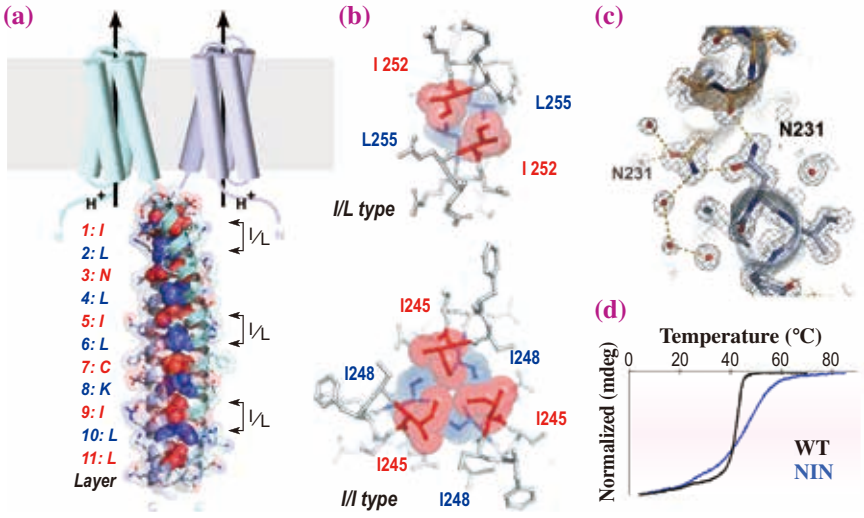

Fig. 1. **(a)** Crystal structure of cytoplasmic dimer coiled-coil. Hydrophobic layers of the coiled-coil core and amino acid residues are indicated. **(b)** Representative geometry of the hydrophobic coiled-coil core (layer-5,6) in the crystal structures: I/L-type dimer (top) and I/I-type trimer (bottom). **(c)** Structure (stick models) and electron density maps in layer-3. **(d)** Temperature dependence of CD signal recorded from WT and the NIN mutant proteins at 222 nm. Signals were recorded while applying a heating temperature gradient.

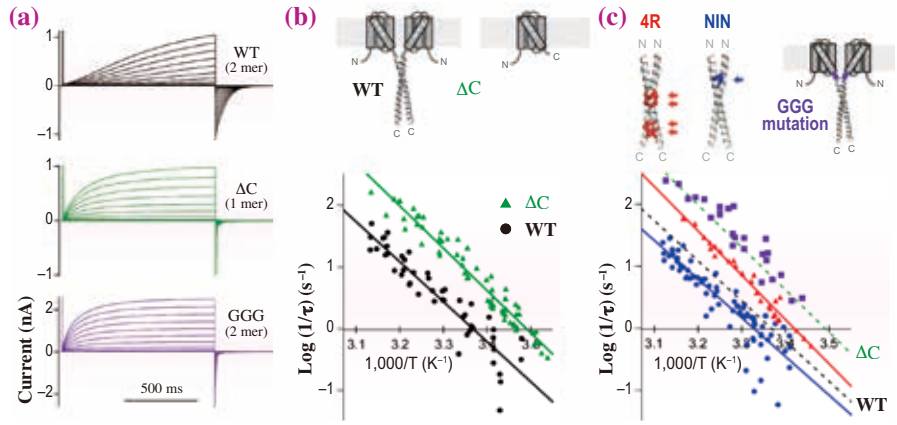

Fig. 2. **(a)** Representative currents through WT and the mutant channels recorded at 25°C from HEK293 cells. **(b, c)** Activation kinetics (Y-axis) of WT and the mutants were analyzed while varying temperature (X-axis). Accumulated data and the linear regression line are shown.

determined the channel activation kinetics in a temperature-dependent manner such that the coiled-coil dimer assembly inhibited channel activation.

The coiled-coil structure we characterized began only five residues downstream of the last transmembrane helix (S4), which is considered to move substantially when the channel opens. Increasing the linker flexibility by Gly-Gly-Gly mutation altered the thermosensitivity relationship to the monomeric ΔC phenotype (Fig. 2), suggesting that a positional proximity of two channels is not sufficient to produce the thermal stability seen in the WT phenotype. The value of the effective gating charge (Zδ) was also decreased to half by the GGG mutation, as shown in the monomeric ΔC channel. This half-Zδ value suggests that two channel subunits gate independently. Thus, the cytoplasmic coiled-coil not only regulates the thermosensitivity of the channel, but also mediates the cooperative gating between the two subunits. These functional regulations are considered to be established by a continuous a-helix consisting of the S4 voltage sensor helix and the coiled-coil strands (Fig. 3).

Ion channel subunits assemble into multimers, sometimes in heteromultimeric, to realize adequate functionality. This study shows that the dimeric coiled-coil assembly regulated the channel activation kinetics in a temperature-dependent manner, such that depolarization-induced increases in H^+ conductance appear to be optimized in the range of body temperature; this may be one of the functional significances of the Hv channel structure. In fact, an Hv channel exhibiting high-temperature dependence is expressed in phagocytes [5] and contributes to immunological responses under conditions of local and whole-body fever. The strong voltage dependence, that is, high Zδ value, in the activation gating underpinned by the dimeric coiled-coil structure also plays an essential role in sustaining the production of reactive oxygen species in the mammalian immune system [5]. In addition, our experimental approaches and findings in this study should bring about appreciable understanding of concepts generalizable to other larger and more complex ion channels.

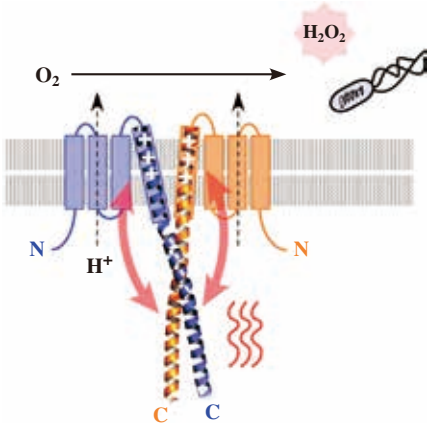

Fig. 3. Hv channel is a key regulator in the production of reactive oxygen species for digestion of invading bacteria. Cytoplasmic coiled-coil mediates the cooperative gating and adjusts the range of temperature over which VSOP/Hv1 operates. Two channel subunits interact via the cytoplasmic coiled-coil assembly. Gating movement in the transmembrane region is physically restricted by the cytoplasmic coiled-coil domain and the rigid linker region, which enables structural change of one subunit to affect the other.

Yuichiro Fujiwara[a,*] and Atsushi Nakagawa[b] and Yasushi Okamura[a]

[a] Department of Physiology, Osaka University
[b] Institute for Protein Research, Osaka University

*Email: fujiwara@phys2.med.osaka-u.ac.jp

References

[1] M. Sasaki *et al.*: Science **312** (2006) 589.
[2] I.S. Ramsey *et al.*: Nature **440** (2006) 1213.
[3] *Y. Fujiwara, T. Kurokawa, K. Takeshita, M. Kobayashi, Y. Okochi, A. Nakagawa and Y. Okamura: Nat. Commun. **3** (2012) 816.*
[4] Y. Fujiwara *et al.*: J. Physiol. **591** (2013) 627.
[5] T.E. DeCoursey: Physiology (Bethesda) **25** (2010) 27.

Structural insights into a bacterial homologue of glucose transporters GLUT1–4

Glucose, one of the essential simple sugars, plays a central role in energy transfer in most living organisms. Mammalian cells take in glucose principally by two subfamilies of glucose transporters, one named GLUT, the other, SGLT.

GLUTs belong to the major facilitator superfamily (MFS), an ancient and the largest secondary transporter superfamily [1]. Previous studies indicate that they facilitate glucose uptake and prevent unwanted glucose analogues from passing through the plasma membrane. GLUTs are highly related to metabolic diseases, such as diabetes mellitus, yet no crystal structure of GLUTs has been obtained up to now. Structures of other MFS members have been obtained. Unfortunately, none of the available structures could provide enough information for further understanding of GLUTs' mechanism at a molecular level, owing to the lack of primary sequence similarity.

Important yet poorly understood, GLUTs are ideal protein targets for X-ray crystallography research. In the case of difficulties in handling eukaryotic membrane protein, we screened prokaryotic homologues and chose XylE originating from *E. coli* as a reasonable substitution. XylE is a H^+: D-xylose symporter with relatively high sequence homology to human GLUTs (especially GLUT1–4) and also has similar biochemical properties. The molecule of D-xylose consists of the same elements of a six-member ring as that of D-glucose.

After data set collection at beamline **BL41XU**, the structure of XylE bound to D-xylose was determined and refined, with the resolution of 2.8 Å (as shown in Fig. 1(a, b)) [2]. It is the first structure binding to its natural substrate in MFS proteins with solved structures. The structure shows that 12 transmembrane α-helices (TMs) are arranged in two domains, each with 6 TMs forming a bundle around the substrate binding center, which is a common feature of the MFS fold. Its amino and carboxy termini are both located in the cytoplasm. In a total view, the structure represents a new conformation of the MFS, namely, an outward facing, partially occluded and ligand-bound structure (Fig. 1(c)). It satisfies a clear step of the putative transport process theoretically

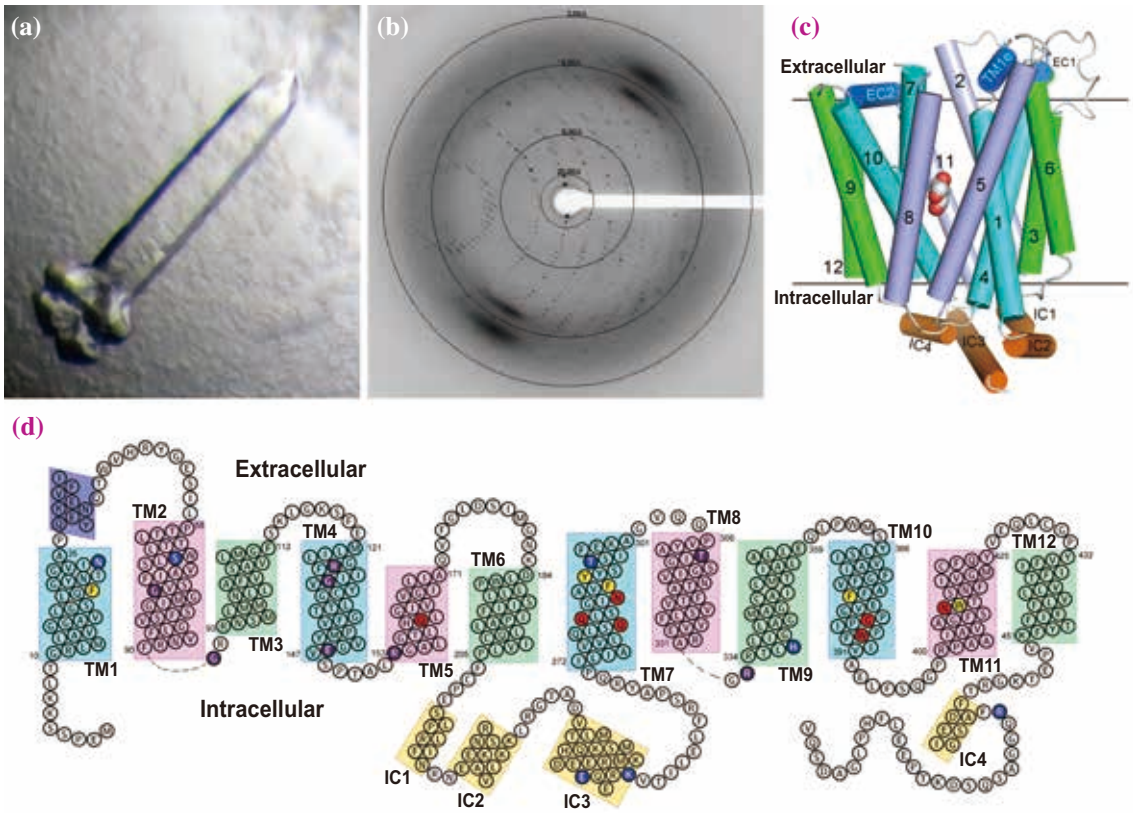

Fig. 1. **(a)** crystal of XylE protein viewed by microscopy, **(b)** diffraction data collected at BL41XU beamline, **(c)** 3D structure of XylE, and **(d)** proposed secondary structure model of GLUT1.

proposed a long time ago.

Distinct from other known MFS structures, XylE contains four more intracellular α-helices in which key residues are conserved in GLUT1–4. Furthermore, XylE is also able to bind D-glucose but not any other natural monosaccharide studied. The binding affinity between XylE and D-xylose or D-glucose is within the same order of magnitude as estimated by ITC. We then successfully captured the structures of XylE bound to D-glucose at 2.9 Å and XylE bound to 6-bromo-6-deoxy-D-glucose (6-BrGlc; a synthesized D-glucose derivative) at 2.6 Å. Br anomalous signals from 6-BrGlc help to locate the precise position and orientation of D-glucose inside XylE. The conformations of the three structures are almost identical.

It is observed that no charged residue is involved in ligand binding in XylE, which differs from other proton symporters. The hydroxyl groups of D-xylose are stabilized through direct hydrogen bonds by polar and aromatic residues including Gln 168, Gln 288, Gln 289, Asn 294, Trp 392 and Gln 415. Some more water-mediated hydrogen bonds are contributed by Tyr 298 and Gln 415. On the basis of the high-resolution data, both *in vitro* and *in vivo* biochemical assays were designed to prove the validity of substrate spacing in XylE. Generally, proteoliposome-based counterflow and cell-based uptake assays are used to measure transport activity. Transport missense mutations of the mentioned residues (to be more specific, single residue mutated to alanine) show loss of function in the transport assays.

Substrate specificity is also examined. Sugar selectivity is in agreement with former reports. With such a delicate hydrogen-bond network, it is not hard to imagine that only one possible form of a sugar ring can be tolerated. The comparisons with structures containing different ligands reveal that D-xylose and D-glucose interact with XylE similarly. Both six-member rings of the sugar molecules are coordinated by hydrogen bonds in a conformed manner. Moreover, residues Gln 168, Gln 175, and Gly 388 contribute additional hydrogen bonds towards the hydroxyl groups of D-glucose. The 6-hydroxyl group of D-glucose is also coordinated through van der Waals contacts by Ile 171 and Phe 383. The extra interactions may explain why XylE can bind to both D-xylose and D-glucose separately but transport only D-xylose.

Most residues participating in substrate recognition of XylE are invariant in GLUT1–4, so that the coordination network is presumably more or less the same between GLUT1–4 and D-glucose. Some reported disease-related mutations in GLUT1–4 could also affect the function of XylE. For instance, single missense mutation of Arg 133 or Arg 341 in XylE (corresponding to Arg 126 or Arg 333 in GLUT1) results in complete loss of transport activities in the assays.

To put the above findings together, we find that XylE is more practical and accurate for functional simulations of GLUTs than any previous models. In the newly built GLUT1–4 structure model based on XylE, the boundaries of transmembrane helices are revised, and four more intracellular α-helices are added, as Fig. 1(d) shows. The signature-sequence conserved, so-called "sugar porter motifs," are highlighted as well. These motifs are usually far from the sugar binding site. However, they may interact with some charged or polar residues on intracellular α-helices, which implies that the transport mechanism is somehow different from those at other branches of MFS. Mutations of these motifs or of the presumed residues involved in interactions still lead to the impairment of transport activity. A more profound mechanism of how proton motivates sugar transport may lie under the sophisticated hydrogen-bond network among transmembrane α-helices and the intracellular domain. Most significantly, the common natural substrate of GLUT1–4, D-glucose, is included in the picture in a detailed pattern that has never been worked out before.

Furthermore, small-molecule inhibitors of GLUTs can now be designed and modified on the basis of the new model. Specific inhibition or activation of one certain GLUT might be achieved as well. Since the MFS-type sugar transporter is widely spread besides mammalian cells, homologue models for other species such as plants and yeasts may also be built by the same approach. These structures and models will shed more light for further deciphering the sugar transporter mechanism and will promote related medical and agricultural research. The above results were published in Ref. [2]. A "News and Views" [3] was published in the same issue to highlight our study.

Linfeng Sun and Nieng Yan*

State Key Laboratory of Bio-membrane and Membrane Biotechnology, Tsinghua University, China

*Email: nyan@tsinghua.edu.cn

References

[1] N. Yan: Trends Biochem. Sci. **38** (2013) 151.
[2] *L. Sun, X. Zeng, C. Yan, X. Sun, X. Gong, Y. Rao and N. Yan: Nature* ***490*** *(2012) 361.*
[3] P.J. Henderson *et al.*: Nature **490** (2012) 348.

Crystal structure of membrane-bound pyrophosphatase, a primary proton pump

Membranes consist of a lipid bilayer and proteins essential for biological functions such as solute transport, signal transduction and numerous metabolic reactions. Vacuoles play many important roles in metabolism and growth of plants. In plants, vacuoles occupy most of the cell volume and accumulate various molecules. There are several transport systems on the plant vacuolar membrane. One important function is to store protons transported from cytoplasm, which maintains the pH balance in cytoplasm and acidifies the vacuole lumen [1].

Since the interior environment of a vacuole is acidic, pumping protons into it is against the chemical gradient. A characteristic feature of plants is that two proton pumping proteins, vacuolar H^+-ATPases (V-ATPases) and H^+-translocating pyrophosphatases (H^+-PPases), coexist on plant vacuolar membranes [2]. To generate a pH gradient, V-ATPase uses ATP as an energy source while H^+-PPase utilizes PP_i, a by-product of many biosynthesis reactions. Both enzymes acidify the vacuolar lumen and establish an electrochemical proton gradient across the vacuolar membrane. However, the structure and function of V-ATPase have been widely studied, whereas those for H^+-PPase are still unclear.

H^+-PPase is primarily found in higher plants, several protozoa, some bacteria, and archaebacteria and shares a high degree of homology of the amino acid sequence with land plants [3]. To understand the three-dimensional structure and detailed mechanisms underlying the enzymatic mechanism and proton translocation reactions of H^+-PPases, we reported the first crystal structure of a *Vigna radiata* H^+-PPase (*Vr*H^+-PPase) in a complex with a non-hydrolyzable substrate analogue, imidodiphosphate (IDP), at 2.35 Å resolution [4]. Structure analysis was carried out using beamlines BL13B1 and BL13C1 in NSRRC, and **BL12B2** and **BL44XU** in SPring-8.

As shown in Fig. 1(a), the overall structure of *Vr*H^+-PPase is a homodimer with a non-crystallographic 2-fold symmetry, and both the N- and C-termini face the vacuolar lumen. The cytosolic region of *Vr*H^+-PPase has many hydrophilic residues, whereas the vacuolar region of the protein protruding out of the membrane is relatively smaller. The root mean square deviation is 0.32 Å among the Cα atoms between the two monomers. Each monomer contains 16 transmembrane helices (M1-M16) and folds into a rosette manner with two concentric walls, the six inner TMs and ten outer TMs. A single IDP molecule in each monomer was located at the core of the inner wall near the cytosolic region, constructing a substrate binding pocket (Fig. 1(b)).

The substrate/IDP binding site is a funnel-shaped pocket formed by six center TMs with an unusually acidic environment resulting from the presence of several acidic residues. In addition, the IDP molecule is surrounded by one K^+ and five Mg^{2+} ions at the binding site. All these Mg^{2+} ions possess octahedral coordination that mediates the interactions between those acidic residues and IDP. These binding interactions confine the substrate completely and precisely at the active site for the hydrolysis of PP_i. Furthermore, a detailed comparison of the pyrophosphate-binding pocket between *Vigna radiata* H^+-pyrophosphatase and water-soluble *Escherichia coli* pyrophosphatase (*Ec*PPase) suggests that membrane-bound H^+-PPases and soluble PPases utilize different strategies to trap the nucleophile for PP_i hydrolysis [5].

Following PP_i hydrolysis, proton translocation will be carried on in H^+-PPase. However, the proton pathway is not found in the dimerization interface as previously thought. A unique proton translocation pathway was made by six center transmembrane helices in each monomer by demonstrating the charged residues in the *Vr*H^+-PPase (Fig. 2 (a)). In the *Vr*H^+-PPase complex, four charged residues, R242-D294-K742-E301, are sequentially lined up and buried in the transmembrane domain exactly beneath the PP_i binding pocket (Fig. 2(b)). The pathway can be vertically dissected into three parts: the

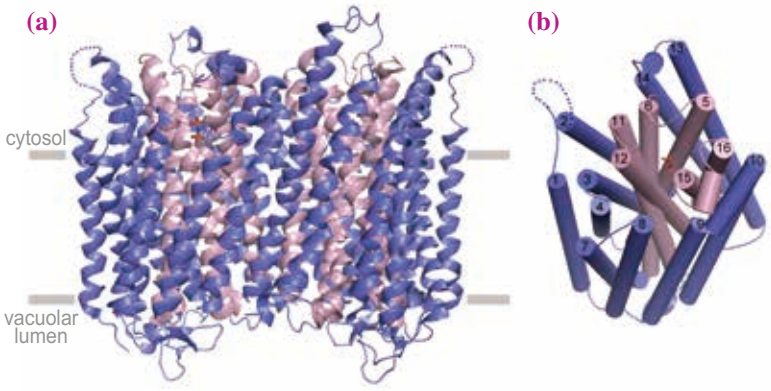

Fig. 1. **(a)** Crystal structure of *Vr*H^+-PPase-IDP complex. **(b)** 16 TMs of *Vr*H^+-PPase.

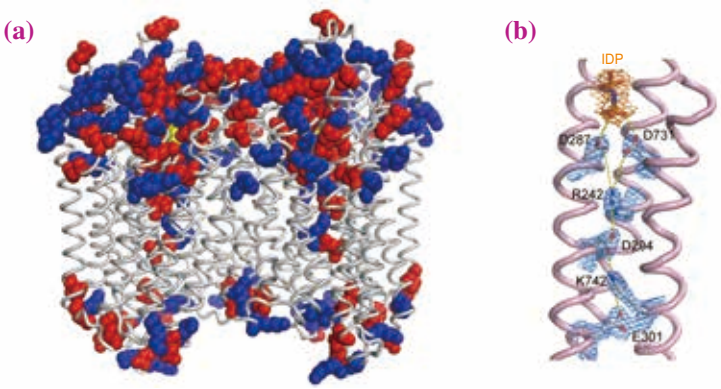

Fig. 2. **(a)** Charged residues of *Vr*H$^+$-PPase-IDP complex. **(b)** Electron density map around the proton transport pathway.

cytosolic region of the channel is solvent-accessible for proton uptake; the middle of the channel is a narrow, compact, and water-restricted route for proton translocation; the vacuolar region is slightly open to enable proton release. Glu301 was completely embedded inside the transmembrane region acting as a constricted neck. Beyond this glutamate are several hydrophobic residues that keep protons of high concentration inside the vacuole from entering the channel. Similar to other proton pumping proteins, two water molecules are confined in the channel of H$^+$-pyrophosphatase to assist the passing of protons. Through a series of protonation and deprotonation among acidic and basic amino acids and bound water molecules in the channel, protons can be translocated from donors and acceptors in a sequential manner.

On the basis of the structure described above and other biochemical studies, a working model for proton translocation in *Vr*H$^+$-PPase was suggested (Fig. 3). Three possible states are indicated: resting state (R-state/ligand free), initiated state (I-state/PP$_i$ bound) and transient state (T-state/ P$_i$ hydrolyzed). In the absence of a substrate (R-state), the structure of the binding pocket in H$^+$-PPase (Fig. 3(a)) is more flexible and rather open to the solvent. In contrast, the lumenal portion of center TMs might orientate into a closed conformation to avoid H$^+$ back reflux to cytosol. Upon substrate (or IDP in our structure) access to the binding site, an initiated state for PP$_i$ hydrolysis (I-state) was formed (Fig. 3(b)). The center transmembrane helices (such as M6 and M16) on the cytosolic side transform into a closed conformation to lock PP$_i$ in the substrate binding pocket. Meanwhile, the lumenal portion of these TMs would be changed to a semi-open conformation for the following H$^+$-translocation. Our structure presents the H$^+$-PPase-IDP complex in an I-state. When PP$_i$ is hydrolyzed, the free phosphate is generated, subsequently followed by proton production (Fig. 3(c)).

In summary, we present that the *Vr*H$^+$-PPase complex is a new transmembrane proton pumping protein of a distinctive folding with an inhibitor IDP bound inside each subunit. A detailed PP$_i$ binding site and the proton pumping pathway are located in close proximity and along a continuous route in the core of *Vr*H$^+$-PPase. A working model is accordingly proposed to reveal the association of PP$_i$ hydrolysis and proton translocation between H$^+$-PPase.

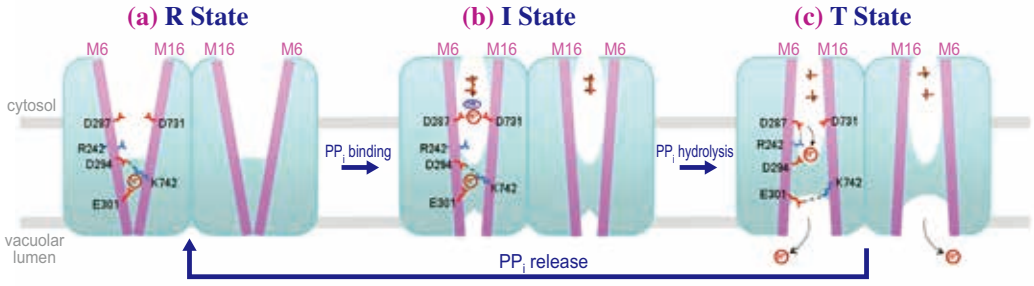

Fig. 3. Working model of proton pumping in *Vr*H$^+$-PPase. **(a)** R state: resting state. **(b)** I state: initiated state. **(c)** T state: transient state.

S.-M. Lin, J.-Y. Tsai, R.-L. Pan and Y.-J. Sun*

Department of Life Science,
National Tsing Hua University, Taiwan

*Email: yjsun@life.nthu.edu.tw

References

[1] F. Marty: Plant Cell **11** (1999) 587.
[2] P. A. Rea and R. J. Poole: Annu. Rev. Plant Physiol. Plant Mol. Biol. **44** (1993) 157.
[3] M. Maeshima: Biochim. Biophys. Acta **1465** (2000) 37.
[4] *S.M. Lin, J.Y. Tsai, C.D. Hsiao, Y.T. Huang, C.L. Chiu, M.H. Liu, J.Y. Tung, T.H. Liu, R.L. Pan, and Y.J. Sun: Nature **484** (2012) 399.*
[5] V. R. Samygina *et al.*: J. Mol. Biol. **366** (2007)1305.

Structure of a presenilin family intramembrane aspartate protease

Alzheimer's disease (AD), a fatal neurodegenerative disease, mostly occurs in elderly people over 65 years of age. However, a rare early-onset AD is diagnosed earlier. With the aging of the population, the incidence of AD is increasing yearly. In 2006, there were approximately twenty-six million AD patients worldwide, and it is estimated that 1 in 85 people will be suffering from this disease by 2050. One of the clinical manifestations of AD is an increasing severity of cognitive impairment, which seriously impacts patients and their families. AD is one of the most expensive diseases in the society of developed countries. However, there is still no effective treatment for this disease.

Recent studies showed that AD is due to the aberrant accumulation of a 42-residue amyloid-β peptide (Aβ42) over a 40-residue product (Aβ40) from an altered cleavage of the amyloid precursor protein (APP), which is caused by mutated presenilin, the catalytic component of γ-secretase. In addition to presenilin, three other components, PEN-2, APH-1 and nicastrin, are also essential for the activity of γ-secretase. Research on the atomic structures of presenilin and γ-secretase will help us to understand the mechanism behind Alzheimer's disease and provide some hints on therapeutic intervention. However, up to now, there has been very limited structural information on presenilin or γ-secretase. This has obviously hampered our understanding of the mechanism of presenilin and γ-secretase, and their relevance to AD.

For protein engineering and the crystallization of PSH, we cloned human presenilin 1 (hPS1) and its eukaryotic homologs from other organisms, such as zebrafish and arabidopsis. For a long time, we have struggled with the low expression level of these targets. We then sought their archaeal homologues. Of 13 archaeal presenilin homologues, only one, from the archaeon *Methanoculleus marisnigri* JR1 (PSH, also known as MCMJR1), could be expressed well and purified successfully. However, its behavior in solution is too poor for crystallization, even after all nonionic detergents are tested. In order to improve the behavior of PSH in solution, we set up a protein engineering system based on the sequence alignment between PSH and other presenilin homologues from archaeal species. First, we replaced the residue of PSH with a residue that is highly conserved between other archaeal homologues at the corresponding positions through sequence alignment. Then, we selected mutations that not only affect its activity but also improve its behavior in solution evaluated by gel filtration, and combined them in the same PSH variant for another cycle selection and possible crystallization trials. Finally, we used V8 protease to delete the flexible surface region for easy crystallization. The PSH used for the final crystallization contained five mutants, D40N, E42S, A147E, V148P, and A229V, and the loop between residues 182 and 209 was also removed. We adopted more than 160,000 crystallization conditions for generating suitable crystals for X-ray data collection.

The high-resolution native data was collected at Shanghai Synchrotron Radiation Facility (SSRF) beamline BL17U. All other diffraction data were collected at SPring-8 beamline **BL41XU**. In order to solve the phase problem, we soaked crystals in a mother liquor containing 2 mM K_2PtCl_4. The platinum-derived crystal was sensitive to radiation damage even at 100 K. We fine-tuned the size of the collimated X-ray beam to maximize the number of exposures on a single crystal to avoid this problem and collected a complete high-redundancy, three-wavelength MAD data set. After more than 100 crystal trials, we finally collected the

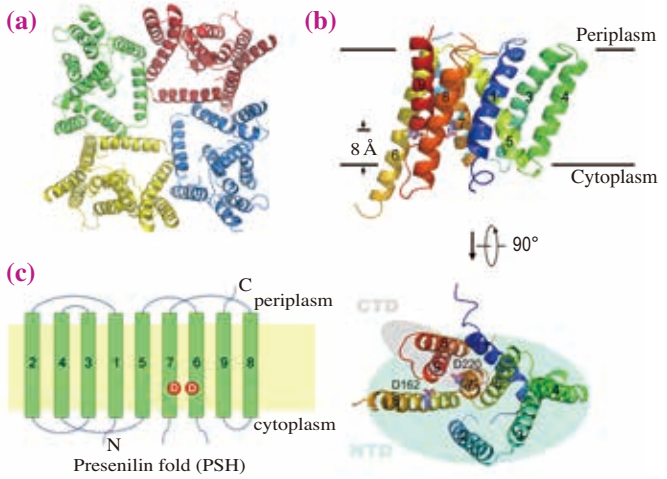

Fig. 1. Overall structure of PSH. **(a)** PSH protein forms a tetrameric complex in *C222* crystals. **(b)** Overall structure of PSH. Nine TMs are divided into NTD (TM1-6) and CTD (TM7-9). Putative catalytic residues Asp 162 and Asp 220 are located on TM6 and TM7, respectively. The structure is rainbow colored, with the N terminus in blue and the C terminus in red. The top and bottom panels represent two perpendicular views. Figures (a) and (b) were prepared using PyMol. **(c)** Membrane topology diagram of PSH. The two putative catalytic residues, Asp 162 and Asp 220, are indicated.

three anomalous data sets from the same crystal with different wavelengths at the peak, inflection, and high-energy remote around the absorption edge of platinum. The PSH variant was crystallized in three space groups, *C222*, $C222_1$, and *P2*. The structure was determined by platinum-based multiwavelength anomalous dispersion (MAD) and refined at 3.3 Å resolution in the *C222* space group with the help of selenium anomalous peak data [1,2].

The structure of PSH protein forms a tetrameric complex in the *C222* crystals (Fig. 1(a)). There are nine transmembrane α-helices in each PSH molecule, which is consistent with previous studies. The amino terminal domain (NTD), comprising TM1–6, forms a horseshoe-shaped structure that partially surrounds TM7–9 of the carboxy terminal domain (CTD). The catalytic residues Asp 162 and Asp 220 in PSH are located at TM6 and TM7, respectively, and approximately 8 Å below the lipid membrane surface from the cytoplasmic side (Fig. 1(b)).

The cleavage of a target peptide within the lipid bilayer by intramembrane protease such as PSH needs the participation of water. Through structural analysis, we find that there is a cavity that links the cytoplasmic side and the two active site aspartates. Water molecules can access catalytic sites without any restriction via this cavity. This finding is also supported by a previous biochemical observation and by the electron microscopic structure study of the γ-secretase complex. The distance between two catalytic aspartates is about 6.7 Å, suggesting the conformation we captured in the PSH crystal structure probably presents a non-active state. After substrate binding, PSH will be active through conformation change. This induced-fit mechanism might protect PSH from non-specific cleavage. Through the analysis of the TM organization of PSH, we find that there are two potential pathways for substrate entry: through the open space between TM6 and TM9 or that between TM2 and TM6. However, there is steric hindrance in the second possibility and the first possibility is supported by previous biochemical evidence.

The topology of PSH is quite different from those of all other membrane proteins of known structures, even rhomboid and S2P one, which are the other two families of intramembrane protease. No entry in the protein data bank is similar to the overall nine transmembranes of PSH, as searched using the DALI program. This suggests that PSH shows a previously unreported protein fold, which we call the presenilin fold (Fig. 1(c)).

The primary sequences of PSH and human presenilin PS1 share more than 50% similarity, especially between the signature motifs for catalysis (Fig. 2). Therefore, the structure features we observed in PSH should be applied to human PS1. Owing to the low expression level and other difficulties in the crystallization process, there is still no atomic structure information on human PS1 or other eukaryotic presenilin homologues. The structure of PSH, an archaeal presenilin homolog, could help us to understand the mechanism of human presenilin and γ-secretase. Furthermore, it will lead to the elucidation of why some mutations on presenilin can cause Alzheimer's disease, enabling us to design small molecules for treating this disease safely and effectively. Future structural studies on other conformations of PSH, especially the activity state, and human presenilin and whole γ-secretase complex will be highly illuminating for this field.

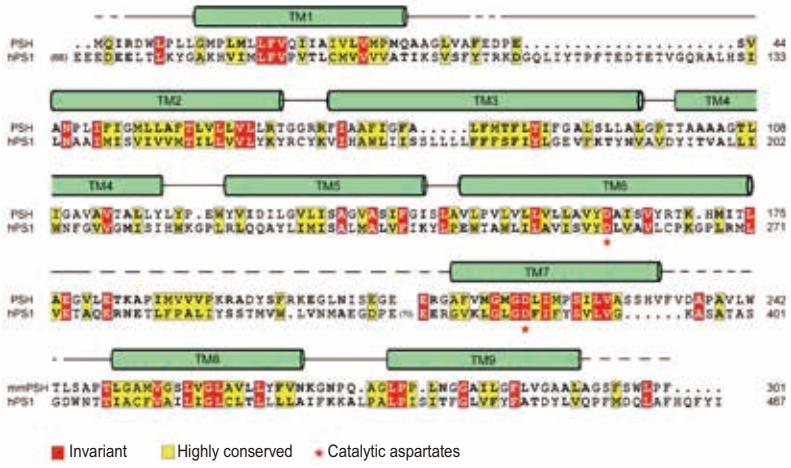

Fig. 2. Sequence alignment of PSH with human presenilin 1 (hPS1). Secondary structural elements of PSH are indicated above the sequences. Invariant and highly conserved amino acids are highlighted in red and yellow, respectively. The two putative catalytic aspartate residues are indicated by red stars. The aligned sequences are PSH (*Methanoculleus marisnigri*, GI: YP_001047832); and hPS1 (*Homo sapiens*, GI: NP_000012). Sequence alignment was carried out using ClustalW.

Shangyu Dang and Yigong Shi*

Center for Structural Biology, Tsinghua University, China

*Email: ygshi@tsinghua.edu.cn

References

[1] *X. Li, S. Dang, C. Yan, X. Gong, J. Wang, Y. Shi: Nature **493** (2013) 56.*
[2] M.S. Wolfe: Nature **493** (2013) 34.

Peristaltic mechanism of bacterial multidrug efflux transport

Multidrug resistance of pathogenic bacteria is a serious problem in current chemotherapy. Multidrug efflux transporters are the major cause of the multidrug resistance of Gram-negative bacteria. Unfortunately, there is no clinically useful drug against multidrug efflux transporters. We first determined the crystal structure of a major multidrug efflux transporter, AcrB, in *E. coli* [1] and then revealed its drug binding structures [2,3].

The most significant characteristic of multidrug efflux transporters is their extraordinarily wide range of substrates including both aromatic and aliphatic compounds. It is difficult to determine the common chemical structures of their substrates. However, multidrug transporters actually distinguish between substrates and others. Our first drug-free structure determination of AcrB in 2002 [1] revealed that it is a homotrimer that acts as a membrane vacuum cleaner, taking up its substrates from the outer surface of the cell membrane and extruding them outside the outer membrane through the outer membrane channel TolC. Since drugs and toxic compounds generally invade cells through the lipid matrix of the cell membrane, this mechanism efficiently stops their invasion at the border. Then, we determined the minocycline- and doxorubicin-binding structures of AcrB in 2006 [2]. Only one drug molecule bound to the AcrB homotrimer. Three monomers show different conformations corresponding to the intermediate steps of drug transport, that is, *access*, *binding*, and *extrusion*. A drug molecule binds only to the *binding* monomer. The *access* and *binding* monomers are inside-open while the *extrusion* monomer is outside-open. Drugs are exported vie ordered conformational change of these three conformations. This mechanism was named the functionally rotating mechanism. When bound minocycline and doxorubicin molecules are superimposed, they only partially overlap. Large parts of both molecules interact with different sets of amino acid residues in their binding site; this is the so-called “multisite-drug binding”, which is a structural basis of multidrug recognition.

As for energy coupling, the driving force of drug efflux is a proton motive force. In the transmembrane region, there are three acidic and basic residues, Asp407, 408 and Lys940, at the middle of TM4 and TM10. In *access* and *binding* monomers, these residues form ion pairs, but in the *extrusion* monomer, the ion pair is dissociated, followed by the two Asp (TM4) and one Lys (TM10) being about 45° twisted in each other probably due to protonation/deprotonation during proton translocation. This conformation change is transmitted to the periplasmic domain to cause a series of conformational changes from *binding* to *extrusion* stages. Therefore, drugs are actively exported by a remote-conformational change.

In 2011, we determined the new drug-binding structures with the high-molecular-weight drugs, rifampicin and doxorubicin (Fig. 1) [3]. Similar to minocycline and doxorubicin, one molecule binds to AcrB trimer, however, surprisingly, the bound monomer is not a *binding* monomer but an *access* monomer. We found an additional multisite drug-binding pocket, named the proximal pocket, active at the *access* stage (Fig. 2). The proximal pocket and the former distal pocket are arranged on the drug translocation channel and separated by a Phe617 loop, which swings, during conformation change from *access* to *binding* stages

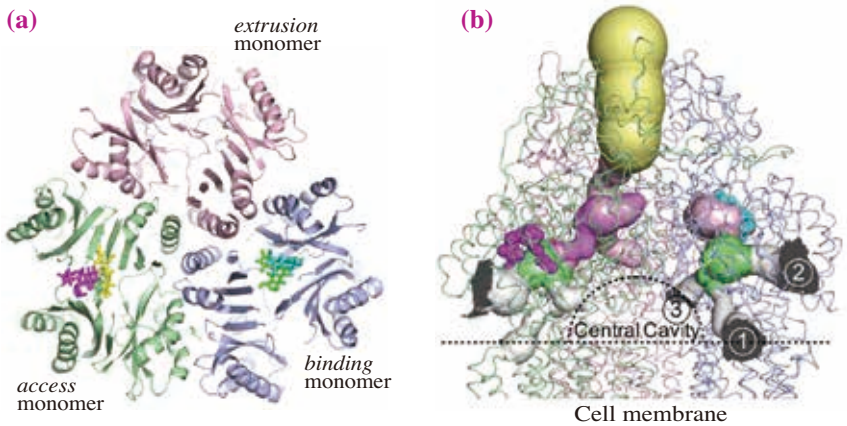

Fig. 1. Drug-binding AcrB structures. **(a)** Horizontal cutaway view of the porter region of AcrB with superimposed bound drugs, rifampicin (purple), erythromycin (yellow), minocycline (blue) and doxorubicin (green). **(b)** Side view of the periplasmic domain of AcrB trimer with intramolecular channels and bound drugs. Intramolecular channels including proximal (green) and distal (pink) binding pockets and the exit funnel (yellow) are depicted by the program CAVER.

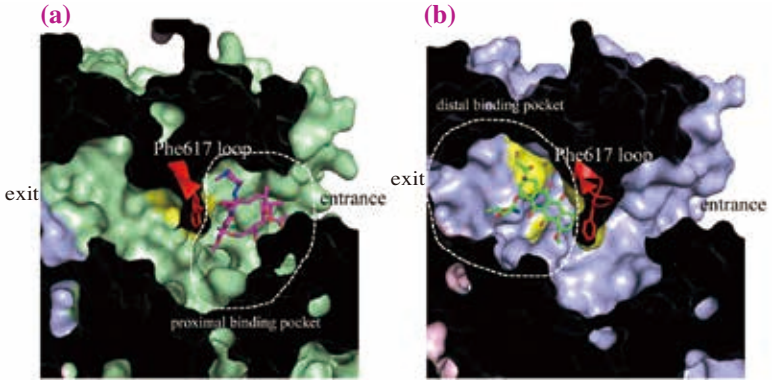

Fig. 2. Cutaway view of the intramolecular channels of the porter region of AcrB. **(a)** Access monomer with bound rifampicin (purple). **(b)** Binding monomer with bound doxorubicin (green). Phe617 loop is depicted in red.

and contributes to the pumping of drugs from proximal to distal pockets. The substrate specificities of both pockets would be different from each other. High-molecular-weight drugs tightly bind to the proximal pocket, and then they are pumped to the distal pocket by protein conformational change and irreversibly occluded in the distal pocket. On the other hand, low-molecular-weight drugs would enter into and tightly bind to the distal pocket without tight binding to the proximal pocket. Therefore, the bindings of high- and low-molecular-weight drugs to the AcrB trimer do not compete with each other. We actually obtained an AcrB crystal in which minocycline and rifampicin simultaneously bind to its distal and proximal pockets, respectively. However, the efflux of distal-binding drugs is competitively inhibited by proximal-binding drugs, indicating that distal- and proximal-binding drugs use the same drug translocation pathway.

In order to verify the role of both pockets in drug transport, we constructed several mutants in proximal and distal pockets. Mutations of proximal residues interacting with proximal-binding drugs showed complete loss of erythromycin (proximal-binding drug) efflux but unaffected doxorubicin (distal-binding drug) efflux. In those mutants, erythromycin no longer inhibits doxorubicin efflux. On the other hand, mutations in distal pocket caused a great decrease in doxorubicin efflux, but only showed a limited degree of effect on erythromycin efflux, indicating that specific interaction with residues in the distal pocket is not necessary for proximal-binding drug transport. The results in this paper revealed that drugs are pumped through the intramolecular translocation channel of AcrB via the entrance → proximal pocket (*access* stage) → distal pocket (*binding* stage) → exit (*extrusion* stage) by a peristaltic motion of the protein (Fig. 3). The presence of dual multidrug binding pockets with different binding spectra would contribute to expanding the substrate specificity. In addition, it should be noted that there are three different entrances that are merged at the proximal pocket (Fig. 1(b)). Three entrances open to the surface of the cell membrane (entrance 1), periplasm (entrance 2) and the central cavity (entrance 3), respectively. Among them, entrances 1 and 2 are proved to act *in vivo* during drug efflux by mutagenesis studies. Such multi-entrances would also contribute to expanding the range of substrates.

In conclusion, our structure determination revealed that the bacterial multidrug efflux transporter is a peristaltic drug efflux pump having dual multisite pockets and multi-entrances. This is the structural basis of this extremely high-performance multidrug efflux pump. These findings should facilitate the structure-based development of efflux-transporter inhibitors.

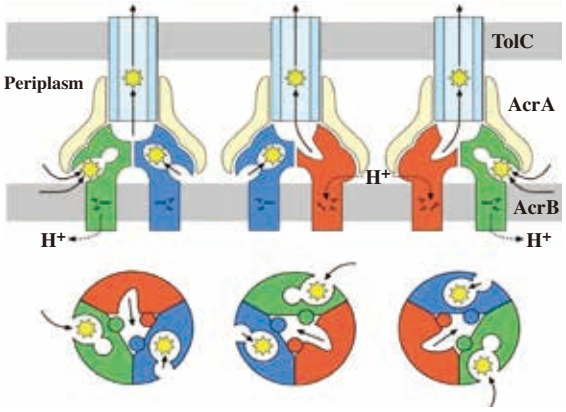

Fig. 3. Peristaltic mechanism of drug transport mediated by AcrB. Drugs first enter into the proxymal pocket at the access stage, translocate to the distal pocket at the binding stage, and finally, are released from the exit at the extrusion stage. Green, blue and red colors indicate the access, binding and extrusion stages, respectively.

Ryosuke Nakashima and Akihito Yamaguchi*

Department of Cell Membrane Biology,
Osaka University

*Email: akihito@sanken.osaka-u.ac.jp

References

[1] S. Murakami *et al.*: Nature **419** (2002) 587.
[2] S. Murakami *et al.*: Nature **443** (2006) 173.
[3] *R. Nakashima, K. Sakurai, S. Yamasaki, K. Nishino and A. Yamaguchi: Nature* ***480*** *(2011) 565.*

Crystal structure of *Shigella flexneri* effector OspI

Many pathogenic gram-negative bacteria such as *Shigella flexneri* deliver virulence factors, called effectors, into host cells via the type 3 secretion system (T3SS) [1]. During bacterial entry into host cells and subsequent intracellular multiplication, the host cells can sense bacterial entry as damage-associated molecular patterns (DAMPs) and bacterial components as various pathogen-associated molecular patterns (PAMPs) by means of cytoplasmic pattern recognition receptors (PRRs), whereby the host cells invoke the alarm signals to activate the innate immune system [2]. To counteract this host defense, some effectors mimic or hijack the host signaling pathway, whereas other effectors interfere with the host's innate immune system. To better understand these mechanisms, we searched for additional *Shigella flexneri* effectors that modulate acute inflammatory responses to bacterial invasion, and we found that OspI plays a pivotal role. In this study, we show that OspI dampens acute inflammatory responses during bacterial invasion by suppressing the tumor-necrosis factor (TNF)-receptor-associated factor 6 (TRAF6)-mediated signalling pathway. We determined the crystal structure of OspI at 2.0 Å resolution. X-ray diffraction data sets for OspI were collected at beamline **BL44XU** [3].

The overall structure of OspI has an α/β fold, with four β-strands (β1-β4), seven α-helices (α1-α7), and a 3_{10} helix. It is organized around a central antiparallel β-sheet, with α-helices packing on both sides of the sheet (Fig. 1). A search of known structures in the Protein Data Bank reveals that OspI shares structural homology with the cysteine protease family and is most closely related to AvrPphB [4] with an r.m.s.d. value of 3.3 Å. AvrPphB is a member of a superfamily of related enzymes containing papain-like cysteine proteases, acetyl transferases, deamidases, and transglutaminases. Although there is considerable divergence across this superfamily in the overall fold, a core anti-parallel β-sheet and an N-terminal helix, which packs against the β-strands, are always present. A potential catalytic triad (Cys62, His145, and Asp160) of OspI was identified through comparison with the active site of AvrPphB. Superimposition of His145 and Asp160 of OspI onto His212 and Asp227 of AvrPphB showed an excellent fit (Fig. 2). Cys62 of OspI, however, existed in three discrete conformations in the crystal structure, and the S_γ position was located on the opposite side of the active site in AvrPphB. This result suggests that the conformational changes at Cys62 are required in the catalytic action. The fractional occupancy of each conformer was estimated

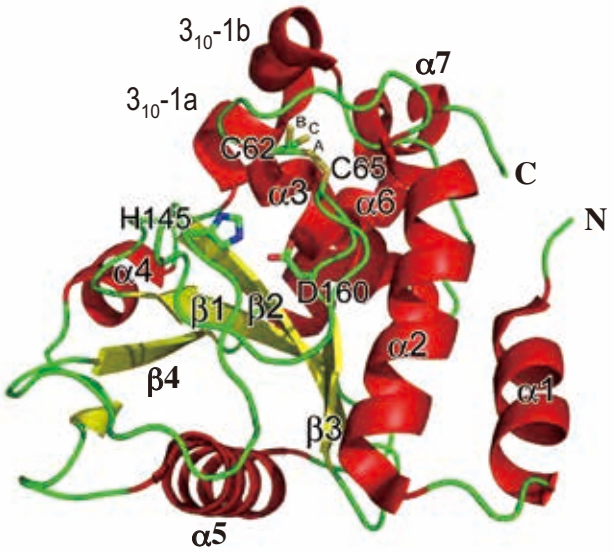

Fig. 1. Overall structure of *S. flexneri* OspI. The secondary structure elements are colored as follows: α-helices, red; β-strands, yellow; and loops, green. The active site residues are shown as stick models.

to be 0.55 (conformation A), 0.35 (conformation B), and 0.1 (conformation C). The highest occupancy site of Cys62 appeared to form a disulphide bond with Cys65 at 2.05 Å (Fig. 2). In this study, we showed that the overexpression of OspI resulted in the strong inhibition of nuclear factor-kappa B (NF-κB) activation with *Shigella* infection. OspI also selectively targeted a diacylglycerol (DAG)-dependent NF-κB signaling pathway. To characterize the active site triad (Cys-His-Asp) identified as the putative OspI catalytic center, we substituted Cys62, His145, and Asp160 with Ser (for Cys62), Ala (for His145), and Ala (for Asp160), and the resulting OspI mutants were investigated for their abilities to suppress the NF-κB activation. The elevated levels of IκBα phosphorylation and *IL-8* induction by *Δosp* infection were cancelled when infected with *ΔospI* mutant complemented by introducing each of the plasmids encoding the *ospI* (*C62S*), *ospI* (*H145A*), or *ospI* (*D160A*) gene. Consistent with this, the NF-κB reporter assay showed that OspI (C62S), OspI (H145A), and OspI (D160A) lost the ability to suppress the NF-κB activity stimulated by *Shigella*. These results supported that Cys62, His145, and Asp160 residues in OspI form the catalytic triad for suppressing NF-κB signaling.

We next investigated which of the steps in

the DAG- CARDs (CARD9, 10, 11, and 14)-Bcl10-Malt1 (CBM) complex -TRAF6-IKKβ-NF-κB pathway becomes the target for OspI. On the basis of the results in the series of experiments, we concluded that OspI interferes with TRAF6 activation in *Shigella* infection. TRAF6 is an E3 ubiquitin ligase cooperating with Ub-activating E1 and Ub-conjugating E2, such as Ubc13 and ubiquitin E2 variant (UEV1A), and to enable of self-ubiquitination, TRAF6 functions with heterodimer E2, which consists of Ubc13 and Uev1A, to synthesize K63-linked polyubiquitin chains on target proteins and TRAF6 itself [5]. This K63-linked poly-ubiquitination leads to the activation of the downstream signaling pathway. We investigated the effect of OspI on the electrophoretic mobility in a native PAGE upon incubation of OspI with each of the putative targets (TRAF6, Ubc13, Uev1A, or Ub) and found that only Ubc13 underwent mobility shift in the OspI dose-dependent manner. Hence we investigated how OspI post-translationally modified Ubc13, using LC-MS/MS. The results showed that the two overlapped tryptic digested peptides of Ubc13 underwent deamidation at Gln100 to Glu100 with OspI. To confirm deamidation of Ubc13 with OspI, we created Ubc13 (Q100E) and found it to have the same mobility shift as that of Ubc13 with Gln100 modified with OspI, but not OspI C62A, H145A, or D160A. On the basis of these results together with the capability of OspI to interact with Ubc13 *in vitro*, we concluded that OspI targets Ubc13 and causes deamination at Ubc13 Gln100, which resulted in dampening of the TRAF6-NF-κB pathway. Here, we identify OspI as a new class of T3SS effector able to selectively deamidate Ubc13, an E2 ubiquitin ligase involved in TRAF6 polyubiqitination, whereby *Shigella* can block the acute NF-κB-mediated inflammatory response at the early stage of invasion of epithelial cells (Fig. 3).

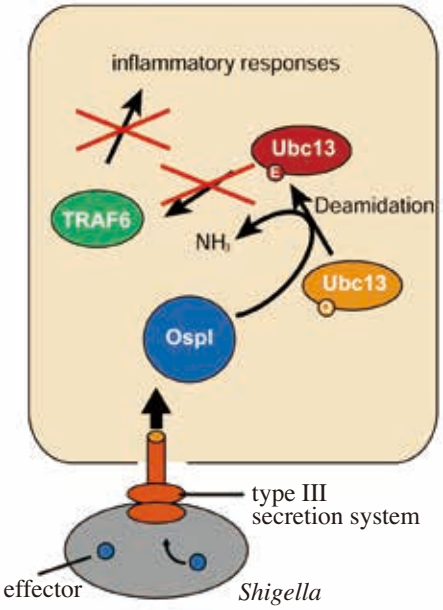

Fig. 3. *Shigella* inhibits acute inflammatory responses at the initial stage of infection. OspI acts as a glutamine deamidase and selectively deamidates Gln100 to Glu100 in Ubc13.

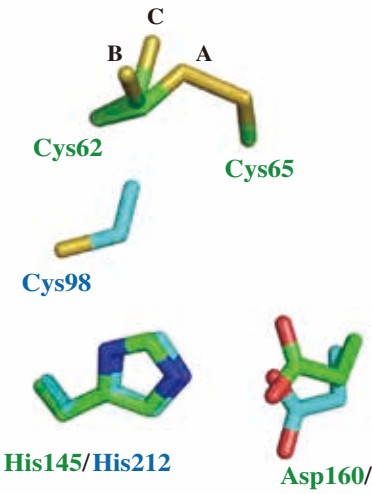

Fig. 2. Alignments of the catalytic cores of OspI with *P. syringae* AvrPphB. All atoms of histidine and the main chain atoms of aspartic acid are shown as reference. *S. flexneri* OspI (PDB ID 3B21: green) and AvrPphB (PDB ID 1UKF: cyan) are shown. C62 in OspI is represented in three alternative conformations with the three conformers labeled A, B, and C.

T. Mizushima[a,*], T. Sanada[b], M. Kim[c] and C. Sasakawa[c,d]

[a] Department of Life Science, University of Hyogo
[b] Dept. of Infectious Disease Control, Institute of Medical Science, The University of Tokyo
[c] Div. of Bacterial Infection Biology, Institute of Medical Science, The University of Tokyo
[d] Nippon Institute for Biological Science

*Email: mizushi@sci.u-hyogo.ac.jp

References

[1] M. Kim *et al.*: Cell Host Microbe **8** (2010) 20.
[2] O. Takeuchi and S. Akira: Cell. **140** (2010) 805.
[3] *T. Sanada, M. Kim, H. Mimuro, M. Suzuki, M. Ogawa, A. Oyama, H. Ashida, T. Kobayashi, T. Koyama, S. Nagai, Y. Shibata, J. Gohda, J. Inoue, T. Mizushima and C. Sasakawa: Nature* ***483*** *(2012) 623.*
[4] M. Zhu *et al.*: Proc. Natl. Acad. Sci. USA **101** (2004) 302.
[5] Z.J. Chen: Nat. Cell Biol. **7** (2005) 758.

The 2.8 Å crystal structure of dynein motor domain

Dyneins are large motor complexes of 1–2 MDa that use ATP as an energy source to move toward the minus ends of microtubules [1,2]. This motor activity is crucial for a variety of cellular processes within eukaryotic cells, including the beating of cilia and flagella, cell division, cell migration, and the intracellular trafficking of various vesicles and organelles along microtubules. Dyneins power a wide range of cellular motility through the coordinated action of a number of subunits of the dynein complex together with various associated cellular components. Among them, the heavy chain (molecular mass ≥500 kDa), belonging to the AAA$^+$ superfamily of mechanochemical enzymes, is solely responsible for dynein's fundamental motor activity. Truncation studies have shown that the C-terminal 380 kDa portion of the heavy chain alone is sufficient to exert the motor activity, thus defining this portion as the dynein motor domain.

Here, we report the 2.8 Å crystal structure of the 380 kDa motor domain of *Dictyostelium discoideum* cytoplasmic dynein [3]. The X-ray diffraction data sets were collected at beamline **BL44XU**. The motor domain comprises the AAA$^+$ ring and three additional structural units: the linker, stalk/strut, and C-sequence (Fig. 1). The central ATP-hydrolyzing ring has six AAA$^+$ modules arranged around the ring central pore. Above the ring's front face, the linker exists as a rod-like structure extending from AAA1 above the ring to the periphery of AAA4. Between AAA4 and 5, two prominent coiled coils protrude and form a Y-shaped structure. The longer coiled coil extending from AAA4 is the stalk that includes the small microtubule-binding site (MTBD) at the tip, and the shorter one extending from AAA5 is the strut that appears to support the microtubule-binding stalk. On the ring's back face, the C-sequence exists as a complex structure comprising six α-helices and an incomplete six-strand antiparallel β-barrel, which spreads over AAA1, 5, and 6.

In the present structure, four ADP molecules are bound to the first four AAA$^+$ modules of the ring (Fig. 2, upper right). The results of detailed structural analyses suggest that dynein has three ATP hydrolysis sites—AAA1, 3, and 4, and one unique ATP and/or ADP binding site, AAA2. Our pre-steady-state kinetic analysis further supports this notion and highlights the importance of the AAA1 ATPase site in dynein motor function. In addition, the ring structure suggests the existence of an ATPase-dependent open/closed transition of the AAA1 and AAA4 ATPase sites, which may affect the ring structure during dynein's mechanochemical actions.

To understand the mechanism of dynein motility, it is critical to elucidate the structural details of interactions between the ATP-hydrolyzing ring and the linker whose swing-like motions have been proposed to be the major contributor to dynein's powerstroke. In the present structure, the linker position is close to that of the post-powerstroke state inferred from the results of EM analysis. When viewed from the ring's front face, the linker appears to bridge AAA1 and AAA4 by spanning the inner edges of AAA2, 3, and 4 (Fig. 2, left). However, as is evident from the side view, there is no direct contact between the linker and AAA3–AAA5, and two finger-like structures, the H2 insert β-hairpin

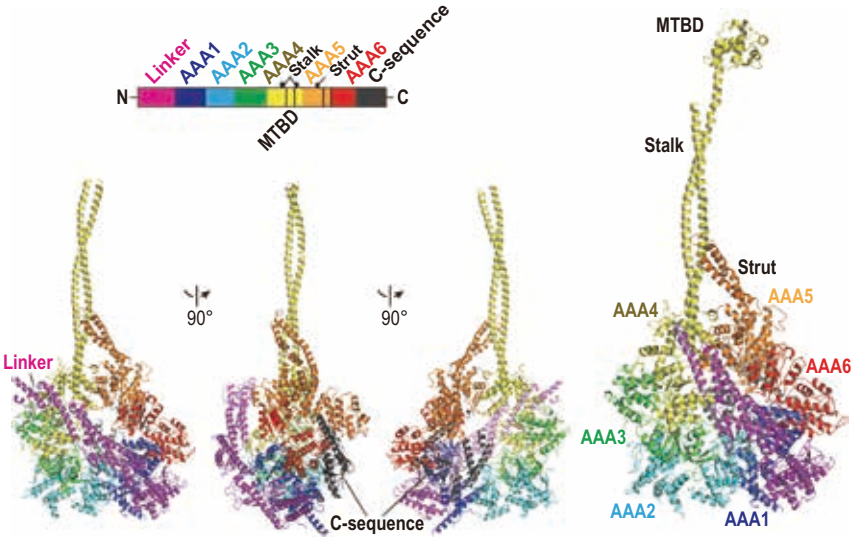

Fig. 1. Structure and sequence diagram of dynein motor domain, showing functional units: linker, six AAA$^+$ modules constituting ring, stalk/strut, and C-sequence.

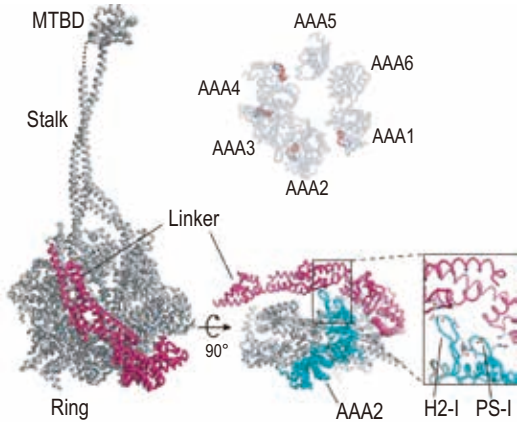

Fig. 2. Front and bottom views of the dynein motor domain showing the four ADP molecules bound to AAA1-AAA4 and the interaction interfaces between the linker and the ring.

and the PS-1 insert loop, protruding from AAA2 are identified as the major interaction interfaces between the linker and ring (Fig. 2, lower right). Our mutational analysis of the H2/PS-1 inserts suggests the critical involvement of the H2/PS-1 inserts in linker swing actions. Then, how do the H2/PS-1 inserts contribute to the force-generating linker swing? In some AAA+ proteins, the H2/PS-1 inserts serve as interaction interfaces with target proteins or DNA to catch and remodel the targets. Thus, our structural and functional analyses show that dynein also uses this remodeling apparatus for the linker swing. We thus hypothesize that during the mechanochemical cycle of dynein, the H2/PS-1 inserts could remodel the linker so that the linker bends around the interaction sites and swings against the ring.

Another key question regarding the dynein mechanism is how the motor coordinates MT binding at the MTBD of the stalk with the primary ATPase at AAA1, which must be communicated over a long distance through several structural units. A widely held assumption is that the information would be propagated through AAA1, 2, 3 and 4 in an ATPase-related manner analogous to other AAA+ proteins, because the first four modules, but not AAA5 or 6, have adenine nucleotide-binding or ATP-hydrolyzing activity. However, mutagenesis of the nucleotide binding sites in AAA2–4 does not completely block the communication between AAA1 and MTBD, and thus does not support this hypothesis. Instead, we propose that the back face sides of AAA5 and 6, that is, the C-sequence and strut, serve as a form of communication, based on the structural feature that these structures directly bridge AAA1 and the stalk (Fig. 3). In support of this model, we have shown that deletion of the C-sequence or the strut from the motor domain results in deregulation of both the microtubule-binding and ATPase activities.

In summary, the dynein motor domain structure at 2.8 Å resolution reveals the unique composite architecture of the AAA+ ATPase ring and dynein-specific force-generating units (linker, stalk/strut, and C-sequence). It also provides new insights into how dynein exploits the unique architecture to generate force and movements along MT. We propose that dynein uses the two distinct molecular machineries embedded on the different ring faces to execute the two fundamental motor actions required for dynein motility: driving of the linker swing for the powerstroke and allosteric regulation of MTBD for the modulation of MT-binding affinity. On the ring's front face, the linker swing could be driven by similar mechanisms as those of remodeling actions in other AAA+ ATPases through the critical participation of the remodeling apparatus, H2/PS-I inserts of AAA2 (Fig. 2). On the ring's back face, the long-range allosteric communication between AAA1 and MTBD required for coupling of the ATPase cycle with the switching of MT affinity could be relayed through dynein-specific structures, i.e., stalk, strut, and C-sequence (Fig. 3). The general AAA+ ATPase-type and dynein-specific actions coordinated by the primary ATPase cycle at AAA1 would drive dynein motility.

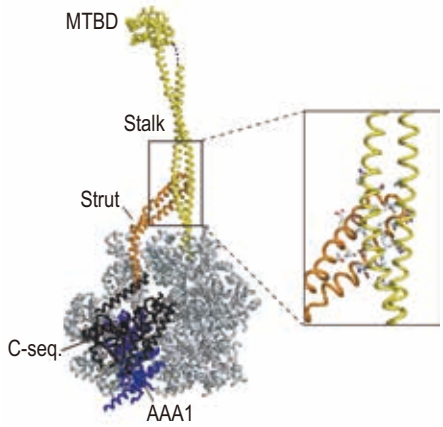

Fig. 3. Back view of the dynein motor domain showing the proposed allosteric communication pathway between the MTBD at the tip of the stalk and the AAA1 ATPase site in the ring. To facilitate visualization of the pathway, a portion of AAA5 (AAA5-extension) is not shown.

Takahide Kon[a,b,*] and Genji Kurisu[a,b]

[a] Institute for Protein Research, Osaka University
[b] Department of Macromolecular Science, Osaka University

*Email: takahide.kon@protein.osaka-u.ac.jp

References

[1] I.R. Gibbons, A.J. Rowe: Science **149** (1965) 424.
[2] B.M. Paschal, R.B. Vallee: Nature **330** (1987) 181.
[3] *T. Kon, T. Oyama, R. Shimo-Kon, K. Imamula, T. Shima, K. Sutoh, G. Kurisu: Nature **484** (2012) 345.*

Crystal structure of CENP-TWSX: A novel histone-fold complex at eukaryotic centromere

During eukaryotic cell division, each and every one of replicated chromosome is faithfully segregated into two daughter cells to keep their genome integrity. Failure in this process could result in chromosome instabilities, which may cause cell death, genomic disorder or even tumor formation. To prevent such catastrophic events, cells tightly regulate the chromosome segregation.

Two mechanisms coordinate to ensure faithful chromosome segregation. One is sister chromatid cohesion which hold the two sister chromatids upon their generation during replication until the onset of anaphase. Another is microtubule attachment to chromosomes. In mitosis, spindle microtubules emanate from two daughter centrosomes and capture chromosomes (Fig. 1(a)). Only the chromosome that is correctly captured by microtubules from two different centrosomes generates a tension that is balanced between the pulling force from microtubules and the resisting force from sister chromatid cohesion. These bi-oriented chromosomes are aligned to metaphase plate during mitosis. Other attachments are futile and are corrected by spindle checkpoint pathway. When all the chromosomes are correctly captured and aligned to metaphase plate, spindle checkpoint is released. This enables sister chromatid cohesion to be dissolved and segregates chromosomes into two daughter cells to complete mitosis.

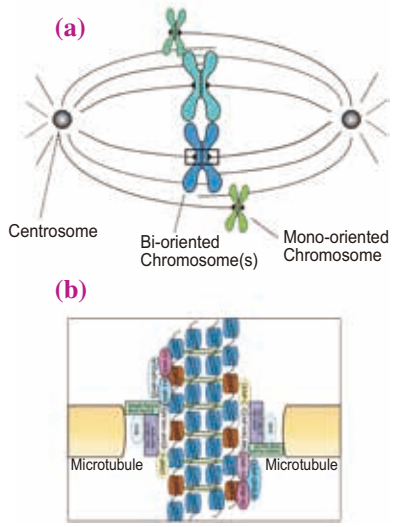

Fig. 1. **(a)** Schematic diagram of eukaryotic chromosome segregation. Replicated chromatids are shown as X-shape and kinetochore is formed at each chromosome denoted by black circles. Spindle microtubules emanate from centrosomes and capture chromosomes through kinetochore. Bioriented chromsomes that are captured by two spindle microtubules align to the metaphase plate. **(b)** Close-up view of the centromere-microtubule attachment site boxed in (a). Only major kinetochore components that are involved in chromosome-microtubule attachments are depicted. Two sister chromatids are held together by sister chromatid cohesion rings.

Robust binding between chromosome and microtubule is mediated by proteinacious structure called a kinetochore that is built at the centromeric region on chromosome [1]. Proteomic analysis of eukaryotic kinetochore revealed that it is comprised of more than 100 components. The function of these components varies from protein-protein interaction to protein-nucleic acid interaction (Fig. 1(b)). These components form an intricate network to connect chromosome and microtubules. One of the mysteries that remain in the field is how the centromere DNA is connected to the microtubule.

To address this question we identified the putative DNA binding kinetochore complexes from both human and chicken cells and analyzed them. CENP-S, -T, -W, and -X are kinetochore components containing histone fold within its sequence. CENP-T and CENP-W forms a heterodimer and CENP-S and CENP-X forms a heterodimer [2,3]. CENP-T and -W are essential for cell viability and deletion/knockdown of CENP-S or CENP-X also causes chromosome segregation defect, although cells with their knockout are still viable. To understand the structural basis of these complexes, we crystallized chicken CENP-TW histone fold and chicken CENP-SX. Diffraction data were collected at **BL38B1** and **BL44XU**. Both CENP-TW and CENP-SX structures were determined by selenium single anomalous dispersion using selenomethionine derivative crystals. Mercury derivative was also used for determination of CENP-SX crystal structure. CENP-TW was a heterodimer and CENP-SX was a tetramer (Figs. 2(a) and 2(b)) [4]. Overall structure of both CENP-TW and CENP-SX was similar to canonical histones and other histone fold complexes. In addition to three helices which are conserved among histone fold proteins, CENP-T contained two extra helices at its carboxyl-terminus (C-terminus) which formed a v-shape. CENP-S similarly contained an extra helix at its C-terminus. Apart from these regions, CENP-T contains ~500 residues of flexible amino-terminus (N-terminus) and CENP-S contains ~40 residues of C-terminal basic tail. Both regions were omitted from crystallization. Surface charge plot of CENP-TW and CENP-SX revealed that both proteins were highly basic and in particular, CENP-TW was globally positively charged with pI of 10.1 whereas pI of CENP-SX was 8.7 (Fig. 2(a) and 2(b)). Based on *in vitro* DNA binding experiment using naked double stranded DNA, we demonstrated that these complexes indeed associate with DNA [4].

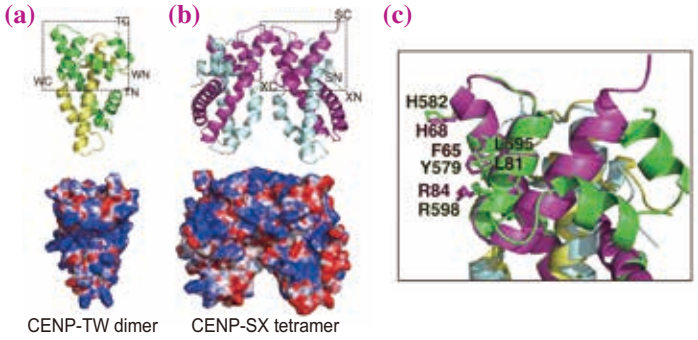

Fig. 2. **(a)** Crystal structure and electrostatic potential of CENP-TW dimer. CENP-T and CENP-W are shown in ribbon diagram and are shown in green and in yellow, respectively. N and C terminus of T or W are labeled. **(b)** Crystal structure and electrostatic potential of CENP-SX tetramer. CENP-S and CENP-X are shown in ribbon diagram and are shown in magenta and cyan, respectively. N and C terminus of S or X are labeled as in (a). **(c)** superposition of CENP-TW and CENP-SX dimer. Boxed regions in (a) and (b) are superimposed. Residues shown in stick model are conserved between CENP-T and CENP-S.

More intriguing fact upon structure determination was that CENP-SX and CENP-TW are more similar to each other than to other histones (Fig. 2(c)). The similarity between the two complexes was also observed in the regions within CENP-SX involved in tetramer formation. Although CENP-TW only forms a dimer in solution, the residues were almost identical. This suggested that CENP-SX and CENP-TW might form a higher order complex. Upon mixture, CENP-SX and CENP-TW formed a stoichiometric complex. We further purified the complex and crystallized them. Two different crystal forms were obtained and the diffraction data were collected at **BL38B1** and **BL44XU**. The structure was determined by molecular replacement using CENP-TW and CENP-SX heterodimer as a template (Fig. 3(a)). Crystal structure visualized the details of CENP-TWSX complex and they formed a heterotetramer using the conserved tetramer interface (Fig. 3(b)) [4].

Biochemical analysis of CENP-TW, CENP-SX, and CENP-TWSX showed that they all possess supercoiling activity and wrapped DNA using basic regions [4]. However, CENP-TW, CENP-SX and CENP-TWSX bound to DNA with different mode. CENP-TW and DNA formed a larger complex upon mixture and there was no distinct complex. On the other hand, CENP-SX had a preference toward ~50 bp dsDNA while CENP-TWSX favored ~80 bp dsDNA. Micrococcal nuclease digestion showed that CENP-TW binds tightly and CENP-SX binds less tightly. CENP-TWSX heterotetramer binding was intermediate showing that this new complex possesses characteristics of both complexes. We created a chicken DT40 cell line in which wild-type CENP-T was replaced with tetramer defective CENP-T mutant and found that the tetramer defective CENP-T mutant did not recruit CENP-S or CENP-X to kinetochore and these cells fail to build functional kinetochore [4]. Similarly, we demonstrated that DNA binding mutant of CENP-TW or CENP-SX loses kinetochore integrity *in vivo*. Thus, we conclude that CENP-TWSX complex forms a structural core for kinetochore formation on centromere using its DNA binding activity.

In addition to the histone fold complex, both chicken and human CENP-T contain long flexible N-terminus where most of the region is predicted to be unstructured. Within the extreme N-terminal 100 residues, there are several cyclin-dependent kinase (CDK) phosphorylation sites and these sites are phosphorylated during mitosis [5]. Phosphorylation of CENP-T enables Ndc80 complex to associate to centromere and this complex binds microtubules. It has recently been shown that homologous complex is conserved not only in higher eukaryotes but also in fission yeast, filamentous fungi and budding yeast. Thus, CENP-TWSX complex seems to be present in most eukaryotes to form a new centromeric chromatin structure and to build kinetochore structure.

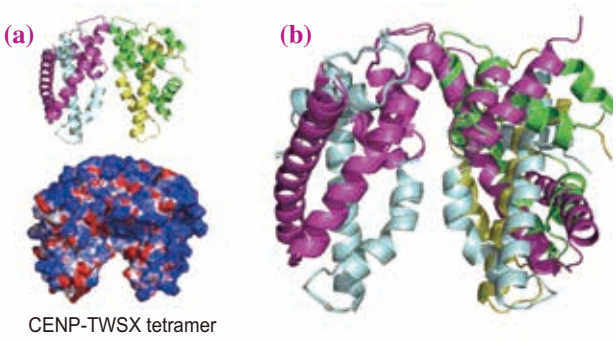

Fig. 3. **(a)** Crystal structure and electrostatic potential of CENP-TWSX tetramer. CENP-T, -W, -S and -X are shown in ribbon diagram. Coloring scheme is same as in Fig. 2. **(b)** Superposition of CENP-SX tetramer and CENP-TWSX tetramer. Two tetramers were aligned through CENP-SX.

Tatsuya Nishino and Tatsuo Fukagawa

Dept. of Molecular Genetics, National Institute of Genetics
The Graduate University for Advanced Studies (SOKENDAI)

*Email: tnishino@nig.ac.jp

References

[1] M. Perpelescu and T. Fukagawa: Chromosoma **120** (2011) 425.
[2] T. Hori *et al.*: Cell **135** (2008) 1039.
[3] M. Amano *et al.*: J. Cell Biol. **186** (2009) 173.
[4] *T. Nishino, K. Takeuchi, K.E. Gascoigne, A. Suzuki, T. Hori, T. Oyama, K. Morikawa, I.M. Cheeseman and T. Fukagawa: Cell **148** (2012) 487.*
[5] K.E. Gascoigne *et al.*: Cell **145** (2011) 410.

Crystal structure of Zucchini, an essential endoribonuclease for piRNA biogenesis

PIWI-interacting RNAs (piRNAs) are expressed in animal germlines and silence transposable elements, thereby maintaining genome integrity [1]. piRNAs are generated through two distinct biogenetic pathways: the primary processing pathway and the secondary ping-pong cycle. *Drosophila melanogaster* has three PIWI proteins (Piwi, AUB and AGO3). Piwi is expressed in ovarian somatic cells and participates in the primary pathway, whereas AUB and AGO3 are expressed in ovarian germ cells and participate in the secondary ping-pong cycle. piRNAs are initially transcribed as a long non-coding RNA precursor from repetitive genomic regions called piRNA clusters (Fig. 1). piRNA precursors are then processed into mature piRNAs by unknown nucleases, and loaded into Piwi in the primary processing pathway. Genetic and biochemical studies revealed that a number of proteins are involved in the primary processing pathway. These include the putative RNA helicase Armitage, and the Tudor domain-containing RNA helicase Yb, which are both localized in Yb bodies, cytoplasmic perinuclear non-membranous organelles, and the putative nuclease Zucchini (Zuc), which are localized on the outer surface of mitochondria.

Zuc consists of an N-terminal mitochondrial localization sequence, a putative transmembrane helix, and a catalytic domain belonging to the phospholipase D (PLD) superfamily, which is characterized by the His-Lys-Asp (HKD) motif. The PLD superfamily members cleave the phosphodiester bond in different substrates, thereby participating in a variety of cellular processes. The PLD superfamily includes a number of enzymes with different substrate specificity, such as PLD, which degrades lipid substrates, and the bacterial nuclease Nuc, which degrades nucleic acid substrates. Zuc shares the highest sequence similarity with Nuc among the PLD superfamily members, suggesting that Zuc may be a ribonuclease involved in piRNA biogenesis. However, previous studies failed to detect the nuclease activity of Zuc. Thus, the molecular identity of a piRNA processing ribonuclease remains elusive, and the molecular mechanism by which Zuc is involved in primary piRNA biogenesis remains unknown.

To understand Zuc's function, we set out to solve the crystal structure of *D. melanogaster* Zuc. The cytoplasmic region of Zuc was expressed in *Escherichia coli*, purified, and crystallized [2]. X-ray diffraction data were collected at beamline **BL32XU**. We solved the crystal structure of Zuc at 1.75 Å resolution by the MAD method using a selenomethionine-labeled protein [3]. The crystal structure revealed that the cytoplasmic region of Zuc consists of a catalytic domain and a zinc-binding domain (Fig. 2(a)). Zuc forms a dimer, in which His169 and Lys171 in the HKD motif in the two molecules create an active-site groove at the dimer interface. The catalytic domain consists of an eight-stranded mixed β-sheet flanked by α-helices on both sides, and shares structural similarity with the other PLD superfamily members. Secondary structure prediction suggested that, unlike other PLD superfamily members, Zuc may have a disordered region between the first β-strand and α-helix in the catalytic domain. The crystal structure revealed that this region unexpectedly forms the zinc-binding domain, in which

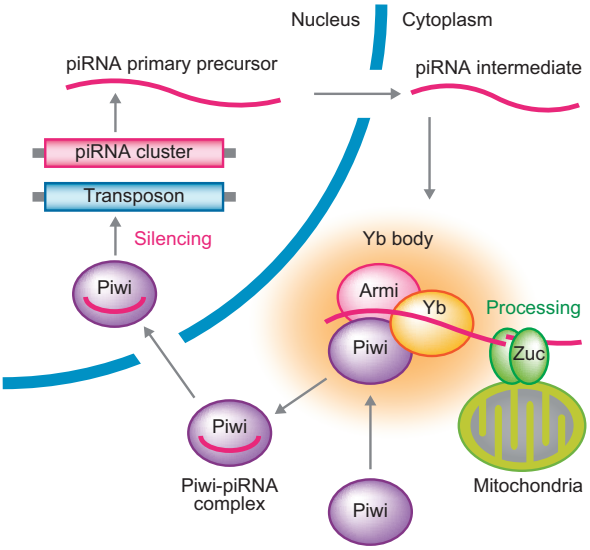

Fig. 1. Model of primary piRNA biogenesis in *D. melanogaster*.

a zinc ion is coordinated by three cysteine residues and one histidine residue. A structural comparison of Zuc with Nuc revealed a notable difference in their active-site grooves. Nuc has a wide, positively charged groove that can accommodate double-stranded nucleic acids (Fig. 2(b)), which is consistent with the data showing that Nuc cleaves both a single-stranded RNA (ssRNA) and a double-stranded RNA (dsRNA). In contrast, Zuc has a narrow catalytic groove, which appears to accommodate ssRNA but not dsRNA (Fig. 2(a)). Zuc has a positively charged surface on the side opposite to the active site, where the N termini of the two molecules are located, which is consistent with the previous data showing that Zuc is localized on the outer mitochondrial membrane. Together, our structural analysis indicated that Zuc is a single-strand-specific nuclease that functions on the mitochondrial surface.

We examined the nuclease activity of Zuc by *in vitro* cleavage assays using radiolabelled synthetic RNAs, and found that Zuc cleaved ssRNA substrates in a non-sequence-specific manner. The mutant Zuc proteins, including H169A and K171A, failed to cleave the ssRNA substrate, confirming the functional significance of the active-site groove. The Zuc mutant lacking the zinc-binding domain showed reduced ssRNase activity, indicating the involvement of the zinc-binding domain in ssRNA binding. Zuc cleaved ssRNA but not dsRNA, indicating that Zuc is a single-strand-specific nuclease. Zuc also cleaved circular ssRNA, indicating that Zuc is an endonuclease. MmZuc also showed ssRNase activity, confirming that Zuc is an evolutionarily conserved nuclease. The cleavage products possess a 5' monophosphate, a hallmark of mature piRNAs bound to Piwi. We further examined the biological relevance of the nuclease activity of Zuc for transposon silencing by plasmid rescue experiments in ovarian somatic cells. We found that wild-type Zuc, but not the active-site mutants showing no ssRNase activity, rescued transposon derepression, indicating that the nuclease activity of Zuc is critical for transposon silencing *in vivo*. Together, our functional analysis revealed that Zuc is a single-stranded-specific endoribonuclease that defines the 5' end of mature piRNAs. We thus propose a model for primary piRNA biogenesis in animal germlines, in which Zuc acts as an endoribonuclease in primary piRNA maturation (Fig. 1).

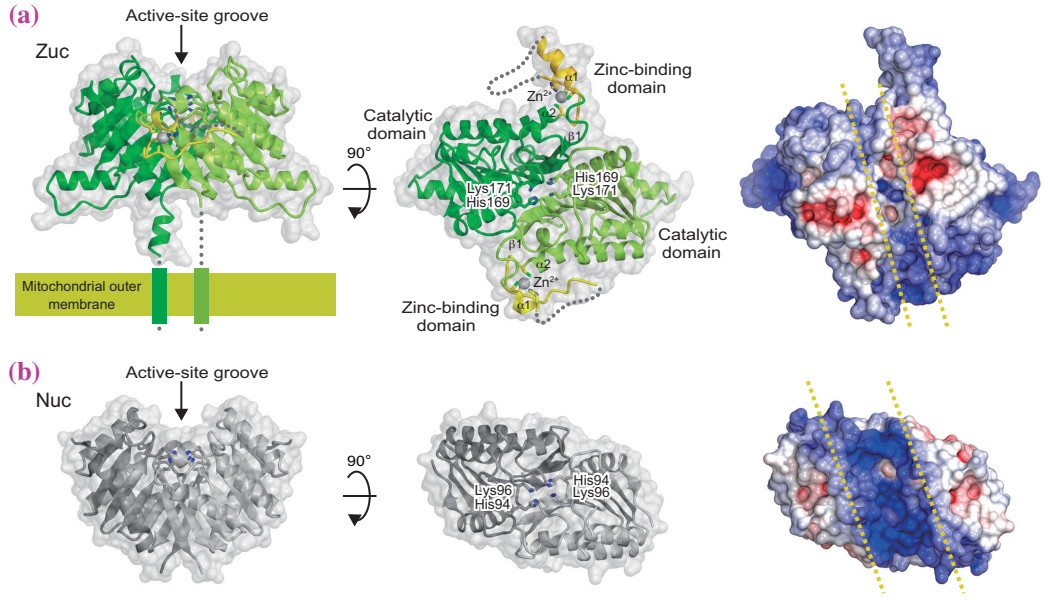

Fig. 2. **(a)** Crystal structure of Zuc. **(b)** Crystal structure of Nuc (PDB: 1BYR). Yellow dashed lines indicate the positively charged active-site groove.

Hiroshi Nishimasu* and Osamu Nureki

Department of Biophysics and Biochemistry, The University of Tokyo

*Email: nisimasu@biochem.s.u-tokyo.ac.jp

References

[1] M.C. Siomi *et al.*: Nat. Rev. Mol. Cell. Biol. **12** (2011) 246.
[2] S. Fukuhara *et al.*: Acta Crystallogr. F Struct. Biol. Cryst. Commun. **68** (2012) 1346.
[3] *H. Nishimasu, H. Ishizu, K. Saito, S. Fukuhara, M. K. Kamatani, L. Bonnefond, N. Matsumoto, T. Nishizawa, K. Nakanaga, J. Aoki, R. Ishitani, H. Siomi, M. C. Siomi, O. Nureki: Nature **491** (2012) 284.*

Life Science:


"Sazanka"- *Camellia sasanqua*

Calmodulin is a ubiquitous protein that plays a major role in intracellular signal transduction in most mammalian cells. When the intracellular Ca^{2+} level increase, calmodulin binds Ca^{2+} and then binds to a target protein to modify its function. In the work of Yamada *et al.*, the structural change of calmodulin after Ca binding was studied at a submillisecond time resolution by small-angle X-ray scattering (SAXS) analysis. There were three state-of-the art techniques used in this experiment. One is the high flux beamline BL40XU that provides 10^{15} photons per second. To avoid radiation damage by the intense X-rays, the sample was continuously moved at a speed of 5 cm/s during the X-ray exposure. The second technique was the use of caged Ca that releases Ca^{2+} upon laser irradiation. The third was the X-ray detector that consists of a high-speed (short afterglow) X-ray image intensifier and a fast CMOS camera. By combining these techniques, a continuous time-resolved measurement of calmodulin upon Ca binding was made at a time resolution of 500 μs. As far as I am aware, this is the first time in the world structural change of a protein was continuously followed by SAXS at a time resolution higher than 1 ms. The results showed that calmodulin undergoes a temporary compact conformation within 20 ms after binding Ca, and this conformation is stabilized when calmodulin further binds to a target peptide. This transient state of calmodulin may have significance in cells where the Ca level can fluctuate spuriously.

Tanaka *et al*. from Glico Co. conducted a microbeam diffraction experiment on tooth enamel to investigate the effect of a chemical compound (phosphoryl oligosaccharide, POs-Ca) that is contained in a chewing gum. This compound is hypothesized to bind Ca and maintain a high level of Ca solubilized in the mouth, which facilitates remineralization of caries in the early stage. As expected, in a remineralization experiment on bovine enamel, a solution containing POs-Ca was more effective than just Ca and phosphate. POs-Ca was

Medical Biology

found to enhance the growth of hydroxyapatite crystallites in enamel. This provides structural evidence of the preventive function for POs-Ca to dental caries.

The phase-contrast CT technique that has been implemented by Hoshino and Uesugi at SPring-8 often produces stunning images of samples. This has already been demonstrated on the eye and brain, but the image of a mouse fetus presented in this volume is also impressive. Developing organs are depicted at high resolution and high contrast. This technique will be useful in detecting defects in transgenic animals. Many genetically modified animals die before birth and it is difficult to determine the cause of death because the fetus is very small and an investigation of the cause requires many pathological sections. By this technique, it is possible to obtain 3D structural information at high resolution, which is useful for finding anomalies during development. This technique has the potential to be used by many researchers in a wide range of fields in biology.

Prof. Matsumoto's group in Osaka University has been working on high-resolution (3 μm) imaging of the structure of bone using monochromatic CT at SPring-8. Its quantitativeness enabled them to estimate the bone mineral density accurately. The results show that vitamin K supplied during the maturation stage may be effective in creating strong bone.

The high flux of SPring-8 helps obtain time-resolved images of a contrast agent flowing through fine blood vessels. The study by Sonobe *et al*. demonstrated, for the first time, that blood vessels in the lung can be visualized in mouse by the angiography technique at SPring-8. The high heart rate (up to 600 beats per min) and small vessel size (100 μm) of mouse require the use of a fast shutter system and a high-resolution imaging detector. Since mouse is often used as a model of cardiovascular diseases, the success of this experiment opens up a new field of circulation physiology.

Naoto Yagi

A compact intermediate state of calmodulin in the process of target binding

Solution X-ray scattering is one of the classical techniques to extract information about the structure of target molecules. The technique is as simple as to irradiate X-rays to an aqueous protein solution, in which constituent molecules are randomly oriented. Simple as it is, one may extract various aspects of structural information from the scattering profile, including $I(0)$ (the forward scattering intensity at a zero angle) and R_g (radius of gyration). $I(0)$ is a direct measure of the molecular weight of protein. From R_g, one can tell the gross shape of the molecule, e.g., the molecule is globular or elongated. An important feature of solution X-ray scattering is that, unlike in protein crystallography, one may perform experiments under physiological conditions, under which proteins can undergo reactions, association and dissociation as would occur in live cells. Here we describe an example in which, by combining this classical technique with intense synchrotron radiation from SPring-8 and state-of-the-art detecting techniques, reaction-associated structural changes of a protein are followed with an unprecedented time resolution.

Calmodulin (CaM) is a low-molecular weight (17 kDa) ubiquitous Ca^{2+}-binding protein, found in all eukaryotic cells. CaM binds to various target proteins and is implicated in various Ca^{2+}-mediated cellular processes including cell growth, proliferation, motility, and apoptosis. A single CaM molecule consists of two globular domains (called N-lobe and C-lobe), connected by a flexible linker. Each of the globular domains has 2 Ca^{2+}-binding motifs (EF-hand motifs), so that the entire molecule can bind up to 4 Ca^{2+} ions. It is known that in the process of Ca^{2+}-binding and subsequent binding to target proteins, CaM undergoes a characteristic structural change: When CaM is free of Ca^{2+} and its target protein, its linker is in an extended form, so that the entire molecule is dumbbell-shaped. Once Ca^{2+} ions are bound, CaM binds to its target protein. In this state the linker is disordered and the entire molecule assumes a more compact structure.

The time course of Ca^{2+}-induced structural change of CaM was studied in detail in the high-flux **BL40XU** beamline. The reaction was started by the light-induced decomposition (photolysis) of caged calcium. A caged substance is an inactive chemical, which is decomposed by intense ultraviolet light and releases a biologically active substance. By decomposing caged calcium by an intense Nd-doped yttrium-aluminum-garnet (YAG) pulse laser (light pulse duration, <10 ns), one may increase the Ca^{2+} concentration in less than a millisecond. Instead of a target protein, a small polypeptide was used (mastoparan, a component of wasp venom). Target proteins are usually larger than CaM, but this peptide is even smaller than CaM, so that it does not mask the structural change of CaM when bound to it.

Irradiation of proteins with X-rays causes radiation damage, and with the extremely intense X-rays from the BL40XU beamline, radiation damage occurs in a matter of milliseconds. To avoid this, the solution containing CaM, mastoparan and caged calcium was put in a thin-walled quartz capillary, and was continually moved along its axis during exposure. By doing so, one can minimize the X-ray dose to each part of the sample. The X-ray scattering was recorded with an ultrafast CMOS video camera at a rate of 2,000 frames/s. At a certain timing of X-ray exposure, the YAG laser was flashed, so that the recorded X-ray movie contained the scattering before flash, and the time course of change of scattering profile after the jump of Ca^{2+} concentration.

Figure 1 shows the time course of change of R_g before and after photolysis, determined in

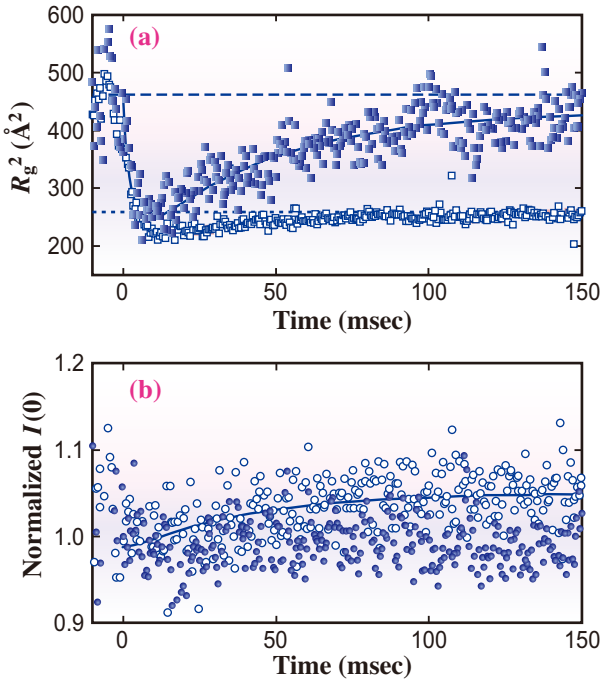

Fig. 1. Results of time-resolved solution X-ray scatteing experiments for CaM with and without mastoparan. **(a)** R_g^2 after photolysis of caged Ca^{2+}: (filled square) without mastoparan and (open square) with mastoparan. The dotted and dashed lines show the average values with and without mastoparan, respectively. **(b)** $I(0)$ after photolysis of caged Ca^{2+}: (filled circle) without mastoparan and (open circle) with mastoparan. The data were normalized by average $I(0)$ before Ca release.

this way. In the presence of both caged Ca^{2+} and mastoparan (Fig. 1(a), open square), the value of R_g is large (~2.0 nm, meaning that the CaM molecule is in an extended, dumbbell-shaped form) before photolysis. After photolysis, the R_g is reduced to a low value (~1.4 nm, meaning that the CaM molecule is in a compact form) within 10 ms and stays low. This final form with low R_g is in agreement with previously published results of static measurement. On the other hand, in the presence of caged Ca^{2+} but in the absence of mastoparan (Fig. 1(a), filled square), R_g is temporarily reduced within 10 ms but gradually returns to a higher value. This indicates that, upon Ca^{2+} binding alone, CaM transiently assumes a compact form but becomes extended again, as has been observed in previous studies.

Figure 1(b) shows the time course of change of $I(0)$, the measure of molecular weight. In the absence of mastoparan (filled circles), the $I(0)$ stays low for the entire period of measurement. On the other hand, the $I(0)$ gradually increases by ~10% in the presence of mastoparan. This can be explained by slow binding of mastoparan to CaM, because the molecular weight of mastoparan is ~10% of that of CaM.

Taken together, CaM is quickly transformed to a compact form after photolysis in the presence of mastoparan, but this is not due to the quick binding of mastoparan to CaM as previously believed, because the mastoparan binding ($I(0)$ increase) is much slower than the reduction of R_g. Whether mastoparan is present or not, CaM quickly (<10 ms) assumes a compact form upon Ca^{2+} binding alone, and this new compact form has not been reported before. Model calculations of reaction kinetics (Fig. 2) suggest that the new compact form occurs when Ca^{2+} binds to the C-lobe alone, because the Ca^{2+} binding to the C-lobe is faster than that to the N-lobe. Finally, both lobes become filled with Ca^{2+} and the CaM molecule become extended again in the absence of mastoparan, but is stabilized in a compact form in the presence of mastoparan.

CaM is one of the most intensively studied proteins, and the proposal of a new reaction scheme (Fig. 2) for such a protein was made possible by the high time resolution provided by the intense synchrotron radiation and advanced detection techniques. The experimental technique as described here is expected to be useful in studying fast reactions of other proteins, for which conventional techniques like stopped-flow mixing is too slow for the purpose.

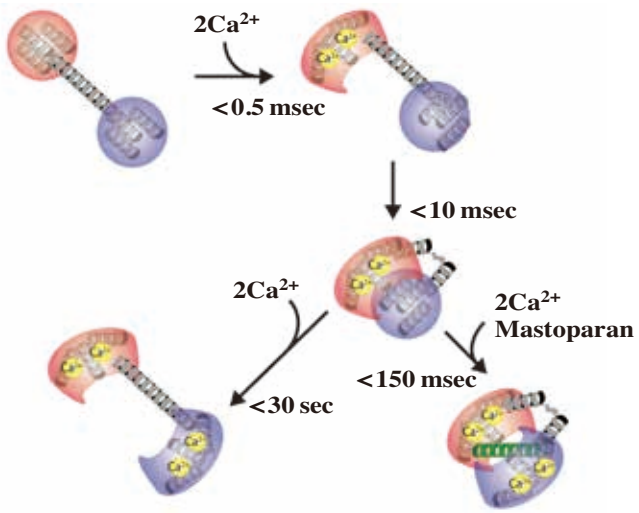

Fig. 2. Schematic illustration of the kinetic reaction of CaM upon Ca^{2+} binding. The N- and C-lobes and Ca^{2+} ions are colored blue, red, and yellow, respectively. The green helix shows mastoparan. Helices in each domain are colored gray.

Y. Yamada, T. Matsuo, H. Iwamoto* and N. Yagi

SPring-8/JASRI

*Email: iwamoto@spring8.or.jp

References

[1] *Y. Yamada, T. Matsuo, H. Iwamoto and N. Yagi: Biochemistry* ***51*** *(2012) 3963.*

Optimization of calcium concentration of saliva with phosphoryl oligosaccharides of calcium (POs-Ca) for tooth enamel recrystallization in the early stage of caries

Teeth are one of the most important organs. Without teeth, we cannot enjoy healthy life. Once we lose a tooth, it is never again regenerated. Furthermore it leads to reduced nutrient intake, and impairs our nutritional condition and might cause us to become bedridden. Thus one of the most important things in a long-lived society such as Japan is to maintain oral health, especially to retain healthy teeth, to safeguard a good quality of life.

Tooth enamel is chemically vulnerable to acid attack. Therefore after every meal, there is always the risk of tooth enamel dissolution by acid attack. Acidic food causes surface erosion. Acid from dental plaque, which is produced by cariogenic bacteria assimilating sugar, dissolves the subsurface of enamel (demineralization). Our study target is this early stage of caries, because subsurface lesions can be restored by remineralization and reversibly cured to restore healthy tooth enamel, whereas a cavity cannot be cured without surgical procedures. Only the supply of calcium and phosphate ions to saliva at adequate concentrations and optimal molar ratios is necessary to enhance the remineralization of the enamel lesions and the restoration of the microstructure of hydroxyapatite (HAp), the calcium salt that is the main component of enamel.

In a previous study [1], phosphoryl oligosaccharides of calcium (POs-Ca®), which is a highly soluble calcium material, was found to effectively remineralize tooth enamel lesions. It has already been elucidated that POs-Ca provides calcium ions to saliva in a bioavailable form without forming calcium-phosphate precipitates. However, the optimal dose of POs-Ca relative to phosphate ions for the remineralization of enamel lesions remains unknown. Thus, we investigated the optimal dose of POs-Ca for enhancing the remineralization of tooth enamel *in vitro* using transversal microradiography (TMR) [2]. First, POs-Ca added to artificial saliva was confirmed to be soluble in the presence of phosphate ions, whereas a proportion of calcium ions from $CaCl_2$ formed an insoluble salt in the presence of phosphate ions at pH 6.5 (Fig. 1). Therefore, POs-Ca was thought to have unique potential as bioavailable calcium in saliva even under non-acidic conditions. Then, the optimal Ca/P molar ratio was investigated. The greatest degree of enamel remineralization was observed at Ca/P molar ratio = 1.67 (Fig. 2). This is identical to the Ca/P molar ratio of HAp (Ca/P = 1.67). In contrast, an excess amount of POs-Ca (Ca/P molar ratio = 3.0) severely

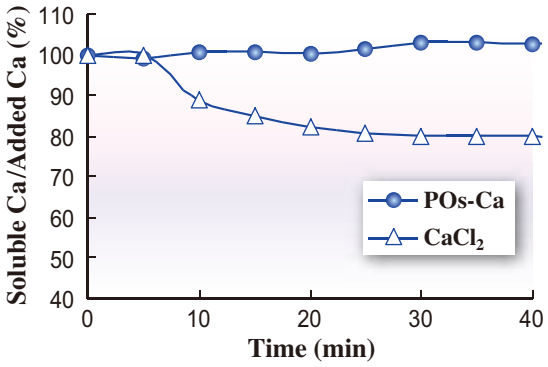

Fig. 1. Time courses of calcium ion concentrations for POs-Ca/$CaCl_2$-containing artificial saliva. The ratio of soluble calcium ions to added calcium was plotted against time from pH adjustment.

reduced the recovery rate of enamel remineralization. This result is consistent with a previous report that a Ca/P molar ratio of 1.67 provides the optimal remineralization rate [3]. An excessive Ca/P molar ratio due to POs-Ca addition might impair mineral exchange between solution and demineralized enamel in terms of kinetics, whereas increasing calcium thermodynamically enhances enamel remineralization.

Next, the effects of two calcium sources, POs-Ca and $CaCl_2$, on enamel remineralization at Ca/P molar ratio = 1.67 were compared. At this ratio, the mineral recovery rate for artificial saliva (AS) containing POs-Ca (24.2 ± 7.4%, n = 5) was significantly higher than that for AS containing $CaCl_2$ (12.5 ± 11.3%, n = 5) (mean ± SD, $p < 0.05$). Treatment with the POs-Ca solution restored the mineral to a depth of 100 μm. Whether free calcium released from POs-Ca itself passes into tooth enamel lesions is not known. However, POs-Ca may pass through the enamel pores because its average molecular weight is ~800, and the calculated molecular length of POs-Ca in the stretched form is < 4 nm [4].

However, TMR results cannot exclude the possibility that random calcium-phosphate precipitation fills the pore of demineralized enamel. Thus, wide-angle X-ray diffraction (WAXRD) analysis at beamline **BL40XU** was used in this study to analyze HAp crystal distributions and orientations. The 6 μm X-ray microbeam was produced by passing the X-ray through a pinhole. The tooth enamel sections were set before the detector. The distance from the sample to the detector was about 150 mm for WAXRD. The sample was moved so that the beam position was moved from surface to base in 5 μm

steps, and serial diffraction images of WAXRD were collected. From the WAXRD images, an arc-shaped spot corresponding to diffraction from the (100) plane of HAp was integrated. The plots of (100) intensity against depth from the surface for enamel remineralized with POs-Ca- and $CaCl_2$ solutions showed profiles (Fig. 3(b)) that indicate the recovery of crystallites. The orientation of the (100) reflection after remineralization was the same as that in healthy tooth enamel (Fig. 3(a)), indicating that the orientation of the regrown crystallites was also the same. Thus, WAXRD showed that the orientations of the HAp crystallites in the remineralized area of enamel treated with either calcium source were identical to those in intact enamel [5]. The recovery rate of HAp crystallites for AS containing POs-Ca (35.7 ± 10.9%, n=11) was also significantly higher than that for AS containing $CaCl_2$ (23.1 ± 13.5%, n=11) ($p<0.05$). These results indicate that most of the calcium and phosphate restored in tooth enamel lesions formed highly organized HAp crystallites, not random HAp crystals or other calcium-phosphate salts, regardless of whether the calcium source in the remineralization solution was POs-Ca or $CaCl_2$. The orientations of HAp crystallites influence the acid resistance and physical strength of the enamel surface, because the chemical nature of the plane perpendicular to the *c*-axis of the HAp, which is usually exposed on the tooth enamel, is different from that of the other planes [6]. Thus, the restoration of demineralized subsurface lesions of tooth enamel HAp implies that the physical and chemical stability of the surface of the lesion is improved by POs-Ca treatment.

WAXRD study confirmed the advantage of POs-Ca compared with other conventional calcium salts in enhancing the recrystallization of enamel and that it may be a beneficial material for maintaining healthy teeth.

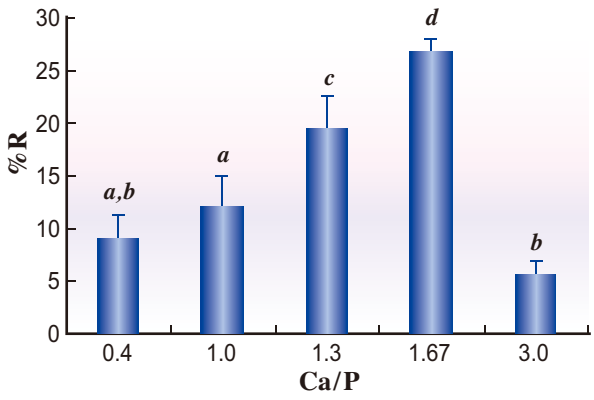

Fig. 2. Recovery rates of enamel treated with 0.4–3.0%-POs-Ca-containing artificial saliva. Histogram and bars represent mean and S.D. of recovery rates from each group, respectively. Each bar with a different letter indicates significant difference ($p < 0.01$, Scheffe's *post hoc* test).

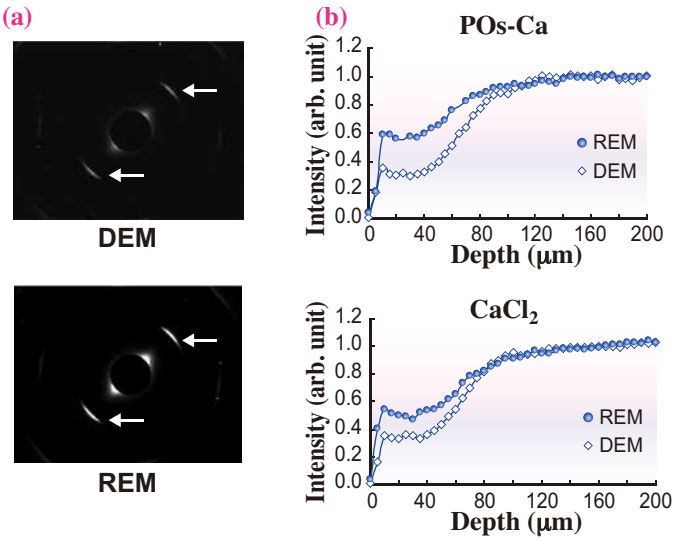

Fig. 3. Wide-angle X-ray diffractions of sound, demineralized, and remineralized zones in enamel treated with POs-Ca and $CaCl_2$. **(a)** Diffraction patterns in the DEM and REM zones at about 30 μm from the surface of POs-Ca-treated enamel. Exposure time was 300 ms. Arrows indicate the (100) equatorial reflections from the HAp crystallites. The direction of the c-axis of the HAp crystal is approximately perpendicular to the enamel surface. **(b)** Plots of (100) intensity against the depth from the enamel surface. The plots are averages of data from five samples from different teeth. Scans were made in six different areas in each of the DEM and REM zones of each enamel sample, and the results were averaged in each zone. To compensate differences in the thickness of the sample, the result from each area was normalized by the average intensity in the depth thickness 100–150 μm.

Tomoko Tanaka*, Takatsugu Kobayashi and Hiroshi Kamasaka

Institute of Health Sciences, Ezaki Glico, Ltd.

*Email: tanaka-tomoko-2@glico.co.jp

References

[1] H. Kamasaka *et al.*: Trends Glycoscience Glycotechnology **15** (2003) 75.
[2] *T. Tanaka, T. Kobayashi, H. Takii, H. Kamasaka, N. Ohta, T. Matsuo, N. Yagi, T. Kuriki: Arch. Oral Biol. 58 (2013) 174.*
[3] R.A.M Exterkate *et al.*: J. Dent. Res. **72** (1993) 1599.
[4] Y. Kitasako *et al.*: J. Dent. **39** (2011) 771.
[5] T. Tanaka *et al.*: Caries Res. **44** (2010) 253.
[6] J.C. Elliot: Structure and chemistry of the apatites and other calcium phosphates. Amsterdam: Elsevier, 1994.

Beneficial effects of vitamin K on morphometric and material bone properties during growth

Vitamin K (VK) facilitates collagen accumulation, osteoblast differentiation, and bone structural integrity, and furthermore, exerts an antiresorptive action on bone. Thus, the VK status is deeply associated with healthy bone growth [1]. However, during childhood and adolescence, bone metabolic activity is high for bone radical extension, and dietary VK intake may be insufficient to satisfy the metabolic VK requirement. Indeed, dietary VK intake and the metabolic VK requirement are reported to be imbalanced in children compared with those in adults [2]. This suboptimal vitamin K status will be responsible, at least in part, for vulnerability to frsacture during growth, which is not only detrimental to healthy bone development but also poses a potential risk of osteoporosis later in life [3]. Thus, supplemental VK during childhood and adolescence may be beneficial for healthy bone growth; in fact, better VK status contributes to the enhancement of bone growth [2]. However, the VK effect on bone strength or quality has not been entirely explored, and there is a lack of experimental insight in this regard. We thus tested the hypothesis that VK is beneficial to the mechanical properties of bones in growing rats [4].

Experiments were conducted with the approval of the Animal Research Committee of Osaka University Graduate School of Engineering Science. Sixteen female Wistar rats at 5 weeks of age were divided into two groups, VK2 diet and control diet (n=8 each), fed with normal diet with and without VK2 treatment, respectively. VK2 (menatetrenone, kindly donated by Eizai, Japan) was given as a dietary supplement; the actual VK2 intake was 22 mg/kg of body weight per day. VK2 was used rather than VK1 because of its advantage over the latter in half-life time. The animals were kept for 9 weeks under standard housing conditions and then euthanized. Serum analysis by sandwich enzyme-immunoassay (EIA) at the end of the feeding period showed a lower ratio of undercarboxylated to γ-carboxylated serum osteocalcin (Glu/Gla-OC) in VK2 diet than in control diet (0.68 *vs* 0.93%, $p<0.05$), indicating improved VK status in VK2 diet. Urinary deoxypyridinoline, a bone resorption marker, did not differ between the two groups. That is, in the present setting, VK2 seemed beneficial to bone formation rather than antiresorption.

Tibial bone was transected, and bone material properties were analyzed by Fourier transform infrared microspectroscopy (FTIR-MS) and nanoindentation testing and bone morphometry by micro-computed tomography (μCT). Figure 1 shows three bone segments measured for each analysis. FTIR spectra were collected in the reflection mode from three regions each at the anterior and posterior cortical midlayers for determining the mineral-to-matrix ratio, mineral crystallinity, and collagen maturity.

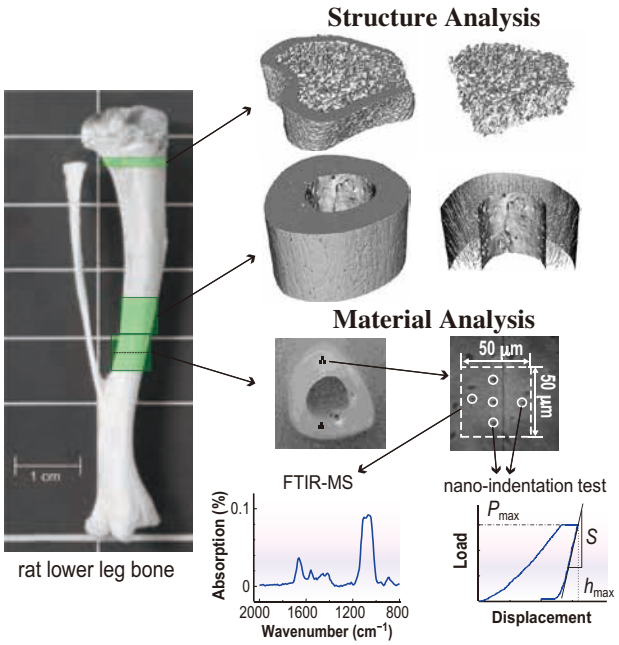

Fig. 1. Bone segments measured for morphometric and material analyses. The indentation test included 5 indents in each of 3 anterior and 3 posterior regions where FTIR spectra were obtained.

Subsequently, the specimens were subjected to the nanoindentation test. Five points were tested with a trapezoidal loading waveform in each region where the FTIR spectra were collected, and the indentation modulus and hardness were obtained from a resulting force-displacement curve according to the method described by Oliver and Pharr [5].

The proximal metaphysis and distal diaphysis were scanned for imaging of the cancellous trabecular architecture and cortical porous network, respectively, by laboratory μCT (12-μm cubic voxel) and by synchrotron radiation μCT (SR μCT, 2.74-μm cubic voxel) at beamline **BL20B2**. By calibration using K_2HPO_4 phantom solutions, bone mineral density was quantitated from SR μCT images. In the cancellous bone, trabecular volume fraction, trabecular thickness, trabecular number density, and trabecular connectivity density were calculated. In cortical porous structure, cortical porosity, mean porous diameter, porous density in the inner and outer cortical surfaces, and density of porous connections were calculated.

There was no effect of VK2 on bone mineral density or mineral-to-matrix ratio, but VK2 increased both the mineral crystallinity (1.7 *vs* 1.5, $p<0.05$) and collagen maturity (3.2 *vs* 2.5, $p<0.05$). Thus, VK2 can contribute to the maturation of cortical bone tissue. An increasing effect of VK2 on bone hardness (1.6 *vs* 1.3, $p<0.05$) was also found. Figure 2 shows the plots of mineral crystallinity, collagen maturity, and hardness for each specimen. Increased mineral crystallinity, rather than increased collagen maturity, seems to be implicated in the increased hardness because collagen maturity affects mainly on the ultimate strength and toughness of bone rather than on the strength. No effect of VK2 was found on cortical porosity or the other indices of porous structure; however, VK2 increased the trabecular volume fraction with increasing trabecular thickness (Fig. 3). Trabecular number also tended to be increased by VK2. A different activity of bone modeling/remodeling between cancellous and cortical bone or a strong linkage between cortical microstructure and intracortical vascularization may be involved in the site-dependent VK2 effect.

In summary, supplemental VK2 improved the VK status, reinforced the trabecular bone architecture, and promoted the maturation of cortical bone tissue in growing rat tibia. Thus, VK supplementation could be beneficial for enhancing bone quality and reducing the risk of fracture during growth spurts.

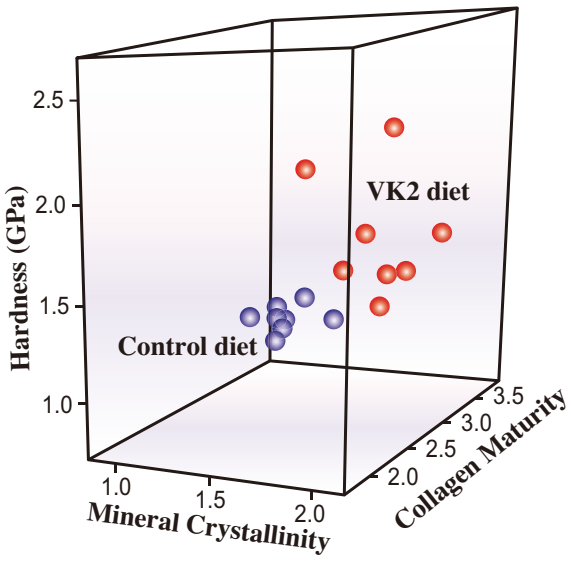

Fig. 2. Scatter diagram of mean values of hardness, mineral crystallinity, and collagen maturity. Blue circles: control diet; red circles: VK2 diet.

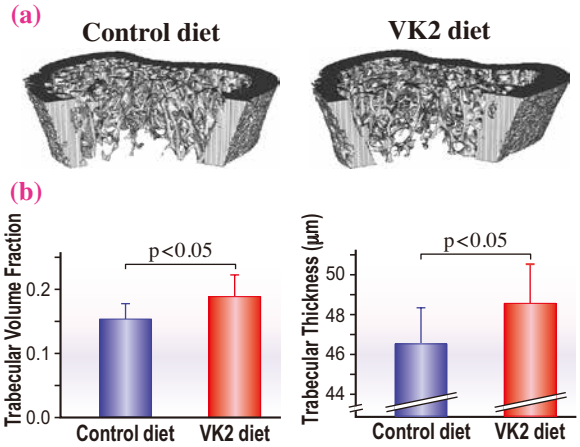

Fig. 3 **(a)** Three-dimensional displays of tibial metaphyses harvested from control- and VK2-diet rats. **(b)** Increases in trabecular volume fraction and thickness with VK2 intake. Bars represent standard deviation. Statistical analysis was performed using the unpaired t-test.

Takeshi Matsumoto

Department of Mechanical Science and Bioengineering, Osaka University

Email: matsu@me.es.osaka-u.ac.jp

References

[1] C.M. Gundberg: J. Bone Miner. Res. **24** (2009) 980.
[2] M.J. van Summeren *et al.*: Br. J. Nutr. **102** (2009) 1171.
[3] R. Rizzoli *et al.*: Bone **46** (2010) 294.
[4] *T. Matsumoto, T. Miyakawa, D. Yamamoto: Metabolism* ***61*** *(2012) 407.*
[5] W.C. Oliver and G.M. Pharr: J. Mater. Res. **19** (2004) 3.

Phase-contrast X-ray microtomography of mouse fetus

Mouse is one of the important animals used in many kinds of experiments. In particular, transgenic mice are now regarded as a common tool for investigating the functions of proteins *in vivo*. Mouse fetuses are extensively studied to determine the roles of genes in development and congenital abnormalities. With the increase in new types of transgenic animals, effective methods of identifying novel phenotypes in these fetuses are crucial. However, up to now, the detailed examination of a mouse fetus has involved thin sectioning for observation under a microscope. Here, we applied phase-contrast X-ray microtomography (CT) to visualize the development of mouse fetuses without the need for sectioning or treatments other than fixation by formalin [1].

In the synchrotron radiation facilities, phase-contrast X-ray CT using an X-ray interferometer has been under development since the 1990s [2]. In general, the compound refractive index in X-rays is represented as $n = 1-\delta + i\beta$, where δ and β represent the phase and absorption factors, respectively. In biological soft tissues composed of low-Z elements such as hydrogen, carbon, nitrogen, and oxygen, the absorption factor β is too small to use for the conventional X-ray absorption radiogram. On the other hand, the phase factor δ is about 1000 times larger than β. Therefore, phase-contrast X-ray CT using δ enables us to visualize the three-dimensional structures in biological soft tissues with much higher contrast than by conventional X-ray CT. From the tomographic reconstruction, a three-dimensional map of $\Delta\delta$ is obtained. Since δ is roughly proportional to the density of the material when it contains only low-Z elements, it is also possible to estimate a three-dimensional map of the density.

To measure phase shift for imaging, a grating-based interferometer, which is called as Talbot interferometer, is used [3]. The Talbot interferometer is typically composed of two transmission gratings: a phase grating (G1) and an absorption grating (G2). Since the Talbot interferometer is a robust technique against disturbances of the system, compared with a crystal-based interferometer, it has been used for many applications. In SPring-8, this technique has been used in structural studies of biological soft tissues such as brain and eye lenses [4]. Since an embryo and a fetus before the calcification of bones are regarded as soft tissues, this technique is suitable for these samples.

The visualization of mouse fetuses by phase-contrast X-ray CT was conducted at bending magnet beamline **BL20B2**. Grating parameters and materials are varied depending on the size of the fetus samples. Embryos of 6 and 9 days were measured at the upstream experimental hutch located 44 m from the source. For these small samples, both gratings are made of tantalum and the pattern thicknesses of G1 and G2 are 0.96 μm and 4.75 μm, respectively. The pitch of both gratings is 5 μm and the grating area size is 5 mm (width) by 10 mm (height). G2 is inclined 60 degrees towards the beam so as to increase the effective X-ray absorption by the grating. The X-ray imaging detector consists of a visible light conversion unit, "beam-monitor," and a charge-coupled device (CCD) camera. The beam-monitor is composed of a 10-μm-thick P43 ($Gd_2O_2S:Tb^+$) phosphor screen and a f = 50 mm camera lens. The CCD camera is a fast read-out one (C9100-02, Hamamatsu Photonics) equipped with a f = 85 mm camera lens. The effective pixel size is 4.9 μm. On the other hand, embryos of 10, 11, 13, and 15 days were measured at the downstream hutch located 200 m from the source. In this case, G1 is made of tantalum and G2 is made of gold with pattern thicknesses of 2.1 μm and 16.6 μm, respectively. The pitch of both gratings is 10 μm and the grating area size is 25 mm (width) by 25 mm (height). The inclination angle of G2 is 45 degrees. The beam-monitor is composed of a 20-μm-thick P43 phosphor screen and an f = 105 mm camera lens. The CCD camera (C4880-41S, Hamamatsu Photonics)

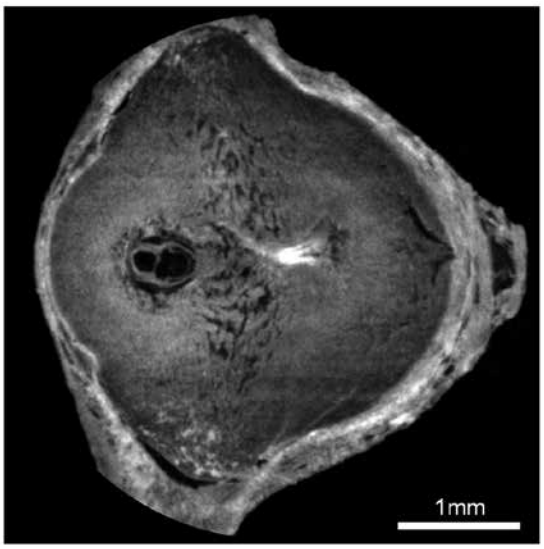

Fig. 1. Phase-contrast X-ray CT image of a mouse fetus at gestational day 6.

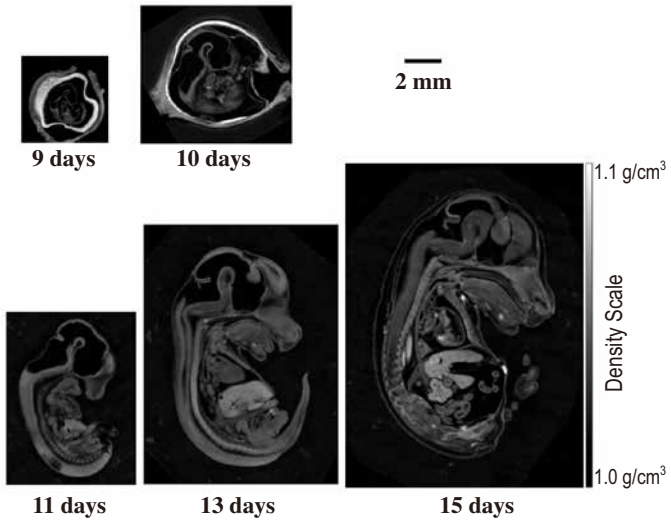

Fig. 2. Phase-contrast X-ray CT images of mouse fetuses at gestational days 9 to 15.

is equipped with an f = 105 mm camera lens. In this case, the effective pixel size is 5.87 μm per pixel. In the actual measurements, the CCD camera is used in the binning mode (4×4 binning with 23.5 μm pixel size).

A cross section of mouse uterus at gestational day 6 is shown in Fig. 1. Only the egg cylinder and remains of the uterine lumen (with higher density) can be observed. Approximately sagittal tomographic sections of mouse fetuses at gestational days 9, 10, 11, 13, and 15 are shown in Fig. 2. The gray scale represents density estimated from the results of phase-contrast X-ray CT. At day 9, the fetus is strongly flexed in a dorsally convex direction. At the center of the embryo is the heart in the early development stage. Other organs are not identifiable, but it is clear that the present technique allows us to visualize the details of early development. At day 11, 32 somites can be counted, and most of the major organs, such as brain tube, heart, liver, stomach, and intestine, are visible, among which liver has the highest density. At 13 days, compared with adult mouse the head is disproportionately large. However, the brain is still undeveloped and large ventricles occupy the major part of the head. On the other hand, the tongue and palatal process are well developed and Meckel's cartilage is present. Chondrification of the vertebrate column is still in progress at 15 days. All these features are well correlated with the microscopic observations of stained sections [5]. In phase-contrast X-ray CT, three-dimensional analysis is also possible, as shown in Fig. 3.

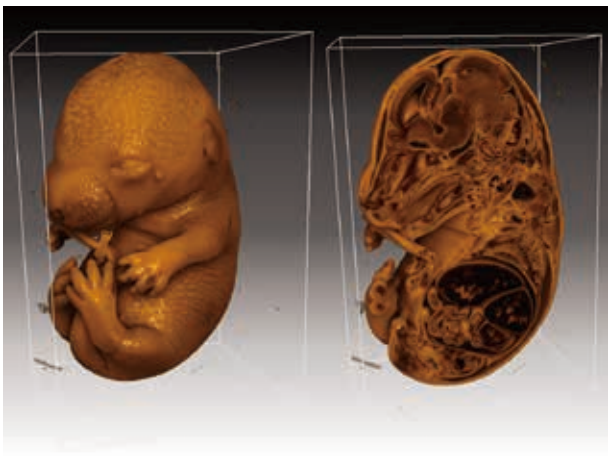

Fig. 3. Three-dimensional rendering of a mouse fetus at gestation day 15.

Masato Hoshino*, Kentaro Uesugi and Naoto Yagi

SPring-8/JASRI

*Email: hoshino@spring8.or.jp

References

[1] *M. Hoshino, K. Uesugi and N. Yagi: Biol. Open* ***1*** *(2012) 269.*
[2] A. Momose *et al.*: Rev. Sci. Instrum. **66** (1995) 1434.
[3] A. Momose *et al.*: Jpn. J. Appl. Phys. **42** (2003) L866.
[4] M. Hoshino *et al.*: PLoS ONE **1** (2011) e25140.
[5] K. Theiller: "The House Mouse: Atlas of Embryonic Development", Springer-Verlag, New York (1989).

Functional microangiography of *in vivo* mouse pulmonary circulation

The underlying mechanisms responsible for the pathogenesis of pulmonary arterial hypertension (PAH) still remain to be fully elucidated. Structural and functional changes in pulmonary microvessels are critical for modulating pulmonary blood flow, which is essential for optimizing ventilation-perfusion matching. Ultimately, dysfunction of the pulmonary microvasculature plays a pivotal role in the pathogenesis of several serious lung diseases. Recently, the ability to produce targeted gene mutations in mice has provided a powerful tool for studying molecular mechanisms of PAH *in vivo*. However, the pulmonary vascular function is still not fully elucidated in the mouse model. One of the limiting factors for measuring pulmonary dynamics in this animal is its small size.

The visualization of the microvascular bed provides invaluable insight for evaluating vasomotor function and, furthermore, understanding the underlying mechanisms that trigger early vessel disorders. Our group designed a unique laboratory X-ray TV system to visualize 100- to 500-μm-diameter pulmonary vessels *in vivo* [1]. This conventional X-ray system contributed to an assessment of the intravital vascular network. However, the limited spatial and temporal resolution of this system necessitated a thoracotomy to expose the lung out of the thorax and made it difficult to assess pulmonary blood flow distribution within the intact chest of a small animal model. In the last decade the technological advances in angiography by synchrotron radiation (SR) microangiography have provided the temporal and spatial resolutions required to visualize microvessels of various organs both *ex vivo* and *in vivo*. In our previous study in SPring-8, we demonstrated the visualization of pulmonary microvessels in a closed-chest rat model and investigated functional changes of the microvessels in experimental pulmonary hypertension [2]. Through successive studies using a rat model, we endeavored to advance the unique SR microangiography technique for visualizing the pulmonary hemodynamics in the mouse model *in vivo* [3].

All animal experiments were performed at beamline **BL28B2**. Briefly, healthy adult C57BL/6 mice (~25 g body weight) were anesthetized and lungs were mechanically ventilated with a small rodent ventilator. Surgical preparation was performed as previously reported using a rat model [2], although major modifications of experimental settings were required for mice imaging. Specifically, right ventricle catheterization via the right jugular vein was performed with a hand-made catheter (outer diameter 0.7 mm) and iodinated contrast medium was directly injected into the right ventricle using a high-pressure injection pump at a speed of 10 ml/min.

SR microangiography was effective for visualizing dynamic changes in the pulmonary vessel caliber using iodinated contrast agent. We observed, frame by frame, that thecontrast agent circulated from the right ventricle to pulmonary vessels in real time. Figure 1 illustrates typical microangiographic images showing the middle portion of left and right lungs from an anesthetized mouse. In our experimental setting, the mouse, which has small thoracic size, was suitable

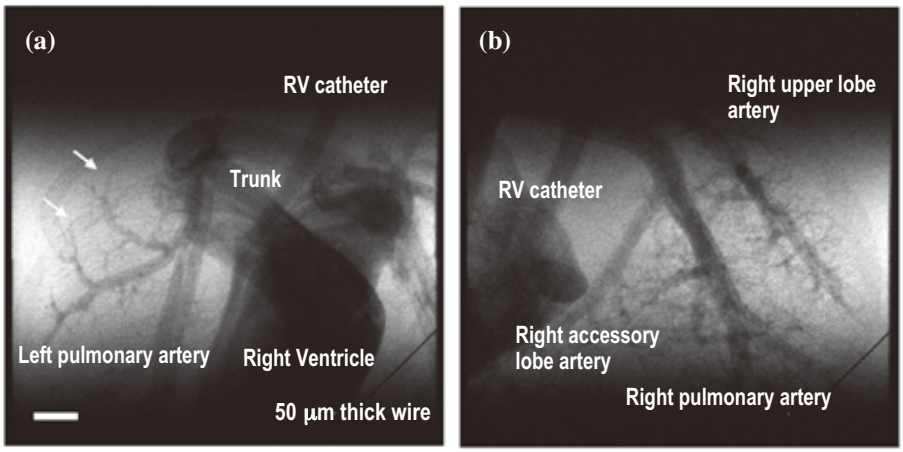

Fig. 1. Typical imaging pattern of mouse left **(a)** and right **(b)** lung circulation. A 50-μm-thick wire for calibration is depicted in the lower right area. **(a)** White arrows indicate the 3rd branches of the left middle lobe artery with less than 100 μm internal diameter. **(b)** Major arteries of the right lung (upper lobe artery, accessory lobe artery and right pulmonary artery) are all evident in a single region of interest. Scale bar = 1000 μm.

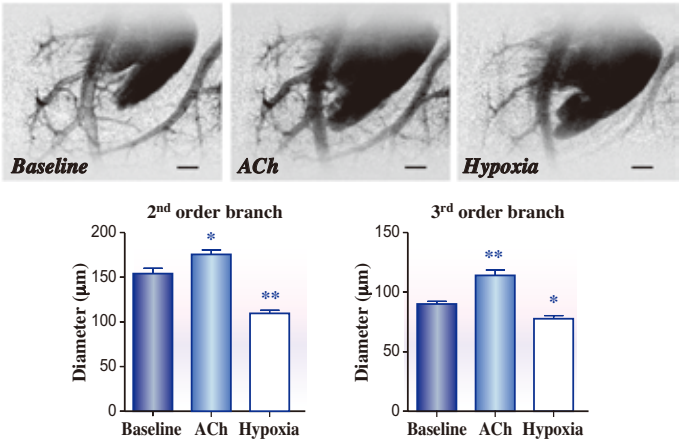

Fig. 2. **Top**: Typical microangiogram of *Baseline*, acetylcholine (*ACh*), and acute 10%-O_2 hypoxic exposure (*Hypoxia*). Smaller arteries partly disappeared in response to hypoxia. Scale bar = 1000 μm. **Bottom**: Magnitude of response to *ACh* and *Hypoxia* in each measurable branching generation (2nd, n=26, 3rd, n=15 vessels). Data show means +/– SE. *P<0.05, **P<0.01, significant difference from baseline.

for including the heart, lung, and most of the large to small pulmonary vessels within a single image. The diameter of the pulmonary trunk (~2 mm) and the 1st (~300 μm) to 3rd (~100 μm) branches from the left main axial artery could be measured, even when smaller than 100 μm. After the baseline angiogram was completed, the second and third angiograms were taken after the administration of a vasodilator (acetylcholine) and a vasoconstrictor (acute 10%-O_2 hypoxic exposure), respectively (Fig. 2). These stimuli changed the diameter of the 2nd and 3rd branches, which are pulmonary resistant vessels <~200 μm diameter (Fig. 2), but not the diameter of the left main axial artery and 1st branches. These analyses contribute to elucidating the regional differences in the vasomotor function among the series-arranged pulmonary vascular segments, and moreover, the target vascular site of the pathological dysfunction in lung diseases. We could also measure beat-by-beat dynamics of large conductance vessels by image analysis. The conductance vessel caliber oscillations in the left main axial artery were smaller and delayed relative to the trunk in the normal mouse (Fig. 3). In all mice, there were approximately 6 frames within each cardiac cycle. At the same time, we could estimate the pulmonary transit time of blood flow using cine imaging of single scan at a speed of 30 frames/s (1 scan = 100 frames over 3 s). The number of frames was counted between the time the contrast medium first appeared in the right ventricle and the time the contrast medium appeared in the left ventricle. Not surprisingly, the injected contrast agent quickly passed through gas-exchange vessels due to the high heart rate (over 400 beats per minute), and therefore, the calculated transit time was approximately within one second in the baseline (0.8 s). We could detect transit time prolongation (1.3 s, $p<0.05$) in acute hypoxic exposure. The transit time and conductance vessel fluctuation are determined by multiple cardiopulmonary factors (e.g., cardiac output, heart rate, and pulmonary vascular resistance and compliance); therefore, these parameters provide invaluable information concerning the cardiopulmonary hemodynamic status in cardiac and lung diseases.

In summary, we have exploited the full potential of monochromatic SR microangiography to show, for the first time, the ability to visualize pulmonary hemodynamics in a mouse model *in vivo*. SR microangiography is a powerful tool for assessing pulmonary hemodynamics in unprecedented detail in mice. Importantly, it can now provide us with the ability to assess the various neurohumoral pathways that modulate the pulmonary vasculature in specific gene-targeted knock-out and transgenic mice. Ultimately, future studies using SR microangiography on transgenic mice will provide important new insights into the pathophysiology of pulmonary dysfunctions and functional adaptation in cardiopulmonary disease.

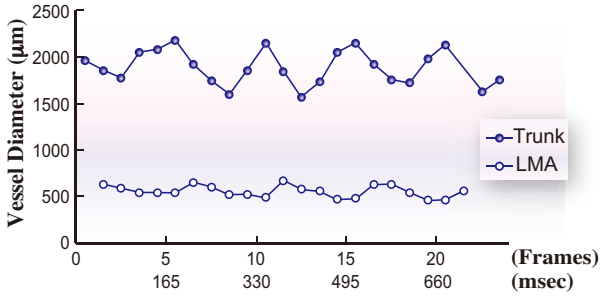

Fig. 3. Fluctuation of vessel diameters. The changes in internal diameter from sequential images of single scan (first 1 s of 3 s scan at 30 frame/s) were measured at the pulmonary trunk (Trunk) and left main axial artery (LMA). Each single frame had a shutter open time of 1.3 ms and a read-out time of approximately 33 ms.

Takashi Sonobe[a,*], Keiji Umetani[b] and Mikiyasu Shirai[a]

[a] Department of Cardiac Physiology, National Cerebral and Cardiovascular Center Research Institute
[b] SPring-8/JASRI

*Email: sonobe@ri.ncvc.go.jp

References

[1] M. Shirai *et al.*: J. Appl. Physiol. **61** (1986) 440.
[2] D. O. Schwenke *et al.*: J. Appl. Physiol. **104** (2008) 88.
[3] *T. Sonobe, D.O. Schwenke, J.T. Pearson, M. Yoshimoto, Y. Fujii, K. Umetani and M. Shirai: J. Appl. Physiol.* ***111*** *(2011) 75.*

Materials Science:

One of the most important missions in materials science is the finding of new phenomena/states, leading to novel properties/functions. In the section "Materials Science: Structure," outstanding research on finding new states (by Yamaura *et al*. and Shibauchi *et al*.), new phenomena (by Seto *et al*. and Moriyoshi *et al*.) and new composites (by Sato *et al*.) by utilizing the advanced measurement and analysis technology available at SPring-8 is introduced. In addition, a new phenomenon that will be developed to a new analysis method (by Matsui *et al*.) is also introduced.

Studies on ordered states such as magnetism and superconductivity have been intensively conducted, and they are still hot topics because of their complexity. For the realization of robust ordered states and of those with high transition temperatures (most ordered states appear at low temperatures), attempts at unveiling the hidden mechanism of complex ordered states have been conducted. Yamaura *et al*. found a new type of three-dimensional spin arrangement as an ordered state, the so-called all-in/all-out configuration, by the resonant X-ray magnetic scattering method (RXMS), while simple parallel and antiparallel configurations have mainly been discussed as ordered states so far. Shibauchi *et al*. have succeeded in the visualization of nematic ordering, which is well known in liquid crystals, in the electronic phase of novel iron-based superconductors by means of the extremely high-q (q: scattering vector) diffraction measurements, and it has been demonstrated that advanced synchrotron radiation analysis is a powerful tool for understanding the electronic nematicity in condensed matter.

STRUCTURE

The dynamics of matter is inseparable from the discussion of novel properties and functions. In 1995, P. W. Anderson wrote that *the deepest and most interesting unsolved problem in solid-state theory is probably the nature of glass and the glass transition*. Seto *et al*. have developed an approach to reply to this message from the viewpoint of the dynamics of glass, and propose a new regime of slow dynamics of glass on the basis of time domain interferometry (TDI) using nuclear resonant scattering (NRS) measurements. Moriyoshi *et al*. have taken a different approach, time-resolved X-ray diffraction, to unveiling the dynamics of matter, and succeeded in the direct observation of lattice dynamics in piezoelectric materials.

Sato *et al*. developed a method to encapsulate individual protein molecules into a molecule with a hollow spherical cage structure through the full use of organic chemistry, and a composite structure consisting of chemical and biological molecules was visualized by the maximum entropy method using high-precision synchrotron radiation X-ray diffraction data. It is expected that the interdisciplinary research involving chemistry, biology and structural science will accelerate the design and control of functional molecules.

The above-mentioned progress in materials science is due to advanced synchrotron radiation measurements. The germ of a new analytical method, the tone reversal image from the negative photographic photoelectron energy-loss process, was found by Matsui *et al*., and this new phenomenon is being developed as a new measurement tool.

In 2012, highlighted research in materials science was carried out in a wide range of research fields, such as physics, chemistry, biology, and interdisciplinary areas, by means of many kinds of measurements. In the future, approaches from many points of view, such as multiple beamline use, will be indispensable in the development of materials science.

Akihiko Fujiwara

Tetra-magnetism: all-in/all-out spin arrangement on the pyrochlore lattice

Pyrochlore oxide is a class of minerals in various substance groups of the form $A_2B_2O_7$ ($A_2B_2O_6O'$). The cubic pyrochlore structure possesses high symmetry in the space group $Fd\bar{3}m$. The structure comprises two interpenetrating networks composed of A-O' and B-O. The pyrochlore lattice is a three-dimensional network of tetrahedra sharing a vertex obtained by connecting only A or B atoms (see the inset of Fig. 1). Pyrochlore oxides have been studied extensively to search for exotic magnetic phenomena. When spins reside on the vertices of tetrahedra and interact antiferromagnetically with each other, a conventional magnetic long-range order like a Néel order tends to be suppressed owing to geometrical frustration. It is theoretically predicted that a quantum mechanically liquid state with a large fluctuation is realized even at zero temperature.

The pyrochlore oxide $Cd_2Os_2O_7$ discovered in 1974 shows a metal-insulator (MI) transition with an antiferromagnetic transition at 225 K [1]. A Slater transition, designated as a mechanism of an MI transition produced by the doubling of the unit cell due to the antiferromagnetic order, has been indicated. However, no magnetic peaks for identifying the magnetic structure in the insulating phase have been observed yet by means of neutron scattering. Thus, to reveal the magnetic structure, the resonant X-ray magnetic scattering method (RXMS) was employed, instead of the neutron scattering method, which suffers from the Cd absorption problem. X-ray magnetic scattering is a method of selectively enhancing the signal of a substance by using a resonant effect at the absorption edge of the element.

The measured sample was a high-quality single crystal of $Cd_2Os_2O_7$ with a 0.2×0.2 mm^2 surface of the (001) plane grown in a temperature gradient furnace. RXMS experiments were carried out at the absorption edge of Os at beamlines **BL19LXU** and **BL02B1**. Figure 1 shows the X-ray absorption spectra near the Os-L_{III} edge and the intensity of the 006 reflection at 10 K [2]. The peak-maximum position of 006 reflection is in good agreement with the Os-L_{III} edge, as depicted by the dotted line, implying the enhancement of the 006 reflection intensity by the resonance effect. The 006 reflection observed indicates the violation of the $Fd\bar{3}m$ extinction rule. Moreover, neither additional reflection breaking of the face-centered lattice nor long-period structures was observed.

Figure 2(a) shows the temperature dependence of the intensity of the 006 forbidden reflection, which increases gradually below 227 K, indicating a continuous second-order transition. Anomalies in forbidden reflection, magnetic susceptibility, and resistivity are observed at nearly the same temperature. Moreover, in the 006 forbidden reflection the polarization dependence emerges as shown in Fig. 2(b); the intensity was observed in only the π (incident beam) - σ' (scattered) channel. From these results, we therefore conclude that a commensurate magnetic structure appears at the propagation vector $\boldsymbol{q} = 0$ at low temperatures in this compound.

The $\boldsymbol{q} = 0$ magnetic structure should be described in terms of an Os tetrahedron because the magnetic primitive cell includes one Os tetrahedron. Here, the possible spin arrangements of the Os site can be classified by representation analysis; that is, the spin arrangements of the 12-basis functions are given. The basis functions represent one and eight kinds of spin arrangement with cubic and tetragonal magnetic symmetries, respectively. All of these magnetic structures are noncollinear antiferromagnetic spin arrangement with a zero net moment on the Os tetrahedron. The other three kinds of spin arrangement represent ferromagnetic spin arrangements. Generally, in a transition metal oxide, the lattice and magnetic structure are strongly coupled through exchange striction and spin-orbit (SO) interaction, resulting in a low-symmetry spin alignment that almost always induces crystallographic distortion. Thus, the magnetic symmetry is expected to be associated with the lattice symmetry in $Cd_2Os_2O_7$. Here, the preservation of the cubic spatial symmetry was confirmed by Raman scattering measurement, which is the most powerful technique for detecting small lattice distortions [2]. Therefore,

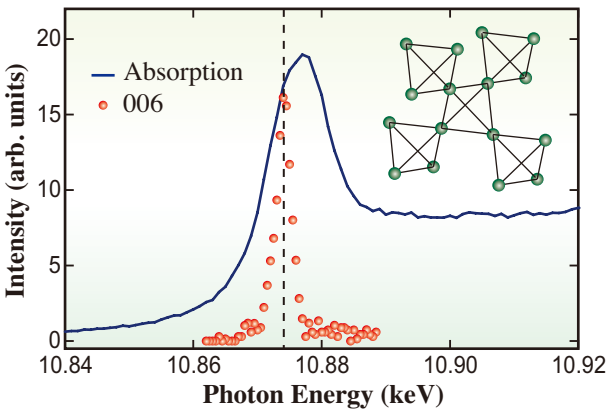

Fig. 1. Spectra of the intensity of the 006 forbidden reflection at 10 K and X-ray absorption near the Os-L_{III} edge at room temperature. The inset shows the pyrochlore lattice.

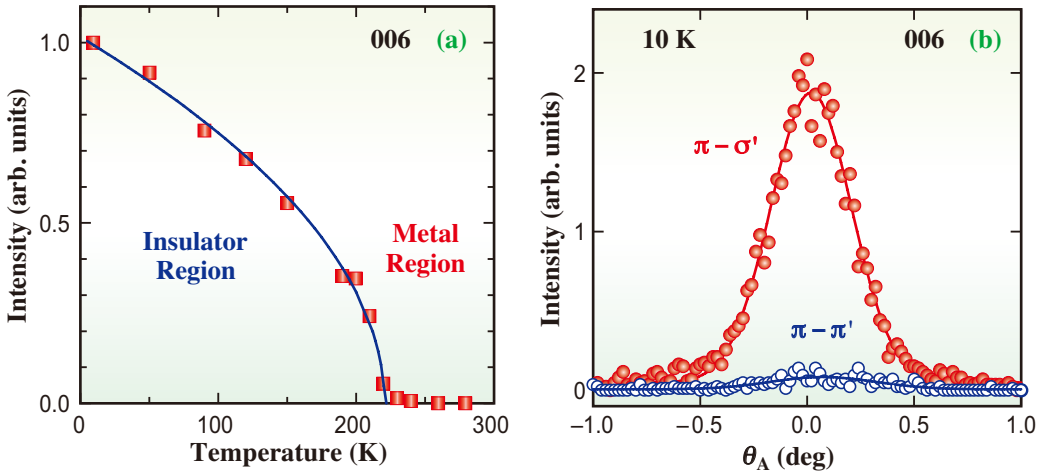

Fig. 2. **(a)** Temperature dependence of the integrated intensity of the 006 forbidden reflection. **(b)** Polarization dependence of the 006 magnetic reflection at the Os-L_{III} edge at 10 K.

only the spin arrangement with cubic magnetic symmetry is a unique solution to the magnetic ordered structure. The arrangement denotes the all-in/all-out antiferromagnetic spin arrangement with a zero net moment on the Os tetrahedron, in which all the spins point to (all-in) or away (all-out) from the center of the tetrahedron, as illustrated in Fig. 3. This spin arrangement is identical to the results of the polarization dependence. The all-in/all-out magnetic structure can be regarded as a negative/positive magnetic octupole: the term "tetra-magnetism" would be designated by the pair of negative/positive magnetic octupoles, which is different from the collinear-type antiferromagnetism and helimagnetism. The tetra-magnetism compound is expected to exhibit interesting physical properties such as an anomalous magnetization and a magnetostriction effect [3].

The present spin arrangement with $\boldsymbol{q}$ = 0 indicates that these transition is not due to Slater-type transitions. Consequently, the band-gap formation of $Cd_2Os_2O_7$ is thought to arise from an alternative mechanism that is presumably related to the all-in/all-out spin arrangement: a tetrahedral magnetic structure on the pyrochlore lattice without any spatial symmetry breaking. The emergence of a tetrahedral magnetic order triggers such cooperative band shifts so as to form a small gap through a strong SO coupling. Actually, it was proposed that the SO coupling plays a significant role in band-gap formation in the band structure calculation [4].

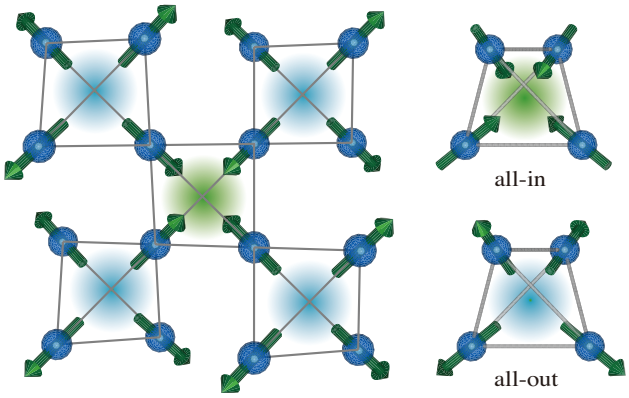

Fig. 3. The all-in/all-out magnetic structure is composed of Os tetrahedral "all-in" and "all-out" units.

Jun-ichi Yamaura†

Institute for Solid State Physics, The University of Tokyo

Email: jyamaura@lucid.msl.titech.ac.jp

†Present address: Materials Research Center for Element Strategy, Tokyo Institute of Technology

References

[1] A.W. Sleight *et al.*: Solid State Commun. **14** (1974) 357.
[2] *J. Yamaura, K. Ohgushi, H. Ohsumi, T. Hasegawa, I. Yamauchi, K. Sugimoto, S. Takeshita, A. Tokuda, M. Takata, M. Udagawa, M. Takigawa, H. Harima, T. Arima and Z. Hiroi: Phys. Rev. Lett.* ***108*** *(2012) 247205.*
[3] T. Arima *et al.*: J. Phys. Soc. Jpn. **82** (2013) 013705.
[4] Y. Shinaoka *et al.*: Phys. Rev. Lett. **108** (2012) 247204.

Nematic and metanematic transitions in iron-based superconductors

Strongly interacting electrons can exhibit novel collective phases, among which the electronic nematic phases are perhaps the most surprising, as they spontaneously break rotational symmetry of the underlying crystal lattice [1]. In the iron-pnictide superconductors, such nematicity has recently been observed in several experiments, and has commonly been associated with the tetragonal-to-orthorhombic structural phase transition at T_s, below which a sizable difference between *a* and *b* lattice parameters is observed with an orthorhombicity on the order of 10^{-3}.

We found in $BaFe_2(As_{1-x}P_x)_2$ systems (Fig. 1(a)) that the electronic nematicity sets in at T^*, which is much higher than T_s [2]. The chemical composition dependence of the nematic transition temperature T^* covers the superconducting dome, as shown in Fig. 1(b). The new phase diagram found in this study resembles the pseudogap phase diagram in high-T_c cuprate superconductors, and may hold an important clue to the mechanism of superconductivity in this class of materials.

Magnetic torque measurements in small pure crystals under in-plane magnetic field rotation, which have recently been developed as powerful probes for rotational symmetry breaking [3], have shown that the two-fold oscillation associated with the electronic nematicity starts to develop below the *x*-dependent temperature T^* [2]. The analysis of the phase of the two-fold oscillation reveals that the in-plane susceptibility shows elongated anisotropy along the Fe-Fe direction, which matches the orthorhombicity direction in the lower-temperature antiferromagnetic phase below $T_N \sim T_s$ (Fig. 1(c)).

To search for a tiny orthorhombic lattice

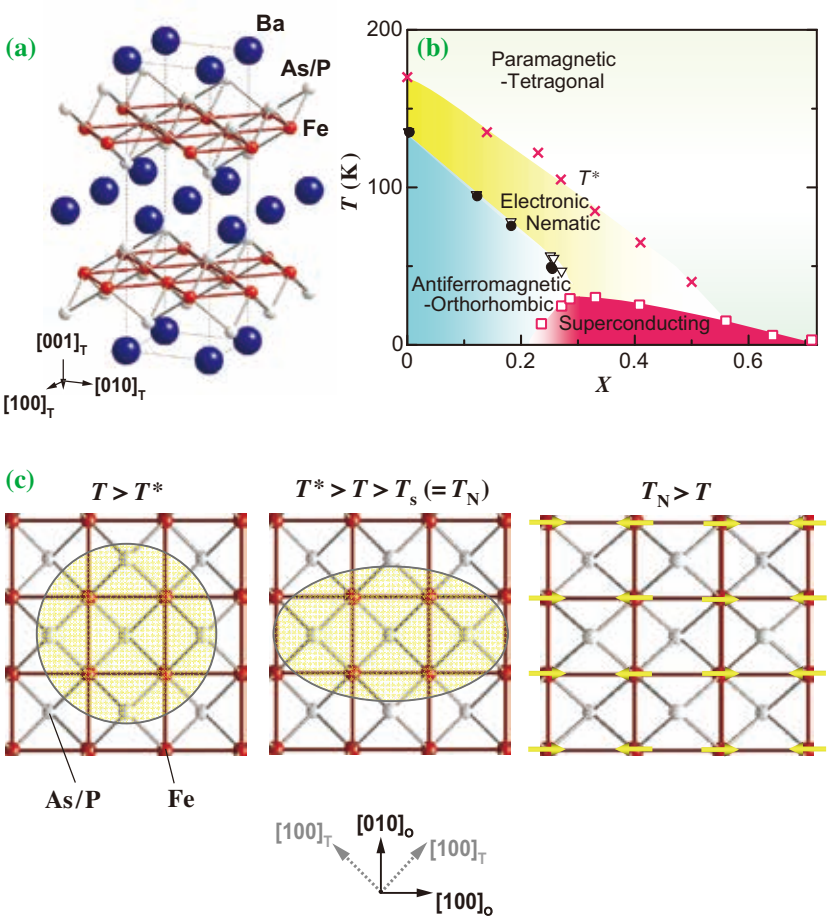

Fig. 1. **(a)** Crystal structure of $BaFe_2(As_{1-x}P_x)_2$. **(b)** Temperature-composition phase diagram. Nematicity appears below T^* (red crosses), which is above T_s (open triangles) and the antiferromagnetic transition temperature T_N (closed circles). T^* line extends to a high composition range covering the superconducting T_c dome (open squares). **(c)** Schematic paramagnetic electronic anisotropy (yellow circles) in the iron planes and the spin configuration below T_N (yellow arrows).

distortion associated with the electronic nematicity, we have performed single-crystal structural analysis at beamline **BL02B1** with a photon energy of 17.7 keV as a function of temperature at several different compositions x. We focus our attention to high-angle Bragg peaks $(hh0)_T$ with h = 7 or 8, which are very sensitive to a small distortion along the Fe-Fe direction. Typical diffraction data as a function of temperature is shown in Fig. 2 for x = 0 and 0.27. At high temperatures above T^*, the Bragg peak is relatively sharp. Below T_s, the peak is completely split into two peaks, indicating the orthorhombic symmetry of the crystal. In the intermediate temperature range between T^* and T_s, the Bragg peak is broader and has some tail structure, and it can be fitted to overlapping two peaks (Figs. 2(c) and 2(d)). This evidences a small but finite orthorhombic lattice distortion below the nematic temperature T^*. We stress that the high-resolution synchrotron X-ray measurements focusing on the high-angle Bragg peaks were the key for detecting such a small distortion in the electronic nematic state.

The orthorhombicity found in the temperature range below T^* immediately indicates that the rotational symmetry in the system is already broken above T_s, at which the tetragonal-orthorhombic crystal structure transition was originally assigned. This raises a question why we have a big jump in the peak splitting at T_s. Our study implies that the true second-order phase transition occurs at the nematic temperature T^*, which accompanies the spontaneous breaking of the fourfold tetragonal symmetry, whereas the apparent transition at T_s is not a true phase transition but rather what we refer to as a 'meta-nematic' transition in analogy to the theory of magnetism. A simple Landau free-energy analysis containing the electronic and lattice contributions leads to two different transition temperatures at which the electronic nematic and orthorhombic lattice order parameters set in, but when a coupling term between the electronic and lattice systems is introduced, both order parameters become finite below T^* and show a jump at T_s [2]. The fact that T^* is higher than T_s suggests that the nematic transition has an electronic origin.

The electronic nematic phases have been discussed for several strongly correlated electron systems, such as the pseudogap phase in high-T_c cuprate superconductors [4], the hidden order phase of the heavy-fermion compound URu_2Si_2 [3], and the field-induced phase of Sr_2RuO_7 [5]. The high-resolution synchrotron X-ray used in the present study will be a useful tool for studying these intriguing phases.

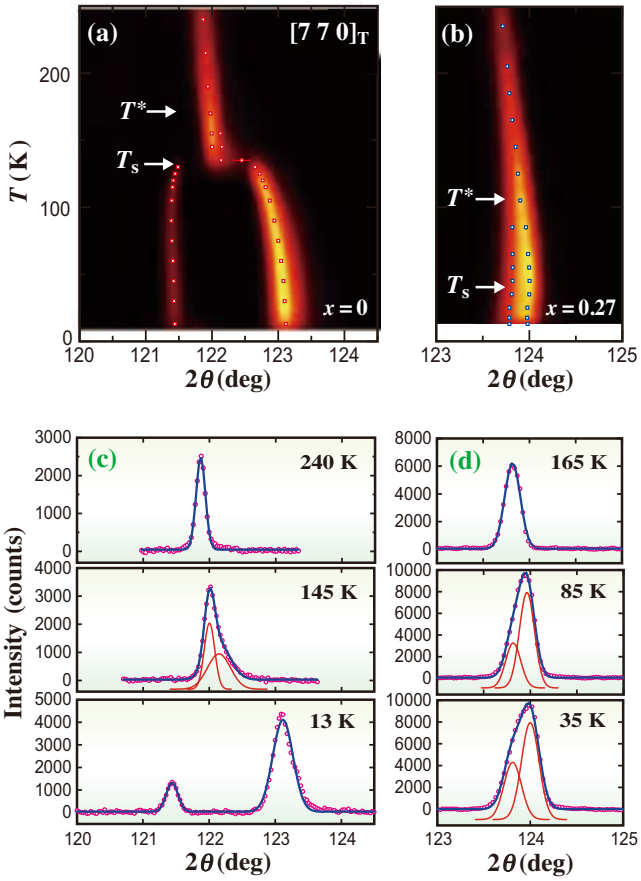

Fig. 2. **(a)** Temperature dependence of the Bragg peak $[7\,7\,0]_T$ for $x = 0$. **(b)** Same plot as that for $x = 0.27$. **(c)(d)** Examples of peak fitting at several temperatures.

Takasada Shibauchi*, Shigeru Kasahara and Yuji Matsuda

Department of Physics, Kyoto University

*Email: shibauchi@scphys.kyoto-u.ac.jp

References

[1] see, for a review, E. Fradkin *et al.*: Matter Phys. **1** (2010) 153.
[2] *S. Kasahara, H. J. Shi, K. Hashimoto, S. Tonegawa, Y. Mizukami, T. Shibauchi, K. Sugimoto, T. Fukuda, T. Terashima, A. H. Nevidomskyy, and Y. Matsuda: Nature* ***486*** *(2012) 382.*
[3] R. Okazaki *et al.*: Science **331**, (2011) 439.
[4] see, for a review, M. Vojta: Adv. Phys. **58** (2009) 699.
[5] R.A. Borzi *et al.*: Science **315** (2007) 214.

Slow dynamics of supercooled liquid *o*-terphenyl

The molecular dynamics in glass-forming liquids and polymers toward glass transition has been studied to understand the nature of glass transition. Relaxation process known as the α process, which is the structural relaxation process induced by molecular diffusion, has been thought to be closely related to glass transition. On the other hand, another relaxation process called the slow β (Johari-Goldstein) process, which seems to branch from the α process with cooling and is thought to play an important role in supercooled liquids approaching to the glass transition, has not been fully understood. So far, the decoupling of the slow β process from the α process has been considered to occur at around the temperature at which the properties of the α-relaxation dynamics change. To understand the decoupling phenomenon, the typical glass-forming molecule *o*-terphenyl has been studied [1] by quasi-elastic scattering measurement known as time-domain interferometry (TDI) using the ^{57}Fe-nuclear resonant scattering (NRS) of synchrotron radiation [2], which is a time-domain analogue of the Rayleigh scattering Mössbauer radiation method [3]. In this method, the beating pattern induced by the interference of the probe and reference NRS is detected in the time domain (examples of the spectra are shown in Fig. 1). The relaxations of the density correlation in the sample are reflected as a disappearance of the beating pattern, which gives the intermediate scattering function; we have assumed the stretched exponential decay function as the intermediate scattering function. The temperature T and momentum transfer q dependences of the mean relaxation times $\langle\tau\rangle$ obtained by the least square fitting of the measured spectra using the function are shown in Fig. 2 and Fig. 3, respectively.

When q = 14 nm^{-1}, the T dependence of $\langle\tau\rangle$ was observed to obey the Vogel-Fulcher-Tammann (VFT) law with a diverging behavior toward a certain

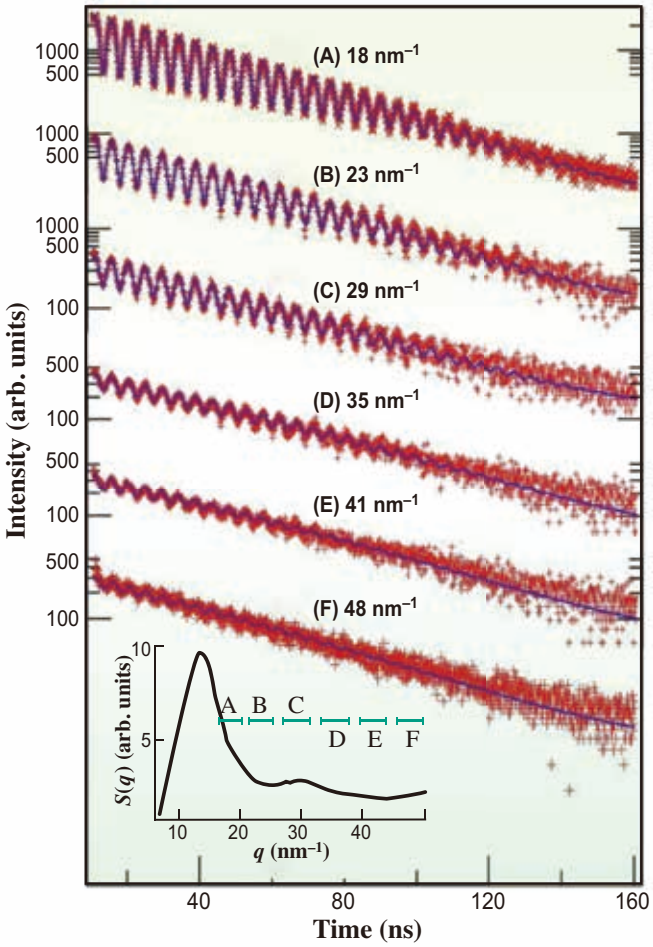

Fig. 1. Examples of TDI time spectra and their fitting curves at various momentum transfers at 265 K. The inset shows the static structure factor and momentum transfer regions used to obtain time spectra.

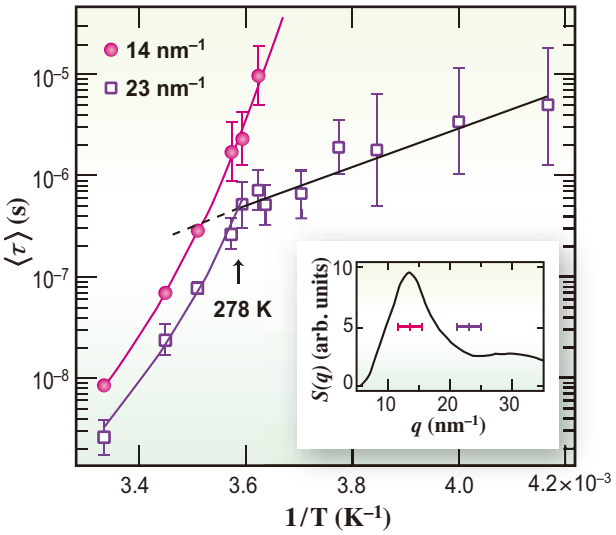

Fig. 2. Temperature dependences of relaxation times at 14 and 23 nm^{-1}. Solid lines indicate the fitting curves of data (see main text). The inset shows the momentum transfer regions used to obtain relaxation times.

temperature near the glass transition temperature, as shown in Fig. 2. Since the diverging behavior is consistent with that reported for the α process and is observed at the peak position of the static structure factor, the relaxation observed at q = 14 nm^{-1} is the structural relaxation due to the α process. On the other hand, at q = 23 nm^{-1}, the character of the T dependence of $\langle\tau\rangle$ was found to change at 278 K. The T dependence of $\langle\tau\rangle$ obeys the VFT law above 278 K, but obeys the Arrhenius law below 278 K. The activation energy of 36 (9) kJ/mol obtained by least square fitting below 278 K is consistent with those of the slow process obtained by the dielectric method. Therefore, the relaxations observed at q = 23 nm^{-1} below 278 K are mainly due to the slow β process and occur at the local length scale in *o*-terphenyl. Since the behavior of the T dependence of $\langle\tau\rangle$ above 278 K at q = 23 nm^{-1} is similar to that at q = 14 nm^{-1}, the relaxation observed at q = 23 nm^{-1} above 278 K is mainly due to the α process. Therefore, the turning temperature of 278 K is interpreted to be the decoupling temperature $T_{\alpha\beta}$ at which the primary source of the relaxation process observed at q = 23 nm^{-1} changes from the α process to the slow β process with cooling. From this result, it can be concluded that the slow β-relaxation process decouples from the relaxation process of the local length scale originating in the α process, which is faster than the mean relaxation of the α process. Owing to the difference in the length scale between the α and the slow β processes, the lines representing these two averaged relaxation times are concluded not to cross in the temperature dependence of the relaxation time as an extrapolation assumed so far.

Since the obtained decoupling temperature is also lower than the changing temperature of the diffusion behavior (290 K) obtained so far, our result indicates that a sufficient solid-like condition achieved by further cooling from 290 K is required for the decoupling of the slow β process from the α process.

Moreover, by measuring the q dependence of $\langle\tau\rangle$ at 265 K (below $T_{\alpha\beta}$) and at q values above the peak of the static structure factor, at which the spatial correlation relaxes mainly by the slow β process, we could obtain an anomalous q dependent behavior of $\langle\tau\rangle$ following the power law $\langle\tau\rangle \propto q^{-n}$ with an n value of 2.9 (5), as shown in Fig. 3. The obtained n value greater than 2 indicates the restricted microscopic dynamical behavior of the slow β process, which is independent of origin. Therefore, we found evidence of the restricted dynamical behavior of the slow β process as an anomalous q dependence of the relaxation time.

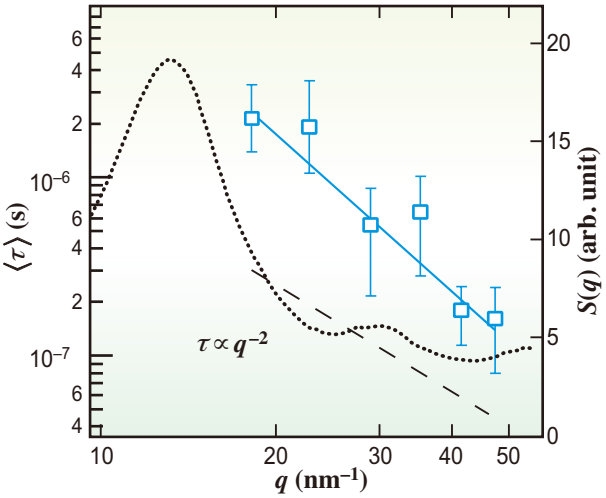

Fig. 3. Momentum transfer dependence of relaxation time at 265 K in higher momentum transfer region than the first peak of the static structure factor. Dot, bold, and dashed lines indicate static structure factor, fitting curve (see main text), and behavior $\langle\tau\rangle \propto q^{-2}$, respectively.

Makina Saito and Makoto Seto*

Research Reactor Institute, Kyoto University

*Email: seto@rri.kyoto-u.ac.jp

References

[1] *M. Saito, S. Kitao, Y. Kobayashi, M. Kurokuzu, Y. Yoda and M. Seto: Phys. Rev. Lett.* ***109*** *(2012) 115705.*
[2] A.Q.R. Baron *et al.*: Phys. Rev. Lett. **79** (1997) 2823.
[3] D.C. Champeney and F.W.D. Woodhams: J. Phys. B. **1** (1968) 620 and references therein.

Capturing instantaneous lattice distortion of tetragonal $BaTiO_3$ induced by application of voltage for millionths of a second

Piezoelectric crystals macroscopically expand, contract, and deform when an electric field is applied. Inversely, electric polarization is generated in crystals when external stress is applied. Piezoelectric devices utilizing this phenomenon are indispensable to our everyday lives; for example, they are used to control the ejection of ink in ink-jet printers and in the touch panels of cell phones. Nowadays, piezoelectricity is also the key for realizing vibration power generation systems for the so-called energy harvesting technique.

Several mechanisms underlying changes in the size and shape of piezoelectric materials have been discussed. To understand the essence of macroscopic piezoelectric deformation, it is necessary to examine the microscopic origin of piezoelectricity; i.e., how much and how fast atoms are displaced in piezoelectric crystals upon the application of an electric field. The atomic displacement induced by the electric field is too small to be detected; even the movement of a crystal lattice has not yet been fully clarified thus far. In this study, by combining two advanced measurement techniques used at SPring-8, i.e., a single-crystal diffraction technique using high-energy X-rays [1] and a high-speed time-resolved measurement [2,3], we succeeded in the *in situ* observation of the change in the crystal-lattice size of piezoelectric single crystals with a time of microsecond order during piezoelectric vibration.

Figure 1 shows the pump-probe-type time-resolved measurement system for collecting single-crystal diffraction images installed at beamline **BL02B1**. The synchrotron radiation (SR) is chopped using an X-ray chopper so that it is synchronized with the waveform of the external voltage. The time resolution of this experiment was 4 μs. There is a timing adjuster between the X-ray chopper and a voltage pattern generator. Time-resolved single-crystal diffraction spots of ferroelectric piezoelectric $BaTiO_3$ were measured at 300 K in the ferroelectric tetragonal phase using a single crystal plate of $5 \times 2.5 \times 0.1$ mm^3 with a pair of gold electrodes. A high-energy SR with a wavelength of λ = 0.35639(2) Å (E = 35 keV) was used. This high-energy SR enables us to obtain many diffraction spots from the inner area of the sample owing to the high transmission to the sample. The tetragonal lattice parameters a and c were analyzed precisely by the least-squares method using about 600 diffraction spot positions observed at each time.

Figure 2 shows the time evolution of the tetragonality c/a of $BaTiO_3$ when an electric voltage of square shape with 600 Hz is applied to the c-axis direction of a $BaTiO_3$ single crystal. The ferroelectric domain structure and crystal structure of $BaTiO_3$ expected in each time region are also shown in the bottom panel of Fig. 2. Tetragonal $BaTiO_3$ has a spontaneous polarization P_s along the c-axis. When the applied voltage is changed from negative (I) to positive, polarization reversal occurs (II), and the crystal lattice in the area of negative polarization slightly contracts in the c-axis direction. At the beginning of the polarization reversal, the lattice parameter in the negative polarization area is mainly observed because the volume ratio of the polarization area is larger than that of the positive area. When

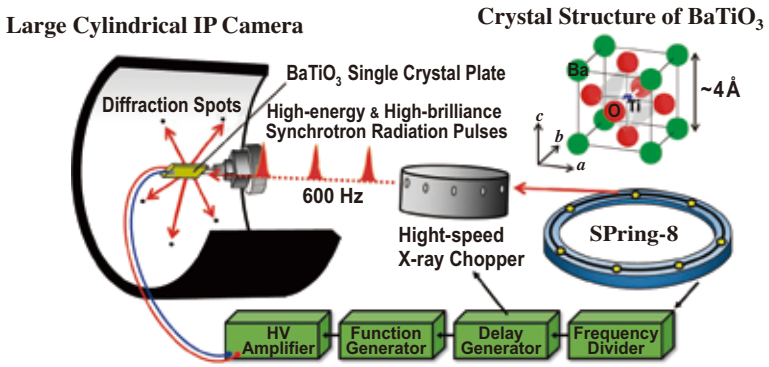

Fig. 1. Time-resolved measurement system for collecting diffraction images installed at BL02B1. The synchrotron radiation is chopped using an X-ray chopper so that it is synchronized with the waveform of the external voltage. There is a timing adjuster between the X-ray chopper and a voltage pattern generator.

the polarization reversal is completed and the whole crystal becomes a positive polarization area (III), the crystal can significantly expand in the *c*-axis direction. After that, *c/a* oscillates with decreasing amplitude (IV, V) and finally returns to its original value (VI). This behavior of *c/a* is similar to the damped oscillation of a spring. The oscillation of *c/a* observed in the regions III-VI is caused by the piezoelectric vibration of the $BaTiO_3$ single-crystal plate sample.

Thus, we succeeded in capturing the instantaneous lattice distortion induced by the application of the voltage for millionths of a second. The achievements of this study are expected to lead to developments in research on the dynamics of atomic displacement of nanosecond or picosecond order and to enable the observation of atoms in an electronic device during operation. Also, this technology is considered to be applicable to the development of new materials for electric storage devices, such as capacitors and batteries.

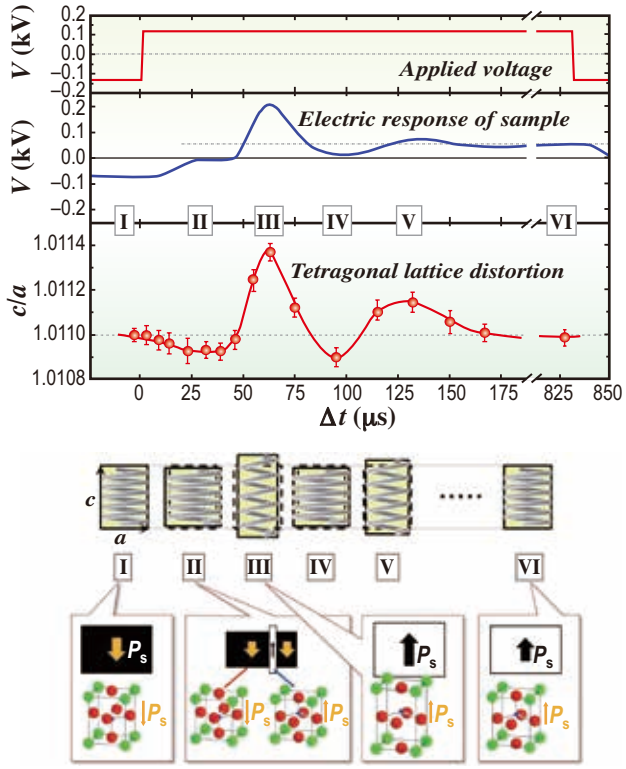

Fig. 2. Change in the tetragonality *c/a* with respect to time when a cyclic electric voltage of the bipolar square-wave type is applied to the *c*-axis direction of a $BaTiO_3$ single crystal. When the applied voltage is changed from negative (I) to positive, polarization reversal occurs (II), and the crystal slightly contracts in the *c*-axis direction. When the polarization reversal is complete (III), the crystal can significantly expand in the *c*-axis direction. *c/a* oscillates with decreasing amplitude and finally returns to its original value (III-VI). This behavior is similar to the damped oscillation of a spring. The ferroelectric domain structure and crystal structure expected in each time region are schematically drawn at the bottom.

Chikako Moriyoshi* and Yoshihiro Kuroiwa

Department of Physical Science, Hiroshima University

*Email: moriyosi@sci.hiroshima-u.ac.jp

References

[1] K. Sugimoto *et al.*: AIP Conf. Proc. **1234** (2010) 887.
[2] Y. Fukuyama *et al.*: Appl. Phys. Express **1** (2008) 045001.
[3] Y. Ehara *et al.*: Appl. Phys. Lett. **99** (2011) 182906.
[4] *C. Moriyoshi, S. Hiramoto, H. Ohkubo, Y. Kuroiwa, H. Osawa, K. Sugimoto, S. Kimura, M. Takata, Y. Kitanaka, Y. Noguchi and M. Miyayama: Jpn. J. Appl. Phys.* ***50*** *(2011) 09NE05.*

Synthesis of hollow spherical cages with polyhedral structures and application to the encapsulation of a whole protein in the cage

In nature, huge capsular structures are constructed by the self-assembly of simple repeating units through many weak interactions like hydrogen bonds, affording well-determined and functionalized cavities at the molecular level. Such capsular structures show biological functions for controlling vital activities through the encapsulation of specific substances in the cavities: for example, virus capsids and the relatively small protein, ferritin, store and release DNA/RNA and iron ions, respectively, and the relatively large protein chaperonin repair three-dimensional structures of trapped proteins.

Chemists have been inspired by the efficient synthesis of capsular structures in natural systems, and a variety of hollow molecules have been synthesized through the self-assembly of artificial molecules connected with weak interactions. The use of coordination bonds between an organic ligand molecule and a metal ion is one of the most successful examples of constructing well-defined, hollow structures owing to the appropriate strength of the bond and the inherent nature of metal ions with defined bond numbers and bond directions around the metal center. The structures of these metal-organic cages are limited to simple Platonic or Archimedean polyhedra and to small molecular sizes, typically approximately 1 to 2 nm, because nature entropically favors a higher symmetry and a smaller number of components.

Here, we report our recent achievements in the synthesis of a self-assembled metal-organic complex with the first stellated polyhedral framework [1] and in the encapsulating of a whole protein within the huge, well-defined cavity [2,3]. We have developed a method for the self-assembly of metal-organic cages from organic ligands (L) bearing two pyridyl groups as coordination sites and transition metal ions (M) with compositions of $M_{12}L_{24}$, where the functionalization of the ligand promises a reliable chemical functionalization of the product complex.

Stellated polyhedron is a mathematically defined polyhedral family with concave surfaces, constructed by extending the faces of a polyhedron until they intersect (Fig. 1(a)). A stellated polyhedral complex is difficult to synthesize owing to its more complicated structure than the reported Platonic or Archimedean polyhedral ones. Therefore, we employed the strategy of firstly constructing an Archimedean polyhedral complex with a cuboctahedral framework, i.e., an $M_{12}L_{24}$ sphere, with the coordination bonds of the pyridyl group **A** shown in Fig. 1(b) in blue and Pd(II) ions, followed by stellation by the 2nd coordination between the pyridyl group **B** shown in red and additional Pd(II) ions. Although the pyridyl groups **A** and **B** have the same coordination properties, the molecular design to use the rigidly fixed pyridyl group **A** and the flexibly tethered pyridyl group **B** enabled us to efficiently prepare the stellated complex based on the robust framework of the $M_{12}L_{24}$ sphere. The product structures of the first $M_{12}L_{24}$ cuboctahedron bearing the free pyridyl group **B** and the final $M_{18}L_{24}$ stellated cuboctahedron were clearly revealed by nuclear magnetic resonance (NMR), mass spectrometry (MS), and finally synchrotron X-ray diffraction studies carried out at beamline **BL38B1** in SPring-8 and at NE3A beamline in the Photon Factory (PF) (Fig. 1(c)).

On the basis of the robust $M_{12}L_{24}$ sphere

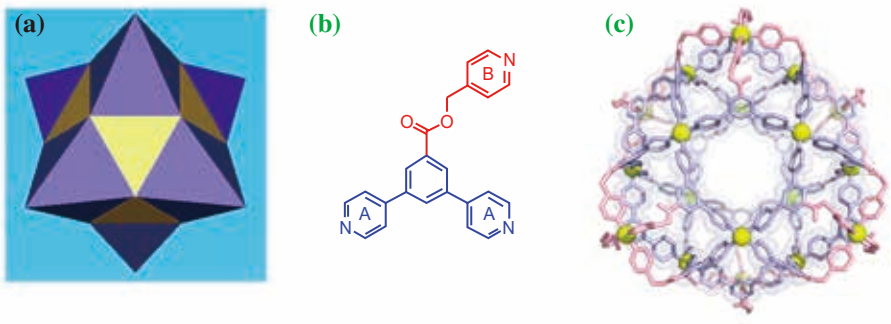

Fig. 1. **(a)** Mathematically defined stellated cuboctahedron. **(b)** Structure of the ligand for the synthesis of metal-organic complex with stellated polyhedral structure. **(c)** X-ray crystal structure of the stellated cuboctahedral complex.

accepting designable functionalization, we mimicked natural cages to encapsulate a whole biomolecule in a well-defined synthetic cage, as collaboration works with a group led by Institute for Molecular Science Professor Koichi Kato. Small organic molecules can be artificially encapsulated in a hollow cage, within which the structure or activity of the guest molecule can be controlled. If the encapsulation of a biomolecule in an artificial host is achieved, the structure and activity of the biomolecule could also be controlled at will through the design of the host, which should be of great use in drug development and other industrial applications. However, so far, it has not been possible to enclose larger biomolecules such as proteins because it has not been possible to increase the size of precisely structured artificial molecular capsules.

We noticed that the $M_{12}L_{24}$ sphere constructed from extended ligands and Pd(II) ions has a diameter of 6.3 nm, and that the cavity could encapsulate a whole protein. A ligand tethered to ubiquitin, a relatively small globular protein (76 residues, 8.6 kDa, approximately 3–4 nm in diameter), and a ligand bearing a hydrophilic sugar chain were synthesized; these organic ligands were then mixed with Pd(II) ions in a solvent. The $M_{12}L_{24}$ sphere encapsulating ubiquitin surrounded by a hydrophilic internal surface owing to the 23 attached sugar moieties was automatically formed through self-assembly (Fig. 2).

The precise structure of the product was revealed by NMR, and the determined diffusion coefficient supported the protein-trapping state in the cage. MS studies to determine the molecular weight were not successful unfortunately; however, collaboration works with a group led by Osaka University Associate Professor Susumu Uchiyama succeeded in analyzing of the molecular weight in solution using ultracentrifugation data, showing that the $M_{12}L_{24}$ sphere preserved the protein stably in solution.

We optimized the crystallization conditions and intensively worked on synchrotron X-ray diffraction studies carried out at **BL38B1**, **BL41XU**, **BL26B1**, and **BL26B2** beamlines in SPring-8 and at NE3A and BL17A beamlines in the PF.

Collaboration works with groups led by the Graduate School of Frontier Sciences (concurrently RIKEN SPring-8 center) Professor Takata and JASRI Group Leader Dr. Kumasaka finally determined the crystal structure by the maximum entropy method (MEM). The complex enclosing the whole protein at the center of the artificial capsule was clearly visualized.

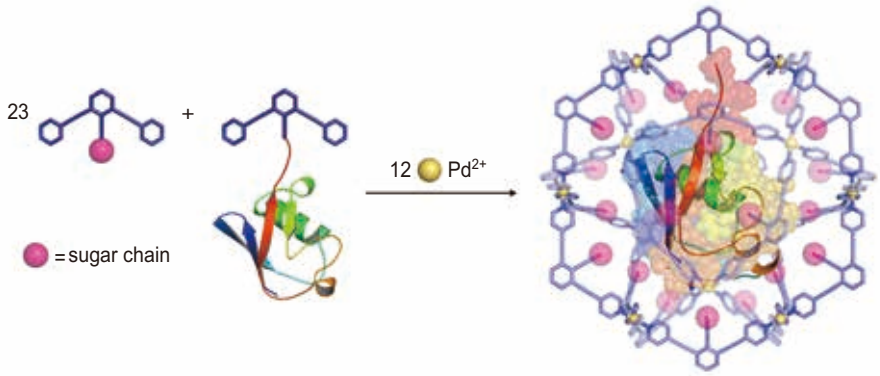

Fig. 2. Synthetic scheme of an $M_{12}L_{24}$ sphere with sugar-decollated inner surface encapsulating a whole ubiquitin molecule in the cavity.

Sota Sato[a,b] and Makoto Fujita[a,b,*]

[a] Department of Applied Chemistry, The University of Tokyo
[b] JST-CREST

*Email: mfujita@appchem.t.u-tokyo.ac.jp

References

[1] Q.-F. Sun, S. Sato and M. Fujita: Nature Chem. **4** (2012) 330.
[2] *D. Fujita, K. Suzuki, S. Sato, M. Yagi-Utsumi, E. Kurimoto, K. Kato and M. Fujita: Chem. Lett.* ***41*** *(2012) 313.*
[3] *D. Fujita, K. Suzuki, S. Sato, M. Yagi-Utsumi, Y. Yamaguchi, N. Mizuno, T. Kumasaka, M. Takata, M. Noda, S. Uchiyama, K. Kato and M. Fujita: Nature Commun.* ***3*** *(2012) 1093.*

"Negative photographic film"-like diffraction phenomenon found in photoelectron energy loss process

Photoelectron diffraction (PD) is an element-selective local structure analysis method. Atomic arrangements around photoelectron emitter atoms are deduced from the directions of forward focusing peaks (FFPs) and the diffraction rings around them. Recently, a direct atomic arrangement reconstruction algorithm from PD patterns has been developed, and the quality of reconstructed images has been significantly improved [1]. Furthermore, FFPs from inequivalent sites appear in different directions, so the position of a photoelectron emitter atom can be specified. PD combined with a spectroscopic method enables the investigation of the local-atomic-site-specific electronic properties [2].

However most emitted electrons undergo energy loss process. Indeed, energy dissipation is a ubiquitous phenomenon. PD patterns are destroyed by inelastic scattering. There were pioneering works on PD by Osterwalder and coworkers [3,4]. However energy-loss electrons were treated as mere obstacles that disturb photoelectron spectral measurement. We investigated this phenomenon in detail and found that completely reversed contrast patterns of the original PD appeared in the energy loss electron angular distribution [5]. This contrast reversal becomes dominant over PD pattern destruction with an energy loss larger than 80 eV. The mechanism of this new phenomenon is explained by the decrease in energy-loss electron intensity caused by absorption through inverse PD process just like a negative photographic film.

All the experiments were carried out using the two-dimensional display-type analyzer installed at the circularly polarized soft X-ray beamline **BL25SU**. Figures 1(a)-1(d) show the set of 2π-steradian Ge 3*p* PD patterns from the Ge(111) surface with photoelectron kinetic energies of 400, 600, 800, and 1000 eV, respectively. PD patterns obtained by both helicity excitations are summed. The positions of highly symmetric directions are indicated in Fig. 1(a). The dotted lines and dashed curves in Fig. 1(d) indicate the $\{1\bar{1}0\}$ and $\{110\}$ planes, respectively.

Three kinds of bright FFPs were observed in the $\langle 11\bar{1}\rangle$, $\langle 110\rangle$, and $\langle 001\rangle$ directions in Ge 3*p* PD patterns. They correspond to the directions of the first-, second-, and fourth-nearest Ge atoms, respectively. Diffraction patterns change markedly as the kinetic energy varies. Blue lines in Fig. 1(d) indicate the diffraction rings around FFPs. Their radii decrease as the kinetic energy increases.

Figures 1(e)-1(g) show a series of 2π-steradian energy-loss electron patterns at a kinetic energy of 600 eV. The photon energy was varied so that the kinetic energy is set to 40, 80, and 160 eV off the Ge 3*p* elastic peak. We found that the PD patterns are destroyed at 40 eV off the elastic peak, as discussed previously [3]. In Figs. 1(f) and 1(g), dark regions appear at the position of FFPs in Figs. 1(a)-1(d). Figure 1(h) is a contrast-reversed presentation of Fig. 1(g), which is almost a complete negative replica of PD in Fig. 1(b). The diffraction rings and Kikuchi-band-like features are identical. A negative 600-eV PD replica was observed in the energy-loss electron pattern from 160 eV and even at 350 eV off the elastic peak. The kinetic energy of the original elastic peak is much larger than those of energy-loss

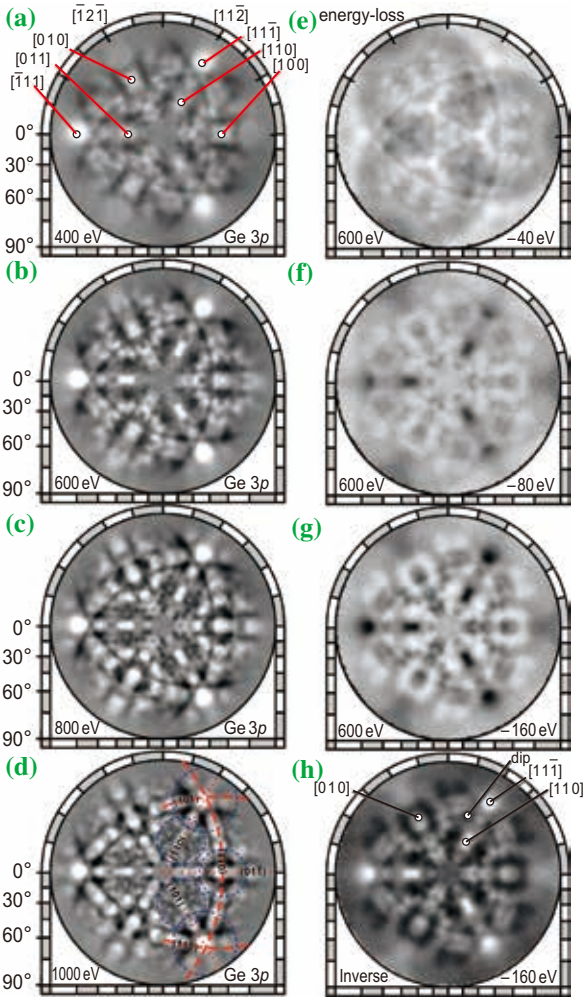

Fig. 1. **(a)-(d)** 2π-steradian Ge 3*p* photoelectron diffraction patterns at kinetic energies of 400–1000 eV. **(e)-(g)** 2π-steradian energy-loss electron patterns at a kinetic energy of 600 eV. Photon energy was varied. **(h)** is a contrast reversed presentation of (g).

electron patterns with the same kinetic energy of 600 eV in Fig. 1(b), but not that with higher or lower kinetic energies. The defocusing effect induced by inelastic plasmon excitation and electron blocking by atomic chains [4] cannot explain the appearance of this same negative replica pattern in the energy-loss electron patterns with different photon energy excitations.

Figure 2 shows a summary of the photon energy dependence of the diffraction and circular dichroism contrasts. The abscissa is the binding energy relative to the Ge 3*p* core level. PD contrasts above and below unity correspond to the constructive and destructive interferences, respectively. Note that the FFP intensities in the [11$\bar{1}$] and [001] directions rapidly decrease as the binding energy increases and then become smaller than unity at 80 eV off the Ge 3*p* elastic peak. The contrast becomes nearly constant at an energy beyond 120 eV. On the other hand, the contrasts of the dips around [11$\bar{1}$] FFPs are below unity, but as the binding energy increases they become larger than unity. The photoelectron spectrum is also shown. Ge 3*p* and 3*s* photoelectron peaks appeared at 0 and 58 eV, respectively. Ticks indicate a series of plasmon loss peaks at an interval of 16 eV. The shoulder structures observed in the diffraction and circular dichroism contrasts at 40 eV are due to Ge 3*s* core level excitation.

Figure 3(a) illustrates the models of normal PD. The dotted arc indicates the position of a display-type detector. PD is the interference of direct waves from a photoelectron emitter atom and of scattered waves generated by the surrounding atoms. As shown in the model, intense FFPs are observed in the direction of the surrounding atoms.

On the other hand, the mechanism of this new phenomenon can be qualitatively explained by the decrease in isotropic energy-loss electron beam intensity caused by absorption process. Figure 3(b) shows an electron wave undergoing scattering and being absorbed by the emitter atom. The proposed model shown in Fig. 3(c) is the absorption process. This absorption process takes place at every atomic site in the crystal. Electrons are partially absorbed, some of which are emitted in vacuum. As a result, dark low-transmission patterns appear.

The circular dichroism pattern observed in the original PD disappeared in the negative replica PD pattern. A similar phenomenon has been observed in electron backscatter diffraction. Therefore, this phenomenon is independent of the excitation source and its polarization. A new method of atomic structure analysis based on this *negative-photographic-film-like* diffraction phenomenon is expected to be realized.

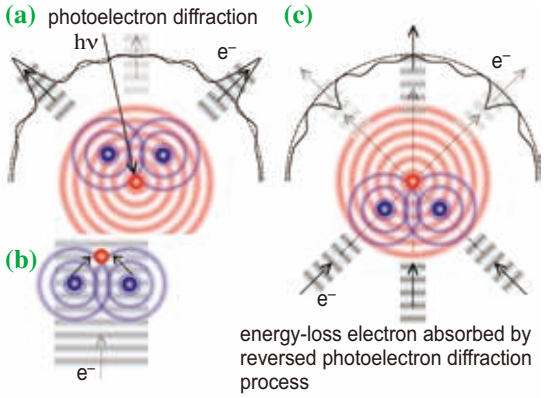

Fig. 3. Schematic illustrations of the mechanisms of **(a)** normal PD, **(b)** electron absorption process, and **(c)** time- and space-reversed PD process. Solid lines indicate the emitted electron intensity.

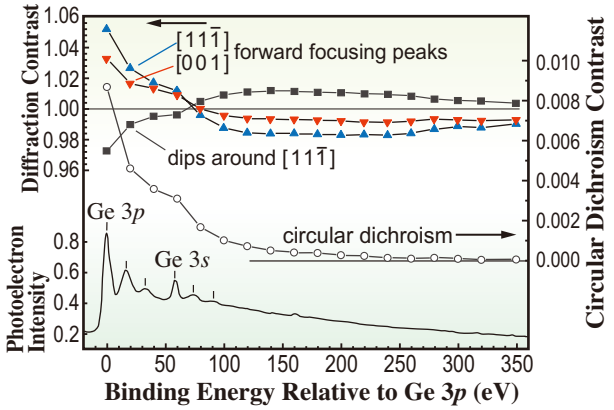

Fig. 2. Energy dependence of FFPs, destructive interference patterns, and circular dichroism contrasts together with photoelectron spectrum.

Fumihiko Matsui[a,*], Tomohiro Matsushita[b] and Hiroshi Daimon[a]

[a] Graduate School of Materials Science, Nara Institute of Science and Technology
[b] SPring-8/JASRI

*Email: matui@ms.naist.jp

References

[1] T. Matsushita *et al.*: Phys. Rev. B **75** (2007) 085419, *ibid.* **78** (2008) 144111.
[2] F. Matsui *et al.*: Phys. Rev. Lett. **100** (2008) 207201.
[3] J. Ostwerwalder *et al.*: Phys. Rev. B. **41** (1990) 12495.
[4] S. Hüfner *et al.*: Phys. Rev. B **42** (1990) 7350.
[5] *F. Matsui, T. Matsushita, M. Hashimoto, K. Goto, N. Maejima, H. Matsui, Y. Kato, and H. Daimon: J. Phys. Soc. Jpn.* ***81*** *(2012) 013601.*

Materials Science:

SPring-8 has a number of beamlines for spectroscopic and scattering experiments to investigate the electronic and magnetic structures of various kinds of materials in a wide photon energy range from the infrared (IR) to hard-X-ray region. Magnetic circular dichroism (MCD) in absorption spectroscopy in both soft-X-ray (BL23SU and BL25SU) and hard-X-ray (BL39XU) regions is utilized in magnetism studies. In this volume, two examples are introduced. Shiratsuchi shows the MCD results and explains the exchange bias mechanism of a Co/α-Cr_2O_3 interface. He further introduces the possibility of isothermal switching of the spin directions in an antiferromagnetic substrate by applying high magnetic field pulses. Suzuki represents the intrinsic nature of Pauli paramagnetism in diamagnetic bulk gold. There are several beamlines available for magnetism studies by methods involving scattering such as Compton scattering (BL08W) and nuclear resonance (BL09XU). Recently, these beamlines have been used not only for studies of magnetism but also for studies of other types of electronic structures. Okada *et al*. introduce the study of the electronic properties of high-temperature liquid using high-energy inelastic X-ray scattering. They develop a levitation technique to hold a liquid sample stably.

Electronic & Magnetic Properties

At BL23SU, investigations to observe the irradiation effects on biosamples are performed. Oka *et al*. combine soft-X-ray absorption spectroscopy with electron paramagnetic resonance spectroscopy (EPR). During ionization irradiation of DNA molecules, they observe a post-collision interaction effect. This provides an important basis for understanding a novel mechanism of DNA damage.

Photoemission spectroscopy (PES; including angle-resolved PES) studies are widely performed at both the soft-X-ray (BL07LSU, BL17SU, BL23SU, BL25SU, and BL27SU) and hard X-ray (BL15XU, BL19XU, BL29XU, BL46XU, and BL47XU) beamlines. Bulk sensitive information on the electronic structures of matter is obtained. Recently, polarization dependences of hard-X-ray photoemission spectroscopy (HAXPES) have been observed in many cases. Both circularly and linearly polarized lights are utilized. Sekiyama *et al*. introduce the dependence for linearly polarized light in HAXPES for gold. They observe the orbital nature of 5*d* bands of gold. In 2009, the Synchrotron Radiation Research Organization in the University of Tokyo constructed a high brilliance soft X-ray beamline with 8 segments of parallel/perpendicular figure-8 undulators in the long straight section of BL07LSU at SPring-8. The aim of this beamline is to perform time-resolved spectroscopy, three-dimensional scanning photoelectron microscopy with a lateral resolution in the sub-100 nm range, ultrahigh-resolution soft X-ray emission spectroscopy, and other advanced spectroscopies. Matsuda introduces the first results of using this beamline. He measured the time evolution of surface photovoltage effects for semiconductor surfaces.

There are still important activities from other beamlines that could not be introduced in this volume. We are certain of further progress and activities in materials sciences.

Toyohiko Kinoshita

Mechanism and functionality of perpendicular exchange bias using α-Cr_2O_3

Exchange bias is an effect that occurs at the interface of ferromagnetic (FM) and antiferromagnetic (AFM) layers. The magnetization of an exchange-biased system is forced in a particular direction against a magnetic-field cycle. This unidirectional nature of the system requires some symmetry breaking of the interfacial spin structure. The exchange bias was discovered more than 50 years ago, but the microscopic mechanism behind this symmetry breaking has been a major subject in this research field. Although the simple theory predicts that the symmetry breaking is caused by the interfacial uncompensated AFM spin that does not reverse with the magnetization reversal of the FM layer, the existence of such spin is still controversial. This is partly because in the intensively studied Co(-Fe)/Mn-Ir system, the interfacial AFM spins can possess many equivalent spin orientations owing to the non-collinear spin alignment of Mn-Ir, and thus, the differently oriented unreversed interfacial AFM spins would be smeared out macroscopically. In this study, we adopted the Pt/Co/α-Cr_2O_3/Pt perpendicular exchange-biased system in which the interfacial AFM spin can be restricted either up or down relative to the surface normal. In this article, we investigated the behavior of the interfacial uncompensated AFM spins detected using soft X-ray magnetic circular dichroism (XMCD) [1].

In practical applications, the exchange bias is utilized in a spin valve, a key element of the read head of hard disk drives. In the conventional devices, once the exchange bias is defined during the film fabrication process, subsequent control is difficult because high-temperature annealing is usually necessary. This constraint means that the conventional exchange bias is a static effect and it also encourages us to develop the isothermally switchable exchange bias that can offer an additional functionality of spin valves. In this article, we also demonstrate the isothermal switching of the exchange bias using a high pulsed magnetic field [2].

The samples, Pt(1.0)/Co(0.5)/α-Cr_2O_3(50, 120)/Pt(20) films grown on α-Al_2O_3(0001) substrates were fabricated in an ultra-high vacuum magnetron sputtering system. The numbers in parentheses represent the thickness of each layer in nanometer units. Soft X-ray absorption spectroscopy (XAS) and XMCD spectroscopy were adopted to detect the weak magnetic signals of the uncompensated AFM Cr spins separately from the strong signals of the FM Co spins. The XMCD measurements were carried out at the soft X-ray beamline **BL25SU**. A total electron yield method was adopted to detect the XMCD signal. For all XMCD measurements, the magnetic field was applied in the out-of-plane direction. For the isothermal switching study, we used the high-magnetic-field XMCD measurement system [3].

Figure 1(a) shows the XAS and XMCD spectra of the Co $L_{2,3}$- and Cr $L_{2,3}$-edges. The spectra were measured at 180 K after cooling in a magnetic field of +4.0 kOe. The spectra shown in Fig. 1(a) are averaged ones recorded under the static magnetic field of ±10 kOe. The XMCD intensity is observed at both Co $L_{2,3}$- and Cr $L_{2,3}$-edges. The Cr XMCD signal supports the presence of the uncompensated Cr spins at the interface with Co. Figure 1(b) shows the magnetic-field dependence of the XMCD intensity, i.e., the element-specific magnetization curve (ESMC), of Cr measured at 180 K. The photon energy was set at that indicated by the arrow in Fig. 1(a). Both horizontal and vertical shifts of the ESMC are clearly observed, as indicated by the broken and dotted lines, respectively. The horizontal and vertical shifts of the curve are attributed to the exchange bias (H_{Ex}) and

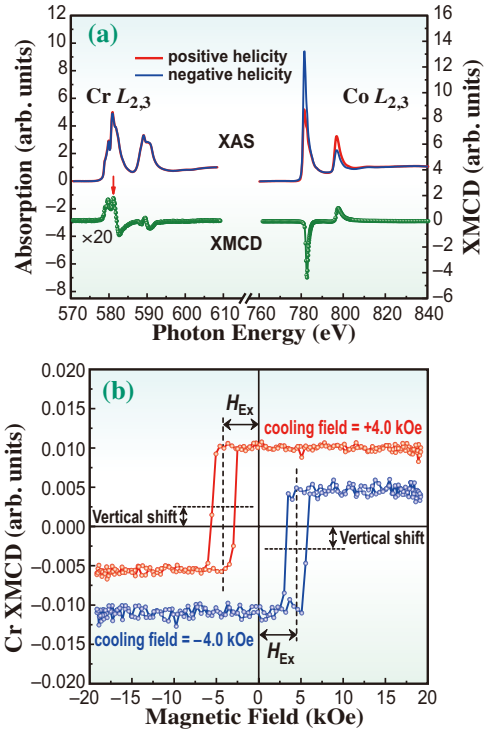

Fig. 1. **(a)** XAS and XMCD spectra at Co $L_{2,3}$- and Cr $L_{2,3}$-edges of Pt/Co/α-Cr_2O_3/Pt/α-Al_2O_3(sub.) film with 120-nm-thick α-Cr_2O_3 layer. **(b)** ESMCs of Cr. Red and blue lines represent the curves measured after applying positive and negative cooling fields, respectively. Broken and dotted lines in (b) represent the exchange bias field H_{Ex} and the vertical shift, respectively [1].

the unreversed uncompensated interfacial Cr spins, respectively. Figure 1(b) also demonstrates that the signs of both horizontal and vertical shifts of the ESMC of Cr are reversed by changing the cooling-field direction. These results indicate the direct relationship between the exchange bias and the unreversed uncompensated Cr spins.

The above finding encourages us to develop the isothermally switchable exchange bias by reversing the usually unreversed interfacial uncompensated Cr spins forcibly by, for example, applying a strong magnetic field. Figure 2(a) shows the ESMCs of Co in the positive pulsed magnetic fields. Measurements were carried out at 77 K after cooling in a negative magnetic field. The photon energy was set at that of the Co L_3-edge. When the maximum field strength was 10 kOe, the XMCD signal, i.e., the Co spin direction, returns to its original orientation after removing the magnetic field owing to the exchange bias. As the maximum applied field strength increases to 80 kOe, the XMCD signal in the remanent state decreases. Finally, the sign of the remanent XMCD is reversed at the maximum applied field strength of 90 kOe. A negative pulsed magnetic field of –10 kOe is subsequently applied and the exchange bias is then observed in the negative direction, as shown in Fig. 2(b). The absolute value of the exchange bias field is conserved after the switching of the exchange bias, meaning that the exchange bias is simply switched from positive to negative. Similar to the case of the positive magnetic field, as the maximum applied field strength exceeds –90 kOe, the exchange bias reverses again from negative to positive. This reversible switching of the exchange bias is qualitatively explained by the spin-flop transition in α-Cr_2O_3 and the exchange coupling between the Co spin and the interfacial uncompensated Cr spin. In Fig. 2(c), the switching process of the interfacial uncompensated Cr spin through the spin-flop excitation is schematically drawn. Assuming that the interfacial uncompensated Cr spins were downward before the application of the magnetic field, after the spin-flop phase is excited by the strong magnetic field above 90 kOe, the interfacial uncompensated spins are reversed to downward during the removal of the magnetic field owing to the interfacial exchange coupling with Co spins. The reversal of the interfacial uncompensated Cr spins causes the switching of the exchange bias. Although, at the present stage, a high magnetic field is employed to switch the interfacial uncompensated Cr spins, another technique with low power consumption and one that is applicable to highly integrated devices will be developed.

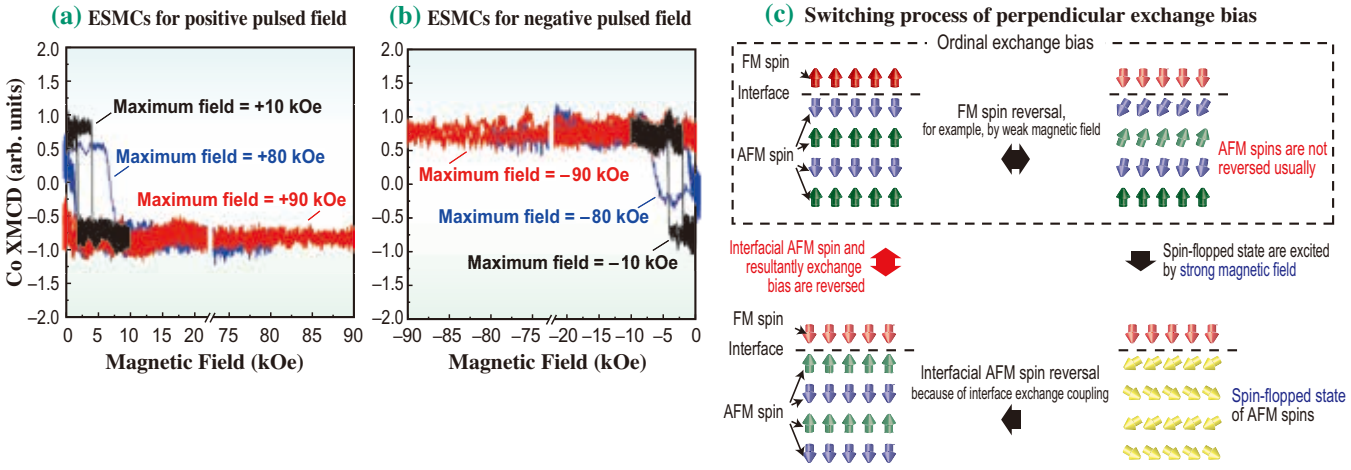

Fig. 2. ESMCs of Co measured under **(a)** positive and **(b)** negative pulsed magnetic fields for the film with a 50-nm-thick α-Cr_2O_3 layer. Black, blue, and red lines represent the curves for the maximum magnetic field strengths of ±10 kOe, ±80 kOe, and ±90 kOe, respectively. **(c)** Schematic representation of the switching process of the interfacial uncompensated Cr spins through the spin-flop transition and accompanying switching of the exchange bias [2].

Yu Shiratsuchi

Department of Materials Science and Engineering,
Osaka University

Email: shiratsuchi@mat.eng.osaka-u.ac.jp

References

[1] *Y. Shiratsuchi, H. Noutomi, H. Oikawa, T. Nakamura, M. Suzuki, T. Fujita, K. Arakawa, Y. Takechi, H. Mori, T. Kinoshita, M. Yamamoto and R. Nakatani: Phys. Rev. Lett.* ***109*** *(2012) 077202.*
[2] *Y. Shiratsuchi, K. Wakatsu, T. Nakamura, H. Oikawa, S. Maenou, Y. Narumi, K. Tazoe, C. Mitsumata, T. Kinoshita, H. Nojiri, and R. Nakatani: Appl. Phys. Lett.* ***100*** *(2012) 262413.*
[3] T. Nakamura *et al.*: Appl. Phys. Express. **4** (2011) 066602; SPring-8 Research Frontiers 2011, p.72.

Unveiling the hidden paramagnetic nature of diamagnetic bulk gold

Since ancient times, gold has presented a "magnetic" attraction to people owing to its eternal brilliance. At the beginning of the 21st century, by using X-ray spectroscopy with circularly polarized synchrotron radiation, scientists revealed that gold is actually capable of being magnetic.

Gold (Au) is one of the noble metals that humans are most familiar with, and its physical and chemical properties are the most studied among the 5*d*-electron systems. Regarding its magnetic properties, it is well known that elemental Au (bulk state) is a typical diamagnetic material with negative magnetic susceptibility. However, Au can have spontaneous magnetic moments when it forms alloys or stacked-film structures with 3*d* transition metals. Furthermore, it has been reported that Au nanoparticles (NPs) modified by some organic polymers at the NP surface exhibit superparamagnetism at low temperature [1] and even ferromagnetism at room temperature [2,3]. Spontaneous magnetization in Au NPs is possibly caused by a modification of the electronic states near the Fermi level. Thorough investigation of magnetism in elemental Au (parent material of Au NPs) would provide us with useful knowledge for elucidating the origin of magnetism in special forms of Au, i.e., NPs. X-ray magnetic circular dichroism (XMCD) spectroscopy is one of the promising techniques for studying the electronic and magnetic states of Au [1,3]. This element-specific tool can detect an imbalance in the density of electronic states with respect to the spin or orbital magnetic moments. It has a high sensitivity to ferromagnetic and paramagnetic moments but no sensitivity to diamagnetic moments. In this article, it is reported that XMCD spectroscopy at SPring-8 successfully unveiled Pauli paramagnetism in bulk Au hidden in a diamagnetic response that is larger than the intrinsic paramagnetic response [4].

A 5-μm-thick polycrystalline Au foil with a purity of 99.99% was studied using the high-resolution XMCD spectrometer at **BL39XU**. The beamline was equipped with a split-type superconducting magnet, and sample environments with a high magnetic field up to 10 T and temperatures as low as 2 K are available. An XMCD signal, the difference in the X-ray absorption spectra (XAS) for right- and left-circularly polarized X-rays, was recorded in the transmission mode by the helicity-modulation (lock-in detection) technique [5], which provided a detection sensitivity of a few parts in 10^5 for dichroic signals with respect to polarization-averaged XAS signals.

The XMCD results present clear and direct evidence of the magnetic response of bulk Au [4]. Figures 1(a) and 1(b) show XMCD spectra of Au foil at the L_3 and L_2 edges, respectively. The measured XMCD amplitude was on the order of 10^{-4} compared with the XAS signal (Figs. 1(c) and 1(d)), but the experiments produced clear dichroism signals with excellent precision owing to the helicity-modulation technique. The negative XMCD structure *A* at the L_3 edge and the positive structure *B* at the L_2 edge indicated that the Au 5*d* moment was aligned parallel to the external magnetic field. The field dependence of the XMCD signal demonstrated a paramagnetic-like response; the signs of the XMCD spectra were reversed for positive and negative magnetic fields of the same magnitude (±10 T), and the spectra for +2, +6, and +10 T were shown to change linearly with applied field.

Figure 2(a) shows the element-specific magnetization curve of the Au foil, i.e., the amplitude of the XMCD structure *A* as a function of the external magnetic field. The linear dependence of the signal on the external field supported the paramagnetic behavior of bulk Au. The slope of XMCD magnetization (Fig. 2(b)) was independent of temperature between 2 and 300 K. From measurements at variable temperatures and magnetic fields, the XMCD amplitude of Au was found to respond linearly with the external magnetic field and to be constant with respect to temperature. These results presumably indicate that bulk Au exhibits Pauli paramagnetism.

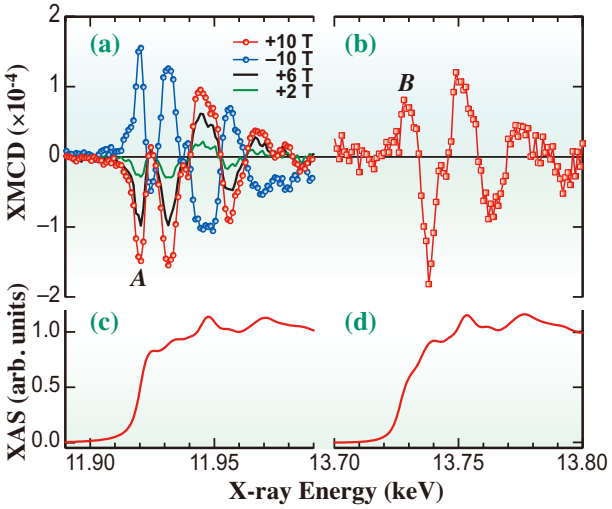

Fig. 1. X-ray magnetic circular dichroism (XMCD) spectra of Au foil measured at Au **(a)** L_3 and **(b)** L_2 edges at 2.3 K. X-ray absorption fine structure (XAS) spectra for (a) and (b) corresponding to the XMCD are shown in **(c)** and **(d)**, respectively. XMCD spectra recordead for different magnetic fields are shown in (a).

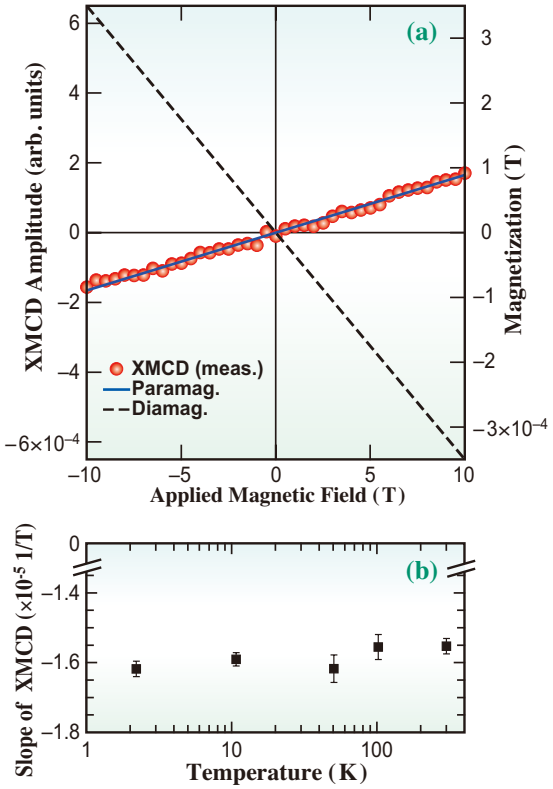

Fig. 2. **(a)** Element-specific magnetization curve of Au foil at 2.2 K, i.e., the amplitude of the XMCD structure at the L_3 threshold as a function of the external magnetic field. The dots represent measured values, and the blue line shows the fitted result using a linear function representing a paramagnetic response. The dashed line shows the diamagnetic response assumed from the reported value of the susceptibility of Au. Note that the sign of the XMCD signal was reversed for clarity. **(b)** Slope of element-specific magnetization curve as a function of temperature.

The spin and orbital magnetic moments of Au 5*d* electrons were determined to be $m_S = 9.8 \times 10^{-5}$ m_B / atom and $m_L = 2.8 \times 10^{-5}$ m_B/atom, respectively, at 10 T and at 2.3 K, using the sum rule analysis. The total moment $m_S + m_L = 1.26 \times 10^{-4}$ m_B/atom corresponds to paramagnetic susceptibility $\chi_{para} = 8.9 \times 10^{-6}$. Figure 2(a) shows the paramagnetic response of bulk Au, deduced from XMCD magnetization curves, and the diamagnetic response determined using the reported value of the diamagnetic susceptibility of Au, -3.5×10^{-5}. The signals originating from Pauli paramagnetism are weaker than those from diamagnetism. In conventional macroscopic magnetometry using a superconducting quantum interference device (SQUID), the Pauli paramagnetic response in Au is hidden by the stronger diamagnetic signal. In contrast, the XMCD spectroscopy measurement successfully yielded the intrinsic paramagnetic state.

The XMCD results for bulk Au provided a useful hint towards understanding the mechanism behind the emergence of magnetism in Au NPs. Figure 3 shows the XMCD spectra of bulk Au and Au nanoparticles protected by poly(allylamine hydrochloride) (PAAHC-Au NPs) [1]. For the NPs, structures *A* and *B* at the thresholds are enhanced at both the L_3 and L_2 edges compared with bulk Au. The strong XMCD features confined at the thresholds suggest that the spontaneous spin polarizations of 5*d* electrons are responsible for the superparamagnetism observed in PAAHC-Au NPs. In bulk Au, the magnetic moments were found to have a considerable orbital contribution, $m_L/m_S = 0.28$. Because a similar value ($m_L/m_S = 0.31$) was obtained for PAAHC-Au NPs, the large orbital contribution in elementary gold was suggested to be one of the possible origins of the spontaneous spin polarization in Au nanoparticles.

In summary, the XMCD study under high magnetic field, at various temperatures, and with a high signal-to-noise ratio, revealed that bulk Au exhibits both Pauli and orbital paramagnetism. XMCD spectroscopy, because of its extremely high sensitivity, is a powerful technique for exploring weak but exotic magnetism in noble metal compounds and nanoparticle systems.

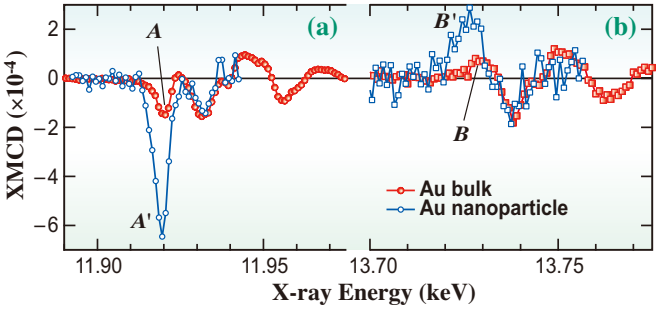

Fig. 3. XMCD spectra at Au **(a)** L_3 and **(b)** L_2 edges in PAAHC-Au nanoparticles (NPs) with mean diameter of 1.9 nm and in bulk Au foil. The data were taken at a temperature of 2.3 K in a magnetic field of 10 T.

Motohiro Suzuki

SPring-8/JASRI

Email: m-suzuki@spring8.or.jp

References

[1] Y. Yamamoto *et al.*: Phys. Rev. Lett. **93** (2004) 116801.
[2] P. Crespo *et al.*: Phys. Rev. Lett. **93** (2004) 087204.
[3] J.S. Garitaonandia *et al.*: Nano Lett. **8** (2008) 661.
[4] *M. Suzuki, N. Kawamura, H. Miyagawa, J. S. Garitaonandia, Y. Yamamoto and H. Hori, Phys. Rev. Lett.* ***108*** *(2012)047201.*
[5] M. Suzuki *et al.*: Jpn. J. Appl. Phys. **37** (1998) L1488.

A new approach for analyzing electronic properties of high-temperature liquids using high-energy inelastic X-ray scattering

The levitation technique has been developed over the last decade so as to hold a liquid sample stable and steady without a sample container, and its use with X-ray or neutron diffraction has enabled progress in research on atomic-level structural properties of high-temperature and undercooled liquids. In this study, in order to investigate the electronic properties of liquid silicon (Si), we have combined a newly developed levitation technique with high-energy, inelastic X-ray scattering, so-called Compton scattering, for the first time. We found, with the help of molecular dynamics simulations, that covalent bonding persists to some degree in the liquid phase. Compton scattering is a bulk-sensitive probe because the incident X-ray energy is as high as 116 keV, and thus the experimental data is not affected by the liquid surface, the temperature of which is difficult to control owing to the occurrence of thermal convection and evaporation. The present study demonstrates how X-ray Compton scattering can provide a novel spectroscopic window on the liquid state [1].

Si transforms into a metal accompanied by a density increase of about 10% upon melting. The resistivity of liquid Si (*l*-Si) at the melting temperature T_m is 0.75 Ωm, which is comparable to that of simple liquid metals such as *l*-Al. Molecular dynamics simulations of liquid Si at 1800 K suggest that approximately 30% of the bonds are covalent and that these covalent bonds possess a highly dynamic nature, forming and breaking rapidly on a time scale of 20 fs [2]. It is remarkable that two completely different types of bonds–metallic and covalent–can coexist in *l*-Si. In fact, the coexistence of two forms of liquid in a single component substance has been predicted to undergo a phase transition as a function of temperature and/or pressure. A recent study reports that *l*-Si could undergo a liquid-liquid phase transition (LLPT) below about 1232 K and above about –12 kB, separating into a high-density metallic liquid (HDL) and a low-density semimetallic liquid (LDL) [3]. However, 1232 K is far below the Si melting temperature of 1683 K, and as a result, the supercooled state has remained inaccessible to current experimental techniques, so that the experimental confirmation of an LLPT in Si remains an open question.

A key requirement for the occurrence of an LLPT obviously is that the metallic and covalent bonds coexist in *l*-Si. Although experimental investigations of the atomic configuration hint at the existence of covalent bonds in *l*-Si, soft X-ray and magnetic susceptibility measurements of electronic properties so far have not supported this viewpoint in that all four valence electrons in *l*-Si appear to behave like free electrons.

Liquid Si is highly reactive with most crucibles. To hold the sample without contamination, a high-temperature electrostatic levitator (HTESL) was used (Fig. 1). The HTESL levitates a spheroid sample of 2 mm diameter in a high vacuum environment (approximately 10^{-5} Pa) using electrostatic forces with feedback computer control [4]. The sample (Si, 99.9999% purity) was heated and melted using the focused radiation of three 50 W semiconductor laser beams with emission at 808 nm. Temperature was controlled within 15 K and measured by pyrometry.

Compton profiles of polycrystalline Si (300 K) and liquid Si (1787 K) were measured with high-energy (116 keV) inelastic X-ray scattering at **BL08W** beamline. In order to analyze the Compton profiles, Car-Parrinello molecular dynamics (CPMD) simulations were performed with the Quantum ESPRESSO package within the framework of the density-functional theory using the generalized gradient approximation. Figure 2 presents the differences between the Compton profiles for the solid and liquid phases [$\Delta J(p_z) = J_{solid}(p_z) - J_{liquid}(p_z)$]. The results of CPMD simulation were obtained by taking the difference between the liquid Compton profile and the spherically averaged profile of the solid. The CPMD results agree very well with the experimental results. In order to analyze the bonding character in *l*-Si obtained through CPMD simulation, the maximally localized Wannier functions

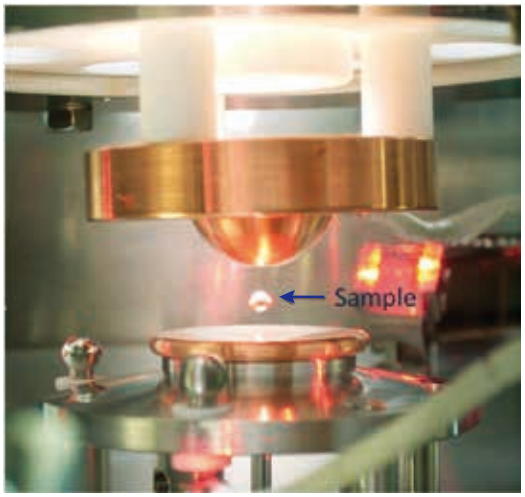

Fig. 1. Interior of electrostatic levitator. A sample of 2 mm diameter is levitated using electrostatic forces via feedback control.

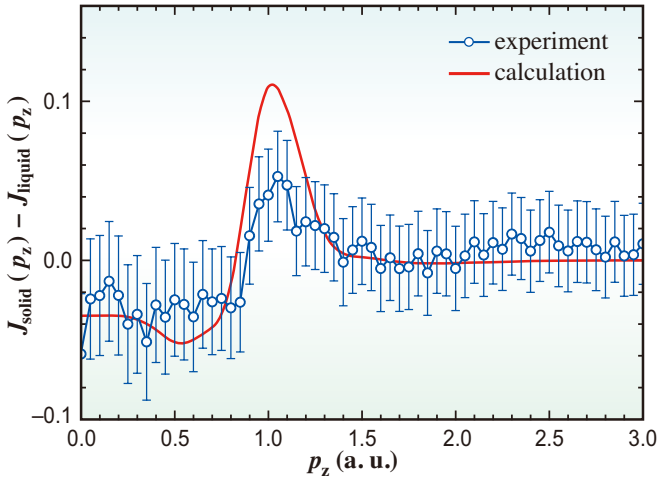

Fig. 2. Difference between the Compton profiles for the solid and liquid phases [$\Delta J(p_z) = J_{solid}(p_z) - J_{liquid}(p_z)$]: experiment (blue) and CPMD simulation (red).

(MLWFs) analysis method is used. We sort the MLWFs into three groups to categorize different types of electron pairs in *l*-Si: covalent bond pairs, lone pairs, and diffuse pairs. We found that, on the average, there are 17%, 83%, and less than 1% of covalent bonds, diffuse pairs, and lone pairs, respectively.

Figure 3 shows a snapshot from the simulation carried out on *l*-Si. The key point of our analysis is that the existence of covalent bonds in metallic *l*-Si is clearly confirmed, and that *l*-Si is not homogeneous at the atomic scale. The coexistence of two different bonding natures in a single-component liquid is a precondition for the occurrence of the LLPT. Our study thus supports the possible occurrence of LLPT in supercooled *l*-Si. Future Compton experiments with intense X-ray pulses will be needed to probe how the silicon bonding properties evolve from the metallic to covalent character and how an LLPT may occur.

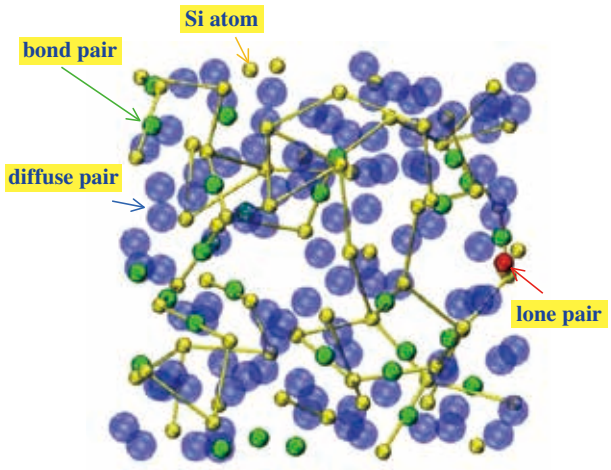

Fig. 3. Snapshot from the simulation on *l*-Si at 1787 K exhibiting Si atoms (yellow), covalent bond pairs (green), lone pairs (red), and diffuse pairs (translucent blue). Bonds connecting Si atoms are only guides for the eyes.

Junpei T. Okada[a,b,*] and Patrick H.-L. Sit[c]

[a] Institute of Space and Astronautical Science, Japan Aerospace Exploration Agency
[b] JST-PRESTO
[c] Dept. of Chemistry, Princeton University

*Email: okada.junpei@jaxa.jp

References

[1] *J.T. Okada, P. H.-L. Sit, Y. Watanabe, Y. J. Wang, B. Barbiellini, T. Ishikawa, M. Itou, Y. Sakurai, A. Bansil, R. Ishikawa, M. Hamaishi, T. Masaki, P.-F. Paradis, K. Kimura, T. Ishikawa and S. Nanao: Phys. Rev. Lett.* ***108*** *(2012) 067402.*
[2] I. Stich *et al.*: Phys. Rev. Lett. **63** (1989) 2240.
[3] P. Ganesh and M. Widom: Phys. Rev. Lett. **102** (2009) 075701.
[4] W.K. Rhim *et al.*: Rev. Sci. Instrum. **64** (1993) 2961.

Novel mechanism of DNA damage induced by soft X-ray irradiation as observed by an electron paramagnetic resonance spectroscopy

During ionizing irradiation of a cell, especially by high-energy radiation such as ion beams applied to cancer therapy, energy of various magnitudes is supplied to DNA molecules leading to multiple radiation damage of DNA molecules in a cell nucleus. Because of technical difficulties in observing physicochemical processes of damage induction, the entire mechanism of DNA damage has not yet been clarified. Monochromatic soft X-rays with specific energies less than 1 keV enable us to investigate the process of DNA damage due to photoelectric effects at carbon, nitrogen, and oxygen atoms, which are the constituent atoms of DNA molecules. Using soft X-rays, we study intermediate species of DNA damage, focusing particularly on unstable unpaired electron species.

Ionization of an electron from a molecule leaves an unpaired electron in a valence orbital. The unpaired electron in DNA is thought to play an important role in the reaction pathways leading to final damage. In general, the unpaired electron species have very short lifetimes because of their high reactivity. Electron paramagnetic resonance (EPR) is a powerful probe for the study of the unpaired electron species. Previous studies using a conventional EPR technique have provided useful knowledge about stable DNA radicals that can exist for more than a few seconds after termination of the irradiation at a liquid helium temperature. In those studies, samples must be kept at liquid nitrogen or helium temperatures during irradiation, transfer from an irradiator to an EPR spectrometer, and EPR measurement. Therefore, the very fast radical processes that are expected to be induced just after the occurrence of photoelectric effect initiated from inner shell photoionization in DNA are rarely observed because the unstable unpaired electron species might decay during the irradiation, sample transfer and EPR measurement.

To overcome the above problem, we have developed a unique EPR system at the synchrotron soft X-ray beamline **BL23SU** (Fig. 1) [1]. This system enables us to examine the EPR "*in situ*" signal of an unstable short-lived unpaired electron species of DNA and DNA-related molecules during soft X-ray irradiation in an EPR microwave cavity inside a high-vacuum chamber [2,3]. In this work, we measured the yield of the unpaired electron species of calf thymus DNA thin film around the nitrogen and oxygen *K*-edge, and discussed the origin of the unpaired electron species [4].

Figure 2 shows the variation in EPR intensity (spin concentration of the unpaired electron species) for DNA thin film as a function of soft X-ray energy. The right-hand axis of the figure shows soft X-ray absorption. As shown in Fig. 2, the EPR intensity changes along with the soft X-ray absorbance. One can see that the EPR intensities were significantly enhanced at energies slightly above the *K*-shell thresholds of nitrogen and oxygen.

After the creation of a *K*-shell hole of a light atom or molecule by soft X-ray absorption, Auger electron emission follows, which normally results in the production of a doubly charged parent cation (Auger effect). However, through the absorption of energy slightly higher than the *K*-shell ionization potential, the charge state of the produced cation is somewhat altered owing to the post collision interaction (PCI), i.e., the first emitted slow photoelectron is decelerated by the appearance of dication core upon the Auger effect. The significant deceleration of slow photoelectrons can lead to their recapture in an unoccupied orbital or a high-lying Rydberg orbital, which then results in unpaired electron species. In order to evaluate the PCI effect on the enhancement of the present EPR intensity, the recapture cross section after the Auger effect in DNA film was calculated using a semiclassical approximation. The calculated result of recapture probability (for the production of a singly charged parent cation) is almost unity at the *K*-shell ionization threshold and steeply decreases to less than 10% at 7 eV above the threshold. The cross section for the recapture, which is the product of the recapture probability and the *K*-shell ionization cross section, shows a sharp increase and a subsequent gradual decrease with increasing soft X-ray energy above the ionizing threshold and reproduces the significant

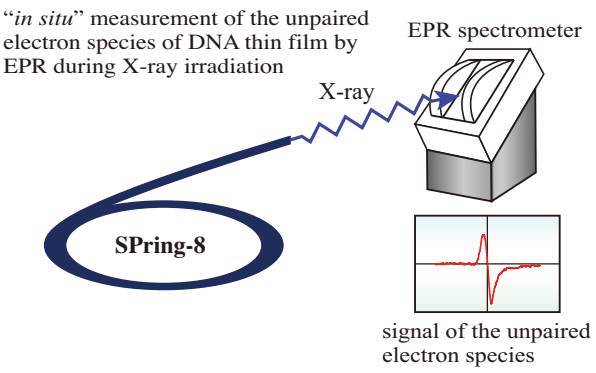

Fig. 1. Schematic of EPR system installed.

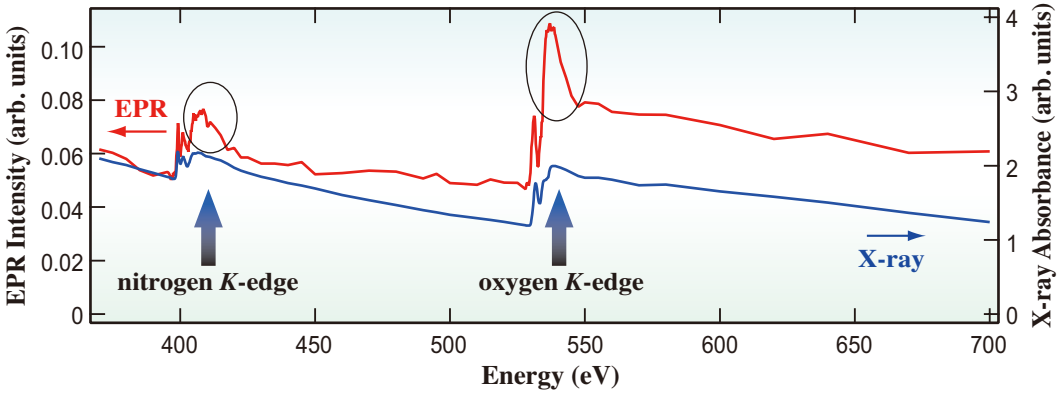

Fig. 2. Variation in EPR intensity for DNA thin film and X-ray absorbance as a function of X-ray energy. The EPR intensity is significantly enhanced around both the nitrogen and oxygen *K*-edges, as indicated by circles in the figure.

enhancement of the EPR intensities. This indicates that the enhanced EPR intensity at the *K*-shell thresholds can be attributed to the recapture of a photoelectron as a result of the PCI effect. The result suggests that the DNA film forms unpaired electron species through the excitation of enhanced electron recapture by the PCI effect (Fig. 3). Our result is the first observation of the PCI effect measured in condensed matter of DNA film. Different from the well-known low photoelectron attachment to an electronegative site in DNA followed by dissociation [5] or the recombination of slow electrons with ion holes, the observed ionization process induced by soft X-ray absorption is a novel mechanism of DNA damage.

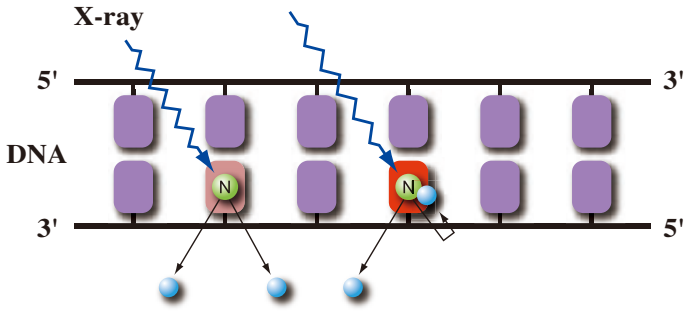

Fig. 3. X-ray absorption processes at the *K*-shell of a specific atom in DNA. Photoelectrons are ejected from the DNA upon irradiation with X-rays of slightly higher energy than the ionization threshold, decelerated and recaptured by PCI, and then detected as unpaired electron species.

Toshitaka Oka[a,†,*], Akinari Yokoya[a] and Masatoshi Ukai[b]

[a] Advanced Science Research Center, Japan Atomic Energy Agency
[b] Department of Applied Physics, Tokyo University of Agriculture and Technology

*Email: kotobuki@m.tohoku.ac.jp

[†] Present address: Department of Chemistry, Tohoku University

References

[1] A. Yokoya, K. Akamatsu: Nucl. Instrum. Meth. A **467-468** (2001) 1333.
[2] A. Yokoya *et al.*: Int. J. Radiat. Biol. **80** (2004) 833.
[3] T. Oka *et al.*: Appl. Phys. Lett. **98** (2011) 103701.
[4] *T. Oka, A. Yokoya, K. Fujii, Y. Fukuda, M. Ukai: Phys. Rev. Lett.* ***109*** *(2012) 213001.*
[5] B. Boudaïffa *et al.*: Science **287** (2000) 1658.

Prominent 5*d*-orbital contribution to the conduction electrons in gold probed by polarization-dependent hard X-ray photoemission

Single-element materials in the same column in the periodic table often show mutually similar features, as seen in alkaline(-earth) metals and halogens. On the other hand, it is known that among noble metals, gold has considerably different chemical stability from that of silver even though their electronic structure near the Fermi level, as well as Fermi surface topology, is thought to be almost equivalent. For instance, it is well known that solid gold is very stable under many circumstances, whereas solid silver is gradually oxidized in air. The valence-band electronic configurations of these solids per atom have so far been recognized to be composed of fully occupied *nd* states (nd^{10}) plus one conduction electron occupying an (n+1)*sp* state (n = 4 for silver and n = 5 for gold), but it has not been experimentally verified whether these configurations are correct or not.

Hard X-ray photoemission spectroscopy (HAXPES) shows, in addition to high bulk sensitivity, such characteristic features as (1) comparable *s* and *ip* (i > 3) photoionization cross sections to those for the *d* and *f* orbitals and (2) orbital-dependent photoelectron angular distribution with respect to the polarization of excitation photons [1]. Figure 1 shows the photoelectron angular distribution for the Ag 4*d*, 5*s*, and In 5*p* (nearly equivalent to the Ag 5*p*) orbitals in the HAXPES region as a function of take-off angle δ, which is defined as the angle between the direction of the electric field (polarization) of photons and the horizontal plane in which the momentum direction of the photoelectrons to be detected is involved. Here, δ = 0° (90°) corresponds to the *p*-polarization (*s*-polarization) configuration. One can recognize from the figure, that the Ag 4*d* photoelectron intensity is not very suppressed in the *s*-polarization configuration compared with that in the *p*-polarization configuration, whereas the Ag 5*s* and 5*p* photoelectron intensities are strongly suppressed in the *s*-polarization configuration. As an overall tendency, the theoretical calculation [1] predicts that the photoelectron intensity at the *s*-polarization configuration relative to that at the *p*-polarization configuration is as low as < 0.1–0.2 for the *s* and *jp* (j > 4) states compared with that for the *d* and *f* states at the photoelectron kinetic energy of ~10 keV, which has been experimentally verified for several inner-core orbitals [2]. Therefore, the orbital contribution in the valence bands in solids could be revealed by linear polarization-dependent HAXPES.

In order to realize the linear polarization-dependent HAXPES, we have switched the linear polarization of the excitation light using a single-crystalline (100) diamond phase retarder with the 220 reflection [2,3] with a thickness of 0.7 mm, placed downstream of the post-monochromator (channel-cut Si crystal). The transmittance of the X-ray at ~8 keV for the diamond was confirmed to be ~35%. The polarization-dependent HAXPES was performed at **BL19LXU** using an MBS A1-HE photoelectron spectrometer. Polycrystalline gold and silver prepared by *in situ* evaporation were measured at 12–15 K. The energy resolution was set as ~280 (~400) meV for the measurement of silver (gold). The spectral weights were normalized by the photon flux. It should be noted that this technique is useful even for polycrystalline samples, as we demonstrate here.

Figure 2 shows the polarization dependence of the valence-band spectra for polycrystalline silver and gold. For silver, the relative spectral weight from the Fermi level (E_F) to the binding energy of

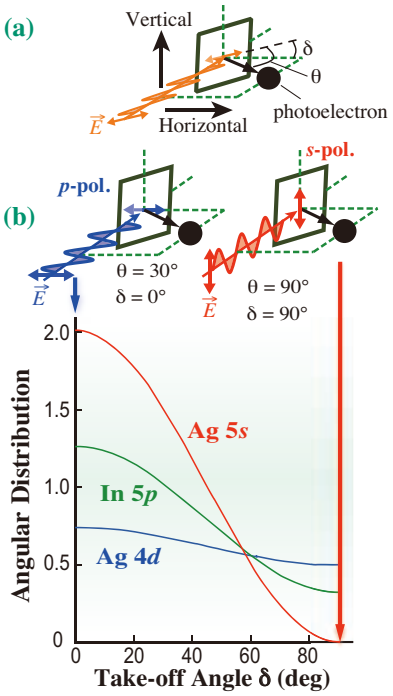

Fig. 1. **(a)** Geometrical configuration representing the directional relationships among the photoelectron propagation to be detected, the excitation-light propagation, and the electric field (linear polarization) of the excitation light for the *s*-polarization, *p*-polarization, and the geometry with the take-off angle of θ. **(b)** Photoelectron angular distribution calculated using parameters in Ref. [1] with respect to the direction of the linear polarization of excitation photons at the kinetic energy of 10 keV for the Ag 4*d*, 5*s*, and In 5*p* orbitals, where the angle between the propagation directions of the excitation photons and the photoelectrons to be detected is fixed at 120°. The angular distribution for the In 5*p* orbital is a substitute for the "Ag 5*p*" orbital (keeping in remind that no occupation is assumed for the 5*p* orbital of a neutral Ag atom, and hence no parameter for the calculation is given to this orbital).

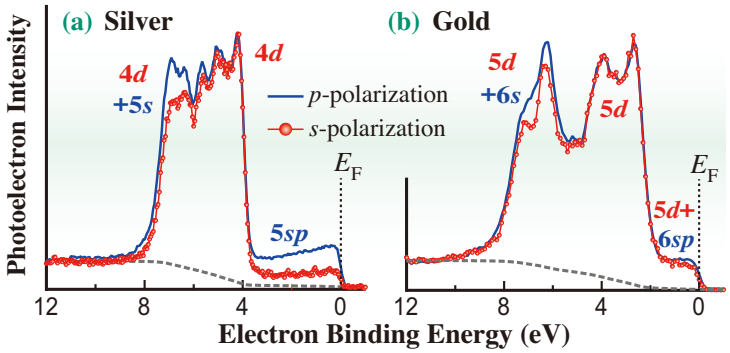

Fig. 2. Polarization-dependent valence-band HAXPES spectra of silver **(a)** and gold **(b)** at hν ~8 keV. The spectra have been roughly normalized by the intensity at the binding energy of 4–5 (2–5) eV for silver (gold).

3 eV is markedly suppressed in the *s*-polarization configuration compared with that in the *p*-polarization configuration, where both spectra are roughly normalized at the intensity at the binding energy of 4–5 eV. This polarization dependence as a function of the binding energy reveals that the 4*d* bands are located far below E_F and are well separated from the conduction 5*sp* band in the energy region from E_F to ~3 eV. It is thus experimentally confirmed that the 4*d* orbitals are nearly fully occupied whereas the conduction electrons are, to some extent, free-electron-like with a negligible 4*d* contribution in the solid silver, as has long been expected. On the other hand, the polarization dependence of the valence-band spectra near E_F for bulk gold is not only quantitatively but also qualitatively different from that for silver. When the spectra are normalized by the intensity in the binding energy region of 2–5 eV, where the Au 5*d* bands are located, the spectral weight near E_F is negligibly suppressed even in the *s*-polarization configuration. Our detailed analysis has shown the prominent (about 50%) 5*d*-orbital contribution to the conduction electrons in gold.

The revealed qualitative difference in the mixing of *d*-orbitals in the conduction bands crossing E_F between silver and gold, which is schematically shown in Fig. 3, originates from the different strengths of the electron correlation. In the case of silver, the Ag 4*d* electron correlation effects cannot be neglected when to discussing its electronic structure, whereas the Au 5*d* correlation effects are much weaker. Considering our finding and the fact that platinum with a band structure almost equivalent to that of gold is also very stable in air, where the 5*d* contribution to the conduction electrons is undoubtedly predominant, we can conclude that the prominent 5*d* contribution to the conduction electrons has a role in protecting gold from oxidization in air.

Our result has also revealed the presence of intrinsic 5*d* holes in gold. It is expected that there are 5*d* holes even in the previously investigated gold nanoparticles that show magnetism at beamline **BL39XU** [4]. The number of 5*d* holes will increase if the conduction electrons are transferred from the nanoparticles to neighboring molecules as discussed in Ref. [4]. In this context, it is natural to consider a role of 5*d* holes in the magnetism of gold nanoparticles, although our result does not give direct evidence of such a situation.

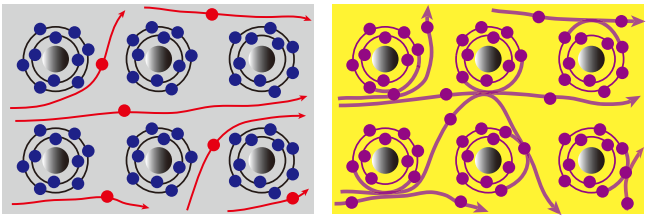

Fig. 3. Schematic picture summarizing our finding, where the 5*sp*-orbital conduction electrons nearly freely moving inside silver (red circles with bold lines) are well separated from the 4*d*-orbital electrons (blue circles), but the 5*d*-orbital electrons are strongly mixed with the 6*sp*-orbital electrons and therefore contribute prominently to the conduction electrons in gold. The large gray circles denote nuclei.

Akira Sekiyama[a,b,*], Atsushi Higashiya[b,c] and Shin Imada[d]

[a] Division of Materials Physics, Osaka University
[b] SPring-8/RIKEN
[c] Faculty of Science and Engineering, Setsunan University
[d] Department of Physical Science, Ritsumeikan University

*Email: sekiyama@mp.es.osaka-u.ac.jp

References

[1] M.B. Trzhaskovskaya *et al.*: At. Data Nucl. Data Tables **92** (2006) 245.
[2] *A. Sekiyama, J. Yamaguchi, A. Higashiya, M. Obara, H. Sugiyama, M. Y. Kimura, S. Suga, S. Imada, I.A. Nekrasov, M. Yabashi, K. Tamasaku and T. Ishikawa: New J. Phys.* ***12*** *(2010) 045043.*
[3] M. Suzuki *et al.*: Jpn. J. Appl. Phys. **37** (1998) L1488.
[4] Y. Yamamoto *et al.*: Phys. Rev. Lett. **93** (2004) 116801.

Observation of oscillatory relaxation of surface photovoltage effect by time-resolved soft X-ray photoemission spectroscopy with synchrotron radiation

Photoinduced phenomena in semiconductors have attracted technological interest in the development of optoelectronic devices, such as solar cells, that have directly led to solutions to problems in global energy issues. In photovoltaic and photocatalytic elements, the most fundamental event is the generation of photovoltage (PV). In the PV effect, an electron-hole pair, created by photoexcitation, is split and the two-types of carriers are spatially separated. The electron-hole separation is induced by their opposite drift forces near the surface, creating a voltage difference between the surface and bulk (the surface photovoltage effect), and by the difference in their diffusion velocities from the surface (the photo-Dember effect). Relaxation of the effect proceeds through electron-hole recombination at the surface. An overall simple picture of the PV effect has been widely accepted, however, the details of the mechanism have remained uncertain. It is of note that, in semiconducting materials, the carriers have been known to respond nonlinearly even under a moderate external field. Such non-equilibrium behaviors have attracted interest in the field of fundamental physics, and their possible applications in optoelectronic technology have also recently been investigated.

The temporal evolution of dynamical phenomena has been empirically probed by time-resolved experiments by various methods, among which the measurement by photoemission spectroscopy has an advantage in being able to trace electronic states (valence bands or molecular orbitals) and chemical shifts (core-level states) directly in *real time*. At the soft X-ray beamline **BL07LSU**, we developed a photoemission spectroscopy system with a time-of-flight spectrometer and with femtosecond-pulse lasers for time-resolved measurements [1]. Pulses of SR and lasers are stably synchronized with jitter time of better than 10 ps and their time delay is limited by time resolution of the SR pulse width (50 ps). With the present system, we performed detailed time-resolved photoemission spectroscopy to elucidate the relaxation mechanism after the PV effect.

Figure 1(a) shows Si 2*p* photoemission spectra of the Si(111)7×7 surface, one of the most famous Si clean crystal surfaces, on an *n*-type Si wafer [2]. Upon laser irradiation, the core-level shift directly corresponds to the variation in the Si bulk band and, thus, to the generation of photovoltage at the surface [3] (Fig. 2). Figure 1(b) shows a plot of the energy variation in the Si 2*p* core-level spectra for a delay time of 1 ns after laser irradiation, taken with various power densities of the pump laser. The energy shift initially increases linearly with logarithmic scale of the power density (stage I) but deviates from linearity above ~10 μJ/cm^2/pulse. Above ~100 μJ/cm^2/pulse (stages II, III), the power dependence saturates. In the conventional surface PV picture, photovoltage increases with photon density, as shown in stage I, and the behavior in stages II, III is extraordinary.

Figure 3 shows time-resolved Si $2p_{3/2}$ core-level spectra after laser irradiation at delay times from 0 to 70 ns [3]. The relative binding energy was measured

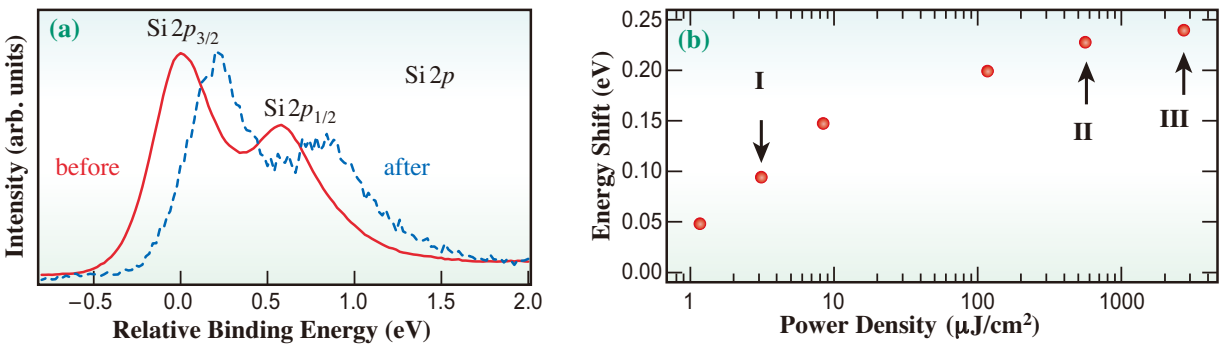

Fig. 1. **(a)** Si 2*p* core-level spectra (hν = 253 eV) before and after the laser irradiation are shown as solid (red) and dashed (blue) lines, respectively. The power density of the pump laser (hν = 1.51 eV) was 2700 μJ/cm^2/pulse. **(b)** Energy shift of Si 2*p* spectra, measured at different power densities or photon densities. The delay time between the pump laser and probe synchrotron pulses was set at 1 ns.

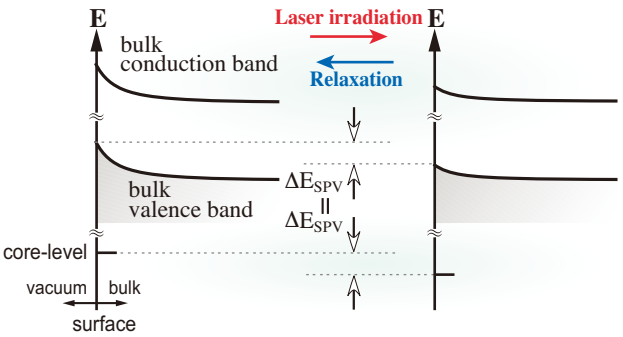

Fig. 2. Schematic of photovoltage effect at semiconductor surface. Bulk bands bend in energy as they approach a surface (surface band bending effect). Energy shift (ΔE_{SPV}) of the bulk band at the surface, induced by laser irradiation, corresponds to that of the core level.

with reference to the energy position before pumping. Whereas the spectral evolution, taken at laser pumping densities of 3.1 (Fig. 3(a)) and 560 (Fig. 3(b)) μJ/cm^2/pulse, shows monotonic decay with time, that at 2,700 μJ/cm^2/pulse exhibits a temporal oscillation (Fig. 3(c)) that includes several frequencies that are higher with shorter delay times. A part of the data can be parameter-fitted (the solid curve in (c)) with the following damped oscillation solution:

$$f(t) = y_0 + \{C_1\cos(\omega t) + C_2\sin(\omega t)\}\exp(-t/\tau) \qquad (1)$$

where y_0 is the offset and C_i's are amplitudes of the sinusoidal functions. The frequency (period) of the fitted oscillation is ω = 11 MHz (91 ns); the oscillations at short delay times are likely to have a similar frequency of several 10 MHz (several 10 ns).

Our experimental data clearly show that, under high laser power density, the excited carriers of the Si(111)7×7 surface layer have long decay times; however, what is unexpected is the observation of periodic behavior in a series of time-resolved spectra (Fig. 3(c)). Typically, surface photovoltage decays continuously with a simple recombination of an electron and a hole, transferred from the bulk. The observation of the oscillation likely indicates the existence of the nonlinear effect during the surface recombination process, which potentially lead to a new technique of ultrafast optical control of photovoltage at the surface. Considerations of theoretical models of carrier kinetics are currently underway in pursuit of a proper understanding of the intriguing phenomena.

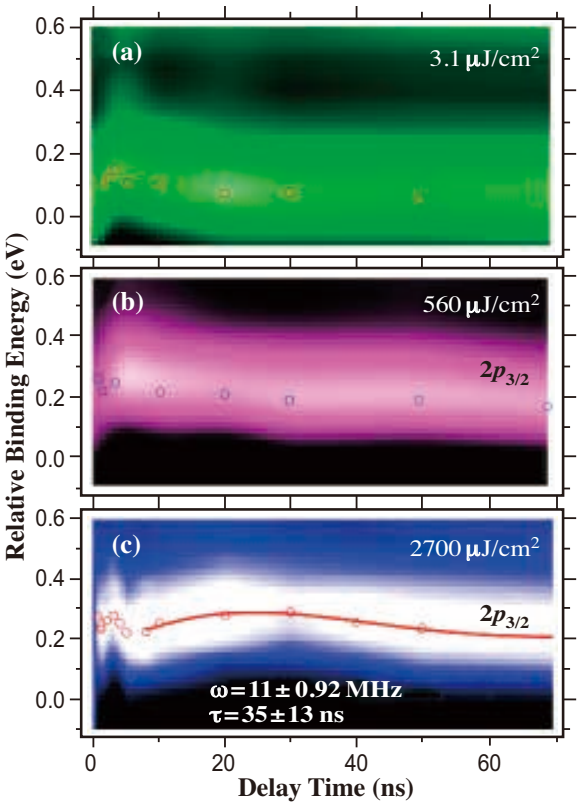

Fig. 3. Time evolution of Si 2*p* spectra taken at different laser power densities per pulse: **(a)** 3.1, **(b)** 560, and **(c)** 2700 μJ/cm^2/pulse, corresponding to stages I, II, and III in Fig. 1(b), respectively. The vertical axis represents relative binding energy with respect to the Si $2p_{3/2}$ peak position before photoexcitation. The open circles correspond to data points. In the map, points in the region between data points are linearly interpolated. The solid line in (c) is the result of fitting Eq. (1).

Iwao Matsuda

The Institute for Solid State Physics,
The University of Tokyo

Email: imatsuda@issp.u-tokyo.ac.jp

References

[1] *M. Ogawa, S. Yamamoto, Y. Kousa, F. Nakamura, R. Yukawa, A. Fukushima, A. Harasawa, H. Kondo, Y. Tanaka, A. Kakizaki and I. Matsuda: Rev. Sci. Instrum.* ***83*** *(2012) 023109.*
[2] *M. Ogawa, S. Yamamoto, R. Yukawa, R. Hobara, C.-H. Lin, R.-Y. Liu, S.-J. Tang and I. Matsuda: Phys. Rev. B* ***87*** *(2013) 235308.*
[3] M. Kamada *et al.*: Surf. Sci. **454** (2000) 525.

Chemical

Reports on state-of-the-art chemical research conducted at SPring-8 have once again been published in major journals this year, covering research such as the visualization of cathode catalyst layers, single-molecule magnets, the dispersion of single-walled carbon nanotubes using discotic ionic liquid crystals, the application of nuclear resonant vibrational spectroscopy to hydrogenase motion analysis, a pressure-induced structural change of a polymer melt, EXAFS avoiding interference of multielectron excitation effects, and the application of SASE-FEL to study energy transfer in Ar-Ne core-shell clusters.

The X-ray computed laminography-X-ray absorption fine structure (XCL-XAFS) has been developed as a powerful tool to visualize the three-dimensional structural information of catalysts. Prof. M. Tada *et al.* (IMS) revealed, at BL47XU, that the XCL-XAFS technique reveals not only the morphology/structure but also provides three-dimensional structural information on Pt cathode catalyst degradation in a nondestructive manner. Quantum tunneling of the magnetization (QTM) between double-well potentials, which is a prominent property of single-molecule magnets (SMMs), is the basis of high-density storage and quantum computing device concepts. Lanthanoid(III)-phthalocyaninato (Ln(III)-Pc) sandwich complexes behave as SMMs. Prof. M. Yamashita *et al.* (Tohoku Univ.) showed the molecular structure and magnetic relaxation properties of dinuclear Ln(III)-Pc multiple-decker complexes at BL02B1 and BL40XU. A variety of soft electrical conductors have been developed by doping carbon nanotubes (CNTs) into organic and polymeric materials. Liquid crystalline (LC) materials are attracting increasing attention for doping CNTs. Prof. Y. Yamamoto *et al.* (Tsukuba Univ.) found, at BL44B2, that discotic ionic liquid crystals of triphenylene derivatives serve as excellent dispersants for pristine single-walled CNTs.

Science

The research team of Prof. S. P. Cramer (UC Davis) applied nuclear resonant vibrational spectroscopy to observe Fe-CN and Fe-CO vibrations in the active site of NiFe hydrogenase at BL09XU. Evidence for the liquid-liquid transition in poly(4-methyl-1-pentene) was obtained by high-pressure *in situ* X-ray diffraction measurements at BL10XU. The modest pressures and temperatures at which these phenomena occur are expected to lead to the intriguing possibility of liquid-liquid transitions as industrial processes to control the physical properties of plastics. Ce(IV) is attracting considerable attention in studies of the photocatalytic oxidation of water for producing H_2 and O_2. EXAFS measurements and DFT calculations for identifying the speciation and complex structure of Ce (IV) aquo species in an aqueous acid solution were performed at BL11XU by Dr. Yaita group of JAEA. To avoid problems due to multielectron excitation effects, the XAS spectra were collected at the Ce *K*-edge (40.443 keV). This also enabled EXAFS spectra to be obtained over a wider *k*-range, providing a higher spatial resolution. A research team led by Prof. Ueda (Tohoku Univ.) and Prof. Yao (Kyoto Univ.) found that more than 90% of the energy absorbed by the Ar core was transferred to the Ne shell in the photoionization of Ar-Ne core-shell clusters by SASE-FEL radiation. Preferential energy injection into the Ar core results in ionization dynamics characterized by a charge transfer from the core to shell. This kind of large energy transfer may be useful for reducing the influence of Coulomb explosion of bio-molecules during X-ray diffraction experiments using X-ray lasers.

The continuing improvement in the emittance of the SPring-8 storage ring, the brightness available from improved undulators, and the stability of the high-resolution X-ray monochromators have all contributed to making the above work possible.

Yuden Teraoka


"Yamabuki"- *Kerria japonica 'Pleniflora'*

Visualization of Pt/C cathode catalyst layers in polymer electrolyte assemblies by X-ray computed laminography XANES

A polymer electrolyte fuel cell (PEFC) is one of the promising power sources, and many trials are being carried out to apply them to clean power generation with highly efficient energy systems. The prevention of degradation of cathode catalyst layers by fluctuations in cathode potential under variable loads and during startup and shutdown is crucial for the practical use of PEFCs. There are many investigations on the degradation processes of Pt cathode catalysts in PEFCs, but the three-dimensional (3D) structural information of the Pt cathode catalyst degradation has not yet been fully investigated because of a lack of nondestructive characterization methods for directly observing the spatial distribution chemical states of cathode catalyst layers inside membrane electrode assemblies (MEAs). We have developed X-ray computed laminography–X-ray absorption near-edge structure (XCL–XANES) analysis as a powerful tool to visualize the 3D structural information of Pt cathode catalysts in MEAs [1].

X-ray computed tomography (XCT) is a typical method for obtaining 3D images of a sample, in which the sample is rotated about an axis perpendicular to the incident X-ray beam. XCT can be applied to a sample smaller than the observation field area in all projected directions of XCT, but it cannot analyze a flat sample. On the other hand, XCL is applicable to partial 3D imaging of such a flat shaped sample. In XCL, the rotation axis of a sample is not fixed at 90° with respect to the incident X-ray beam, and the sample is inclined. We applied the XCL technique to XAFS spectroscopy, which provides not only morphological/structural information but also the 3D distribution of Pt catalysts and their chemical states in cathode catalyst layers in MEAs.

MEAs were commercially prepared using 50 wt% Pt/C (TKK) as a cathode catalyst. A fresh MEA was subjected to 4 cycles of current steps held for 30 s each. A degraded MEA was subjected to 150 cycles of aging and 200 cycles of accelerated degradation testing. Each MEA has a layered structure of a cathode catalyst layer with the Pt/C catalyst, polymer

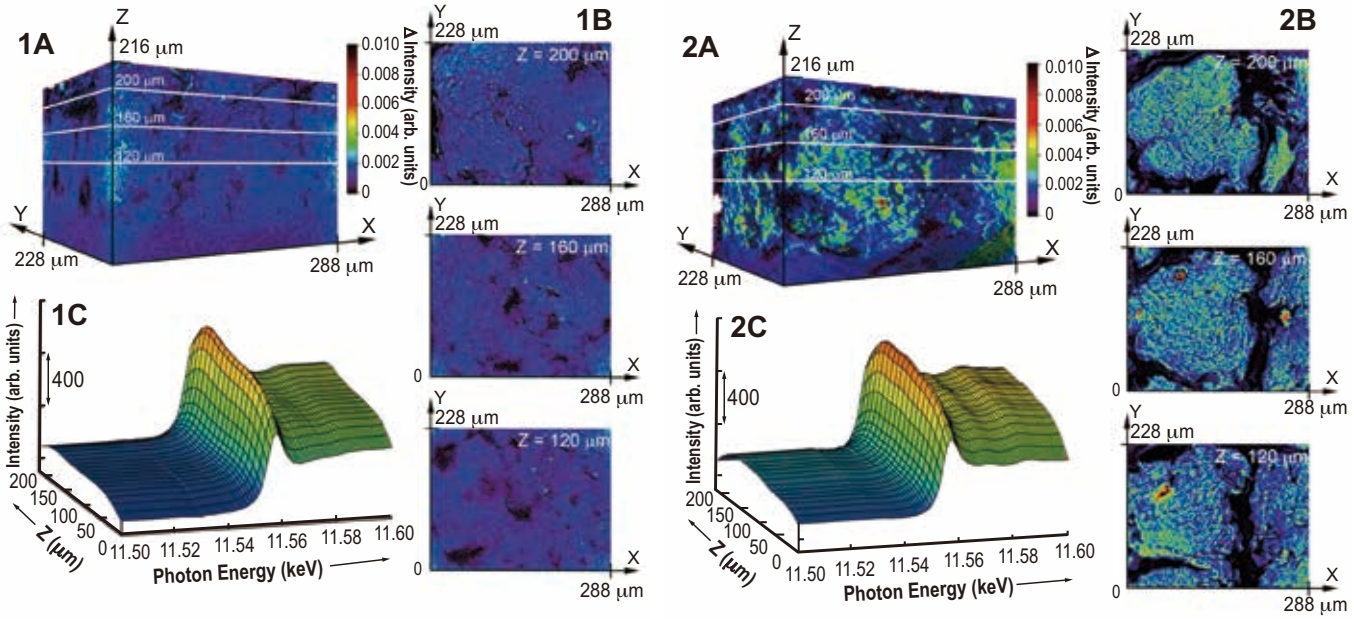

1: Fresh MEA **2: Degreaded MEA**

Figs. **1A** and **2A**: 3D spatial distribution of the Pt catalysts in the cathode catalyst layers of a fresh MEA (**1A**) and degraded MEA (**2A**) observed by XCL-XANES spectroscopy. Figs. **1B** and **2B**: Cross sectional images of Figs. **1A** and **2A** in the X-Y plane at Z = 120, 160, and 200 μm. Figs. **1C** and **2C**: Series of depth-resolved Pt L_{III}-edge XCL-XANES spectra along the Z-axis for the cathode catalyst layers, **1C** for a fresh MEA and **2C** for a degraded MEA. The XANES spectra are presented every 12 μm depth.

electrolyte, and anode catalyst layer with a Pd/C catalyst. The average particle sizes of Pt cathode catalysts in the fresh and degraded MEAs were 3.5±0.9 nm and 5.4±2.1 nm, respectively, observed by TEM. The treated MEAs were cut into 10×10 mm^2 pieces for XCL measurements and clipped a 300-nm-thick SiC membranes. 3D XCL-XANES spectra were recorded at **BL47XU**, and the rotational axis of the MEA was inclined 30° from the normal toward the downstream direction. The incident X-ray beam to a high spatial resolution X-ray image detector, which consisted of a visible light conversion unit and a CCD camera, was converted to visible light by an LSO crystalline scintillator, and a visible light image was focused onto the CCD camera using a microscope objective. Transmission images of MEAs were acquired from 360° rotation, and the number of transmission images was 1800 per energy scan. Sectional images were reconstructed using a filtered back-projection method considering the inclination of the rotational axis. 83 XCL images were obtained for Pt L_{III}-edge in the X-ray energy range of 11.394–11.609 keV. The field of view of a sectional image (X-Y section) obtained from laminography reconstruction became 400×400 μm^2.

XCL images obtained at 11.496 keV before the Pt L_{III}-edge provided 3D morphology images of cathode catalyst layers in the MEAs. For the fresh MEA without the accelerated degradation testing, many cracks in a random pattern were observed in both SEM and XCL images. On the other hand, cracks in the degraded MEA, whose cathode catalyst layer was about 115–210 μm in thickness, were much more conspicuous. SEM and XCL provided similar images of the MEAs.

We obtained a series of XCL images of incident X-rays at the Pt L_{III}-edge, and the reconstruction of the series of XCL images at different energies provided the XCL-XANES spectra for the first time. XCL-XANES provided both 3D images of the spatial distribution of Pt catalysts and their chemical states at the cathode catalyst layers in the two MEAs. The spatial distribution of Pt catalysts was visualized by mapping the Pt L_{III}-edge intensity, which corresponds to the difference in the intensity of X-ray absorption at 11.572 keV (isosbestic point of Pt and PtO_2) from that at 11.496 keV (before Pt L_{III}-edge) (Fig. 1A). Bright areas indicate high-Pt-concentration areas and the contrast in the images was clear. In the fresh MEA, Pt catalysts were almost fully loaded throughout the cathode catalyst layer (Fig. 1A), whereas the Pt distribution was heterogeneous throughout the entire cathode catalyst layer in the degraded MEA (Fig. 1B), which suggests that Pt migration, aggregation, and cracking spread throughout the cathode catalyst layer in the degraded MEA. Cross sectional images (Figs. 1B and 2B) of the MEAs clearly show the differences in the Pt spatial distribution in the cathode catalyst layers.

Pt L_{III}-edge XCL-XANES spectra were obtained for every piece of the cathode catalysts layers, whose depth-resolved XANES spectra are presented in Fig. 1C. A difference in the edge intensity of the Pt L_{III}-edge XANES spectra indicates a difference in the Pt quantity in the MEAs along the Z depth. In the fresh MEA, the Pt quantity gradually increased with depth and reached a maximum at about 170 μm in depth (Fig. 1C). In contrast, a series of depth-resolved laminography-XANES spectra of the degraded MEA were wavy in the Z depth, probably reflecting the degradation of the MEA (Fig. 2C). The XCL-XANES spectra at different positions were different in the degraded MEA, suggesting that the chemical states of Pt catalysts depend on the area/position in the cathode catalyst layer in the MEA. The XCL-XANES spectra indicated the heterogeneous chemical states of the Pt nanoparticle catalysts in the cathode catalyst layer in the degraded MEA, which cannot be monitored by conventional XAFS. They also indicated that the Pt catalysts in the degraded MEA were in the form of larger Pt nanoparticles with a lower Pt L_{III}-edge white-line intensity. We observed large aggregated areas of μm sizes in the XCL images of the degraded MEA. *In situ* XCL-XANES would potentially reveal the degradation process of Pt catalysts at each part of a cathode catalyst layer in an MEA under PEFC operating conditions.

Takahiro Saida[a] and Mizuki Tada[a,b,*]

[a] Dept. of Materials Molecular Science, Institute for Molecular Science
[b] Research Center for Materials Science, Nagoya University

*Email: mtada@chem.nagoya-u.ac.jp

References

[1] *T. Saida, O. Sekizawa, N. Ishiguro, K. Uesugi, M. Hoshina, T. Uruga, S. Ohkoshi, T. Yokoyama and M. Tada: Angew. Chem. Int. Ed.* ***51*** *(2012) 10311.*

Multiple-decker phthalocyaninato dinuclear terbium (III) single-molecule magnets with dual-magnetic relaxation processes

In principle, a single spin can be used as a 'bit' of information to prepare high-density storage and quantum computing devices [1]. Quantum tunneling of the magnetization (QTM) between double well potentials, which is a prominent, characteristic property of single molecule magnets (SMMs), underpins this concept. SMMs behave like magnets with frozen spins, and a potential exists across two energy barriers at low temperatures, known as the blocking temperature (T_B). In the case of 3*d* cluster SMMs, an easy axis-type magnetic anisotropy, which is represented by a negative zero-field splitting constant (D), occurs due to magnetic interactions among high-spin 3*d* metal ions in the clusters. Researchers have been studying complexes with higher values of T_B than that of a well-known Mn cluster. In recent years, lanthanoid(III)-phthalocyaninato (Ln(III)-Pc) sandwich complexes have been shown to be SMMs, which originates from the ligand field (LF), and researchers have utilized their QTM and magnetic relaxation behavior [2]. Ln(III)-Pc molecules showing SMM behavior have significantly large axial magnetic anisotropies, which occur by a different mechanism than those for known 3*d* metal cluster SMMs. On the other hand, in the case of Ln(III) SMMs, the LF of the Ln^{3+} ion controls the anisotropy. The LF potential around a Tb^{3+} ion ($4f^8$) with a total angular momentum (J) of 6 splits the ground multiplet so that the lowest sublevel has the largest J_z value ($|J_z| = 6$, corresponding to up/down spin states) and large energy gaps to the remaining sublevels. Being able to control the QTM of Ln(III)-Pc SMMs will make it possible to design new spintronics devices.

In this study, we report the molecular structure and magnetic relaxation properties of dinuclear Ln(III)-Pc multiple-decker complexes: quadruple-decker {[Ln(obPc)$_2$]Cd[Ln(obPc)$_2$]} (**1**:Ln = Tb^{3+}, **2**:Ln = Dy^{3+}), triple-decker Ln_2(obPc)$_3$ (**3**:Ln = Tb^{3+}, **4**:Ln = Dy^{3+}), double-decker Ln(obPc)$_2$ (**5**:Ln = Tb^{3+}, **6**:Ln = Dy^{3+}), and quintuple-decker {[Tb(obPc)$_2$]Cd(obPc)Cd[Tb(obPc)$_2$]} (**7**). Our work shows that the SMM/QTM properties can be fine-tuned by introducing weak intermolecular magnetic interactions in controlled spatial arrangements of lanthanides ions [3].

In order to control the spin orientation in the molecules, we designed **1**–**7** so that the two Ln^{3+} ions are along the anisotropy axis (Fig. 1). The SMM behavior of dinuclear Ln(III)-Pc multiple-decker complexes (Ln = Tb^{3+} and Dy^{3+}) with large energy barriers and slow-relaxation behavior were explained by using X-ray crystallography (Figs. 2(a) and 2(b): **BL02B1** and **BL40XU** beamlines) and static and dynamic susceptibility measurements [3]. There was a decrease in the in-phase (χ_M') and out-of-phase (χ_M'') peaks in different T ranges, which were dependent on the frequency (f), indicating that dinuclear Ln(III)-Pc multiple-decker complexes (Ln = Tb^{3+} and Dy^{3+}) are SMMs. In micro-SQUID experiments, quadruple-decker **1** and **2** clearly exhibited SMM behavior (Fig. 2(c)) [3].

Dinuclear Tb(III)-Pc multiple-decker SMMs **1**, **3**, and **7** exhibited dual magnetic relaxation processes (Fig. 3) [3]. These magnetic relaxation processes have T-independent (τ_1) and T-dependent (τ_2) regimes in the low T region. The dual magnetic relaxation behavior was observed not only for discreet dinuclear Tb(III)-Pc complexes but also for the spatially closed Tb(III)-Pc double-decker complex **5** [4]. On the other hand, mononuclear system **5a**, where the effects of intermolecular interactions in **5** have been eliminated, exhibited only a single magnetic relaxation process [4]. In the case of the dinuclear Tb(III)-Pc complexes, the value of T_B and the distance between Tb^{3+} ions follows the strength of the dipole-dipole interactions (D_{ij}), and T_B shifted to the high-T side, indicating that the Tb^{3+}–Tb^{3+} interactions affect the spin dynamics (Fig. 2(d)). Moreover, the presence of the dual magnetic relaxation processes is related to the distance between Tb^{3+} ions sites in the dinuclear complexes (Fig. 3).

In other words, the magnetic relaxation mechanism depends heavily on the dipole-dipole (f-f) interactions between the Tb^{3+} ions in the dinuclear systems [3]. The above results demonstrate that even weak exchange interactions can have a large influence on the quantum properties of Ln(III)-Pc type SMMs. Two magnetic relaxation processes occur under the

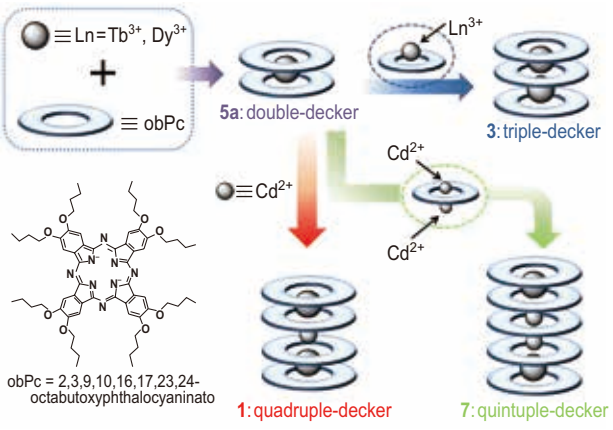

Fig. 1. Schematic illustration of sequential synthetic routes for multiple-decker phthalocyaninato dinuclear lanthanoid (III) single-molecule magnets [3].

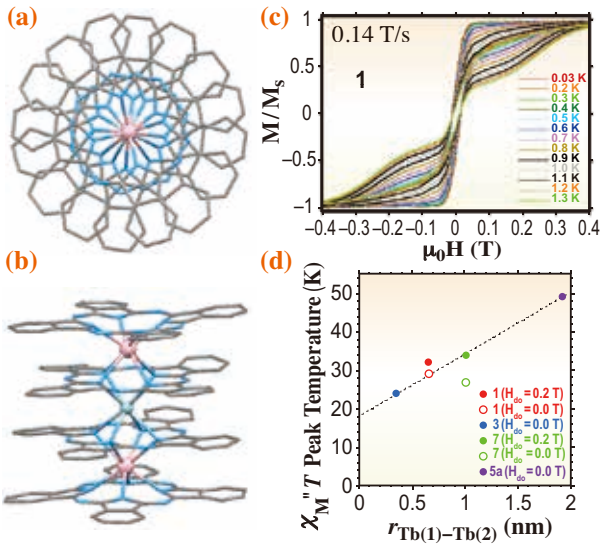

Fig. 2. Crystal structure and SMM behavior of Tb(III) quadruple-decker complex (**1**). **(a)** Top view and **(b)** side view. *n*–butoxy substituents omitted for clarity. Tb(III): pink, Cd(II): pale blue, C: gray, and N: light blue. **(c)** Hysteresis loops for **1** (single crystal) at different temperatures and a constant field sweep rate of 0.14 T s^{-1}. **(d)** Correlation between the $\chi_M''(T)$ peak temperature (T_B) and the distance between the two Tb^{3+} ions along the anisotropy axis ($r_{Tb(1)\text{-}Tb(2)}$) in the discrete Tb(III) dinuclear complexes [3].

following two conditions. First, two Tb^{3+} ions must be crystallographically equivalent or nearly equivalent in the molecule. In other words, they must have the same LF potentials. Second, the spatial arrangement and distance between the Tb^{3+} ions (r_{ij}) in the molecule must allow for ferromagnetic dipole-dipole coupling.

The individual Tb^{3+} dinuclear complexes show different behavior in relation to the QTM process (Fig. 3) [3]. Considering only the QTM process, the magnetic interactions in **1** and **7** are on the same order of magnitude in the presence of zero dc magnetic field (H_{dc} = 0). On the other hand, **3** and **5** showed QTM in the presence of a dc magnetic field (H_{dc} = 0.3 T). From one viewpoint, each half of the Tb^{3+} dimer acts as a field bias on its neighbor, shifting the tunnel resonances to new positions relative to the magnitude of the dipole-dipole interactions between the Tb^{3+} ions. In other words, it should be the same QTM process, which occurs to the same extent as the field bias does.

Recently, dual-magnetic relaxation processes have been observed for SMMs regardless of the type and number of metal ions in the complexes. It is well known that the magnetic relaxation properties reflect the local molecular symmetry and are extremely sensitive to tiny distortions in the coordination geometry, i.e., LF. Our results suggest that the dual magnetic relaxation properties in the Tb(III)-Pc multiple-decker systems has magic number of "two", i.e., the number of Tb^{3+} sites. However, why is a dual magnetic relaxation process not observed for Dy(III)-Pc multiple-decker complexes with same LF? The relaxation processes are most likely due to distinct anisotropic centers. Thus, Dy(III)-Pc SMMs do not exhibit a dual magnetic relaxation process. Further experiments involving the ground-state multiplets are needed to fully elucidate the mechanisms.

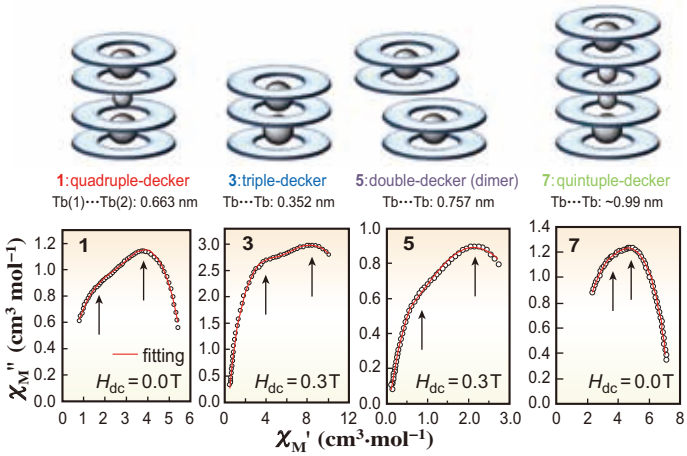

Fig. 3. Molecular structures (top) and Argand plots for **1**, **3**, **5** and **7** measured at 4 K (bottom). [3] Arrows indicate dual-magnetic relaxation processes in the Argand plot. In the case of the Argand plots in a field of 0.2 T, the magnetic relaxations of **1** and **7** showed only a single component. On the other hand, **3** and **5** showed a single component system at a zero dc magnetic field.

Keiichi Katoh[a,*], Nobuhiro Yasuda[b] and Masahiro Yamashita[a]

[a] Department of Chemistry, Tohoku University
[b] SPring-8/JASRI

*Email: kkatoh@m.tohoku.ac.jp

References

[1] T. Komeda *et al.*: Nature Commun. **2** (2011) 217.
[2] K. Katoh *et al.*: J. Am. Chem. Soc. **131** (2009) 9967.
[3] *K. Katoh, Y. Horii, N. Yasuda, W. Wernsdorfer, K. Toriumi, B.K. Breedlove and M. Yamashita: Dalton. Trans.* ***41*** *(2012) 13543.*
[4] K. Katoh *et al.*: Coord. Chem. Rev. **255** (2011) 2124.

Discotic ionic liquid crystals as excellent dispersants for single-walled carbon nanotubes

A variety of soft electrical conductors have been developed by doping carbon nanotubes (CNTs) into organic and polymeric materials, where better electrical properties are realized by the dispersion of a larger amount of CNTs. Recently, liquid crystalline (LC) materials have attracted increasing attention for hybridization with CNTs, since LC materials have the potential to orient CNTs for anisotropic electrical conduction. However, the reported LCs possess rather low miscibility with pristine CNTs of less than 0.01 wt%. Here we report that discotic ionic liquid crystals (ILCs) of triphenylene (TP) derivatives, ILC_{col} and ILC_{cub} (Fig. 1(a)) [1,2] bearing six imidazolium ion pendants, serve as excellent dispersants for pristine single-walled CNTs (SWNTs) [3]. The resultant composite materials can maintain their LC properties up to the SWNT content of ~8 wt%, which is 2–3 orders of magnitude greater than those reported previously. Of further interest, the ILC composites, when sheared, display anisotropic conducting properties, since SWNTs are oriented along the shear direction. This orientation is kept for at least half a year.

In 2003, we reported that imidazolium ion-based ionic liquids (ILs), when being ground with SWNTs, are transformed into physical gels (bucky gels), where SWNTs are highly dispersed by a p-cation/p-electronic interaction and eventually form a 3D network structure associated with an interionic interaction of ILs [4]. As reported previously [1,2], the discotic ionic liquid crystals ILC_{col} and ILC_{cub} (Fig. 1(a)), utilized for the present study, assemble into hexagonal columnar (Col_h, 134–18°C on cooling) and cubic (Cub, 221–18°C on cooling) mesophases, respectively, over a wide temperature range including room temperature [2].

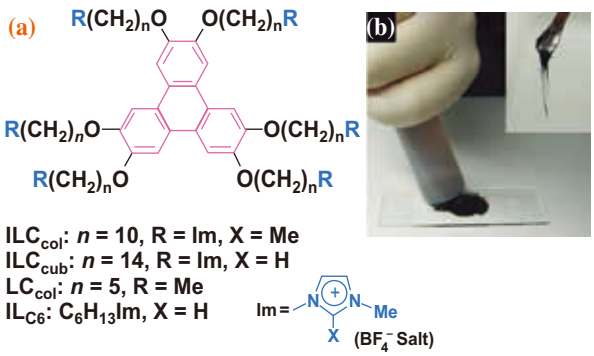

Fig. 1. **(a)** Molecular structures of ionic liquid crystals ILC_{col} and ILC_{cub}, together with those of nonionic liquid crystal LC_{col} and monovalent ionic liquid IL_{C6} as references. **(b)** Pictures of an ILC_{col}/SWNT composite.

As a typical example of the hybridization of ILCs with SWNTs, pristine HiPco SWNTs were added at 150°C to ILC_{col} (isotropic melt) with an SWNT content of 5 wt%, and the mixture was ground with a pestle for 30 min (Fig. 1(b)), whereupon it turned to a viscous black paste (Fig. 1(b), inset). As observed by optical and cross-sectional transmission electron microscopy, only a very small amount of SWNT agglomerates was detected in the black paste. Similar black pastes were obtained when the SWNT contents employed were in the range of 3–15 wt%. However, upon further increase in the doping level to 30 wt%, the mixture lost its fluidity and became semisolid. Although doped SWNTs affected the phase diagram of ILC_{col} to a certain extent, the LC clearing temperature decreased only by 18°C (134 → 116°C) when ILC_{col} was doped with even 5 wt% SWNTs. Likewise, SWNTs dispersed very well in ILC_{cub}, where the resulting composite again displayed only a marginal decrease in the LC clearing temperature (221 → 205°C on 5 wt% SWNT doping). Of interest, the effects of doped SWNTs on the X-ray diffraction (XRD) profiles of ILC_{col} and ILC_{cub}, observed at **BL44B2**, were essentially different from one another (Fig. 2). In the case of ILC_{cub}, as the doping level of SWNTs was higher, the diffraction peaks shifted toward a lower 2θ region (Fig. 2(b), inset). In contrast, the diffraction peaks of ILC_{col} hardly shifted upon increment of the content of SWNTs (Fig. 2(a), inset). These contrasting observations indicate that ILC_{cub} incorporates SWNTs into its cubic lattice, whereas ILC_{col} prefers to maintain its original 2D hexagonal lattice without incorporating SWNTs.

In the course of the above studies, we noticed that the discotic LC columns of ILC_{col}, upon being doped with SWNTs, align homeotropically with respect to the substrate surface, while SWNTs are randomly oriented just as they are in the isotropic melt. However, a shear treatment of the ILC/SWNT composites induces a horizontal orientation of SWNTs with respect to the substrate surface. Accordingly, shear treatment in combination with annealing gave rise to three different states **States 1–3** in terms of the orientations of the LC columns and SWNTs (Fig. 3). Namely, the ILC_{col}/SWNT composite, upon shear treatment, gave **State 1**, where both LC columns and SWNTs were coaxially oriented horizontally with respect to the glass plates. Subsequent short annealing of the sheared composite for 5 min gave **State 2**, where the LC columns were oriented homeotropically, while maintaining the horizontal orientation of SWNTs. Further annealing

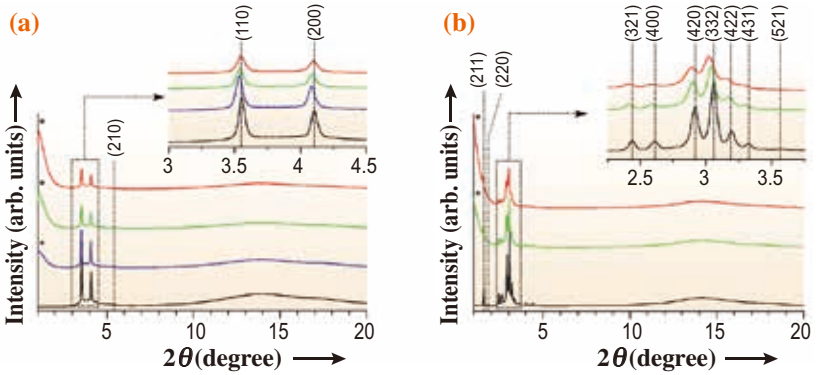

Fig. 2. XRD patterns (25°C) of ILC_{col} (**a**) and ILC_{cub} (**b**) alone (black), and their composites doped with 1 (blue), 3 (green), and 5 (red) wt% SWNTs. An X-ray beam with a wavelength of 1.08 Å was used. The asterisked diffraction at $2\theta < 2$ degrees in each XRD pattern is due to scattering by SWNTs.

of the composite for 1 h gave **State 3**, where SWNTs were oriented randomly in the homeotropically oriented LC columns. The horizontal orientation of SWNTs, once generated by the shear treatment, was maintained for at least half a year at room temperature unless the material was heated. Namely, thermal reorientation of SWNTs occurs much less rapidly than that of the LC columns.

The orientation of SWNTs is a dominant factor for charge-carrier transport properties of the ILC_{col}/SWNT composite (Fig. 3). When ILC_{col} doped with 1 wt% SWNTs was sandwiched by indium tin oxide (ITO) electrodes, the DC conductivity across the film at 25°C in **State 1** (red circles) was nearly two orders of magnitude smaller than that in **State 3** (black squares). In contrast, **State 1** and **State 2** (blue rhomboids) were comparable to one another in terms of DC conductivity, indicating a negligibly small contribution of the LC columns to the observed conduction profile. On the other hand, at higher doping levels of SWNTs (3 and 5 wt%), the three states showed a much smaller difference (~20 times) in their DC conductivities, possibly owing to an increased probability of carrier hopping between SWNTs.

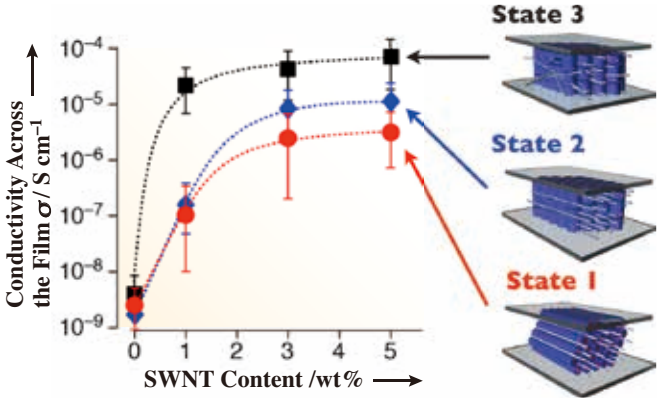

Fig. 3. Plots of conductivities across the film of States 1–3 at 25°C of ILC_{col} films doped with 0, 1, 3, and 5 wt% SWNTs, sandwiched by ITO electrodes with a separation of 12.5 μm.

Jeongho Jay Lee[a] and Yohei Yamamoto[b,*]

[a] Department of Chemistry and Biotechnology, The University of Tokyo
[b] Division of Materials Science and TIMS, University of Tsukuba

*Email: yamamoto@ims.tsukuba.ac.jp

References

[1] J. Motoyanagi *et al.*: Chem. Commun. (2005) 101.
[2] M.A. Alam *et al.*: J. Am. Chem. Soc. **131** (2009) 17722.
[3] *J.J. Lee, A. Yamaguchi, M.A. Alam, Y. Yamamoto, T. Fukushima, K. Kato, M. Takata, N. Fujita and T. Aida: Angew. Chem. Int. Ed.* ***51*** *(2012) 8490.*
[4] T. Fukushima *et al.*: Science **300** (2003) 2072.

A dynamic view of [NiFe] hydrogenase by means of nuclear resonance vibrational spectroscopy

Hydrogenases (H_2ases) are enzymes that catalyze both the production and consumption of molecular hydrogen [1,2]. They play an important role in biology, allowing organisms to efficiently use protons as electron acceptors and evolving H_2, and also allowing capture of H_2 in their role as 'uptake H_2ases' [3]. They are also of interest for potential applications in a hydrogen economy, either used directly or serving as inspirational targets for biomimetic inorganic catalysts [4]. A detailed knowledge of the catalytic mechanisms of H_2ases is thus an important goal for biology, chemistry, and clean energy technology.

In the [NiFe] family of H_2ases, catalysis takes place at a Ni-Fe dimetallic center (Fig. 1). In this unique active site, Fe is linked to Ni by a pair of cysteine thiolate ligands. Depending on the redox poise or degree of aerobic deactivation, the Fe and Ni centers may also be bridged by hydride, oxo/hydroxo, and possibly hydroperoxo ligands. The Fe site also carries one CO and a pair of CN^- ligands. [NiFe] H_2ases also possess additional Fe-S clusters that relay electrons to and from the active site.

Although crystallography has revealed many essential features about the NiFe active site, there are additional details that are more easily addressed by spectroscopy. For example, infrared spectroscopic studies have revealed more than ten different chemical species, using the CO and CN^- stretching bands in the 1800–2100 cm^{-1} region. Only a few forms of the enzyme can be crystallized as homogeneous chemical species, and even then, it is hard to see all of the details by crystallography with atomic resolution. The alternate species often differ by the bridge between Ni and Fe, which is often hard to see clearly in the crystallographic data. In the oxidized, inactive forms Ni-A and Ni-B, it is proposed that Ni and Fe are bridged by O^{2-}, OH^- or even OOH^- species, while the reduced and active forms 'Ni-C' and 'Ni-R' are both thought to possess a hydride (H^-) bridge. However, the critical hydride bridge is not visible in the crystal structures. In the current study [5], we employed a relatively new technique called Nuclear Resonance Vibrational Spectroscopy (NRVS), which is only sensitive to motion of ^{57}Fe, to identify H_2ase Fe-CN and Fe-CO modes in the 400–600 cm^{-1} region. Such studies, combined with measurement of model compounds and Density Functional Theory (DFT) calculations will help characterize the geometry of the bridges to iron and the nature of hydrogen activation.

NRVS has evolved into a powerful technique for probing the dynamics of Fe in metalloproteins. The measurement employs scanning a highly monochromatic (meV) X-ray beam through a nuclear resonance. Unlike Mössbauer spectroscopy, which detects 'recoil-free' nuclear transitions, NRVS detects the inelastic events that involve creation or destruction of phonons. The resulting spectrum is similar to a conventional IR or Raman spectrum, but with different selection rules. The NRVS intensity for a given normal mode is related to the amount of motion of the resonant nucleus (in this case ^{57}Fe) in that mode. One can therefore observe only the ^{57}Fe-based vibrations for a protein sample involving thousands of other atoms. The measurements were conducted at beamline **BL09XU**.

As seen in Fig. 2, the NRVS of H_2ase is dominated by contributions from the Fe-S clusters in the electron transport chain. The structure around 150 cm^{-1} derives from cluster breathing and bending modes, while the features between 200 and 400 cm^{-1} are mostly Fe-S stretching modes. Fortunately, the Fe-S cluster NRVS dies out rapidly above 400 cm^{-1}, and at

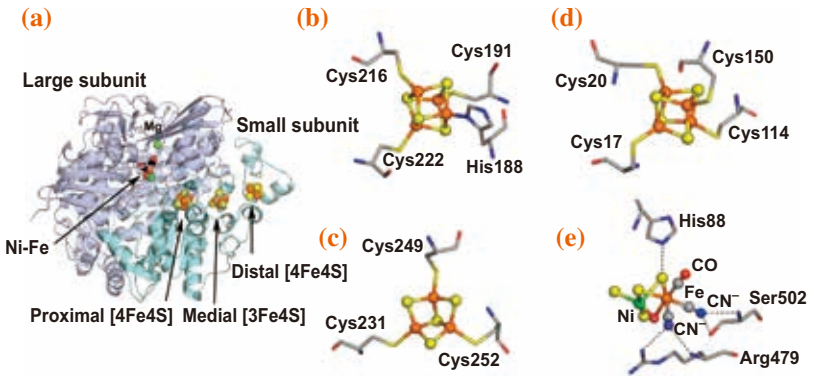

Fig. 1. The structures of the Fe sites in H_2ase. **(a)** overall view of the electron transport chain. **(b-e)** detailed views of individual clusters, including: **(b)** 'distal' [4Fe-4S] cluster, showing Cys_3His ligation, **(c)** 'medial' [3Fe-4S] cluster, **(d)** 'proximal' [4Fe-4S], and **(e)** Ni-Fe active site. The atoms are Fe (brown), Ni (green), S (yellow), C (gray), N (blue) and O (red).

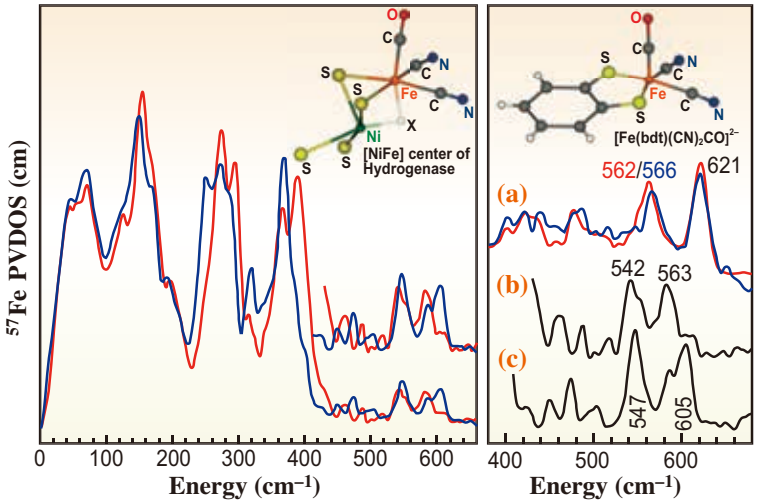

Fig. 2. NRVS-derived PVDOS for Fe sites in H_2ase. Left: overall spectra for oxidized (—) *vs* reduced (—) H_2ase. Right: close-ups for Fe-CO/CN region. Top to bottom: **(a)** $(NEt_4)_2[^{57}Fe(bdt)(CN)_2(CO)]$ (—) and $(NEt_4)_2[^{57}Fe(tdt)(CN)_2(CO)]$ (—), **(b)** oxidized H_2ase, and **(c)** reduced H_2ase.

still higher frequencies it is still possible to distinguish Fe-CN and Fe-CO stretching and bending modes from the active site Fe. Upon reduction of the protein, we were able to see modest upshifts in the Fe-CO stretch that correlated with shifts seen in the mid-IR CO stretching bands.

Going forward, a truly exciting prospect of this work is the potential for observation of Fe hydride/deuteride stretching and bending modes. In recent work on a Ni-H/D-Fe model compound (Fig. 3), we found that weak Fe-H stretches could be seen past 1500 cm^{-1}, while much stronger Fe-H-Ni bending modes were visible near 800 cm^{-1}. Finding the position of these bands in H_2ase will provide valuable information about the nature of hydrogen activation at the active site. The continuing improvement in the emittance of the SPring-8 storage ring, the brightness available from improved undulators, and the stability of high-resolution X-ray monochromators have all contributed to make this work possible.

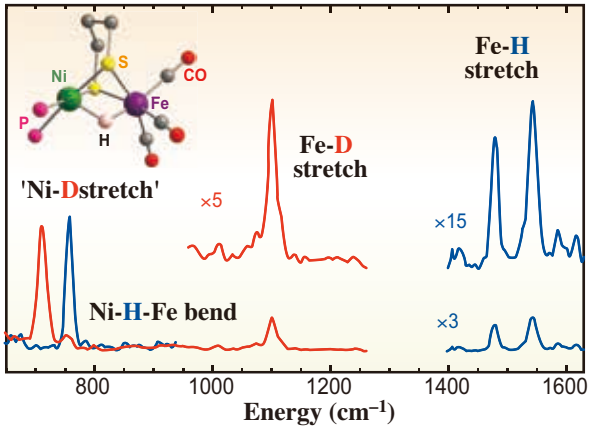

Fig. 3. Recent NRVS data on $[(CO)_3{}^{57}Fe(pdt)H/DNi(dppe)]BF_4$ (blue for H and red for D) - a Ni-Fe model for NiFe H_2ase. The model structure is as shown in the insert.

H. Wang[a,c], H. Ogata[b], W. Lubitz[b,*] and S. P. Cramer[a,c,*]

[a] Department of Chemistry, University of California, USA
[b] Max Planck Institute for Chemical Energy Conversion, Germany
[c] Physical Biosciences Division, Lawrence Berkeley National Laboratory, USA

*Email: wolfgang.lubitz@cec.mpg.de, spjcramer@ucdavis.edu

References

[1] P.M. Vignais *et al.*: FEMS Microbiol. Rev. **25** (2001) 455.
[2] F.A. Armstrong: Curr. Opin. Chem. Biol. **8** (2004) 133.
[3] I. Valdez-Vazquez, H.M. Poggi-Varaldo: Renew. Sust. Energy Rev. **13** (2009) 1000.
[4] C. Tard, C.J. Pickett: Chem. Rev. **109** (2009) 2245.
[5] *S. Kamali, H. Wang, D. Mitra, H. Ogata, W. Lubitz, B.C. Manor, T.B. Rauchfuss, D. Byrne, V. Bonnefoy, F.E. Jenney Jr., M.W.W. Adams, Y. Yoda, E. Alp, J. Zhao and S.P. Cramer: Angew. Chem. Int. Edit.* ***52*** *(2013) 469.*

Pressure-induced structural change of intermediate-range order in a polymer melt

Pressure-induced liquid-liquid phase transitions have attracted much attention. These are transitions between two liquids with different macroscopic properties such as density, viscosity, and entropy, and different microscopic structures. Similar transitions in crystalline and, more recently, amorphous solids have been a focus of study so far, but the discovery that it is possible to have such pressure driven transitions in liquids is novel, and has posed some interesting technological and theoretical problems. The existence of a first-order transition of liquid phosphorous (*l*-P) is now well known [1]. In the low-pressure range, *l*-P is a P_4 molecular liquid, in which the molecules have a tetrahedral structure, but at high pressures, approximately 1 GPa, its structure and properties change as it polymerizes. The transition is first-order, and takes place in the liquid state near the kink of the melting curve in the pressure-temperature phase diagram.

This kink of the melting curve has been considered to be a smooth maximum [1], as schematically shown in Fig. 1(a). If a liquid can be transformed into a crystal by the application of pressure at point A in Fig. 1(a), and then by continuing to increase the pressure transformed back into a liquid at B, it is reasonable to conclude that the low- and high-pressure liquids are different, either simply because the liquid is more compressible or because it has a completely different structure. Indeed, some studies indicate that any material that has the maxima in the melting curve in the pressure-temperature plane is likely to have a pressure-induced liquid-liquid transformation [2]; although the transformations will usually be continuous and not first-order.

If there are similar liquid-liquid transformations in polymer melts, they will take place at much lower temperatures and pressures than in liquids such as *l*-P, since the polymer molecules have high degrees of freedom and flexibility with interactions mostly involving weak forces, such as intermolecular or configurational forces. This would make such a phenomenon much easier to access than in *l*-P, water, or other liquids currently known to have pressure-induced structural changes. Although there have been studies on so-called liquid-liquid transitions in polymers [3], most of the studies have focused on a certain type of transition, which is intrinsically related to changes not in static structure but in relaxation phenomena. These changes occur in a variety of glass forming polymers, and presumably in any other glass forming systems, at relatively low temperatures of approximately 1.2 times the glass transition temperature T_g. To investigate changes in a static structure, measurements as a function of pressure are preferable because applying pressure can alter interatomic potentials more directly.

The aim of our study [4] is thus to carry out an *in situ* search for a liquid-liquid transformation in a polymer melt by the path shown in Fig. 1(a). A good candidate material is isotactic poly(4-methyl-1-pentene) (P4MP1) (Fig. 1(b)), which has a maximum in the melting curve. High-pressure *in situ* X-ray diffraction measurements were conducted at constant temperatures at the beamline **BL10XU**.

Figure 2(a) shows the pressure dependence of X-ray diffraction patterns of the P4MP1 melt at 280°C. The intensity of the peak at approximately 0.6 $Å^{-1}$, which we call the first sharp diffraction peak (FSDP), shows a remarkable decrease with pressure, as does the ratio of the intensities of the FSDP to the second peak (Fig. 2(b)). This kind of change observed in the FSDP shows a structural change in intermediate-range order, which is a structural order intermediate between short-range discrete chemical bonds and long-range crystalline lattices. Figure 2(b) shows the change in the slope (pressure dependence) at 0.5 and 0.7 kbar at 280°C and 290°C, respectively. This change in slope was also observed for the pressure dependence of the position of the FSDP [4]. We have also performed measurements of specific volume. The result shows high compressibility at low pressures, and we found an increase in the bulk modulus at a certain pressure for each temperature, which indicates the second-order transition [4]. Thus we observed changes in the pressure dependence of the microscopic structure as well as that of the macroscopic density.

In polymers, the FSDP is usually assigned

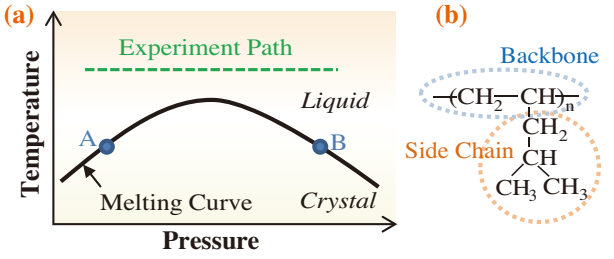

Fig. 1. **(a)** Maximum of melting curve in pressure-temperature phase diagram. We conducted high-pressure *in situ* X-ray diffraction measurements at constant temperatures as shown by the broken line. **(b)** Molecular structure of P4MP1.

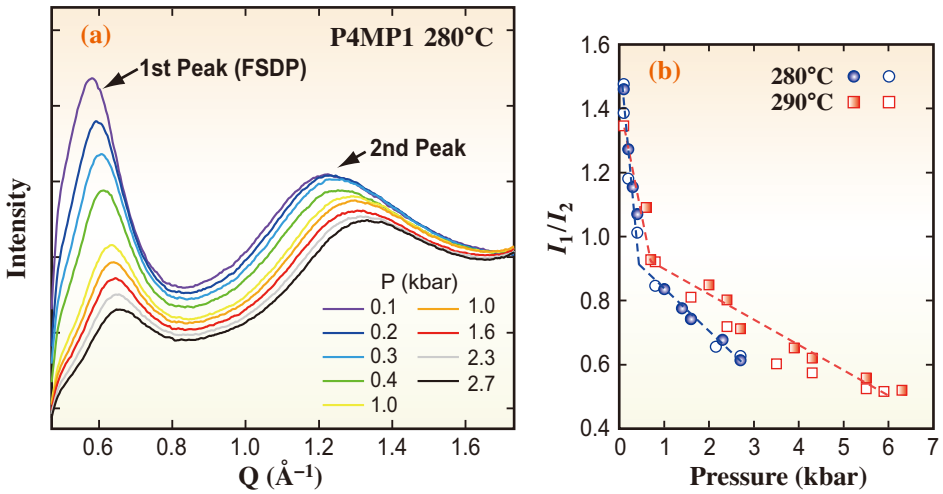

Fig. 2. **(a)** X-ray diffraction patterns of P4MP1 melt at 280°C. **(b)** Pressure dependence of the ratio of the intensities of the FSDP (I_1) to that of the second peak (I_2). Filled symbols show the data obtained under increasing pressure and open symbols under decreasing pressure. Broken lines are guides for the eyes.

to backbone-backbone correlation [5]. This is a correlation of dense backbones surrounding voids that are sparsely filled by the bulky side chains (Fig. 1(b) and Fig. 3(a)). Given that the origin of the FSDP is related to the correlation between backbones (Fig. 3(a)), we can assume that the rapid decrease in the intensity of the FSDP with pressure (Fig. 2) indicates a disordering of backbone-backbone correlations, and the shift to higher momentum transfers (Fig. 2 (a)) indicates a reduction of the void spaces between backbones. That is, the high compressibility we observe in the low-density melt is due to compaction of the void space, which suppresses the backbone-backbone correlations (Figs. 3(a) and 3(b)).

In this study, we found evidence of the liquid-liquid transition (or continuous but sharp transformation) in P4MP1, which is characterized by a change in intermediate-range order. The finding that such a large change occurs in P4MP1 at easily accessible pressures is noteworthy, and originates from the nature of the loosely packed structure of the polymer with a bulky side chain. This and the moderate pressures and temperatures at which these phenomena occur open up the intriguing possibility of using liquid-liquid transitions as an industrial process to control the physical properties of plastics.

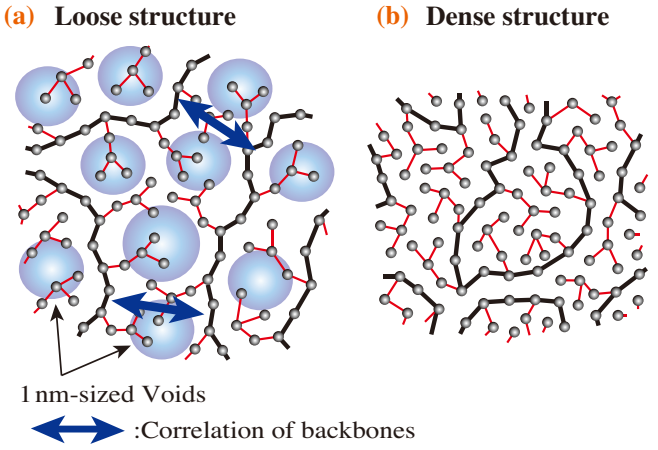

Fig. 3. Schematics of possible structures of P4MP1 melt. **(a)** Low-density melt and **(b)** high-density melt. Small spheres indicate carbon atoms, and thick black and thin red lines indicate the main and side chains, respectively. Blue arrows indicate correlations between backbones (main chains) and large blue circles indicate void spaces, both of which would cause the intermediate range order.

Ayano Chiba[a,*], Nobumasa Funamori[b] and Mikihito Takenaka[c,d]

[a] Department of Physics, Keio University
[b] Department of Earth and Planetary Science, The University of Tokyo
[c] Department of Polymer Chemistry, Kyoto University
[d] SPring-8/RIKEN

*Email: ayano@phys.keio.ac.jp

References

[1] Y. Katayama *et al.*: Nature **403** (2000) 170.
[2] E. Rapoport: J. Chem. Phys. **46** (1967) 2891.
[3] S.S.N. Murthy: J. Polym. Sci. Pol. Phys. **31** (1993) 475.
[4] *A. Chiba, N. Funamori, K. Nakayama, Y. Ohishi, S.M. Bennington, S. Rastogi, A. Shukla, K. Tsuji, M. Takenaka: Phys. Rev. E* ***85*** *(2012) 021807.*
[5] R.L. Miller and R.F. Boyer: J. Polym. Sci. Pol. Phys. **22** (1984) 2021.

Dinuclear complexes of tetravalent cerium in an aqueous perchloric acid solution

Tetravalent cerium (Ce(IV)) is a widely known inorganic oxidizing agent, particularly in the field of organic synthesis [1]. More recently, Ce(IV) has attracted considerable attention as an electron sacrificial oxidant in studies of the photocatalytic oxidation of water to produce H_2 and O_2 for energy sources [2]. Since its compounds are commercially available and reasonably priced, a continuous demand for Ce(IV) is still anticipated in various basic and applied research fields.

For a powerful chemical reagent, Ce(IV) is often employed in the form of an aqueous solution, meaning that Ce(IV) species interact with the target substances to be oxidized or activated as aquo species. The nature of Ce(IV) aquo species is, however, far less well understood, as compared with that of trivalent cerium (Ce (III)). Several preceding studies have also implied the formation of soluble polymeric species with oxo- and/or OH-bridging, although their speciation and structure are not yet identified. Despite this finding, Ce(IV) aquo species in applied chemical and biochemical research are generally regarded as a monomeric species. Obviously, the chemical reactions related to Ce(IV) species depend strongly on whether they exist only as monomeric species in the system, or if they form other polymeric species. For instance, the most plausible role of Ce(IV) aquo species in the photocatalytic oxidation of water is as a "single-electron" oxidant, which indirectly produces active metal oxo complexes through two-step single electron transfer reactions [2]. However, if Ce(IV) species interact with the targets as a dimer, the formation of the metal oxo complexes may take place via a one-step two-electron transfer event, or the bridging oxo/OH groups in the dimer may directly cause the introduction of oxo group into the target complexes. From these viewpoints, detailed characterization of Ce(IV) aquo species must be indispensable for elucidating the appropriate reaction schemes in which Ce(IV) species play an important role. Therefore, the EXAFS and DFT calculation studies for identifying the speciation and complex structure of Ce (IV) aquo species in an aqueous perchloric acid ($HClO_4$) solution were performed [3]. The studies were carried out at **BL11XU**.

An X-ray absorption study of lanthanides is

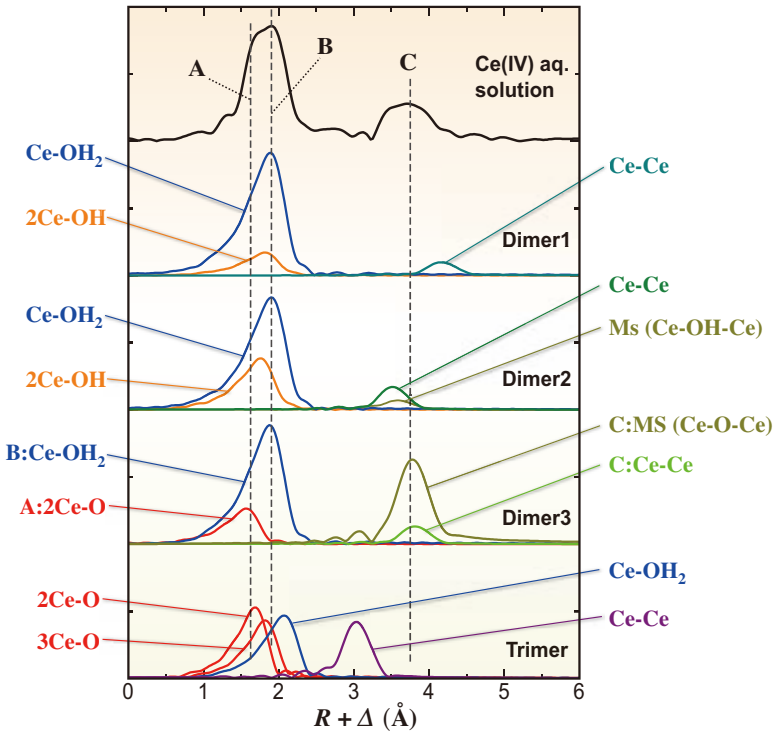

Fig. 1. Fourier transformed Ce *K*-edge EXAFS spectrum for Ce(IV) in 2 M $HClO_4$ (top, black) and the simulated spectra for the DFT-optimized complexes illustrated in Fig. 2 (colored data in the lower spectra). **A**, **B**, and **C** positions denote dominant components in the raw data (black spectrum in the first column), and those agreed well with three peaks of **Dimer 3**. The Ce concentration in the solution samples was 0.05 M. Each color was used only for distinction of each atomic distance in the same simulated spectrum. MS: multiple scattering derived from the Ce–OH–Ce arrangement.

generally performed at their L_{III}-edges (5–10 keV). However, the available range of their EXAFS spectra (in particular lighter lanthanides including Ce) is rather narrow. Furthermore, the spectra often suffer from the multi-electron excitation effect (MEE), which increases errors in determining coordination numbers and interatomic distances from EXAFS data [4]. To avoid the interference of MEE, we have collected the XAS spectra of our samples at the Ce *K*-edge (40.443 keV). This also enables us to obtain EXAFS spectra with a wider *k*-range, providing higher distance resolution on the data analysis for EXAFS. The EXAFS Fourier transform (FT) of the Ce(IV) aquo species (black spectrum in Fig. 1) exhibits two well-defined peaks at approximately $R+\Delta$ = 1.8 and 3.7. The first peak at $R+\Delta$ = 1.8 Å corresponds to the coordination of water molecules and possibly hydroxide ions. On the other hand, we can interpret the second peak at $R+\Delta$ = 3.7 Å as either the scattering from heavy atoms or the enhanced multiple scattering of linear coordinating ligands. Since perchlorate ions are highly unlikely to coordinate to Ce(IV), the second peak can be assigned to the scattering from distant Ce atoms. This clearly indicates the presence of polymeric Ce(IV) species in the present sample solution.

To probe the probable structural arrangement of polymeric Ce(IV) species, DFT geometry optimization was carried out for di- and trinuclear Ce(IV) complexes in the aqueous phase. The geometry optimization was converged for three dinuclear and one trinuclear complexes, as shown in Fig. 2. The simulated EXAFS-FT spectra of these DFT-optimized complexes (colored spectra in Fig. 2; each color was used only for distinction of each atomic distance in the same simulated spectrum) indicate that the Ce–Ce peak for the **Trimer** appears at a much shorter *R*-range than the observed second peak at $R+\Delta$ = 3.7 Å, and its Ce–O(H_2O) peak also deviates from the observed first peak at $R+\Delta$ = 2.0 Å. Therefore, it is more reasonable to assign the peak at $R+\Delta$ = 3.7 Å to dinuclear complexes, rather than tri- or larger polymeric ones. On the basis of the detailed analysis of EXAFS data and the results of DFT calculation, we concluded that the "single oxo-bridging" dinuclear complex (**Dimer3**) is the most dominant form of the Ce(IV) species in the aqueous solution. The dinuclear complexes shown in Fig. 2 are energetically close to one another, implying that all of these species are potentially involved in the dimerization process of Ce(IV), although the final species is likely to settle into the "single oxo-bridging" structure. The bridging-oxo (and potentially OH) groups of the dinuclear complex are expected to be chemically active. Therefore, they possibly contribute to the remarkably high reactivity of Ce(IV) aqueous solution, in addition to its large reduction potential.

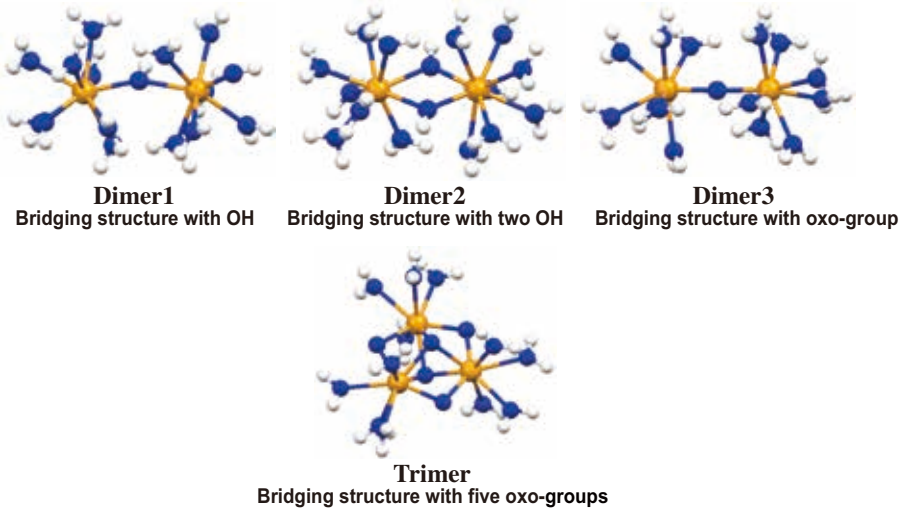

Fig. 2. Di- and tri-nuclear complex structures optimized using molecular orbital calculations based on the DFT theory (yellow: Ce(IV), blue: oxygen, white: hydrogen). **Dimer 3** is most probable.

Atsushi Ikeda-Ohno and Tsuyoshi Yaita*

SPring-8/JAEA

*Email: yaita@spring8.or.jp

References

[1] A.K. Das: Coord. Chem. Rev. **213** (2001) 307.
[2] Y. Hirai *et al.*: Angew. Chem., Int. Ed. **47** (2008) 5772.
[3] *A. Ikeda-Ohno, S. Tsushima, C. Hennig, T. Yaita and G. Bernhard: Dalton Trans. **41** (2012) 7190.*
[4] P.G. Allen *et al.*: Inorg. Chem. **39** (2000) 595.

Charge and energy transfer in argon-core-neon-shell clusters irradiated by free electron laser pulses at 62 nm

The recent advent of self-amplified spontaneous emission (SASE) free electron laser (FEL) light sources has opened new research fields on the interaction of intense short-wavelength laser pulses with matter [1-3]. Atomic clusters are ideal objects for such studies, not only because their size can be varied from a single atom to a bulk-like macroscopic object, but also because there is no energy dissipation into the surrounding medium. Pioneering works on clusters have revealed characteristic ionization dynamics induced by intense FEL pulses, such as sequential photoabsorption [4], charge recombination [5,6], and inhomogeneous charge redistribution [6,7].

A deeper insight into the spatial origin of the charge distributions can be obtained from core-shell heterogeneous systems. An Ar-Ne cluster is known to be self-assembled to a core-shell structure [8]. We have carried out experimental studies on Ar core-Ne shell clusters irradiated by intense 62 nm (20 eV) pulses from a free electron laser [9]. At this photon energy, one photon suffices for the ionization of an Ar atom (whose ionization potential is 15.8 eV) whereas at least two-photon absorption is needed for the ionization of a Ne atom (whose ionization potential is 21.6 eV). This results in preferential energy injection into the Ar core, and thus the ionization dynamics followed by a charge transfer process can be studied by varying the Ar core size. This type of study may be of great importance with respect to suggestions to delay and reduce the Coulomb explosion of bio-molecules by embedding them in a tamper [10,11] for future X-ray diffraction imaging experiments using X-ray lasers.

Experiments were performed at the SPring-8 compact SASE source (SCSS) test accelerator in Japan [2]. Figure 1 is a schematic of the experimental setup employed in this experiment [12]. Briefly, the FEL beam was back-focused onto the cluster beam by a multi-layer focusing mirror. The FEL beam was partially blocked by a beam stopper before the ionization region so that the unfocused beam did not irradiate the cluster beam directly. The estimated power density at the focus was ~10^{14} W/cm^2 at the full power of the FEL in the present experiment. The Ar core-Ne shell clusters were prepared by adiabatic expansion of Ne-Ar premixed gas (1% and 3% Ar in Ne) through a pulsed 250 μm nozzle. The stagnation pressures and the nozzle temperature were adjusted to control cluster size. We measured the time-of-flight mass spectra and the kinetic energy distributions (KED) of ions with our momentum imaging spectrometer [12].

The most representative results of the present experiments were the Ar concentration dependence of KED. As shown in Fig. 2, the fragment Ne^+ from the 1% Ar-Ne cluster has a kinetic energy up to ~60 eV, whereas those from the 3% Ar-Ne cluster have much higher energies (up to ~90 eV). In addition, we found a clear tendency that the number of fragment Ne^+ ions increases with Ar concentration (i.e., Ar core size). These results indicate that a portion of the charges produced in the Ar core are transferred to the Ne shell before the fragmentation. The kinetic energy of Ar^+ ions was much smaller than that of Ne^+ ions. This indicates that the prepared Ne-Ar premixed cluster surely has the Ar core-Ne shell structure.

We have estimated the number of transferred charges and energies from Ar to Ne within a core-shell cluster by assuming a uniformly charged sphere model [9]. Here, we simply assume the Ar core-Ne shell cluster as an ideal concentric sphere, and that its core is uniformly charged with the total charge Q_{Ar} and its shell with Q_{Ne}. The kinetic energies of Ne^+ ions and Ar^+ ions produced via Coulomb explosion can be easily calculated within classical mechanics.

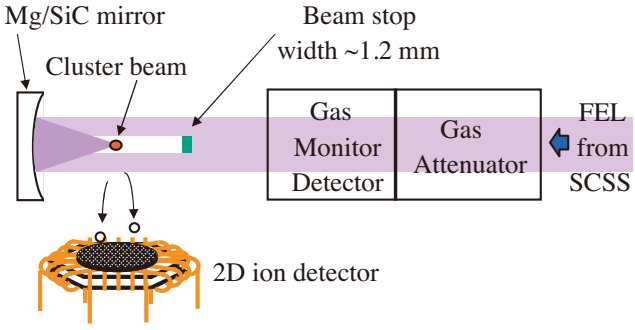

Fig. 1. Schematic illustration of the experimental setup.

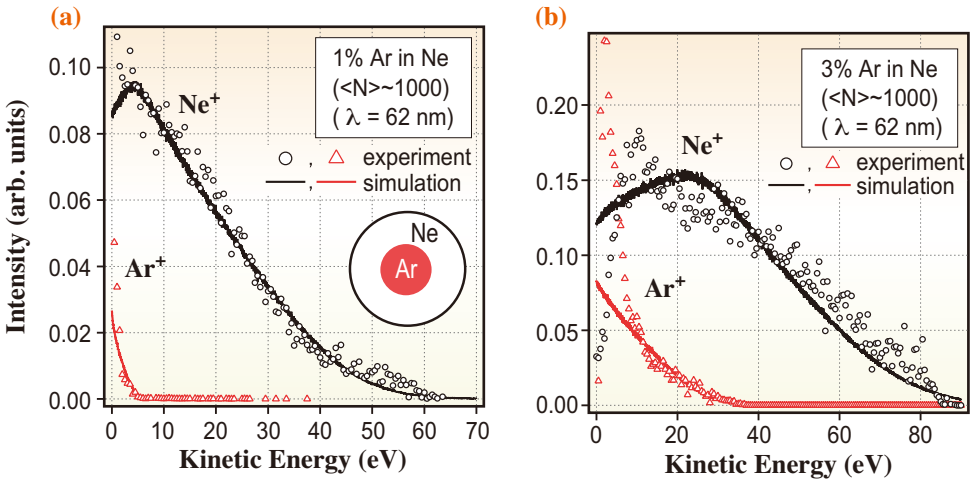

Fig. 2. Kinetic energy distributions of Ne^+ and Ar^+ ions from **(a)** core-shell clusters from 1% Ar-Ne and **(b)** core-shell clusters from 3% Ar-Ne. The observed kinetic energy spectra are shown by symbols (open circles for Ne^+ ions and open red triangles for Ar^+ ions) and the simulated kinetic energy spectra are plotted with lines (black lines for Ne^+ ions and red lines for Ar^+ ions).

The estimated numbers of charges created in the Ne and Ar core-Ne shell clusters, are listed in Table 1, in addition to the energies stored in the Ar core and Ne shell. The number of charges transferred from the Ar core to the Ne shell is estimated by the difference between the number of charges obtained by the Ne shell and that obtained by the pure Ne cluster. This is ~10 for 1% Ar-Ne and ~39 for 3% Ar-Ne. For the estimation of transferred energy, we assume that some part of the energy initially created in the Ar core migrates to the Ne core and the rest remains in the core. The latter is directly obtained from the experiments, and the former is estimated as the difference between the average energy stored in the Ne core of a core-shell cluster and that in a pristine Ne cluster. Hence we determine that about 0.03 keV is left in the Ar core and 0.8 keV (= 2.9 – 2.1 keV) is transferred to the Ne shell in the 1% Ar-Ne clusters, whereas 0.44 keV remains in the Ar core and more than 4.4 keV is transferred to the Ne shell in the 3% Ar-Ne clusters. These results indicate that more than 90% of the energy absorbed by the Ar core is transmitted to the Ne shell. The present results strongly support the usefulness of a tamper [10,11]. Embedding biomolecules in a tamper would make it possible to reduce the influence of Coulomb explosion during the X-ray diffraction experiments using X-ray lasers.

	Total Charge	Charge in Ne Shell (stored energy)	Charge in Ar Core (stored energy)
Ne cluster	+48	+48 (2.1 keV)	
1% Ar in Ne	+60	+58 (2.9 keV)	+1.6 (0.029 keV)
3% Ar in Ne	+100	+87 (6.5 keV)	+13 (0.44 keV)

Table 1. Estimated number of charges created in the Ne clusters and the Ar core-Ne shell clusters (1% and 3% Ar-Ne). The listed value represents the charge number, which is obtained from a cluster with <**Ni**> = 1000 at the focus point. The energy stored in the Ar core or the Ne shell is listed in parentheses.

K. Nagaya[a,c,*], M. Yao[a,c], H. Fukuzawa[b,c] and K. Ueda[b,c]

[a] Department of Physics, Kyoto University
[b] Institute of Multidisciplinary Research for Advanced Materials, Tohoku University
[c] SPring-8/RIKEN

*Email: nagaya@scphys.kyoto-u.ac.jp

References

[1] C. Bostedt *et al.*: Nucl. Instrum. Meth. A **601** (2009) 108.
[2] T. Shintake *et al.*: Nat. Photonics **2** (2008) 555.
[3] B. McNeil: Nat. Photonics **3** (2009) 375.
[4] C. Bostedt *et al.*: Phys. Rev. Lett. **100** (2008) 133401.
[5] M. Hoener *et al.*: J. Phys. B: At. Mol. Opt. Phys. **41** (2008) 181001.
[6] H. Thomas *et al.*: J. Phys. B: At. Mol. Opt. Phys. **42** (2009) 134018.
[7] H. Iwayama *et al.*: J. Phys. B: At. Mol. Opt. Phys. **43** (2010) 161001 .
[8] M. Lundwall *et al.*: J. Chem. Phys. **126**, 214706 (2007).
[9] *A. Sugishima et al.: Phys. Rev. A* ***86*** *(2012) 033203.*
[10] S.P. Hau-Riege *et al.*: Phys. Rev. Lett. **98** (2007) 198302.
[11] B. Ziaja *et al.*: Phys. Rev. A **84** (2011) 033201.
[12] K. Motomura *et al.*: J. Phys. B: At. Mol. Opt. Phys. **42** (2009) 221003; H. Fukuzawa *et al.*: Phys. Rev. A **79** (2009) 031201-1.

EARTH & PLANETARY

"**Noibara**"- *Multiflora rose*

SCIENCE

Synchrotron radiation X-rays have spawned a new phase of *in situ* observation of materials subjected to extreme conditions, leading to a greater understanding of the Earth's and planetary deep interiors. Constantly evolving synchrotron-based and static high-pressure techniques, since the beginning of public use in 1997, increasingly enhance the high-pressure research program for Earth and Planetary Science. In recent years, the combined techniques of X-ray diffraction with synchrotron or non-synchrotron spectroscopy, which allow multiple measurements to be performed on the same samples under high-pressure and high-temperature conditions, have provided complementary information of material properties. This chapter provides an overview of selected challenges in high-pressure Earth and Planetary Science in 2012.

To simulate the behavior of liquid iron alloy in the early Earth magma ocean, Terasaki investigated the interfacial tension of liquid iron alloy droplets in silicate melt under high pressure and high temperature by X-ray radiography, and discussed the effect of the presence of light elements on liquid pure iron. Shibazaki *et al*. determined the phonon dispersion and volume compression of iron hydride by high-pressure inelastic X-ray scattering and X-ray diffraction. On the basis of geophysical observations of sound velocity and density distributions, they constrained the hydrogen concentration in the Earth's inner core.

Murakami and Ohta experimentally determined the properties of the Earth's lower mantle minerals under the relevant high-pressure conditions using a diamond-anvil cell technique in combination with X-ray diffraction and Brillouin scattering or thermoreflectance, respectively. The former, based on reliable shear velocity and density data, suggested that the composition of the lower mantle is compatible with that in the chondritic model, being different from that of the upper mantle. The latter found that the conventionally assumed thermal conductivity in the bulk lower mantle was reasonable, and the core-mantle boundary heat flow could be fully explained by new data concerning the thermal conductivity of silicates. Tange precisely determined the equation of state of $MgSiO_3$ perovskite, the primary mineral of the lower mantle, and MgO under high-pressure and high-temperature conditions relevant to the lower mantle, in order to apply it to a mineralogical model of the Earth's lower mantle.

Yasuo Ohishi

Interfacial tension of Fe-alloy liquids under pressure: Size of core-forming liquid in terrestrial magma ocean

In a terrestrial magma ocean, which is considered to form during planetary accretion, liquid Fe-alloy droplets settle through silicate melt and metal segregation occurs in the planet interior (Fig. 1). The size of Fe-alloy droplets in a magma ocean is closely related to both the sinking velocity, i.e., the time scale of metal/silicate separation and the extent of chemical equilibration between Fe-alloy and silicate melt [1]. Therefore, the interfacial tension of liquid Fe-alloy under high pressure is a crucial factor for understanding metal/silicate separation in terrestrial magma oceans.

We have measured the interfacial tension of Fe-Si liquid under high pressure and temperature, combined with synchrotron X-ray radiography to determine the droplet size of core-forming metallic liquid in a magma ocean. High-pressure experiments were performed using a 1500 ton Kawai-type multi-anvil device installed at beamline **BL04B1**. A 2-mm-diameter pellet of Fe-Si powder packed within $Na_2Si_2O_5$ glass powder was placed in a boron nitride capsule. The X-ray beam transmitted from the sample was acquired as an X-ray radiographic image using a high-resolution CCD camera. All experiments were performed at a pressure of 1.5 ± 0.3 GPa and up to 2173 K.

To determine the interfacial tension of the liquid, the sessile drop method was applied. When liquid Fe-alloy rests on the smooth flat solid surface of a capsule in contact with overlying silicate liquid, the liquid Fe-alloy adopts the form of a rounded drop as a result of force equilibrium between gravity and interfacial tension. From the X-ray radiographic images, we obtain the shapes of the liquid Fe-Si droplets at high pressure and temperature (Fig. 2). As the shape of the liquid droplet can be expressed by combining the classical Laplace and Young's equations, we can calculate the interfacial tension of Fe-Si liquid. Further details of this method are described elsewhere [2,3].

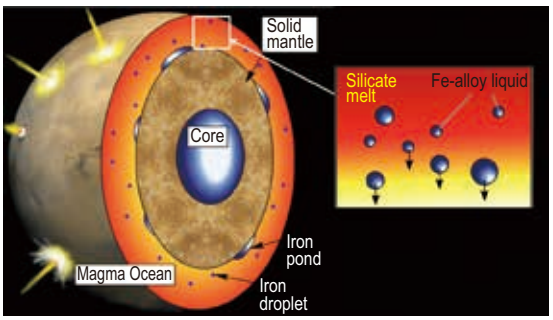

Fig. 1. Schematic view of interior of early Earth. Liquid Fe-alloy droplets settle in the magma ocean during the core formation stage.

The effects of temperature on the interfacial tension of Fe-Si liquid are plotted in Fig. 3(a). The interfacial tension of Fe-Si liquid decreases with increasing temperature [4]. This observed trend might be due to the following reason. Interfacial energy, which causes interfacial tension, depends on the excess energy at the interface compared with the energy of the droplet interior. When the thermal motion of Fe and Si atoms in the Fe-Si liquid increases at higher temperatures, the difference in energy between the interface and the interior may be reduced, thus causing a reduction in the interfacial tension at high temperature.

The interfacial tension decreases with increasing Si content, suggesting that Si behaves as a surface active element that reduces the interfacial tension [4]. The interfacial tension of Fe-Si liquid at 1.5 GPa is plotted as a function of the light element content in Fig. 3(b), together with the data of Fe-S and Fe-P liquids [3]. Comparing the effects of different alloying elements (S, Si, and P) on interfacial tension, S is found to be the most effective in causing a reduction, and silicon has a relatively moderate effect. In contrast, the effect of P is negligible. Therefore, the effects of each light element on the interfacial tension of liquid iron are all different. These trends at 1.5 GPa are similar to those measured at ambient pressure, which suggests that interfacial properties of liquid Fe-alloy are approximately constant, at least up to 1.5 GPa. However, the difference in the interfacial tension among different light elements becomes smaller at higher pressure.

The characteristic size of Fe-alloy droplets in a magma ocean is determined by the force balance

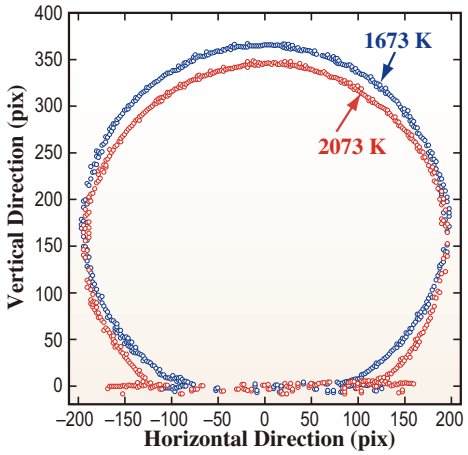

Fig. 2. Interface plots of Fe-Si (Si=25 at%) liquid obtained from radiography images at 1673 and 2073 K.

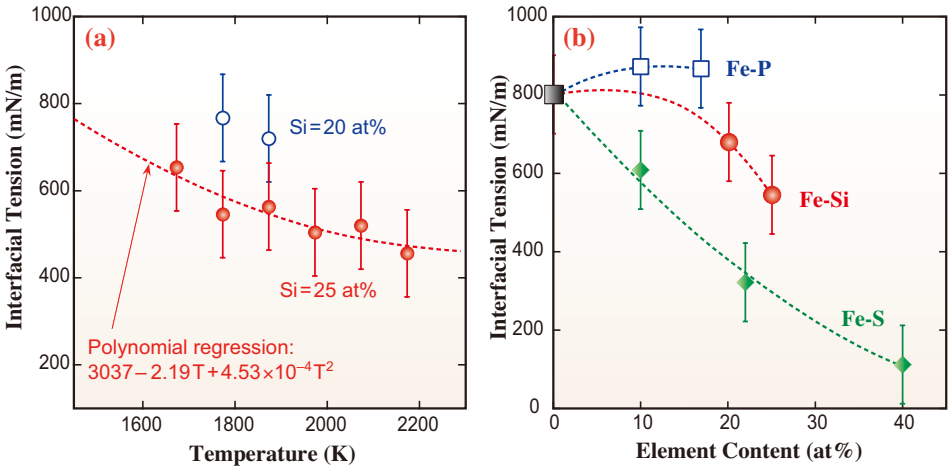

Fig. 3. **(a)** Effect of temperature on interfacial tension. Red and blue symbols represent the interfacial tension of $Fe_{75}Si_{25}$ and $Fe_{80}Si_{20}$ liquids, respectively. Polynomial regression curve is also shown. **(b)** Interfacial tension as a function of light element content at 1.5 GPa. Red circles show results for Fe-Si liquid at 1873 K. Black square, green diamonds, and blue squares show the results for Fe, Fe-S, and Fe-P liquids at 1.5 GPa and 1943 K, respectively [3].

between the viscous stress, which causes disruption of the droplet, and the interfacial tension, which inhibits breakup and disruption [1,5]. On the basis of the results of the current and previous studies on the interfacial tension of Fe-alloy liquids, the settling velocity for Fe-alloy liquids in a magma ocean is calculated at 1.5 GPa and 2500 K, assuming that the interfacial tension of Fe-alloy liquid in the magma ocean is the same as that in $Na_2Si_2O_5$ liquid. The calculated setting velocity of liquid Fe-alloy is plotted as a function of silicate melt viscosity in Fig. 4. The droplet size of Fe liquid is calculated to be 7 – 11 mm if the viscosity of the magma ocean lies in the range of 10^{-2} – 10^{-1} Pa-s. The droplet size of Fe-Si liquid is found to be larger by ~15% than that of Fe liquid. This suggests that the effect of Si on the density is stronger than its effect on interfacial tension, which therefore leads to the increase in droplet size. S causes a significant decrease in droplet size (*ca.* 33% decrease in size) with increasing S content from 10 to 40 at%. The settling velocity of droplets in the magma ocean decreases with increasing Si and S contents. In particular, the settling velocity of $Fe_{60}S_{40}$ liquid decreases significantly (~46%) compared with that of Fe liquid.

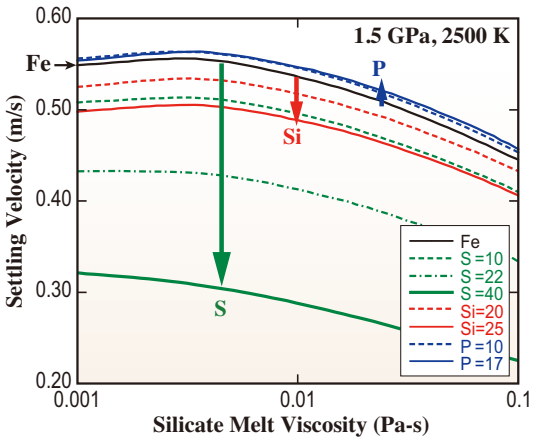

Fig. 4. Calculated settling velocity of Fe-alloy liquids as a function of silicate melt viscosity. Green, red, and blue arrows indicate the alloying effects of S, Si, and P on the settling velocity of liquid Fe.

If the core-forming liquid is enriched in S, the droplet size and the settling velocity are smaller than those for pure Fe liquid. Hence, chemical equilibrium between the droplet and surrounding silicate melt is established faster. Since smaller droplets tend to be entrained upward by the convective flow of silicate melt [5], smaller Fe-S droplets stay suspended for longer in the magma ocean compared with larger Fe, Fe-Si, or Fe-P droplets. In the present estimates, however, the droplet size and the settling velocity were calculated under the conditions of a shallow magma ocean. Further measurements of interfacial tension at higher pressures are required to determine droplet sizes in a deep magma ocean.

Hidenori Terasaki

Department of Earth and Space Science, Osaka University

Email: terasaki@ess.sci.osaka-u.ac.jp

References

[1] D.C. Rubie *et al.*: Earth Planet. Sci. Lett. **205** (2003) 239.
[2] Y. Rotenberg *et al.*: J. Colloid Interf. Sci. **93** (1983) 169.
[3] H. Terasaki *et al.*: Phys. Earth Planet. Int. **174** (2009) 220.
[4] *H. Terasaki, S. Urakawa, D.C. Rubie, K. Funakoshi, T. Sakamaki, Y. Shibazaki, S. Ozawa, E. Ohtani: Phys. Earth Planet. Int.* ***202-203*** *(2012) 1.*
[5] H. Ichikawa *et al.*: J. Geophys. Res. **115** (2010) B01404.

Sound velocity measurements in dhcp-FeH by inelastic X-ray scattering method: Implications for the hydrogen concentration in the Earth's core

The distributions of density and sound velocities of the Earth's interior are well investigated through geophysical observations. According to proposed models (e.g., Preliminary Reference Earth Model (PREM) [1]), the inner core, which is solid, is about 2–5% less dense than pure iron. Therefore, it is accepted that the core consists of iron and light elements. Hydrogen is one of the most plausible light elements in the core.

A large number of high-pressure experiments on iron alloys, including iron hydride (FeH), have been carried out in order to discuss the core composition. However, most of the previous works have constrained the abundances of light elements in the core by matching *only* density *or* sound velocity of the iron alloy to the PREM data. The important point is that iron alloy, the density ρ *and* sound velocity V of which are the same as ρ and V of the Earth's core *at* the pressure and temperature conditions of the core, can be a candidate for the constituent of the core. Therefore, we determined the density evolution of the sound velocity of FeH by inelastic X-ray scattering (IXS) and X-ray diffraction (XRD) analyses, and thereby constrained the abundance of hydrogen in the Earth's core by matching *both* density *and* velocity to the PREM data [2].

The IXS and XRD experiments were conducted up to 70 GPa at room temperature. High-pressure conditions were generated using a symmetric diamond anvil cell. The iron sample was compacted from a powder into a foil and hydrogen initially pressurized to 0.18 GPa was loaded to the sample chamber. Double-hexagonal-close-packed (dhcp) FeH was synthesized at around 4 GPa.

The IXS experiments were performed at **BL35XU**. We used the Si (9 9 9) configuration, which provides an incident photon energy of 17.794 keV with an energy resolution of 2.8 meV full width at half-maximum. The beam size was focused to 15 μm × 17 μm using a Kirkpatrick-Baez (KB) mirror pair. The scattered X-rays were analyzed with 12 crystals arranged in a 2-dimensional array (3×4 array). The XRD experiments were carried out at **BL10XU**. The X-ray beam was collimated to 15 μm in diameter and a typical wavelength used was 0.41348(7) Å. An XRD pattern of the sample was collected after each IXS measurement in order to obtain the density data of the sample at each pressure.

A typical IXS spectrum collected at 70 GPa and room temperature is shown in Fig. 1. The

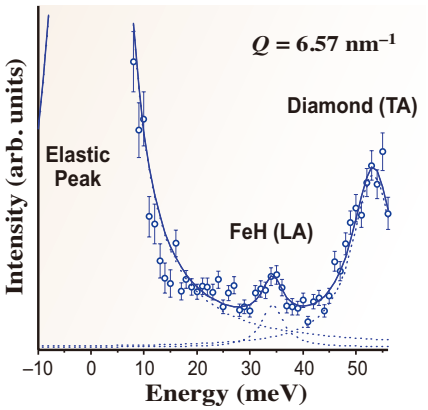

Fig. 1. Typical IXS spectrum of dhcp-FeH at 70 GPa and room temperature (Q = 6.57 nm^{-1}). The peak at zero energy is attributed to elastic scattering. Solid line is fitted result for elastic, longitudinal acoustic (LA) phonons of dhcp-FeH, and transverse acoustic (TA) phonons of diamond, contributions and dotted lines are the corresponding individual components.

compressional sound velocity (V_P) was determined by fitting the phonon dispersion with a sine function:

$$E[\mathrm{meV}] = 4.19\times10^{-4}\, V_P[\mathrm{m/s}]\times Q_{max}[\mathrm{nm^{-1}}]\sin\left(\frac{\pi}{2}\frac{Q[\mathrm{nm^{-1}}]}{Q_{max}[\mathrm{nm^{-1}}]}\right) \quad (1)$$

where E and Q are the energy and momentum of the phonon, respectively, and Q_{max} is approximately the first Brillouin zone edge. Figure 2 shows the dispersion curves up to 70 GPa. The determined velocity is an aggregate sound velocity averaged over crystal orientations because our sample was polycrystalline.

The measured V_P for dhcp-FeH is presented as a function of density in Fig. 3, and compared with PREM in the inner core [1]. The V_P for dhcp-FeH above 8.0 g/cm^3 (about 30 GPa) follows Birch's law (a linear relation between velocity and density). In contrast, the velocity is not linear when density is below 8.0 g/cm^3. Since it has been reported that dhcp-FeH loses its magnetism between 22 and 42 GPa (a ferromagnetic to nonmagnetic transition), the difference below and above 8.0 g/cm^3 is due to the loss of magnetism. This indicates that magnetism significantly affects the sound velocity.

We discussed the hydrogen concentration in the Earth's inner core using a linear mixing model under the assumption that the average density ρ and sound velocity V of a two-component ideal solid are given by

$$\rho = t\rho_{FeH} + (1-t)\rho_{Fe} \quad (2)$$

and

$$V = \frac{V_{FeH}\, V_{Fe}}{(1-t)\, V_{FeH} + t V_{Fe}} \qquad (3)$$

where t is the volume fraction of FeH. We assigned $\rho = \rho_{PREM}$ and $V = V_{PREM}$, where ρ_{PREM} and V_{PREM} are the density and compressional sound velocity of the PREM inner core [1], respectively. The density of iron ρ_{Fe} was estimated from the equation of state [3], and the sound velocity of iron V_{Fe} was calculated from the shock wave data [4]. In addition, the shear sound velocity V_S was derived by combining V_P with ρ and the bulk modulus K derived from the equations of state of dhcp-FeH [5] or hcp-Fe [4] according to the relation:

$$V_S^2 = \frac{3}{4}\left(V_P^2 - \frac{K}{\rho}\right) \qquad (4)$$

From the set of equations (2) and (3), we obtain $x = 0.13(3)$ in FeH_x (0.23(6) wt% H), and $\rho_{FeH} = 9.8(7)$ g/cm^3 at the inner core boundary (ICB) and 10.5(7) g/cm^3 at the center of the Earth (COE). According to the equation of state of dhcp-FeH [e.g., 5], the values of $\rho_{FeH} = 9.8(7)$ and 10.5(7) g/cm^3 are reasonable for the densities of dhcp-FeH at ICB (328.9 GPa and 5000 K) and COE (363.8 GPa and 6000 K) conditions within the range of uncertainty, respectively.

On the other hand, the estimated V_S for $FeH_{0.13(3)}$ (lower gray diamonds in Fig. 3) is much higher than the PREM V_S data. Recent *ab initio* calculations of hcp-Fe showed that V_S significantly decreases with temperature owing to anharmonic effects, i.e., V_S is reduced by about 29% from 0 K to 5000 K at the ICB density. Considering the anharmonic temperature effect, V_S for $FeH_{0.13(3)}$ at 5000 K and ICB pressure (white diamond in Fig. 3) is in good agreement with the PREM data at ICB condition.

Since the density *and* both V_P and V_S of $FeH_{0.13(3)}$ (0.23(6) wt% H) *at* the ICB pressure and temperature are consistent with the PREM data at ICB, $FeH_{0.13(3)}$ determined in this work is suitable as the Earth's inner core composition, assuming that the light element in the core is only hydrogen.

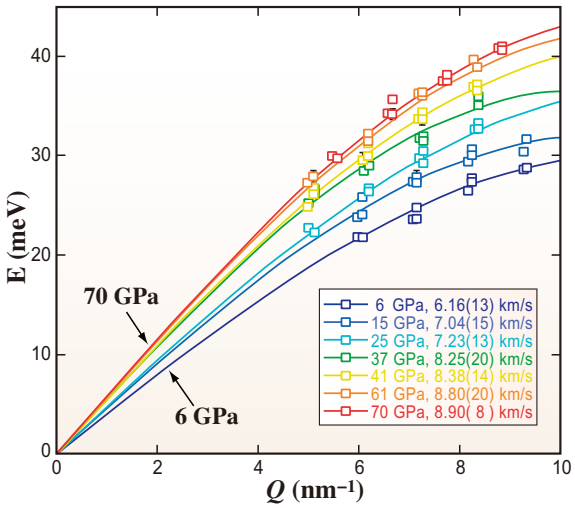

Fig. 2. Dispersion curves of LA phonons of dhcp-FeH at room temperature and pressures of 6, 15, 25, 37, 41, 61, and 70 GPa from bottom to top, together with each V_P value. Solid lines are the dispersion curves obtained by fitting the experimental data with equation (1) in the text. Vertical error bars (about 1% uncertainty) fall within the size of symbols if they are not apparent.

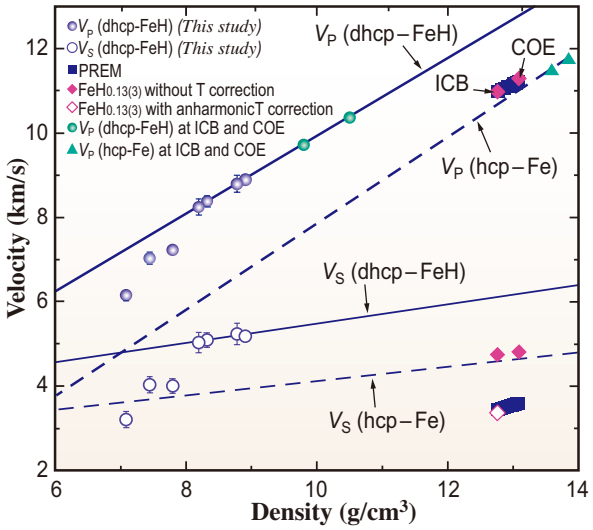

Fig. 3. V_P and V_S as a function of density, compared with the seismic observations. Solid and open circles are V_P and V_S for dhcp-FeH in this study, respectively. The solid squares are the PREM data in the inner core [1]. The solid lines indicate Birch's laws for nonmagnetic dhcp-FeH in this study and the dashed lines indicate those for hcp-Fe calculated from the shock data [4]. The solid triangles are V_P for hcp-Fe at ICB and COE conditions [3,4]. The green solid circles and pink solid diamonds denote our estimated densities and sound velocities for dhcp-FeH and $FeH_{0.13(3)}$ at ICB and COE pressures, respectively. The open diamond denotes our estimated V_S for $FeH_{0.13(3)}$ at 5000 K and the ICB pressure. Uncertainties in our estimations (sound velocities of $FeH_{0.13(3)}$) are about 2% for V_P and about 4% for V_S, which are not plotted for clarity.

Yuki Shibazaki[a,*], Eiji Ohtani[b] and Hiroshi Fukui[c,d]

[a] Geophysical Lab., Carnegie Institution of Washington, USA
[b] Department of Earth and Planetary Material Sciences, Tohoku University
[c] Graduate School of Material Science, University of Hyogo
[d] SPring-8/RIKEN

*Email: yshibazaki@ciw.edu

References

[1] A.M. Dziewonski *et al.*: Phys. Earth Planet. Inter. **25** (1981) 297.
[2] *Y. Shibazaki, E. Ohtani, H. Fukui, T. Sakai, S. Kamada, D. Ishikawa, S. Tsutsui, A.Q.R. Baron, N. Nishitani, N. Hirao, K. Takemura: Earth Planet. Sci. Lett.* ***313-314*** *(2012) 79.*
[3] T. Uchida *et al.*: J. Geophys. Res. **106** (2001) 21799.
[4] J.M. Brown *et al.*: J. Geophys. Res. **91** (1986) 7485.
[5] N. Hirao *et al.*: Geophys. Res. Letter **31** (2004) L06616.

Mineralogical model of lower mantle inferred from high-pressure and -temperature sound velocity data

It is widely accepted that at least the Earth's uppermost mantle, perhaps down to the top of the mantle transition zone, has a peridotitic (pyrolitic) bulk composition, on the basis of petrological evidence. On the other hand, a variety of chemical compositions, ranging from peridotitic to chondritic, have been proposed for the lower mantle. This has long remained controversial owing to the lack of conclusive arguments. The mineral assemblage of the lower mantle has been examined from density measurements under high *P*-*T* conditions. However, recent computational simulations demonstrated that such experimentally derived density and bulk moduli do not place unique constraints on the mantle composition because of their intrinsic uncertainties, whereas shear velocity (V_S) data strongly constrain the lower mantle models. It is thus crucial to obtain reliable V_S data of the major lower mantle constituents, silicate perovskite (pv) and (Mg,Fe)O ferropriclase (fp), under relevant high *P*-*T* conditions. Recent progress in Brillouin scattering spectroscopy optimized for extreme high-pressure conditions has so far enabled us to measure V_S of $MgSiO_3$-pv [1], post-perovskite [2], and MgO periclase [3] up to 172 GPa. Although those sound velocity data indeed provide valuable information on the lower mantle mineralogy, the effects of chemical impurities, such as iron and aluminum, and high temperature remain unsettled. More importantly, sound velocity measurements of pv and fp have never been performed under simultaneously high-*P* and high-*T* conditions corresponding to the lower mantle environment. Here, we determined V_S of aluminous silicate pv and fp up to 124 GPa at 300 K. The high *P*-*T* measurements were also conducted on $MgSiO_3$ pv and MgO at a temperature of 2700 K up to 91 GPa using the newly developed Brillouin scattering system at beamline **BL10XU** [4,5].

We obtained very sharp Brillouin peaks from the transverse acoustic modes of each phase over the entire *P*-*T* range we explored (Fig. 1). No significant peak broadening was observed with increasing pressure. The angle-dispersive synchrotron X-ray diffraction measurements were conducted simultaneously to determine the volume of the sample and the pressure at BL10XU, the synchrotron X-ray source of SPring-8 in the energy range of 30–50 keV. The X-ray diffraction peaks for each sample were very sharp, and two-dimensional X-ray diffraction images showed clear circular Debye rings with fairly uniform intensity distribution along the circle, indicating that the sample did not undergo significant grain growth or lattice preferred orientation under high pressure and high temperature. On the basis of the fit of the finite strain to the *P*-V_S profiles of Al-pv and fp, we obtained the best-fit values of G_0 = 166(1) GPa (shear modulus) and G_0' = 1.57(5) (pressure derivative of shear modulus) for Al-pv. The G_0' of Al-pv coincides with the 1.56(4) of pure $MgSiO_3$ pv, indicating a minimal effect of Al on G_0'. For fp, the finite strain was fitted separately for low- (5–40 GPa) and high- (60–121 GPa) pressure ranges, because anomalous behavior was observed around 50 GPa owing to spin crossover. The fitting result gives G_0 = 113(2) GPa and G_0' = 2.15(5) for the HS state, and G_0 = 130(2) GPa and G_0' = 2.04(5) for the LS state. Extrapolation of the HS data to high pressure does not reproduce the LS data, supporting the claim that the spin crossover of iron is not associated with the elastic softening. These G_0 and G_0' values for Al-pv and fp are plotted together with previous data in Fig. 2 as a function of iron or aluminum content. With such relationships, we can estimate G_0 and G_0' for the representative mantle composition (X_{Mg} = 79 for fp and X_{Al2O3} = 4 wt% for pv). The high *P*-*T* measurements on pure $MgSiO_3$ pv and MgO showed the velocity reduction by ~4% and ~6%, respectively, on average at 2700 K from the room-*T* data at lower mantle pressures. A linear fitting of the shear moduli against pressure, combined with the reported values of G_0 and G_0' [1,3], provides temperature derivatives of the shear modulus: dG/dT = −0.020(1) GPa/K for both pv and MgO. The shear strain derivatives of the

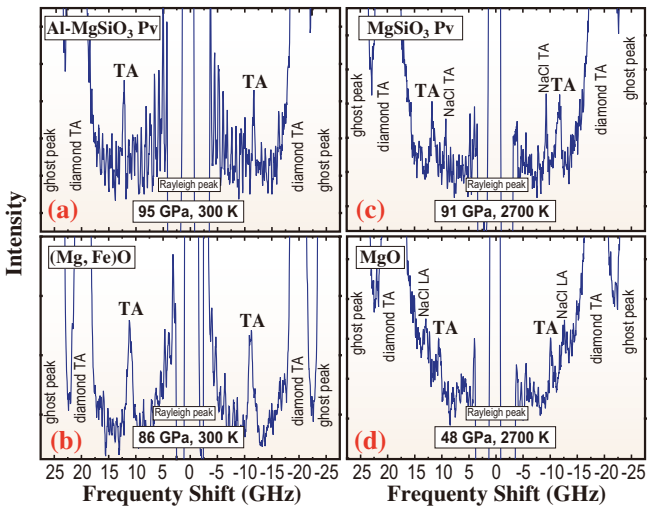

Fig. 1. Brillouin spectra of lower mantle phases: **(a)** $MgSiO_3$(+4 wt% Al_2O_3) pv at 95 GPa/300 K; **(b)** $(Mg_{0.92}Fe_{0.08})O$ at 86 GPa/300 K; **(c)** $MgSiO_3$ pv at 91 GPa/2700 K; and **(d)** MgO at 48 GPa/2700 K. TA and LA indicate transverse and longitudinal acoustic modes of Brillouin shift, respectively.

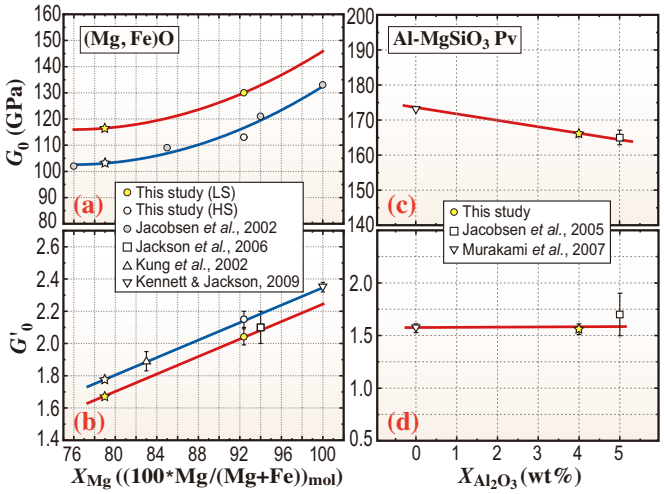

Fig. 2. Effect of Al and Fe on shear modulus (G_0) and its pressure derivative (G_0'). **(a,b)** (Mg,Fe)O fp, and **(c,d)** Al-bearing $MgSiO_3$ pv. Stars correspond to G_0 or G_0' for representative iron/alumina content of X_{Mg} = 79 mol% for fp and $X_{Al_2O_3}$ = 4 wt%. Lines show the best-fit trends. Blue and red lines in (a) and (b) indicate the trends of (Mg,Fe)O at HS and LS states of iron, respectively.

Grüneisen parameter (γ) are estimated to be η_{S0} = 2.4(2) for pv and 3.0(3) for MgO.

Present measurements performed over a wide *P-T* range that covers almost the entire range of lower mantle conditions allow us to constrain the lower mantle mineralogy. We model the lower mantle as a two-phase mixture of pv and fp in the SiO_2-MgO-FeO-Al_2O_3 system, in which (Al,Fe)-bearing pv contains 4 wt% Al_2O_3 with X_{Mg} = 94 and fp has X_{Mg} = 79. A constant Mg-Fe partitioning coefficient between pv and fp is assumed for the entire lower mantle. The V_S profiles of these pv and fp were calculated along the typical temperature profiles (Fig. 3(a)). The PREM is best fitted by the mixture of 95% pv and 5% fp in volume (X_{Pv} = 0.95) (Fig. 3(b)). The velocity of fp increases steeply by ~4% across the spin crossover, however, such an anomalous feature is not clear in the calculated profile of the pv+fp mixture, suggesting that the spin crossover of iron in fp may be seismologically invisible. On the other hand, the V_S profile for a peridotitic (pyrolitic) mantle (X_{Pv} = 0.80) is shown to be lower by up to 3.2% than the PREM throughout the pressure range of the lower mantle, indicating that the conventional peridotitic model is incompatible with the seismological observations.

The present results indicate that the conventional peridotitic mantle model is not compatible with the seismic properties of the lower mantle and suggest that the lower mantle is dominated by perovskite (~95 vol%) and therefore is silica-rich in comparison with the upper mantle. The different chemical compositions between the upper and lower mantle could be a consequence of fractional crystallization of the magma ocean extending to the deep lower mantle in the early history of the Earth. The primordial chemical stratification may have been preserved through the subsequent solid-state convection until the present day. The layered mantle convection is presumed to have been predominant in early Earth, indicating limited mass transport between the upper and lower mantle. The seismic tomography images of subducting slabs or upwelling plumes penetrating the upper/lower mantle boundary may not represent whole-mantle convection but intermittent/transitional stages between layered and whole mantle-convections.

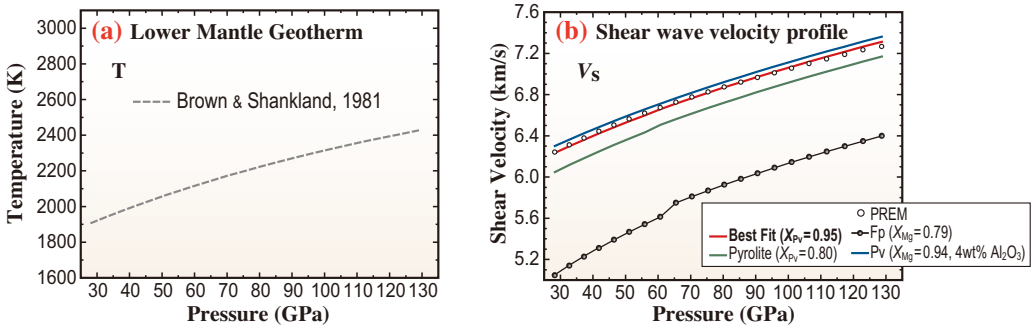

Fig. 3. Representative lower mantle geotherm **(a)** and calculated shear wave velocity profiles of fp (black lines) and pv (blue lines) **(b)**. Velocity profile for the pyrolite model is shown as the green line. Best-fit model to the PREM is shown as a red curve.

Motohiko Murakami

Department of Earth and Planetary Materials Sciences, Tohoku University

Email: motohiko@m.tohoku.ac.jp

References

[1] M. Murakami *et al.*: Earth Planet. Sci. Lett. **256** (2007) 47.
[2] M. Murakami *et al.*: Earth Planet. Sci. Lett. **259** (2007) 18.
[3] M. Murakami *et al.*: Earth Planet. Sci. Lett. **277** (2009) 123.
[4] M. Murakami *et al.*: Phys. Earth Planet. Inter. **174** (2009) 282.
[5] *M. Murakami, Y. Ohishi, N. Hirao and K. Hirose: Nature* ***485*** *(2012) 90.*

Toward precise thermal/chemical modeling of lower mantle

The lower mantle is the largest part in the solid Earth, and composes more than 50% of the volume and mass. Therefore, the chemical composition of the lower mantle has a great influence on the bulk composition of the planet. The chemical composition of the upper mantle is well known to be peridotitic on the basis of geological evidence. Hence, if we know the chemical composition of the lower mantle, we can estimate the material recycling and chemical differentiation history in the mantle from the difference between the chemical compositions of the upper and lower mantle. In addition to its abundance, the lower mantle has other important features. The lower mantle consists of silicate and oxide, and it has much lower thermal conductivity and higher viscosity than the metallic liquid outer core, which is the second largest convecting part in the solid Earth. Thus the lower mantle can be considered as a thermal insulator controlling the cooling history of the solid Earth. In the material recycling and cooling history, convection is the most important mechanism, and pressure-volume-temperature equations of state (*P-V-T* EOS) and the knowledge of the thermodynamic properties such as thermal expansion coefficients and heat capacities of constituent materials are essential for understanding the mantle convection.

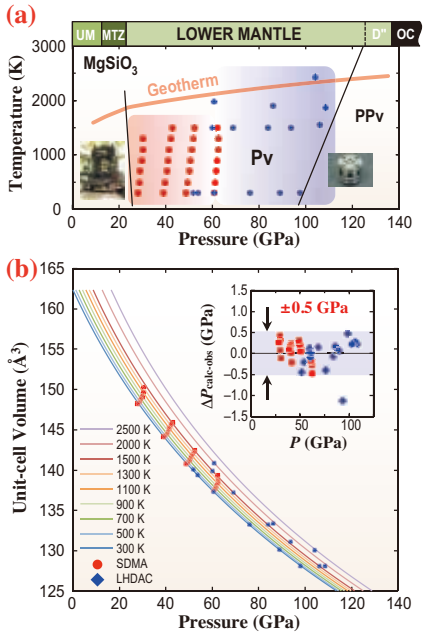

Fig. 1. Measured *P*, *T* conditions in $MgSiO_3$ **(a)**, and *P-V-T* data along with the isotherms at 300-2500 K **(b)**. Red circles and blue diamonds represent the results obtained in the experiment using sintered-diamond multianvil apparatus (SDMA) and laser-heated diamond anvil cell (LHDAC). Inset in (b) shows differences between measured data and determined EOS model.

$MgSiO_3$ is the most abundant end component of the dominant lower mantle phase, magnesium-rich silicate perovskite. Therefore, numerous reports of high-pressure and high-temperature *in situ* X-ray diffraction studies of $MgSiO_3$ perovskite using synchrotron radiation sources can be found in the literature, indicating that the thermoelastic properties of $MgSiO_3$ perovskite are constrained. However, thermal properties remain uncertain because of uncertainties in pressure scales and/or differences in high-pressure techniques. In order to clarify these uncertainties, we carried out high-pressure and high-temperature *in situ* measurements for $MgSiO_3$ perovskite based on a large-volume high-pressure technique developed at **BL04B1** using a multianvil apparatus "SPPED-Mk.II" [1], and at **BL10XU** using a laser-heated diamond anvil cell. In addition, we used a new EOS of MgO, which was determined from pressure-scale-free experimental data, as a primary pressure scale for static high-*P,T* experiments [2].

Using two high-pressure devices with one of the most reliable pressure scales, *P-V-T* EOS and thermodynamic properties of $MgSiO_3$ perovskite were precisely determined on the basis of robust experimental results obtained in the entire stability field of $MgSiO_3$ perovskite up to 110 GPa and 2500 K (Fig. 1; Ref. [3]). The new EOS of $MgSiO_3$ perovskite is consistent with that of MgO. In addition to the magnesium-rich silicate perovskite, ferropericlase (magnesiowüstite) is another main phase in the lower mantle, and MgO is the dominant end component making up more than 80 mol% of the ferropericlase in pyrolitic bulk composition (e.g., Ref. [4]). The comprehensive *P-V-T* EOS and thermodynamic properties of $MgSiO_3$ perovskite and MgO determined in this study will play a critical role in the mineralogical and thermal modeling of the Earth's lower mantle.

Figure 2 shows comparisons of calculated density and adiabatic bulk modulus values and those observed using the geophysical model known as PREM [Dziewonski and Anderson, 1981]. Here, the density and adiabatic bulk modulus were calculated referring to the model geotherm of Brown and Shankland (1981). Absolute values of density are tightly constrained within the uncertainty of 0.01 g/cm at most for both $MgSiO_3$ perovskite and MgO (Fig. 2(a)). The densities of $MgSiO_3$ perovskite and MgO are much lower than those obtained by PREM owing to a lack of iron in the system. When we carry out mineralogical modeling, we must take into account the effects of iron incorporation on mass and volume in both $MgSiO_3$

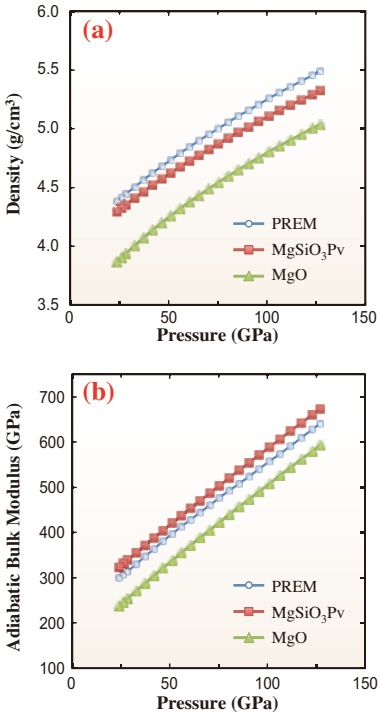

Fig. 2. Density **(a)** and adiabatic bulk modulus **(b)** of $MgSiO_3$ perovskite and MgO, compared with PREM. Error bars for those properties are smaller than the symbol size.

perovskite and MgO, and also on Fe-Mg partitioning between (Mg,Fe)SiO_3 perovskite and (Mg,Fe)O. The volume increase in perovskite due to Fe-incorporation and Fe-Mg partitioning of (Mg,Fe)SiO_3 perovskite and (Mg,Fe)O was already investigated at BL04B1 using a sintered-diamond multianvil apparatus [4,5], and the results will be merged in the lower mantle modeling in the near future. In addition, the adiabatic bulk modulus is also precisely determined with the uncertainties of less than 5 GPa up to 100 GPa (Fig. 2(b)). In order to improve current EOS models, precise high-temperature (2000 K) elastic measurements (±5 GPa in uncertainties) are required at pressures in the Mbar region. In the case of the bulk modulus of perovskite, the effect of iron incorporation is known to be marginal, and current results are applicable to the mineralogical modeling up to the Mbar region. On the other hand, although the effect of iron incorporation is complicated in ferropericlase because of the spin-state transition in ferrous iron, its effects on density and thermoelastic properties will be clarified using the results for MgO as a reference. Consequently, the newly established comprehensive adiabatic bulk moduli of $MgSiO_3$ perovskite and MgO support a bulk pyrolitic lower mantle rather than a perovskite-rich composition. If we employ a bulk perovskite composition, extraordinarily high temperatures (additional > 1000 K) are required to reproduce the K_S observed seismologically, because of a small $\partial K_S/\partial T$ of $MgSiO_3$ perovskite (~0.02 GPa/K) in the deep lower mantle.

In addition to applications to chemical modeling, current EOS models can contribute to the thermal model of the lower mantle. The lower mantle is considered to be convecting and thus its temperature profiles would be close to adiabatic. The adiabatic temperature profile is derived by integrating a fundamental thermodynamic relationship, $(\partial T/\partial P)_S = \alpha VT/C_P$ or $(\partial T/\partial P)_S = \gamma T/K_S$, where α, C_P, and γ are the thermal expansion, isobaric heat capacity, and Grüneisen parameter, respectively. The integrating operation requires one reference *P-T* condition, and Fig. 3 shows a result obtained with the reference temperature of 1900 K at 23 GPa, corresponding to a depth of 660 km in the Earth. The present EOS models of $MgSiO_3$ and MgO yield intermediate temperature profiles compared with previous models proposed of Brown and Shankland (1981) and Anderson (1982), and they are rather close to that by Stacey and Davis (2004). Our new EOS models give the current CMB potential temperature between 2570 K and 2750 K. In the near future, the temperature profile and the mineralogical model will be refined comprehensively using the present EOS as standards, and hopefully will provide insights on the chemical differentiation and cooling history of the solid Earth.

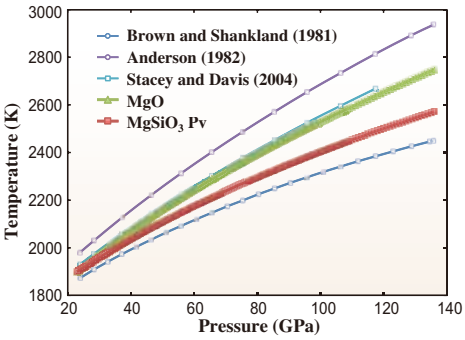

Fig. 3. Adiabatic temperature profiles derived using current EOS models of $MgSiO_3$ and MgO under lower mantle conditions and previous models proposed by Brown and Shankland (1981), Anderson (1982), and Stacey and Davis (2004).

Yoshinori Tange

Geodynamics Research Center, Ehime University

Email: tan@sci.ehime-u.ac.jp

References

[1] Y. Tange *et al.*: High Press. Res. **28** (2008) 245.
[2] Y. Tange *et al.*: J. Geophys. Res. **114** (2009a) B03208.
[3] *Y. Tange, Y. Kuwayama, T. Irifune, K. Funakoshi and Y. Ohishi: J. Geophys. Res.* ***117*** *(2012) B06201.*
[4] T. Irifune *et al.*: Science **327** (2009) 193.
[5] Y. Tange *et al.*: J. Geophys. Res. **114** (2009b) B02214.

Lattice thermal conductivity of $MgSiO_3$ perovskite and post-perovskite at the core-mantle boundary

Heat in the Earth's interior is transported dominantly by convection in the mantle and core, and by conduction at thermal boundary layers. The thermal conductivity of the bottom thermal boundary layer of the mantle determines the magnitude of heat flux from the core, and is intimately related to the instability of the boundary layer and the formation of mantle plumes, the thermal evolution of both the mantle and the core, and driving force for generation of the geomagnetic field [1]. Core heat loss can be estimated quantitatively from the temperature gradient in the boundary layer and the thermal conductivity of the lowermost mantle. However, the thermal conductivity has been poorly constrained at high pressure. The lattice thermal conductivity and related thermal diffusivity of $MgSiO_3$ perovskite (Pv), a primary mineral in the Earth's lower mantle, have only been measured at 1 bar and 26 GPa [2,3]. Its pressure dependence therefore remains uncertain. The value of $MgSiO_3$ post-perovskite (PPv), a high-pressure polymorph of $MgSiO_3$ Pv, has only been speculated. Previous estimates of the lower mantle thermal conductivity range widely between 5 and 30 W/m/K, with a typical value being 10 W/m/K [1,4].

In this study [5], we determined the lattice thermal conductivity of $MgSiO_3$ Pv and PPv over the entire lower mantle pressure range of up to 144 GPa and at room temperature by means of a newly developed pulsed light heating thermoreflectance technique in a diamond-anvil cell (DAC) (Fig. 1(a)). We used polycrystalline $MgSiO_3$ Pv as a sample, which was synthesized in a multi-anvil apparatus prior to the thermal diffusivity measurements. Since complete transformation from Pv to PPv was found to be difficult when using Pv as the starting material, we also used $MgSiO_3$ gel as the starting material for the measurements of PPv. The sample plate was coated with sputtered platinum (Pt) film on both sides for laser heating and thermoreflectance measurement. It was loaded into a hole in a rhenium gasket, together with NaCl layers that served as both a pressure medium and thermal insulator (Fig. 1(a)). Before each thermoreflectance measurement, the sample was annealed by heating with a multi-mode Nd:YAG laser or two 100 W single-mode Yb fiber lasers to ~1800 K, except below 22 GPa. PPv was synthesized directly from the gel starting material by heating with the fiber lasers to 2000 K for 60 min. The high-intensity monochromatic X-ray beam at beamline **BL10XU** enabled us to obtain high-resolution X-ray diffraction (XRD) patterns from the sample, in which we could observe sharp XRD peaks from $MgSiO_3$ Pv or PPv (Fig. 1(b) for example).

After phase identification by synchrotron XRD measurements, the lattice thermal diffusivities of both Pv and PPv were measured in a DAC by the thermoreflectance technique. A 50–100 μm area of the Pt film was heated from one side by a pulsed Nd:YAG laser with a pulse duration of 2 ns. The applied heat was conducted through the sample to the Pt film on the opposite side. The temperature rise after pulse heating was monitored as a change in reflectivity of the Pt film (Fig. 1(c)). The reflectivity was probed using a linearly polarized continuous-wave diode laser (782 nm in wavelength). The obtained transient

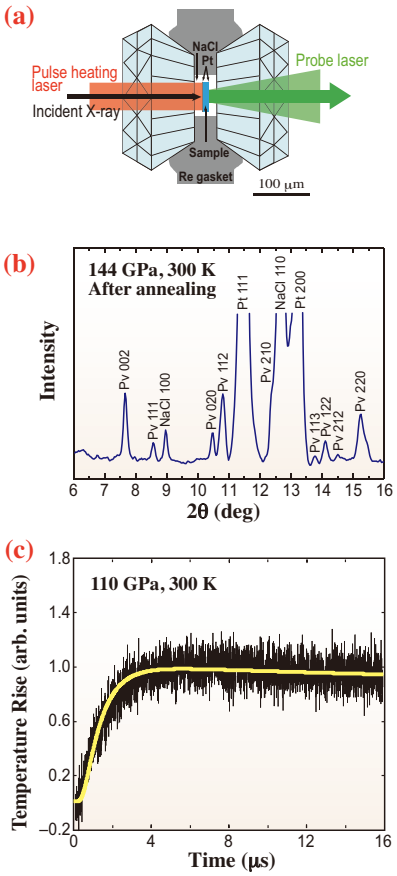

Fig. 1. **(a)** Schematic drawing of sample configuration. A monochromatic incident X-ray beam was collimated to about a 6 μm area on the sample (black arrow). Angle-dispersive XRD spectra were collected on a CCD detector at BL10XU before the thermoreflectance measurements. After pulse laser heating of Pt film on one side (red), the heat was transported by conduction through the sample to the Pt film on the other side. This heat diffusion time was determined from the change in reflectivity of the latter Pt film, which was monitored using a continuous-wave laser (green). **(b)** Representative XRD pattern of $MgSiO_3$ Pv at 144 GPa and 300 K after thermal annealing. **(c)** Transient temperature curves for $MgSiO_3$ Pv at 110 GPa and room temperature. Yellow curve shows fitted result.

temperature curves, such as that in Fig. 1(c), were analyzed considering one-dimensional heat diffusion to determine the heat diffusion time of the sample (see [5] for details). The thickness of both the sample and the Pt foils at high pressure was estimated after the thermoreflectance measurement. We determined the thermal diffusivity of Pv and PPv at high pressures from the heat diffusion time and the sample thickness obtained in this study, and then calculated the lattice thermal conductivity of Pv and PPv at high pressures as the product of their thermal diffusivity, density, and heat capacity at constant pressure.

We conducted ten separate experiments to measure the lattice thermal diffusivities of $MgSiO_3$ Pv from 11 to 144 GPa at room temperature. As plotted in Fig. 2, the thermal diffusivity of Pv varied with increasing pressure; it increased from 2.5 ± 0.2 mm^2/s at 11 GPa to 11.6 ± 2.5 mm^2/s at 144 GPa. In addition, we measured the lattice thermal diffusivities of $MgSiO_3$ PPv at 135 and 141 GPa at room temperature. The diffusivities of PPv at 135 and 141 GPa were 19.0 ± 4.4 mm^2/s and 20.0 ± 4.6 mm^2/s, respectively, which were 72% greater than those of Pv at equivalent pressures (Fig. 2). The calculated conductivities of Pv and PPv were 9.0 ± 1.6 and 16.8 ± 3.7 W/m/K, respectively, at 135 GPa and 3700 K, which corresponds to the proposed condition at the core–mantle boundary (CMB) (Fig. 3(a)). We also computed the bulk lattice thermal conductivity of an 80 vol% $MgSiO_3$ Pv and 20 vol% MgO periclase (Pe) mixture using the recent results for Pe [3] (Fig. 3(b)). Our results yielded a Pv-dominant lowermost mantle conductivity of about 11 W/m/K, which is comparable to the conventionally assumed value of 10 W/m/K. We also found that PPv-bearing rock exhibits 60% higher conductivity than Pv-dominant rock.

The bulk lower mantle thermal conductivity has been conventionally assumed to be about 10 W/m/K [4]. The lattice thermal conductivity of Pv+Pe rock (4:1 mixture for pyrolitic lower mantle) estimated above is consistent with this value, and therefore, our findings do not indicate any significant increase or decrease relative to previously employed values. Because all previous calculations of heat flow for the PPv double crossing assumed a lowermost mantle conductivity of 10 W/m/K, compatible with the value for Pv obtained in this study, the present findings do not significantly alter the magnitude of CMB heat flow implied by this model. Indeed, the present results support the notion of high CMB heat flow (46.6 TW) along with a high degree of secular core cooling, and are in accord with the idea of an extensively molten lowermost mantle in Earth's distant past [1].

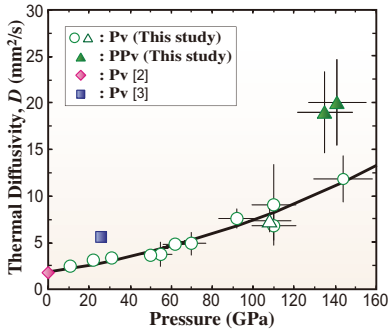

Fig. 2. Lattice thermal diffusivity (D) of $MgSiO_3$ Pv and PPv at high pressure and 300 K. Circles: Pv (samples synthesized in a multi-anvil apparatus, this study); open triangle: Pv at 108 GPa (sample synthesized from gel starting material in a DAC, this study); diamond: Pv at 1 bar [2]; squares: Pv at 26 GPa [3]; filled triangles: PPv (this study).

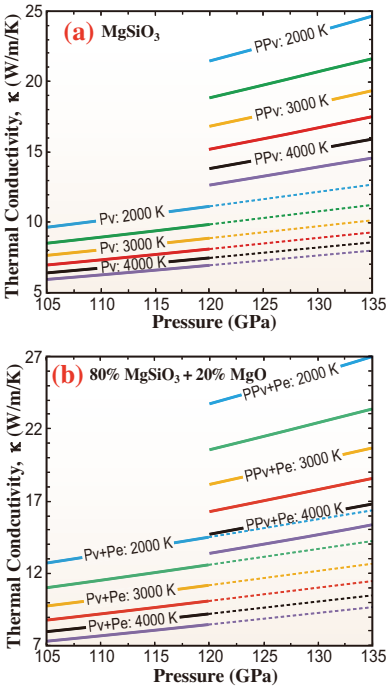

Fig. 3. Lattice thermal conductivity (κ) of deep lower mantle. 4:1 mixture of $MgSiO_3$ Pv/PPv and Pe [3]. Isotherms are at 500 K intervals between 2000 and 4500 K. The uncertainty of present estimates is about 20%.

Kenji Ohta

Center for Quantum Science and Technology
under Extreme Conditions, Osaka University

Email: ohta@hpr.cqst.osaka-u.ac.jp

References

[1] T. Lay *et al.*: Nature Geosci. **1** (2008) 25.
[2] M. Osako and E. Ito: Geophys. Res. Lett. **18** (1991) 239.
[3] G. Manthilake *et al.*: Proc. Natl. Acad. Sci. **108** (2011) 17901.
[4] F. Stacey: in Physics of the Earth, 3rd ed. Brookfield, Brisbane, Australia (1992).
[5] *K. Ohta, T. Yagi, N. Taketoshi, K. Hirose, T. Komabayashi, T. Baba, Y. Ohishi, J. Hernlund: Earth Planet. Sci. Lett.* ***349-350*** *(2012) 109.*

Environmental

SCIENCE

In environmental science, research targets are often in very small, dilute and amorphous forms. Thus, SR-based XRF and XAFS methods are used frequently for clarifying the distribution and/or chemical state of elements in the environmental samples. Recently, the research quality in this field has improved in conjunction with the development of the measurement techniques described below. First, combined methods of micro-SR technique and the other microscopic techniques conducted for the same field of view in the sample have been developed to yield information about the sample state directly related to its chemical state with high spatial resolution. Second, the performance of the micro-SR methods has been improved in various points, such as spatial resolution, measurement energy region, and measurement time. In particular, the newly installed Kirkpatrick-Baez focusing mirror system in BL37XU and BL39XU improved the spatial resolution of scanning microscopic XRF/XAFS imaging from 800 nm to 100 nm. Third, an XAFS measurement system in the soft X-ray region, including a scanning microscopy system, was installed at BL25SU. New findings obtained with these measurement systems are expected to be published in the near future. Finally, the XAFS measurement system has been upgraded to realize high-quality XAFS spectra, which makes it possible to perform the chemical state analysis more accurately by comparison of EXAFS, profiles in addition to conventional XANES analysis.

In the first study, Mitsunobu *et al*. developed a novel combined method of micro-XAFS and fluorescence in situ hybridization, and successfully characterized biominerals associated with a targeted microbe.

In the second study, Yamaguchi *et al*. measured, in rice, the distribution of cadmium, zinc and manganese using micro-XRF and that of sulfur using an electron probe microanalyzer. They found that the transport of these elements was controlled by the functional interconnection of vascular bundles in the rice node.

The third study concerns lead in contaminated shooting-range soils. Hashimoto *et al*. revealed the immobilization mechanism of lead from ammunition shells by chemical speciation of soil lead using XAFS.

In the fourth study, Takahashi revealed the solubility change of iron in Asian dust in seawater during transport from China to Japan by characterizing iron species using XAFS, and discussed that this change affects the global environment through growth of phytoplankton in the sea.

Tomoya Uruga

"Sakura"- *Cherry blossom*

New method of observing *in situ* microbe-metal-mineral interaction by μ-XAFS-FISH technique

Microorganisms in the environment critically impact global geochemical cycles and redox reactions of various elements. Many geochemical important redox reactions are largely associated with microbial activity and are energy sources for microorganisms. In addition, microbes can mediate mineral formation by a process called biomineralization. For instance, recent studies suggest a significant relationship between Fe(II)-oxidizing bacteria and ancient banded iron formation (BIF), one of the large geochemical events in Earth's history [1]. Biominerals have unique morphologies and characteristics such as nanoparticles, high surface area, and reactivity. The biominerals could be important sorbents for a range of metals and often play a critical role as natural catalysts in oxidation-reduction reactions for the metals [2].

The general ecological importance of environmental microbial reaction and biomineralization has been well recognized; however, the specific factors of the reactions in the environments, such as the reaction rate, spatial dynamics, and controlling factors, are poorly understood, even in sediments and soils. For example, in sediments and soils, which have heterogeneous components (e.g., water, organic materials, microorganisms, and primary and authigenic minerals), the local chemical profiles (e.g., pH and abundance of oxygen and nutrients) drastically change at the micrometer scale. Depending on such profiles, microbial reactions and habitability vary locally and form a complex geochemical network in the environments. Hence, it is necessary to develop new analytical techniques that allow the simultaneous determination of both microbial community composition and elemental characteristics in high spatial resolutions, in order to understand the linkage between microbial activity/reaction and biomineralization.

Here, we directly coupled a synchrotron microprobe analysis (μ-XAFS) and an *in situ* phylogenetic analysis, fluorescence *in situ* hybridization (FISH), to determine simultaneously the chemical species and distributions of microbial groups at the micrometer scale (Fig. 1). Coupling of μ-XAFS and FISH provides more direct information on the identity and localization of microbially catalyzed redox processes and the associated minerals, which leads to a better understanding of the role of microorganisms in the geochemical cycling of elements. In this study, we applied the "μ-XAFS-FISH" technique to one of the most ubiquitous and important environmental biomineralizations, Fe(III) mineral deposition by Fe(II)-oxidizing microbes.

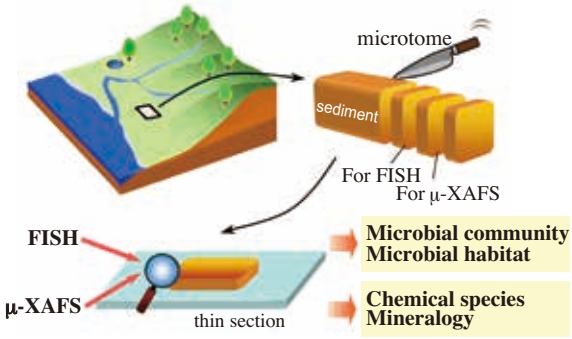

Fig. 1. Schematic figure showing coupled XAFS-FISH technique.

Natural Fe(III) oxyhydroxide mats were collected near the Sambe hot spring in Shimane Pref., Japan. Orange Fe microbial mats cover the floor of the spring flow path, which extend to tens of meters from the spring site (Figs. 2(a) and 2(b)). For μ-XAFS and FISH analyses, we prepared a thin section of the Fe mat sample. Fe *K*-edge μ-XRF-XAFS experiments were performed at **BL37XU** at SPring-8 and at BL4A at KEK-PF. The incident beam was monochromatized with a Si(111) double-crystal monochromator and focused to 0.9 (V) μm × 1.3 (H) μm.

The 16S rRNA gene phylogenetic analysis indicated that neutrophilic chemolithotrophic Gallionella-related bacteria of Betaproteobacteria was involved in the biogenically mediated oxidation of Fe(II) in the Sambe mats. First, we attempted to visualize the potential Fe(II) oxidizers in thin-sectioned mats by the FISH technique using a specific probe for Betaproteobacteria. Bright-field and FISH images obtained with a Betaproteobacteria probe for thin sections are given in Figs. 2(c) and 2(d), respectively. The FISH analysis of the Fe mat thin section showed the localization of Betaproteobacteria (presumably related to *Gallionella* and involved in Fe oxidation) in the upper 10–15 μm of the mat. Assuming that *Gallionella* was involved in Fe oxidation in this layer, we would expect that larger amounts of biogenic Fe oxides should also be found in this layer owing to microbial activity. Furthermore, we expected that the Fe oxides would carry a biogenic signature, as has been previously observed in the stalks produced by Fe(II)-oxidizing bacteria [3]. To address these hypotheses, we characterized the Fe chemical speciation and mineralogy in the mat by Fe μ-EXAFS with high spatial resolutions.

Fe k^3-weighted EXAFS spectra of reference materials, Sambe spots 1–3, and bulk mats are given in Fig. 3(b). The spectral features of spots 1–3

and the bulk sample were more similar to those of ferrihydrite than to those of goethite or lepidocrocite, which indicates that the Fe mats are mainly composed of short-ordered Fe(III) (oxyhydr)oxides, such as ferrihydrite. However, a small peak at $k = 7.0-7.5$ Å^{-1} was observed in ferrihydrite, the Sambe bulk sample, and spot 3 (dotted line box in Fig. 3(b)), whereas this peak was not found in spots 1 and 2 of the Fe mats. This implies that the coordination environment for Fe-Fe linkages in spots 1 and 2 (*Gallionella*-accumulating parts) was different from the others, because the observed small peak is dominantly derived from the Fe-Fe coordination in the Fe(III) (oxyhydr)oxides. EXAFS simulation analysis indicated that Fe(III) oxyhydroxides in spot 1 (*Gallionella*-accumulating part) are dominantly composed of edge-sharing linkages of Fe-O_6 octahedra [4], showing the Fe(III) oxyhydroxides with secondary structures.

In the present study, we developed a novel method using μ-XAFS combined with FISH to determine directly the microbial communities and chemical speciation of elements with high spatial resolutions (1–5 μm), and applied it to bacteriogenic Fe deposition. Our novel approach has many merits for investigating the relationship between microbes and chemical species: (i) simultaneous analysis by FISH and μ-XAFS allows us to characterize directly the biomineral associated with a targeted microbe, while most of the previous studies lack *in situ* phylogenetic information on a specific microbe; (ii) nondestructive analytical techniques, such as μ-XAFS with high sensitivity, elemental specificity, and spatial resolution, are useful in tracing various biogenic reactions in natural environments and characterizing resultant biominerals; and (iii) both FISH and μ-XAFS are cultivation-independent methods. These advantages enable us to obtain direct information on a specific biogenic reaction mediated by its target microorganism in environmental samples by the μ-XAFS-FISH technique.

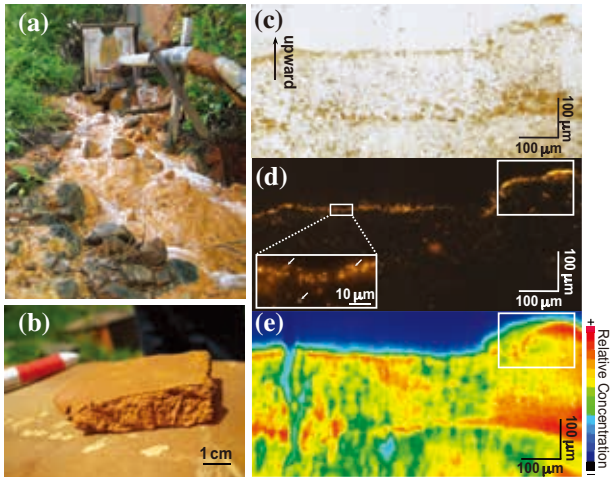

Fig. 2. **(a, b)** Photographs of sampling location and collected Fe mats at Sambe hot spring, respectively. **(c)** Bright-field image of thin-sectioned Sambe Fe mat. **(d)** FISH image of the same field stained by *Gallionella*-specific FISH probe and the magnification of high population area. Arrows in the magnified image stand for rod-shaped cells typical of *Gallionella* relatives. **(e)** Fe concentration map of the same field collected by μ-XRF. White-line boxes in (d) and (e) show the area analyzed by μ-XAFS in Fig. 3

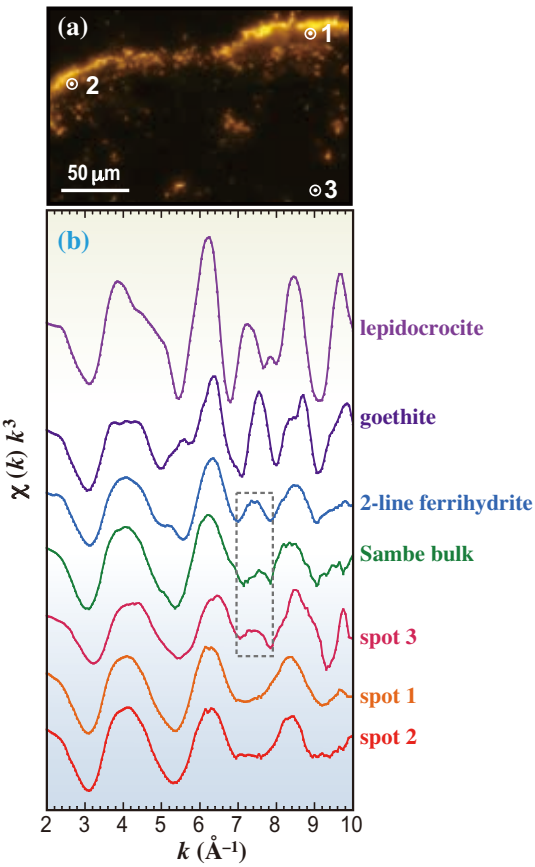

Fig. 3. **(a)** FISH image of area analyzed by Fe μ-XAFS. White circles in the image (spots 1–3) indicate points of interest in Fe μ-XAFS measurements. **(b)** Micro- and bulk-Fe *K*-edge EXAFS spectra of the points in Sambe thin section, bulk sample, and reference materials (lepidocrocite, goethite, and 2-line ferrihydrite).

Satoshi Mitsunobu[a,*] and Fumito Shiraishi[b]

[a] Institute for Environmental Sciences, University of Shizuoka
[b] Department of Science, Hiroshima University

*Email: mitunobu@u-shizuoka-ken.ac.jp

References

[1] A. Kappler *et al.*: Geology **33** (2005) 865.
[2] W. Stumm and J.J. Morgan: Aquatic Chemistry, John Wiley & Sons: New York, (1996).
[3] C.S. Chan *et al.*: ISME J. **5** (2011) 717.
[4] *S. Mitsunobu, F. Shiraishi, H. Makita, B. N. Orcutt, S. Kikuchi, B. B. Jorgensen, Y. Takahashi: Environ. Sci. Technol.* ***46*** *(2012) 3304.*

Role of node in controlling traffic of cadmium, zinc and manganese toward rice grains

Chronic intake of cadmium (Cd) causes human health problems, such as renal dysfunction. Approximately half of Cd intake is attributed to rice consumption for typical Japanese. To reduce health risk caused by Cd intake, it is effective to develop a strategy to reduce Cd concentration in rice grains. For this purpose, it is necessary to understand the mechanism governing the transport of Cd to rice grains.

In rice plants, elements absorbed from the roots through the transpiration stream are redirected in the nodes, where vascular bundles linked with the roots, leaves, and panicles are interconnected (Fig. 1) [1]. Vascular bundles toward the flag leaf that become enlarged and elliptical when they reach the nodes are named enlarged vascular bundles (EVBs). The xylem parenchyma between the EVBs and diffuse vascular bundles (DVBs) serves as a bridge for the horizontal intervascular transfer of metals and is referred to as the parenchyma cell bridge (PCB). Metals transferred to the DVBs move toward the panicles (Chonan, 1993). The intervascular transfer of metals in the nodes is an important pathway for the redirection of metals from the xylem through the transpiration stream to the panicles. In this complex pathway that redirects elements from the roots to the flag leaf or panicles, toxic and essential elements are differentiated.

Metals accumulate in a particular part of a tissue when they are left behind by the flow because of the lack of a mechanism for transporting them into the adjacent cells. In addition to poor transport, storage and sequestration processes also cause metal accumulation. In this study, we compared the distribution of Cd around the vascular bundles in a rice node and those of zinc (Zn) and manganese (Mn), in order to determine where these elements were differentiated [2].

A rice plant (*Oryza sativa* cv. Koshihikari) was grown in a greenhouse and one week after heading, a node beneath a panicle was sampled and immediately frozen in hexane cooled by dry ice. 50-μm-thick cross sections were prepared by using a cryomicrotome (CM1850, Leica, Wetzlar, Germany) and then freeze-dried. By using a synchrotron micro-X-ray fluorescence spectrometer equipped with a recently developed mirror system that allows higher-brilliance microfocusing at beamline **BL37XU** [3], Cd, Zn, and Mn were detected simultaneously to determine the tissues in which they were accumulated in the node cross sections. The distribution of sulfur (S) was determined with an electron probe microanalyzer (EPMA; JXA-8500F, JEOL, Tokyo). Cd *K*-edge microfocused X-ray absorption near-edge structures (μ-XANES) were obtained at the Cd-accumulated points in the EVB.

Different distribution patterns of Cd, Zn and Mn in node I were observed, as shown in Fig. 2. Cd and S were accumulated in the xylem of the EVB, whereas Zn was localized in the PCB between the EVB and the DVB. Mn was localized around the protoxylem of the EVB. The Cd:Zn ratio was higher in the EVB and DVB, indicating that Cd flow was slower than Zn flow in these vascular bundles. The XANES analyses indicated that Cd was coordinated by S, probably in a form bound to a S-containing ligand.

Figure 3 illustrates the transport pathway of

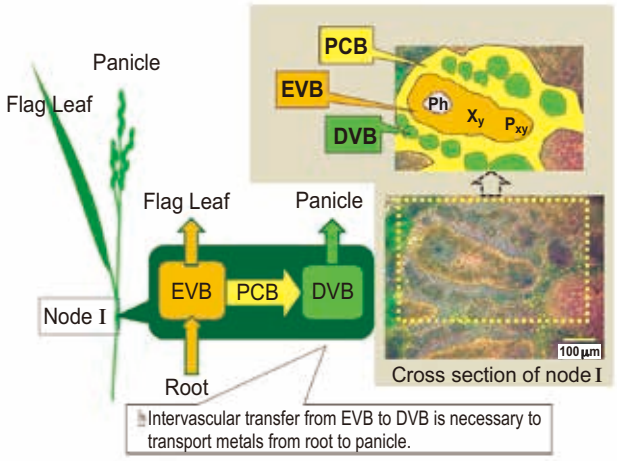

Fig.1. Interconnection of vascular bundles in node I. EVB: enlarged vascular bundle, PCB: parenchyma cell bridge, DVB: diffuse vascular bundle, Xy: xylem, Ph; phloem, Pxy; protoxylem.

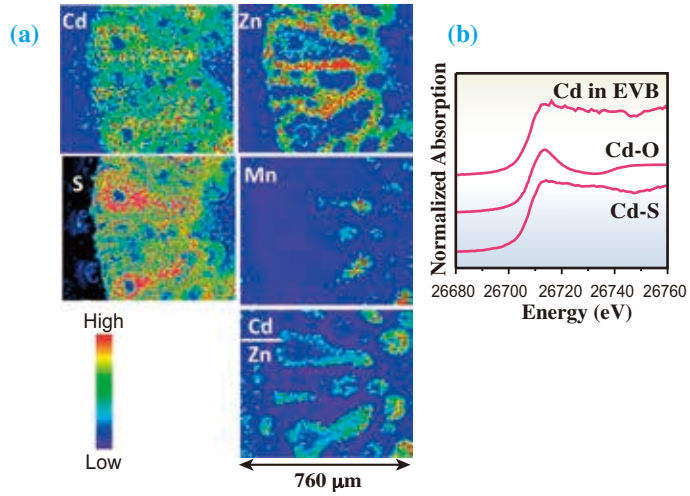

Fig. 2. **(a)** Distributions of cadmium, zinc, manganese, sulfur and cadmium-to-zinc ratio on the cross section of node I. **(b)** Cd *K*-edge μ-XANES spectra of reference materials (CdO and CdS) and Cd that accumulated in the xylem of enlarged vascular bundle.

Cd, Zn and Mn in node I. The accumulation of Mn in node I was minimal because the redirection of Mn in the node was not affected by any retardation processes, such as sequestration and insufficient transfer from cells of certain tissues to adjacent ones. Mn was observed to be preferentially transported toward the flag leaf. The restricted flow of Cd and Zn resulted in their accumulation in node I, indicating that the node redirected Cd and Zn. Cd and Zn were clearly discriminated in the node by the regulation of Cd transport, which is nonessential. Vascular or cytoplasmic sequestration with the S-containing ligand is known as an important mechanism for Cd detoxication [4,5]. The Cd in the xylem of the EVB might have been sequestrated in a vacuole in a S-containing ligand-bound form. Zn accumulation in the PCB may contribute to the maintenance of a relatively constant Zn concentration for transport to the grains. Once stored in the PCB, Zn is preferentially transported to panicles through the DVB, compared with Cd.

Our results show the first evidence indicating that the transport of Cd, Zn and Mn is controlled by the functional interconnection of vascular bundles in the rice nodes. Understanding the mechanisms governing Cd transport to rice grains is important for engineering rice cultivars with a reduced Cd concentration in the grains.

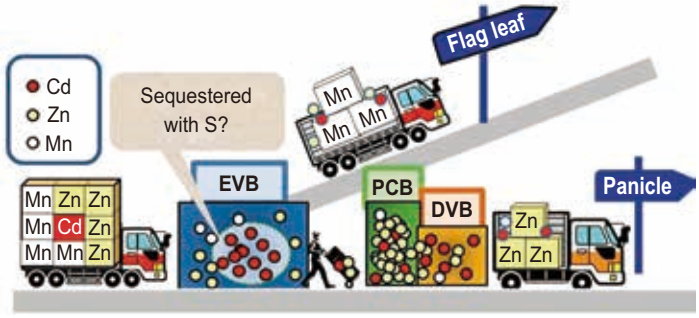

Fig. 3. Metal trafficking in node I.

Noriko Yamaguchi[a,*], Satoru Ishikawa[a], Yasuko Terada[b]

[a] National Institute for Agro-environmental Science
[b] SPring-8/JASRI

*Email: nyamag@affrc.go.jp

References

[1] N. Chonan: Science of the rice plant: Morphology, (1993) Nobunkyo,187.
[2] *N. Yamaguchi, S. Ishikawa, T. Abe, K. Baba, T. Arao, Y. Terada: J. Exp. Bot.* ***63*** *(2012) 2729.*
[3] Y. Terada *et al.*: Nucl. Instrum. Meth. A **616** (2010) 270.
[4] H. Miyadate *et al.*: New Phytol. **189** (2011) 190.
[5] D. Ueno *et al.*: Proc. Natl. Acad. Sci. USA **107** (2010) 16500.

Chemical speciation of Pb in contaminated soils: (Im)mobilization by plant root growth and chemical amendments

The environmental impact of soil contamination around shooting ranges is closely related to the chemical speciation of Pb in spent pellets. When a shot pellet has been released into the soil, the surface of the metallic Pb is gradually oxidized to PbO and subsequently transformed into carbonate phases (e.g., $PbCO_3$). These species are thermodynamically labile and have been recognized as a primary phase controlling Pb solubility in soils. In addition to these Pb species, recent investigations using synchrotron-based XAFS have revealed that Pb in shooting range soils is also present in association with organic matter and Fe/Mn (oxy)hydroxides [1]. These characterizations of soil Pb were achieved using synchrotron-based XAFS. In the next phase of our study, we have investigated how Pb solubility and speciation of shooting range soils were affected by plant root growth and chemical amendments [1,2]. Lead in contaminated shooting range soils (Japan and South Korea) and over 20 reference compounds were analyzed by Pb L_{III}-edge EXAFS spectroscopy at beamline **BL01B1** in transmission and fluorescent modes.

Plant roots can alter metal solubility via rhizosphere processes that physically and biochemically modify the properties of the soil at root interfaces. The rhizosphere processes are derived from root exudates containing protons and various organic acids, and such chemicals induce metal (mineral) dissolution in soils. To examine the effect of root growth on the dissolution of Pb pellets, plants were grown in a soil amended with Pb pellets for 100 days, and then acid-extractable Pb concentrations were measured. Figure 1(a) illustrates how the growth of roots induces the dissolution of Pb from pellets to soils. The average extractable Pb concentration in the pH 4.5 soil was about 13-fold greater in rhizosphere (with root growth) than in bulk (without root growth) treatments (Fig.1 (a)). Compared with the acid soil, the acid-extractable Pb concentration was decreased in the alkaline soil (pH 7.5), although Pb dissolution from pellets still occurred more in the rhizosphere than in the bulk soils.

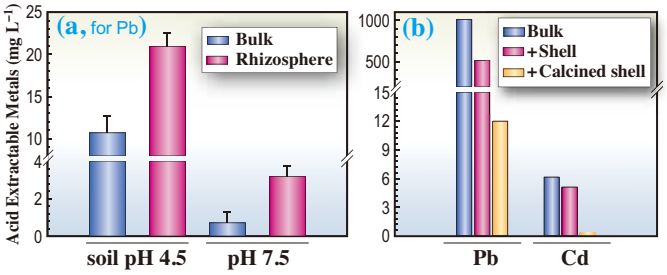

Fig. 1. Acid extractable metals from contaminated bulk and rhizosphere (plant grown) soils **(a)** and from contaminated soil with non-calcined and calcined shell additions **(b)**.

To assess the effect of root growth on Pb speciation, buckwheat and grass were grown in a Japanese shooting range soil, and their Pb L_{III}-edge EXAFS spectra were simply compared (Fig. 2(a)). Compared with the bulk soil, the growth of buckwheat and grass modified the fine structure in EXAFS spectra. Also, the EXAFS spectra of buckwheat and grass soils were different in fine structure. These results indicate that (i) transformations of preexisting soil Pb species were induced by plant root growth, and (ii) such transformations depended on plant species. The linear-combination fitting (LCF) procedure with known Pb references revealed that Pb in the bulk soil existed in the form of $PbCO_3$ (37%), and Pb sorbed on ferrihydrite (Pb-Fe, 36%) and on organic matter (Pborg, 15%) (Fig. 2(a)). The predominance of these Pb species could be supported by soil chemical constraints, including the abundance of Fe hydroxides, organic matter and carbonate minerals. The buckwheat-grown soil had more Pb-Fe (51%) and less $PbCO_3$ (25%) than the bulk soil. These notable modifications of Pb species occurred owing to the acidification of buckwheat rhizosphere soil whose pH value was significantly lower than that of the bulk soil. Compared with the buckwheat soil, the grass-grown soil had a subtle difference in the proportion of each Pb species, although their EXAFS spectra were notably different in fine structure. This result suggests that a subtle difference in the relative abundance of metal species may not be determined by using the LCF procedure.

There have been several investigations regarding remediation studies of Pb-contaminated shooting range soil, with the main emphasis being on immobilization technologies. The mechanism of immobilization is based on the formation of inert and highly insoluble species of metals using soil amendments. We have studied several types of natural waste materials, including egg and oyster shells, as metal immobilizing amendments, and demonstrated their effectiveness on reducing metal solubility [3]. According to X-ray diffraction results, the mineralogical structure of egg and oyster shells is basically $CaCO_3$ (Fig. 3). The structure of these shells can be altered to CaO by heating at high temperatures (calcination). The calcination process increases the pH and surface area of the material, which induces a much greater ability to immobilize metals in contaminated soils.

Figure 1(b) shows the acid extractable Pb and Cd from a contaminated soil amended with calcined and non-calcined shells, demonstrating a significant decrease in metal solubility with the addition of these amendments.

We performed XAFS spectroscopy to identify the Pb species were present in the soils with these amendments. Unlike a Japanese soil, Pb in the soil collected from a Korean shooting range was mainly present in association with kaolinite and humus (Fig. 2(b)). The Pb-EXAFS spectra obtained from the soils amended with calcined and non-calcined shells were visually different in structure, suggesting that Pb in these soils was immobilized in different forms. Although the exact Pb species were not identified, the EXAFS spectrum for the calcined-shell-amended soil was similar to that of $Pb(OH)_2$ and $PbSiO_3$, and it was clearly different from that for bulk and shell-amended soils. The association of Pb with Si was likely derived from the dissolution of (phyllo)silicate minerals under highly elevated soil pH conditions by the addition of calcined shells. The increases in soil pH and Ca concentration in the soil amended with calcined shells may enhance the formation of calcium silicate hydrate with Pb in its structure [4]. The association of Pb with Si and Ca are supported by the elemental distribution map illustrating the presence of these elements at the same position on the soil surface [2]. Owing to the large possible number of heavy metal species in soils, identifying at least the major species is a challenging task but critical in understanding the metal behavior in a certain environment.

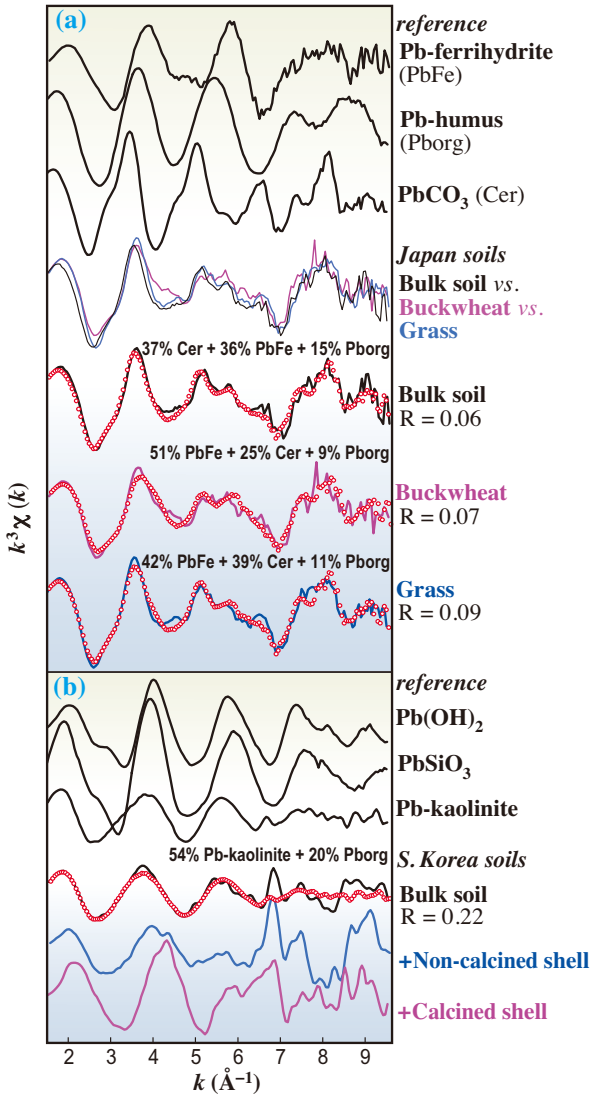

Fig. 2. L_{III}-edge Pb EXAFS spectra of selected references and contaminated shooting range soils grown with different plants **(a)** and amended with non-calcined and calcined shells **(b)**. Open circles indicate the best LCF spectra obtained using the Pb references.

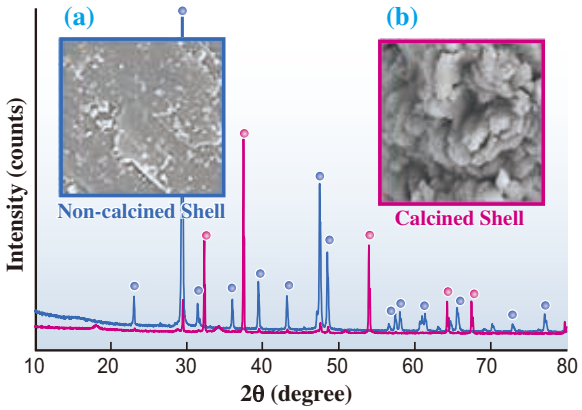

Fig. 3. XRD spectra of non-calcined and calcined oyster shells. Filled blue and magenta circles indicate $CaCO_3$ and CaO phases, respectively.

Yohey Hashimoto[a,*], Yong-Sik Ok[b] and Masaki Takaoka[c]

[a] Dept. of Bioapplications and Systems Engineering, Tokyo University of Agriculture and Technology
[b] Dept. of Biological Environment, Kangwon National University, Republic of Korea
[c] Dept. of Urban and Environmental Engineering, Kyoto University

*Email: yhashim@cc.tuat.ac.jp

References

[1] Y. Hashimoto, M. Takaoka, K. Shiota: J. Environ. Qual. **40** (2011) 696.
[2] *M. Ahmad, Y. Hashimoto, D.H. Moon, S.S. Lee, Y.S. Ok: J. Hazard. Mater.* ***209*** *(2012) 392.*
[3] Y.S. Ok *et al.*: Environ. Earth Sci. **61** (2010) 1301.
[4] R. Badreddine *et al.*: Environ. Sci. Technol. **38** (2004) 1383.

Changes in iron species and iron solubility in Asian dust during the long-range transport from western China to Japan

Iron (Fe) is an essential micronutrient and has been identified as a limiting factor for the growth of phytoplankton in high-nitrate low-chlorophyll (HNLC) regions of the ocean [1]. In the North Pacific, one of the HNLC regions, transport and deposition of mineral dust from Asia can be one of the major sources of Fe. In the atmosphere, Fe can be found and transported in various chemical forms, both water-soluble and water-insoluble. It is generally believed that the soluble fraction of Fe is mainly considered as bioavailable for phytoplankton in the open ocean [2].

The overall solubility of atmospherically transported Fe at seawater pH is estimated to be 0.8–2.1%. However, large uncertainties exist in the estimates of bioavailable Fe deposited from the atmosphere, owing to a wide Fe solubility range in seawater. Although it has been suggested that atmospheric processes can change the solubility of Fe as it moves from the source region on land to the deposition area in oceans, actual chemical processes affecting Fe species in the solid phase in mineral dust are not clear. For example, photoreductive processes, in-cloud processes, and uptake of secondary acids can increase the solubility and bioavailability of Fe in dust particles. However, a change in Fe species during long-range transport based on actual data on the Fe species has not been widely studied up to now, which must be performed because the bioavailability of Fe is affected by its solubility, which in turn depends on the chemical species of Fe contained in Asian dust.

To accurately assess the biogeochemical impact of the atmospheric input, therefore, an attempt was made in this study to identify the Fe species and quantify each species by synchrotron-based X-ray absorption fine structure (XAFS) spectroscopy, a powerful technique used to investigate chemical speciation in aerosol samples [3,4]. In addition, leaching experiments were conducted for natural Asian dust samples with complete information on Fe species contained in the dust, by which it was possible to show the relationship between Fe species and its solubility.

In this study, we focus on the speciation of Fe in mineral aerosols transported from Aksu (western China near Taklimakan Desert) to Qingdao (eastern China) and Tsukuba (Japan) [5]. By the fitting of the X-ray absorption near-edge structure (XANES; Fig. 1) and extended X-ray absorption fine structure (EXAFS; Fig. 2) measured in both fluorescence and electron yield modes at beamline **BL01B1**, it was revealed that Fe species changed from illite and chlorite (both are clay minerals frequently found at Earth's surface) originally contained in the dust in Aksu to illite and

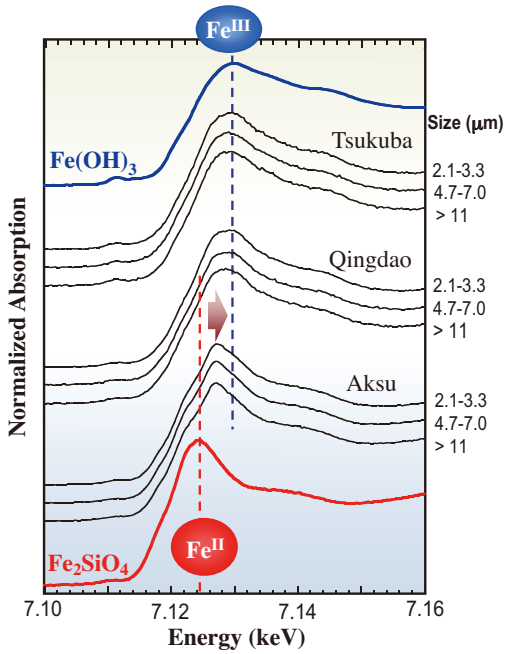

Fig. 1. XANES spectra of Fe in dust samples collected in Aksu (western China), Qingdao (eastern China), and Tsukuba (Japan) with reference materials Fe(II) and Fe(III). The shift in peak energy suggests the oxidation of iron during the long-range transport.

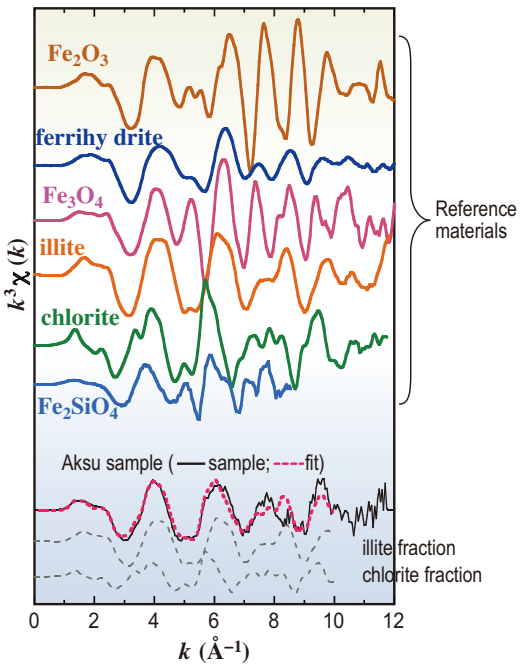

Fig. 2. Example of EXAFS fitting (k space) to estimate Fe species in dust sample collected at Aksu in western China.

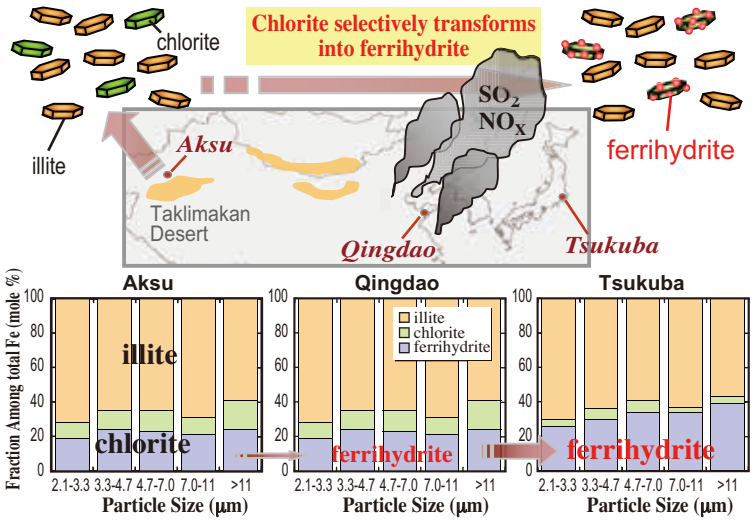

Fig. 3. Transformation of illite into ferrihydrite during the transport from western China to Japan.

ferrihydrite (amorphous iron hydroxides abundant at earth's surface) in Qingdao and Tsukuba (Figs. 1-3). The validity of the speciation determined by XANES and EXAFS was confirmed by X-ray diffraction and chemical extraction methods. The speciation showed that chlorite originally contained in the dust was selectively transformed into ferrihydrite during the long-range transport from Aksu to Qingdao and Tsukuba (Fig. 3). The high reactivity of chlorite compared with illite has been suggested in alteration experiments of the two minerals in mineralogical studies, which supports our results. Since the alteration of calcite to gypsum due to the reaction of calcite with sulfuric acid and also the enrichment of Pb in finer particles were found in Qingdao and Tsukuba for the same samples examined here [4], it is most likely that the transformation of chlorite to ferrihydrite is facilitated by anthropogenic effects (Fig. 3). Solubility experiments showed that Fe in ferrihydrite is more soluble than those in illite and chlorite. For natural samples, Fe in Tsukuba samples (main Fe host phases: illite and ferrihydrite) was more soluble than that in Aksu samples (illite and chlorite), as shown in Fig. 4. The results demonstrate that the transformation of chlorite to ferrihdyrite in aerosols during the long-range transport can increase the solubility of Fe in dust to seawater. In particular, it is strongly suggested that the dust passing through the highly populated and industrialized regions in eastern China has ample opportunity to be subject to the effects of pollutants, which can enhance the primary productivity and CO_2 uptake of the ocean, assuming that the anthropogenic emission of SO_2 and NO_X has some effects on Fe dissolution from mineral dust.

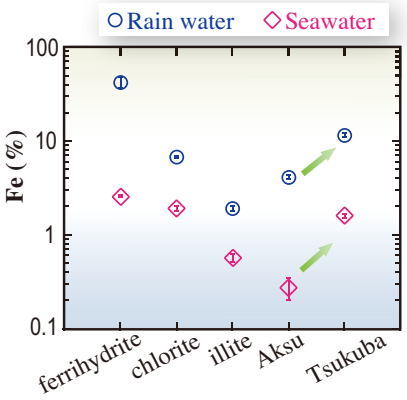

Fig. 4. Solubilities of Fe in simulated rainwater and seawater for standard minerals (illite, chlorite, and ferrihydrite) and aerosol samples collected in Aksu and Tsukuba.

Yoshio Takahashi

Department of Earth and Planetary Systems Sci., Hiroshima University

Email: ytakaha@hiroshima-u.ac.jp

References

[1] J.H. Martin and S. E. Fitzwater: Nature **331** (1988) 341.
[2] J.D. Jickells *et al.*: Science **308** (2005) 67.
[3] Y. Takahashi *et al.*: Environ. Sci. Technol. **40** (2006) 5052.
[4] Y. Takahashi *et al.*: Environ. Sci. Technol. **43** (2009) 6535.
[5] *Y. Takahashi, M. Higashi, T. Furukawa and S. Mitsunobu: Atmos. Chem. Phys.* ***11*** *(2011) 11237.*

Industrial

In 2011, seven contract beamlines for industrial application were in operation, and the total number of corporate users in all of SPring-8 decreased to 3088 from 3,471 in 2010. It is considered that the reason behind the 10% decrease in the number of corporate users is the influence of the Tohoku Earthquake that occurred on March 11, 2011. The issue on energy attracted much attention in the Japanese society after the earthquake, and companies struggled to develop technologies for energy generation, energy storage, energy saving, and energy control. Thus, the major topics of this issue are investigations on the storage, generation, and saving of energy.

In the present issue, six topics have been chosen to represent the works carried out in Industrial Applications. The first four topics are in the field of energy, and the other two topics are investigations on fibers. We selected these topics in XAFS, grazing-incidence X-ray diffraction, XMCD, X-ray topography, microbeam X-ray diffraction and FT-IR to introduce the diversity of industrial applications of SPring-8.

The first topic by Takamatsu is the application of total-reflection fluorescence XAFS at BL01B1 and BL37XU to investigate phenomena occurring at the interface between a $LiCoO_2$ electrode and an electrolyte solution of a Li-ion battery. In his experiment, incident X-rays impinged on the electrode interface at an angle smaller than the critical angle for total reflection, in order to extract the interfacial phenomena. He successfully observed the reduction of Co ions at the surface of the $LiCoO_2$ electrode with an organic electrolyte solution. This irreversible behavior, which was also observed at the surface of $LiCoO_2$ during the first charge/discharge process, may indicate the start of the deterioration of Li-ion batteries.

Applications

Recently, organic solar cells have been paid considerable attention since the easy and cheap production of flexible and large-area cells is expected. The crystallinity and crystalline orientation of organic thin films strongly influenced the performance of solar cells, as does the type of organic material itself. Drs. Osaka and Takimiya found that bulk-heterojunction solar cells composed of a novel semiconducting polymer based on naphthobisthiadiazole (PNTz4T) and [6,6]-phenyl C61-butyric acid methyl ester (PC61BM) have high power conversion efficiencies. Good crystallinity and the desired crystalline orientation of the blended thin film of PNTz4T and PC61BM were revealed by a grazing-incidence X-ray diffraction experiment at BL19B2.

The strongest permanent magnet in the NdFeB magnet widely used in motors and sensors. In particular, large numbers of NdFeB magnets are used in motors in both electric and hybrid electric vehicles. The third topic, investigating the texture of NdFeB magnets by XMCD, was performed at the contract beamline BL16XU established by electronics, steel, and automobile companies. Dr. Nambu and his colleagues found a clear relationship between magnetic moment and Nd concentration in simultaneously obtained Nd L_{II} XMCD and fluorescence yield data.

Silicon carbide (SiC) bipolar devices (e.g., IGBT and p-n diodes) are promising candidates for next-generation high-voltage power applications in various industrial, traffic, automobile, and power-transmission systems. The fourth topic concerns the application of X-ray microbeam three-dimensional topography at BL24XU to develop depth-resolved crystallographic analysis of SiC crystals.

The other two topics are investigations on fibers. Dr. Matsuba studied the shear-induced conformational fluctuations in polystyrene melts at BL43IR, since the final properties of polymer fibers strongly depend on the processing history, such as the external fields applied in extrusion or injection. Prof. Tashiro separately determined Young's modulus of skin and core parts of monofilaments in carbon fiber by microbeam X-ray diffraction at BL47XU and BL03XU. I am very happy for this opportunity to introduce the first research conducted at contract beamline BL03XU established by the Advanced Softmaterial Beamline Consortium.

Ichiro Hirosawa

"Ume"- *Plum blossom*

In situ total-reflection XAS study on $LiCoO_2$ electrode/electrolyte interface of lithium-ion batteries

Rechargeable lithium-ion batteries (LIBs) are widely used as electrical energy storage devices for technologies such as portable electronics and electric and hybrid vehicles, and they are considered to be promising power storage candidates for smart-grid electricity systems. Commercialized LIBs are composed of positive and negative electrodes separated by a liquid electrolyte containing dissociated salts, which enables lithium-ion transfer between the two electrodes. The hierarchical structure of LIBs extends over a wide scale, from greater than 1 mm to less than 1 nm, as schematically shown in Fig. 1(a). Traditionally, research in the field has focused on battery improvement through a choice of new or existing materials for the positive and negative electrodes, as the bulk properties of the electrodes primarily limit the charge capacity and power. However, the durability of LIBs is strongly dependent on side reactions that occur at the electrode/electrolyte interface, especially those at the positive electrode. Figure 1(b) shows the proposed interface structure scheme under battery operating conditions; that is, an electrical double layer in the liquid electrolyte and a space charge layer in the solid electrode form at the interface because of the potential difference between the electrode and electrolyte. The scale of this interfacial region is speculated to be on the order of a few nanometers, which shall be deemed as approximately the Debye length. This indicates that the structural and chemical information should be tracked with a resolution of a few nanometers or less to reveal the phenomena at the electrode/electrolyte interface. However, characterization of the electrode surface at the nanoscale level under battery operating conditions remains insufficient because of a lack of suitable observation techniques.

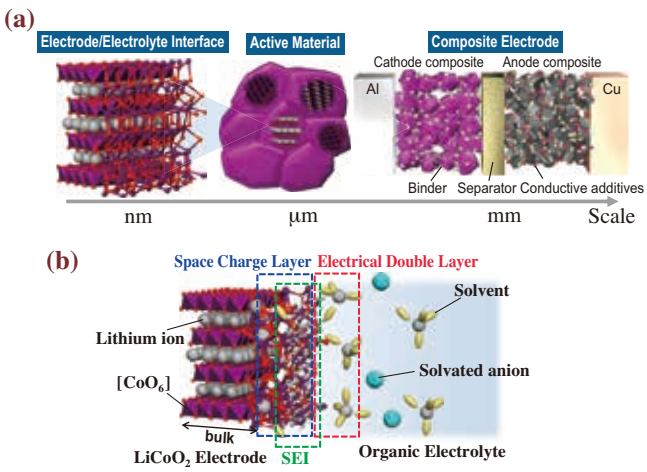

Fig. 1. **(a)** Schematic image of the hierarchical structure of LIBs and **(b)** proposed structure of the $LiCoO_2$ electrode/electrolyte nano-interface under battery operating conditions.

X-ray absorption spectroscopy (XAS) is a potent and versatile technique for resolving the chemical states of lithium-ion electrode materials independent of their crystallinity. To extract the interfacial phenomena by XAS, we applied total-reflection fluorescence XAS (TRF-XAS), which integrates the fluorescence-yield XAS spectra obtained under total-reflection conditions. We utilized polycrystalline $LiCoO_2$ thin films prepared by pulsed laser deposition (PLD) as the model electrodes; they are flat at the nanometric scale and have similar structural properties to the actual composite electrode. TRF-XAS measurements were performed at **BL01B1** and **BL37XU** using a solid-state detector. Co *K*-edge XAS spectra were obtained. An original spectro-electrochemical cell, composed of a $LiCoO_2$ film on a platinum (Pt) substrate as a working electrode (WE), lithium metal as a counter electrode (CE), 1 mol·dm^{-3} $LiClO_4$ in a 1:1 volumetric mixture of ethylene carbonate (EC) and diethyl carbonate (DEC) as the electrolyte, and a microporous membrane as a separator, was used for *in situ* measurement, whose schematic is illustrated in Fig. 2(a). The behavior at the top surface of the $LiCoO_2$ film and that in the bulk were comparatively studied while controlling the incident angle of the X-ray into the $LiCoO_2$ films. When the incident angle was set at 0.2° (a smaller angle than the total-reflection angle), the penetration depth was estimated to be ~3 nm (denoted as "Surface"). The bulk information was obtained by setting the incident angle at 2.2°; under this condition, the penetration depth was estimated to be greater than 50 nm (as the thickness of the $LiCoO_2$ film was *ca.* 50 nm, it was denoted as "Bulk"). Figure 2(b) shows the normalized Co *K*-edge XANES spectra obtained from the bulk and the surface before and after electrolyte soaking. The bulk XANES spectra were unchanged by electrolyte soaking. In contrast, the surface XANES spectra were significantly changed by electrolyte soaking. The energy level shifted toward a lower energy in the surface XANES spectra, which was attributable to the reduction of the Co ions at the top surface of the $LiCoO_2$ electrode in contact with the electrolyte solution. As the bulk XANES spectra were unchanged by electrolyte soaking, the reduction of the Co ions must have occurred within a depth of a few nanometers from the surface of the electrode.

Figure 3(a) shows the bulk and surface Co

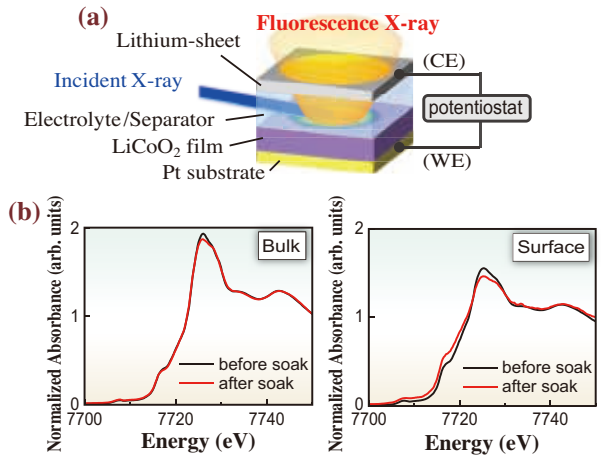

Fig. 2. **(a)** Schematic illustration of (two-electrode) spectroelectrochemical cell used for *in situ* TRF-XAS measurements. **(b)** Co *K*-edge TRF-XANES spectra of the bulk of $LiCoO_2$ film, and those at the surface before (black) and after (red) electrolyte soaking.

K-edge XANES spectra obtained at each state of charge under potential control conditions. The bulk XANES spectra shifted continuously toward higher (Co oxidation) and lower (Co reduction) energy levels as electrochemical charging and discharging proceeded, respectively. Figure 3(b) shows the absorption energy at the normalized intensity of 0.5 in the XANES spectra during the course of the electrochemical experiments. In the case of the bulk, the energy returns back to the original position after charge and discharge, suggesting that the $LiCoO_2$ bulk maintains its layered structure and shows good electrochemical reversibility. As the energy levels of the surface XANES spectra also changed during the charge/discharge processes, it is suggested that the surface Co species are still electrochemically active. However, the behavior at the surface is essentially irreversible, in contrast to the good reversibility in the bulk. It appears that the surface Co^{2+} species formed during the electrolyte soaking process are oxidized during the charging, but the reduction is insufficient. Figure 3(c) shows a scheme of the proposed deterioration mechanism that occurs at the electrode/electrolyte interface in LIBs. The Co ions (Co^{3+}) at the surface of $LiCoO_2$ are reduced to Co^{2+} by organic electrolyte soaking. The local structure is distorted when Co^{3+} reacts with the electrolyte and is reduced to Co^{2+}, and this distortion propagates during the consecutive charge/discharge processes. Accordingly, the initial deterioration that starts at the surface of $LiCoO_2$ on electrolyte immersion can lead to the loss of durability that occurs during longer time scales.

In conclusion, we have succeeded in direct observation of the electronic and local structures of the $LiCoO_2$ system and their changes at the electrode/electrolyte interface during charge/discharge processes. The Co ions are reduced at the surface of the $LiCoO_2$ electrode that is in contact with organic electrolyte solutions. Irreversible behavior was observed at the surface of $LiCoO_2$ during the first charge/discharge process. This Co reduction that occurs at the nano-interface of the electrode/electrolyte can be the initial deterioration that occurs in LIBs [1].

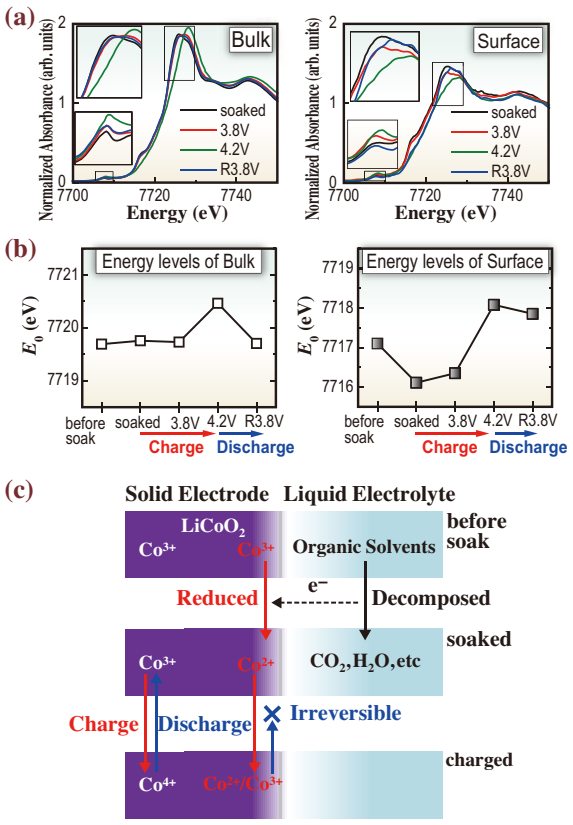

Fig. 3. **(a)** Co *K*-edge XANES spectra of the $LiCoO_2$ film measured at each state upon applying voltage and **(b)** corresponding measured absorption energy levels of the bulk and surface. **(c)** Schematic illustration of the proposed reaction of the initial degradation that occurs at the electrode/electrolyte nano-interface.

Daiko Takamatsu†

Office of Society-Academia Collaboration for Innovation, Kyoto University

Email: takamatsudik@rising.saci.kyoto-u.ac.jp

†Present address: Hitachi Research Laboratory, Hitachi, Ltd.

References

[1] *D. Takamatsu, Y. Koyama, Y. Orikasa, S. Mori, T. Nakatsutsumi, T. Hirano, H. Tanida, H. Arai, Y. Uchimoto and Z. Ogumi: Angew. Chem. Int. Ed.* ***51*** *(2012) 11597.*

Structure-property relationships of a semiconducting polymer based on naphthobisthiadiazole

There has been considerable attention focused on semiconducting polymers in the field of organic electronics because their solution processability, thermal stability, and mechanical properties are expected to lead to the realization of large-area, flexible next-generation devices [1]. Organic field-effect transistors and solar cells are of particular current interest in the field. Recent advances in the development of new materials, mostly small bandgap polymers with donor-acceptor systems, have brought about great improvements in device performances [2]. A key issue for the materials is to build a strong π–π stacking structure, which facilitates charge carrier transport through the π-orbital overlaps between the cofacially stacked polymer backbones. Thus, the choice of building unit to ensure strong π–π stacking is crucial for the development of high-performance polymers.

In this report, we present the structure-property relationships of a novel semiconducting polymer based on naphthobisthiadiazole (PNTz4T, Fig. 1) in comparison with those of an analogue polymer based on benzothiadiazole (PBTz4T, Fig. 1) [3]. Naphthobisthiadiazole (NTz) is a doubly benzothiadiazole (BTz)-fused heterocycle [4]. Since NTz is expected to be a more rigid π-extended ring than BTz, its incorporation into the polymer main chain should enhance the intermolecular interaction and thereby promote a strong π–π stacking structure due to the more coplanar and better arranged backbone structure than that of the BTz-analogue. In fact, the UV-vis absorption spectra of the polymer thin films show that PNTz4T gives a more defined structure, in which the absorption peak is more sharpened, than PBTz4T (Fig. 2). The red-shift of the absorption range for PNTz4T compared with that for PBTz4T should be due to the stronger electron-accepting nature of the NTz moiety than BTz, which would lower the level of the lowest occupied molecular orbital and thus the bandgap.

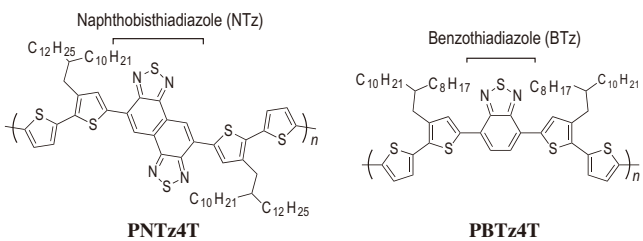

Fig. 1. Chemical structures of a naphthodithiophene-based semiconducting polymer (PNTz4T) and a benzothiadiazole-based analogue (PBTz4T).

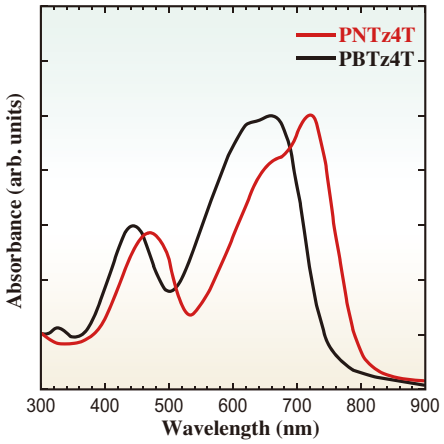

Fig. 2. UV-vis absorption spectra of PNTz4T and PBTz4T in thin films.

Transistor devices of the polymers are fabricated and evaluated using top-contact, bottom-gate devices using the polymer thin films spin-coated from o-dichlorobenzene (DCB) solutions, which are subsequently annealed at 200°C. Figure 3(a) depicts the typical current-voltage curves of the transistor devices based on PNTz4T and PBTz4T. Mobilities evaluated from the saturation regime for PNTz4T are as high as 0.6 cm^2/Vs and typically in the range of 0.2–0.4 cm^2/Vs with current on/off ratios of ~10^7. The mobility of PNTz4T is one order of magnitude higher than that of PBTz4T, typically 0.05 cm^2/Vs, indicating the high potential of the NTz core.

Bulk-heterojunction solar cells are fabricated by spin coating a solution of the polymer blended with [6,6]-phenyl C61-butyric acid methyl ester ($PC_{61}BM$) in DCB. Current density-voltage curves of the devices under one sun of simulated AM 1.5 G solar irradiation (100 mW/cm^2) are displayed in Fig. 3(b). While PBTz4T shows power conversion efficiencies (PCEs) of ~2.6% with a polymer to $PC_{61}BM$ weight ratio (p:n) of 1:1, in which the short circuit current (J_{SC}) is 5.6 mA/cm^2, the open-circuit voltage (V_{OC}) is 0.74 V, and the fill factor (FF) is 0.63, PNTz4T shows a maximum PCE of 6.3% with J_{SC} = 12.0 mA/cm^2, V_{OC} = 0.76 V, and FF = 0.69 at p:n = 1:1.5. The significantly higher J_{SC} for the devices with PNTz4T than for those with PBTz4T is likely to be partly a result of the wider absorption range of PNTz4T.

In order to further understand these higher performances of PNTz4T in transistors and solar cells, the ordering structures of the polymers are investigated by grazing incidence X-ray diffraction measurements with a two-dimensional detector. The diffraction images of the polymer-only films and polymer/$PC_{61}BM$

blend films are displayed in Fig. 4, where they reflect the ordering structures in the transistors and solar cells, respectively. In the polymer-only film of PNTz4T (Fig. 4(a)), diffractions assignable to the lamellar ($q_z \approx 0.25$ Å^{-1}) and π–π stacking structures ($q_{xy} \approx 1.7$ Å^{-1}) appear on the q_z and q_{xy} axes, respectively, indicating the predominant edge-on orientation, i.e., the polymer backbones are oriented vertically on the substrate surface [5]. In addition, the π–π stacking distance of PNTz4T is determined to be 3.5 Å, which is very narrow for semiconducting polymers and clearly explains the high mobilities of PNTz4T in transistors. In contrast, PBTz4T shows largely arcing diffraction corresponding to the lamellar structure, indicating that there is no preferential orientation (Fig. 4(b)). PBTz4T does not show clear diffraction corresponding to the π–π stacking structure, indicative of the much lesser crystalline nature of PBTz4T in the thin film. This large difference in the ordering structure between PNTz4T and PBTz4T is in good agreement with the fact that the transistor performances are quite distinct.

In the PNTz4T/$PC_{61}BM$ blend film, it is interesting that PNTz4T is mainly oriented in a face-on manner, i.e., the polymer backbones lie on the substrate, as the diffraction corresponding to the π–π stacking appears on the q_z axis (Fig. 4(c)). It should also be noted that PNTz4T still has the narrow π–π stacking distance of 3.5 Å in the blend film. Meanwhile, PBTz4T results in much lower crystallinity in the blend film, where there is no π–π stacking diffraction. The predominant face-on orientation and the preserved narrow d_P of PNTz4T in the blend film should allow efficient charge transport in the cells, where the films are sandwiched between the electrode, which could be one of the main reasons why PNTz4T shows a high PCE exceeding 6% and greater performances than PBTz4T.

In summary, the structure-property relationships of a novel semiconducting polymer based on NTz are presented. A striking structural feature of the polymer is the strong π–π stacking structure with a narrow distance of 3.5 Å, most likely owing to its π-extended rigid structure, allowing better arrangement of the main chain and the side chain. In addition, the polymer spontaneously orients in the desired directions for transistors and solar cells in the corresponding films. These results are in good agreement with high mobilities and high photovoltaic properties of PNTz4T.

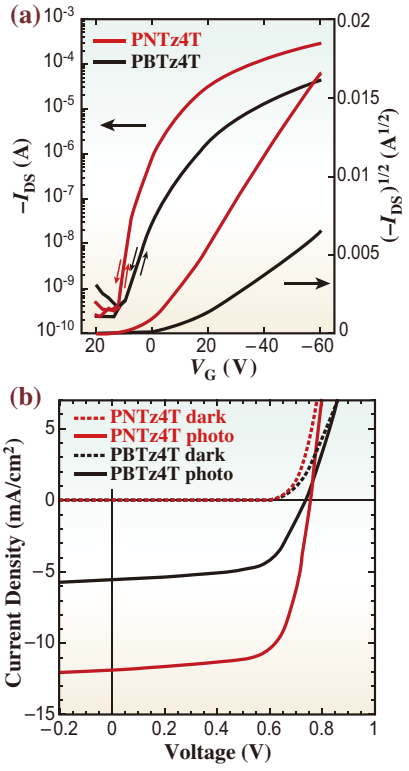

Fig. 3. Current-voltage curves of the transistor devices **(a)** and solar cells **(b)** using the polymers.

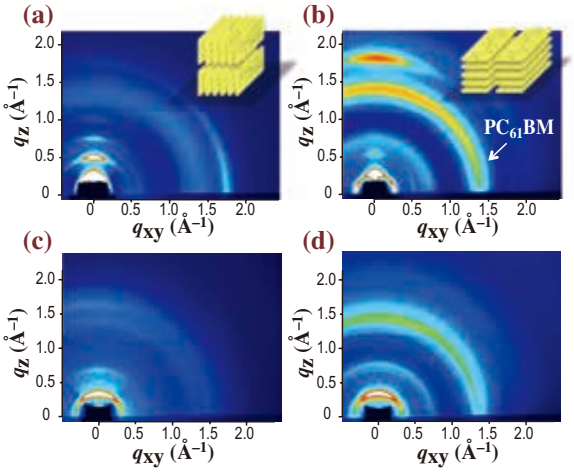

Fig. 4. 2D-GIXD images of the PNTz4T thin film **(a)**, PNTz4T/$PC_{61}BM$ blend film **(b)**, PBTz4T thin film **(c)**, and PBTz4T/$PC_{61}BM$ blend film **(d)**. The illustrations shown in (a) and (b) depict motifs of the edge-on and face-on orientations, respectively.

Itaru Osaka[a,b,*,†] and Kazuo Takimiya[a]

[a] Department of Applied Chemistry, Hiroshima University
[b] PRESTO - JST

*Email: itaru.osaka@riken.jp

[†]Present address: RIKEN Center for Emergent Matter Science

References

[1] A. Facchetti: Chem. Mater. **23** (2011) 733.
[2] P.M. Beaujuge and J.M.J. Fréchet: J. Am. Chem. Soc. **133** (2011) 20009.
[3] *I. Osaka, M. Shimawaki, H. Mori, I. Doi, E. Miyazaki, T. Koganezawa, K. Takimiya: J. Am. Chem. Soc. 134 (2012) 3498.*
[4] M. Wang *et al.*: J. Am. Chem. Soc. **133** (2011) 9638.
[5] H. Sirringhaus *et al.*: Nature **401** (1999) 685.

Development of hard X-ray magnetic circular dichroism microscope and its application to NdFeB magnet

A Nd-Fe-B magnet (neodymium magnet) [1] is the strongest permanent magnet ever made and has been used for a wide range of applications in modern products, such as motors in cordless tools, hard disk drives, magnetic fasteners and synchrotron undulators. These magnets are produced by sintering and annealing processes and thus exhibit multiphase microstructures. One of the major drawbacks of neodymium magnets is their low curie temperature. In order to overcome this drawback, some of the Nd is replaced with Dy. It is considered that Dy atoms in the borders of micrograins play an important role in improving the Curie temperature. To understand this mechanism, observation of the microstructure and revealing the relationship between the microstructure and micromagnetics are indispensable. In this study, the magnetic microstructures and element distributions in a Nd-Fe-B magnet were observed by a hard X-ray magnetic circular dichroism (HXMCD) microscope with Kirkpatrick-Baez (K-B) mirrors at beamline **BL16XU**, and it was found that the local magnetic moment and the concentration of Nd are strongly correlated [2].

Figure 1 shows the composition of our microscope system at beamline BL16XU [3]. Monochromatized linearly polarized X-rays are converted to either left circularly polarized (LCP) or right circularly polarized (RCP) X-rays by passing them through a diamond X-ray phase retarder (XPR). Then, the X-rays enter a pair of K-B mirror systems to form a focused beam. At the time of our experiments, the size of the focused beam on the sample was estimated to be 1.92 (horizontal) × 1.83 (vertical) μm^2. A sample of the neodymium magnet was placed in a 2 T electromagnet. Figure 2 shows how the (H)XMCD spectrum was measured and an example of the Nd L_{II} HXMCD spectrum of the neodymium magnet. The concept of XMCD spectroscopy was first proposed by Schütz *et al.* in 1987 [4]. One can understand the mechanism of X-ray absorption as the transition of electrons from an occupied inner state to an empty outer state. For a magnetic material, the outer shell has a spin moment, which is given by the imbalance of spin-up and spin-down electrons or equivalently (except for the sign) by the imbalance of spin-up and spin-down holes. If we can make spin-dependent X-ray absorption, it will be possible to detect the difference in the number of empty states with up spin and down spin. This spin-dependent X-ray absorption is realized by the use of RCP absorption and LCP absorption, which transfer their angular momentum to the excited photoelectrons. As a result of absorption measurements by RCP and LCP, the spectra show a slight difference, and the difference is the so-called (H) XMCD spectrum.

For our mapping experiments, the photon energy was fixed to 6.721 keV, which is the standard characteristic of Nd L_{II} XMCD and Nd L_{II} XAFS (see Fig. 2). For the XMCD mapping, the signal of Nd L_{II} XMCD was derived from the fluorescence of Nd $L\beta$. Figure 3(a) shows the fluorescence Nd-$L\alpha$ intensity map for a 44 × 20 μm^2 rectangular area, which reflects the Nd concentration. It should be noted that the fluorescence of Nd $L\beta$ contains the XMCD signal because its origin is the relaxation from the spin polarized N5 shell, while Nd $L\alpha$ contains little of the XMCD signal because its origin is the relaxation from the unpolarized (filled) M shells. Several islands with areas of several μm^2 with relatively high Nd concentrations can be observed in Fig. 3(a). Figure 3(b) shows the mapping of the magnetic moment per Nd atom derived from HXMCD signals. With our experimental configuration, only the magnetic moment parallel to the horizontal direction can be detected. It is possible to find similar regions by comparing Figs. 3(a) and 3(b). In area (A) in Fig. 3, the HXMCD signal is strong and the Nd concentration is low. In contrast, area (B) exhibits a weaker HXMCD signal and a higher Nd concentration than those in the surrounding areas. We conclude that area (A) is a crystalline $Nd_2Fe_{14}B$ alloy while area (B) consists of paramagnetic Nd-rich precipitates, as previously reported. This strongly indicates that Nd-rich three-grain junction precipitates are paramagnetic in the neodymium materials.

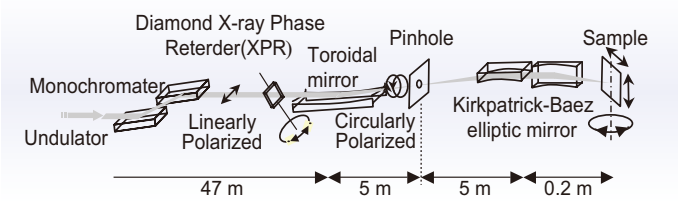

Fig. 1. Schematic drawing of our magnetic/elemental microscope system at BL16XU.

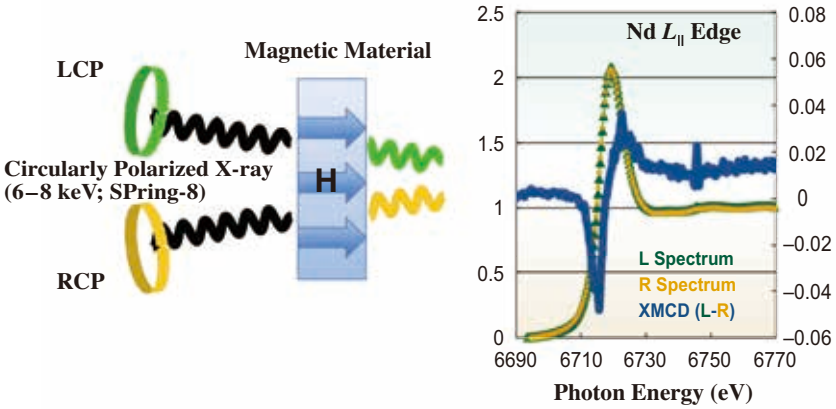

Fig. 2. (Left) Conceptual drawing of (H)XMCD measurement. The arrows in the magnetic material indicate the direction of magnetization. The X-ray absorption probability depends on the relation (parallel/antiparallel) between the X-ray helicity (LCP/RCP) and magnetized direction. (Right) Example of Nd L_{II} HXMCD spectrum derived from two spin-dependent spectra.

In this work, we performed simultaneous 2D mapping of fluorescence X-ray and HXMCD signals by scanning a hard X-ray microbeam and demonstrated the feasibility of studying magnetic materials with our microscope system. Our results clearly indicate the correlation between the Nd concentration and the magnetization of Nd-rich three-grain precipitates. The results also show that microspectrometry with hard X-rays is a powerful tool for revealing the correlation between the magnetic microstructure and the mapping of element buried under the surface oxide layer. Our technique shows strong potential for *in situ* observation of the magnetization reversal of bulk rare-earth magnets under a high magnetic field.

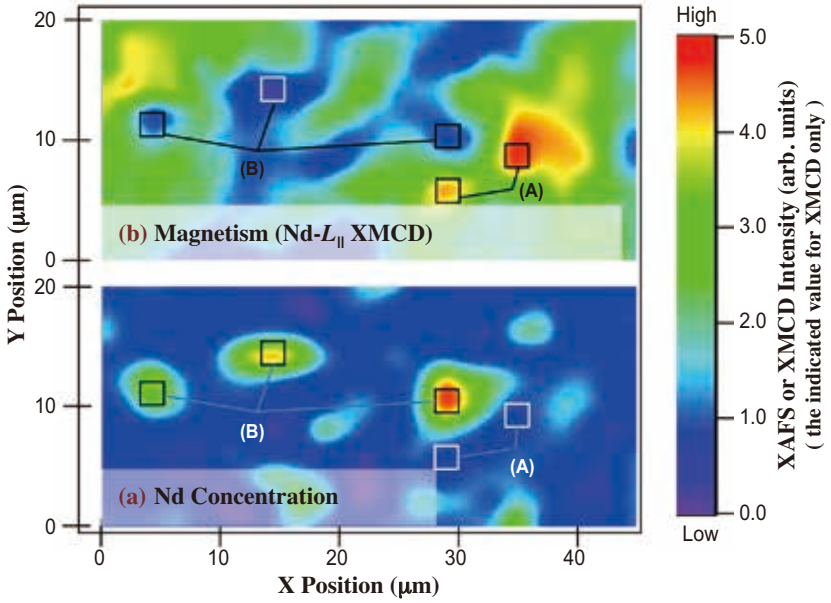

Fig. 3. Experimental results obtained using our magnetic/elemental microscope at BL16XU. **(a)** Elemental map for Nd concentration obtained by measuring Nd-*Lα* fluorescence and **(b)** HXMCD signal map of Nd-*Lα* XMCD. Area (A) is a crystalline $Nd_2Fe_{14}B$ alloy and area (B) consists of Nd-rich paramagnetic precipitates.

Akira Nambu

Central Research Laboratory, Hitachi, Ltd.

Email: akira.nambu.tw@hitachi.com

References

[1] M. Sagawa *et al.*: J. Appl, Phys. **55** (1984) 2083.
[2] *K. Ueda, A. Nambu, A. Yoneyama, A. Sugawara, S. Heike, T. Hashizume, H. Suzuki and M. Komuro: Appl. Phys. Lett. **97** (2010) 022510.*
[3] Y. Hirai *et al.*: Nucl. Instrum. Meth. A **521** (2004) 538.
[4] G. Schütz *et al.*: Phys. Rev. Lett. **58** (1987) 737.

X-ray microbeam three-dimensional topography imaging and strain analysis of basal-plane dislocations and threading edge dislocations in 4H-SiC

Silicon carbide (SiC) bipolar devices (IGBT and p-n diodes, etc.) are promising candidates for next-generation high-voltage power applications in various industries, traffic control, automobiles, and power-transmission systems. However, basal plane dislocations (BPDs) in an epilayer can cause an increase in the forward voltage drop of SiC bipolar devices, hindering their extensive commercialization. A promising method of reducing BPD density in an epilayer is to convert BPDs to threading edge dislocations (TEDs) near the epilayer/substrate (E/S) interface. To ensure perfect BPD-TED conversion, however, better understanding of the conversion mechanism is necessary [1].

X-ray microbeam three-dimensional (3D) topography has been developed for the depth-resolved crystallographic analysis of semiconductor crystals. This method enables us to investigate the behavior of dislocations near a deep E/S interface. This article describes the application of X-ray 3D topography to the study of BPD-TED conversion [2].

The sample examined is an 8°-off-cut (0001) Si-face 4H-SiC wafer with a 20-μm-thick epilayer. The setup of 3D topography measurements is shown in Fig. 1. The measurements were conducted at beamline **BL24XU** using an X-ray microbeam with photon energy of 15 keV. The full widths at half maximum (FWHMs) of the microbeam were typically 1.9 and 0.6 μm in the horizontal and vertical directions, respectively. The X-ray 3D topography uses a special slit with a V-shaped valley (V-slit) for microbeam X-ray diffraction. The incident X-ray penetrates the sample, generating a ribbon-shaped diffraction beam (**g** = 1 1 $\bar{2}$ 12) that impinges on the V-slit. After passing through the V-slit, a thin X-ray beam reaches a scintillation counter (SC) through a fully opened receiving slit (RS). We thus conducted pinpoint measurement at point Q where the incident beam intersects the extension of the beam passing through the V-slit. Scanning the sample provides a depth-resolved 3D topograph. Unlike conventional X-ray topography, dislocation images in a 3D topograph are dominated by kinematical direct images due to the extinction contrast [2].

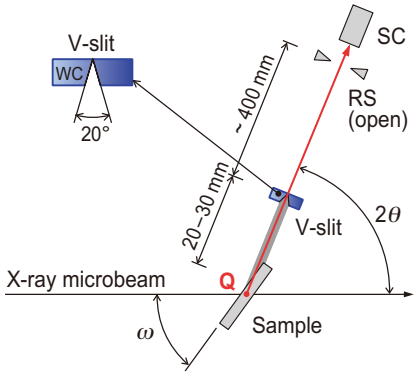

Fig. 1. X-ray diffraction geometry for 3D topography measurements. [2]

Measurements were carried out in 3D-single-scan (3DSS) and 2D-multiscan (2DMS) modes. In the 3DSS mode, sample positions were scanned in three dimensions at a fixed ω value to obtain a 3D topograph. In the 2DMS mode, the 2D data of reflection intensities were acquired for a desired cross section at step-scanned ω values to obtain an image of effective misorientations ($\Delta\omega$ map).

Figure 2 compares the conventional back-reflection X-ray topography and the 3D topography. The conventional topography (Fig. 2(a)) shows two BPDs, one of which (BPD1) is converted to a TED (TED1), and the other (BPD2) propagates to the epilayer surface. At the same position, a 3DSS

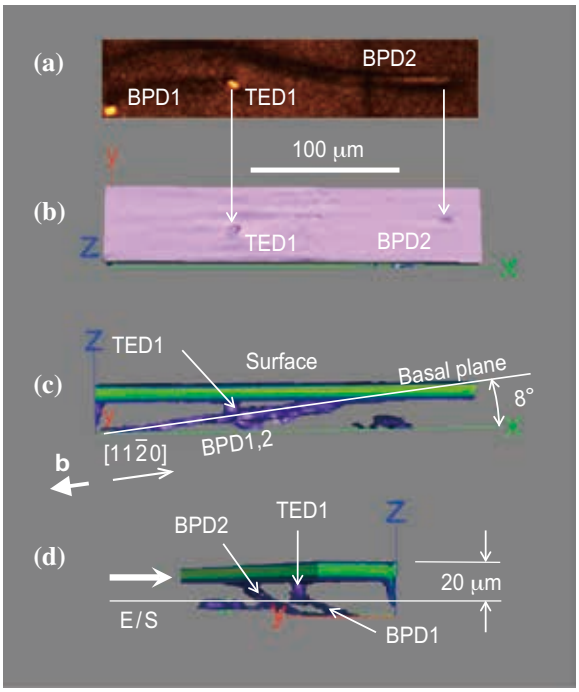

Fig. 2. X-ray 3D topography images of a TED (TED1) and two BPDs (BPD1 and BPD2) in comparison with conventional back-reflection X-ray topography. BPD1 is converted to TED1, whereas BPD2 propagates to the epilayer surface.

measurement was carried out with 2.5-μm cubic voxels within a 30-μm-deep region from the surface, providing the stereographic isosurface images shown in Figs. 2(b)-2(d). The top view (Fig. 2(b)) indicates two pits corresponding to TED1 and BPD2. The side view (Fig. 2(c)) shows that TED1 is almost perpendicular to the surface, while BPD1 and BPD2 lie on the basal plane at an angle of 8° from the surface. From the oblique camera angle (Fig. 2(d)), we can confirm that BPD2 propagates from the substrate to the epilayer, whereas BPD1 is converted to TED1 near the E/S interface at a depth of 20 μm. The horizontal high-intensity region along the surface (arrow in Fig. 2(d)) is caused by surface strain.

Figure 3 presents an expanded 3D topograph of BPD1 and TED1. This image was provided by a fine-step 3DSS measurement (1-μm cubic voxels) near the conversion point. Note here that the BPD1 image narrows just before the conversion as indicated by the thick arrow. Similar narrowing was also observed in other BPD-TED conversion cases. However, such narrowing did not occur in non-conversion cases such as BPD2. It is known that BPDs in a substrate are dissociated into pairs of partial dislocations separated by a stacking fault, and the two partial dislocations are constricted before converting to TEDs [3]. We consider that the narrowing of BPD1 is related to the constriction of the partial dislocations before the conversion.

Strain analysis was conducted on TED1 for cross sections perpendicular and parallel to the sample surface (C_{ZY} and C_{XY}, respectively, in Fig. 3). The 2DMS measurements were carried out with 1-μm square pixels at relative ω values ranging over ±84 μrad with an interval of 7 μrad. The $\Delta\omega$ map for C_{ZY} is shown in Fig. 4(a), where the surface corresponds to the level of $z = 0$. In this figure, BPD1 appears from behind and converts to TED1 at a depth of about 20 μm below the surface. The positive $\Delta\omega$ along the surface (dashed ellipse) indicates compressive strains, which are responsible for the superficial high-intensity region shown in Fig. 2. Figure 4(b) shows the $\Delta\omega$ map for C_{XY}. The TED is confirmed by analysis of the conventional synchrotron back-reflection X-ray topography to have a Burgers vector **b** pointing in the opposite direction to the step-flow [1 1 $\bar{2}$ 0] direction and to create an extra half-plane towards the left side [4]. Strain analysis indicates compressive and tensile strains on the left and right sides, respectively, which correlate to the direction of the extra half-plane. Strain on the order of $\pm10^{-5}$ around the TED is revealed from the value of $\Delta\omega$ (±10 μrad). Figure 4(c) shows the line profile ($\Delta\omega$) and its difference curve ($-\delta\Delta\omega$) along the dashed line L in Fig. 4(a). The peak width (FWHM) of $-\delta\Delta\omega$ indicates that the imaging spatial resolution is 1-2 μm.

We now have a new methodology of imaging and strain analysis using X-ray diffraction. X-ray 3D topography is useful for not only research on SiC-related materials, but also the strain analysis of dislocations and microstructures in various semiconductor crystals.

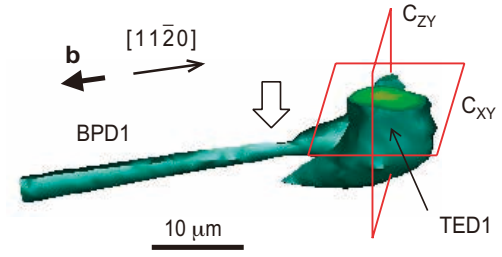

Fig. 3. Fine 3D topography image near BPD-TED conversion point.

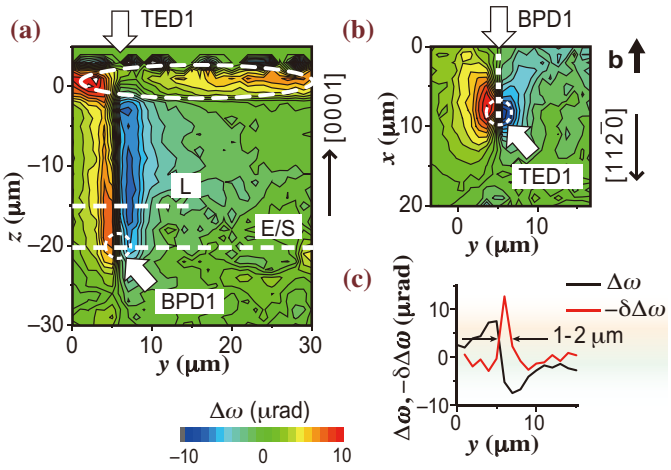

Fig. 4. Strain analysis of a TED. **(a)** $\Delta\omega$ map for the cross section C_{ZY} in Fig. 3. **(b)** $\Delta\omega$ map for the cross section C_{XY} in Fig. 3. **(c)** Line profile ($\Delta\omega$) and its difference curve ($-\delta\Delta\omega$) along line L in (a). [2]

Ryohei Tanuma

Materials Science Research Laboratory,
Central Research Institute of Electric Power Industry (CRIEPI)

Email: tanuma@criepi.denken.or.jp

References

[1] H. Tsuchida *et al.*: Phys. Status Solidi B **246** (2009) 1553.
[2] *R. Tanuma, D. Mori, I. Kamata and H. Tsuchida: Appl. Phys. Express* ***5*** *(2012) 061301.*
[3] S. Chung *et al.*: J. Appl. Phys. **109** (2011) 094906.
[4] I. Kamata *et al.*: J. Cryst. Growth **311** (2009) 1416.

Synchrotron microbeam X-ray diffraction system provides an important hint for developing better carbon fiber

Carbon fiber is now being applied in much wider fields including in the main structure of jet airplanes, the propellers of wind power generators, the main bodies of automobile cars, and so forth. In this sense, it is therefore necessary to further improve the physical properties of carbon fiber enable its use in a wider range of application with higher reliability. However, current commercial carbon fiber products include a contradiction regarding their mechanical properties: a carbon fiber with higher fracture strength has a lower Young's modulus along the fiber direction, whereas a fiber with a higher Young's modulus possesses lower strength. A higher strength means that the carbon fiber can safely support a heavier weight, whereas a material with a higher Young's modulus is more resistant to instantaneous mechanical deformation. In other words, an ideal carbon fiber should have the mechanical properties of the highest possible fracture strength and the highest possible Young's modulus, which may result in extreme robustness even for the case of a strong externally applied mechanical stimulus.

How can we develop such an ideal carbon fiber? One solution is to clarify the mechanical deformation behavior of a carbon fiber by focusing on the crystalline part. As is well known, a carbon fiber has a complicated aggregation structure of crystalline and amorphous regions, as shown in Fig. 1, in which graphite meshes are stacked together to form a relatively regular crystalline region. When an external tensile force is applied, the graphite network is deformed, which can be traced by measuring the shift of the corresponding X-ray diffraction peak. Since the crystalline region may be assumed to take essentially the same structure, mechanical deformation may be common among the various types of sample produced under different preparation conditions, for example, with different heat-treatment temperatures at which the original poly(acrylonitrile) fiber (precursor) is annealed to transform it to the carbon fiber with higher quality. A carbon fiber prepared in this manner was set in a stretching device and the WAXD pattern was measured under tension. The strain of the deformed crystal lattice was evaluated from the shift of the diffraction peak. On the other hand, the stress applied to the crystal region cannot be found directly, and therefore a serious assumption must be made that the stress acts homogeneously throughout the sample. The plot of stress versus strain gives a straight line in an infinitesimally small deformation region, the slope of which gives the Young's modulus. The thus-estimated Young's modulus of the crystalline region is called the apparent crystallite modulus (E_c^{app}) since a homogeneous stress distribution is assumed. As mentioned above, E_c^{app} should be common to samples prepared under various conditions as long as the assumption of a homogeneous stress distribution is reasonable. If the E_c^{app} value varies among the samples, then it must be concluded that the local stress acting on the crystalline region is different depending on the sample morphology. This means that the assumption of a homogeneous stress distribution cannot be employed anymore and that the heterogeneous stress distribution must be evaluated quantitatively [1,2]. This concept has been verified for the case of carbon fiber. It is also necessary to know the difference in the stress distribution among the various local parts of the fiber. This can be determined by performing X-ray diffraction measurement with an X-ray microbeam incident on a monofilament of about 6 μm diameter under the application of a tensile force. Such an experiment requires high accuracy and was successfully performed for the first time by utilizing a microbeam X-ray diffraction system coupled with a highly sensitive CCD detector at beamlines **BL47XU** and **BL03XU** [3,4]. The X-ray measurement was made

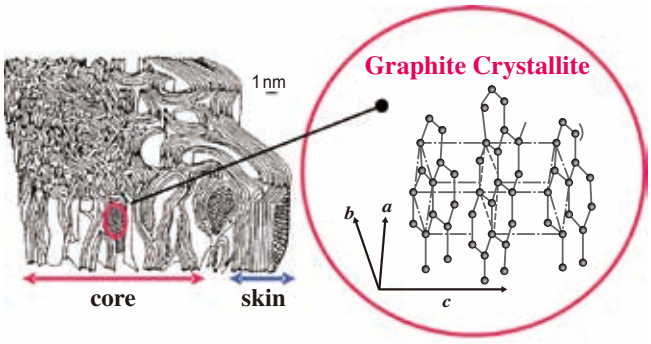

Fig. 1. Schematic illustration of inner structure of carbon fiber.

along the width direction at intervals of 0.2 μm using a beam of 0.5 μm radius. The results were as follows: (i) The E_c^{app} value was appreciably different among various samples. (ii) E_c^{app} was almost the same at various positions of a monofilament with a low Young's modulus (252 GPa), while it was largely different between the skin and core parts of a monofilament with a higher Young's modulus (445 GPa).

Similar measurements were also carried out to obtain the Raman spectra of the samples [5]. The tensile force deforms the net plane structure of graphite and the related vibrational bands are shifted to same extent. In the case of measuring the Raman spectra, however, an incident laser beam is absorbed by a black carbon fiber, and information is only obtained for the mechanical deformation on the outermost surface to a depth of several tens of nanometers. Also, it was found that the observed band shift in Raman spectra was different among the samples with various preparation histories.

Both the X-ray and Raman scattering data clearly indicated that the stress is not homogeneously distributed among the crystalline, amorphous, and outermost surface parts. A complex mechanical model was built up to interpret these experimental data quantitatively, which consisted of an inner fiber and an outermost surface. As illustrated in Fig. 2, the inner part (skin and core) consists of serially arrayed mechanical elements representing crystalline (C2) and amorphous (A) regions and a parallel element representing the crystalline region (C1). *a* and *b* in this figure are the fractions of these mechanical elements. The outermost surface was also taken into account in the theoretical derivation of the mechanical equations. Although the details are omitted here, the values of *a* and *b* in Fig. 2 were determined on the basis of the above-mentioned experimental data, from which the distribution of stress was estimated as schematically illustrated in Fig. 3 [4]. For example, in the case of a carbon fiber sample with a 445 GPa Young's modulus, an externally applied stress is concentrated on the outermost surface. If a tiny point of mechanical weakness exists on this surface (a structural defect such as a void, kink, or misoriented crystalline region), it may easily cause a breakage starting from the surface part. On the other hand, the sample with a lower Young's modulus of 255 GPa is mechanically tough because the stress concentration occurs mainly on the parallel mechanical element inside the fiber. In this way, we have achieved a breakthrough in clarifying the contradictory mechanical properties regarding the toughness and hardness of carbon fiber [4]. A carbon fiber with excellent mechanical properties must possess as homogeneous structural distribution as possible over the cross section of the fiber. Although our achievement is only a starting point, it provides a quantitative basis for the production of carbon fiber with superior mechanical properties.

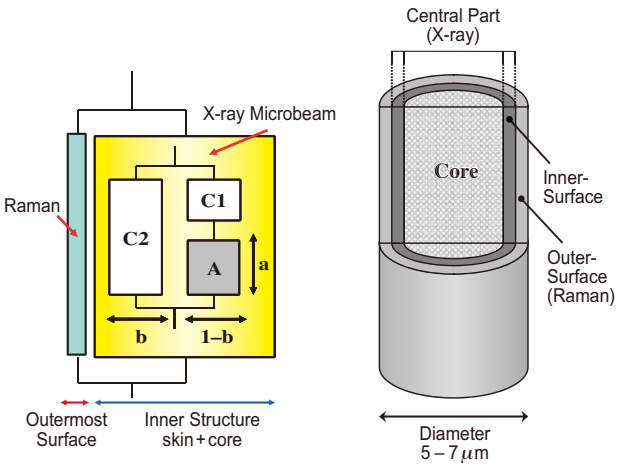

Fig. 2. Carbon fiber and complex mechanical model.

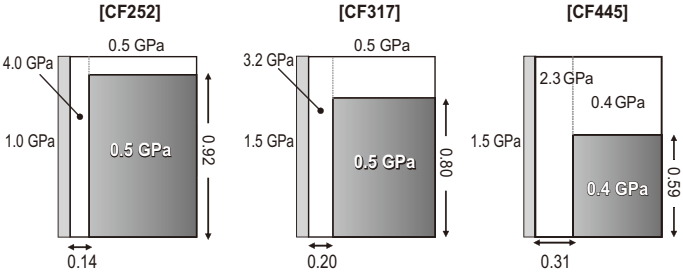

Fig. 3. Stress distribution among various mechanical elements of carbon fibers with different Young's moduli, where each fiber is subjected to a bulk tensile stress of 1 GPa.

Takayuki Kobayashi[a], Kazunori Sumiya[a] and Kohji Tashiro[b,*]

[a] Corporate Research Laboratories, Mitsubishi Rayon Co. Ltd.
[b] Graduate School of Engineering, Toyota Technological Inst.

*Email: ktashiro@toyota-ti.ac.jp

References

[1] K. Tashiro *et al.*: Polymer **29** (1988) 1768.
[2] S. Nakamoto *et al.*: J. Polym. Sci: Part B: Polym. Phys. **41** (2003) 444.
[3] *T. Kobayashi, K. Sumiya, Y. Fujii, M. Fujie, T. Takahagi, K. Tashiro: Carbon **50** (2012) 1163.*
[4] T. Kobayashi *et al.*: Carbon **53** (2013) 29.
[5] T. Kobayashi *et al.*: Carbon **49** (2011) 1646.

Shear-induced conformational fluctuations of polystyrene probed by 2D infrared microspectroscopy

Many studies on flow-induced polymer crystallization have been performed since the 1960s. However, the nature of flow-induced crystallization is still a poorly understood fundamental problem owing to its nonequilibrium property. Furthermore, because of the wide use of semi-crystalline polymers, external fields are inevitably applied during polymer processing such as extrusion or injection. Thus, considerable interest has been aroused in polymer engineering as the final morphology and properties of polymer products strongly depend on the processing history.

We discovered the existence of some string-like objects of macroscopic size in isotactic polystyrene (*iPS*) melts at temperatures above the nominal melting temperature (T_m) after applying a shear flow [1]. These aligned objects were assigned as 'row-nucleated' or 'shish-kebab-like' precursors since the epitaxial growth of crystals from them was observed during isothermal crystallization. No specific X-ray scattering intensity was observed on the precursors because there was little or no electronic density fluctuation. After cooling below T_m, we were able to observe the fiber structure, the so-called shish-kebabs structure, in these precursors by X-ray scattering and optical microscopy measurements as shown in Fig. 1.

In this study, the shear-induced conformational fluctuations of 'row-nucleated' or 'shish-kebab-like' precursors in *iPS* melts at temperatures above T_m were studied [2]. A macro-imaging map was demonstrated to investigate intra-molecular ordering of the precursors with the help of the powerful 2D infrared microspectroscopy station at beamline **BL43IR**. A Bruker IFS 120HR/X interferometer with a wide spectral range (100 – 20,000 cm^{-1}) was employed [3]. Because of the long distance (100 mm) between the Schwarzschild mirrors, a Linkam CSS-450 high-temperature shear cell was installed to perform *in situ* rheo-FTIR measurements. The temperature protocol for the shear experiments was as follows: (a) samples were heated to T_{melt} (290°C) from room temperature at a rate of 30°C/min; (b) they were held at T_{melt} for 5 min to erase the thermal history; (c) they were cooled to the shear temperature (T_{shear} = 250°C) at a rate of 30°C/min; (d) they were held at T_{shear} for 2 min to reach the temperature equilibrium and then subjected to a pulse shear flow; (e) after cessation of the shear flow, samples were held at the same temperature for 90 min; (f) finally, *iPS* samples were heated to T_{melt} again. The shear rate was 30 s^{-1}.

It is well known that *iPS* exhibits diverse 3/1 helical bands [4]. The critical sequence length, defined as the minimum length of a helical conformation, is represented by the number of monomeric units *m*. For example, 898 cm^{-1}, $m \geq 16$; 920 and 1053 cm^{-1}, $m \geq 10$; 1194 cm^{-1}, $m \geq 6$; 1084cm^{-1}, $m \geq 5$. On the other hand, the amorphous bands had wavelengths of 1194 and 1084 cm^{-1} as well as weak band at 1053 cm^{-1}.

Figure 2(a) shows the morphology and conformational fluctuations of *iPS* after applying a pulse shear flow (shear rate = 30 s^{-1}) using polarized optical microscope (POM) and 2D FTIR measurements. A 'row-nucleated' or 'shish-kebab-like' precursor in the flow direction was found in the POM measurements. 2D FTIR mapping was performed in a region of 200 × 100 μm^2 (red rectangle in Fig. 2(a)), as shown in Fig. 2(b), with a resolution of 10 × 10 μm^2. The integral wavenumber ranges were 895 – 900 cm^{-1} ($m \geq 16$) and 1050 – 1055 cm^{-1} ($m \geq 10$) and were assigned to the long 3/1 helical segments. The red domains with a high integral intensity in Fig. 2(b) were

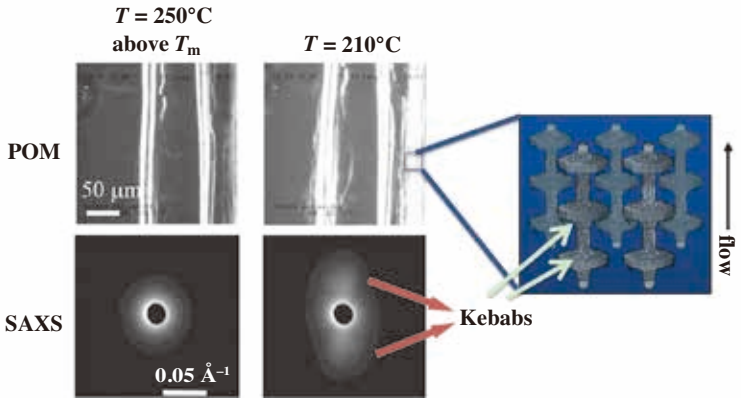

Fig. 1. Polarized optical microscope (POM) figures and in situ small-angle X-ray scattering profiles immediately after applying shear flow (250°C) and after crystallization at 210°C. Schematic drawing on the right is the so-called shish-kebab structure.

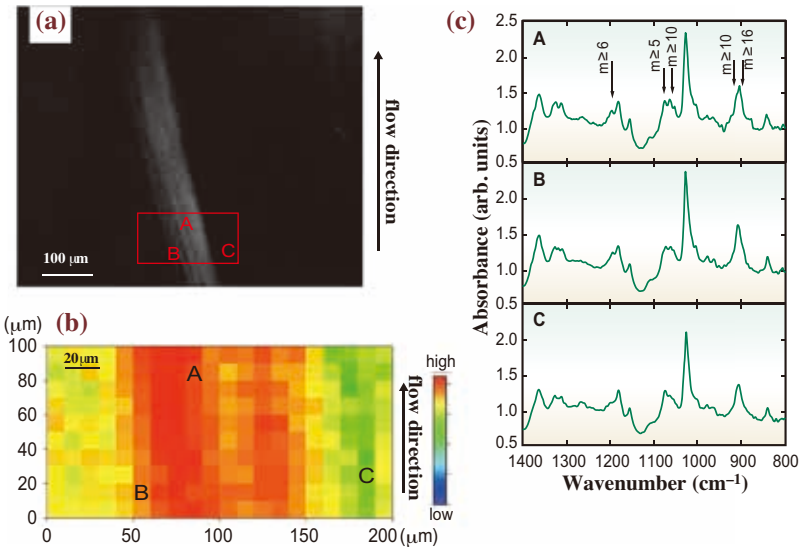

Fig. 2. **(a)** POM observation after cessation of flow. **(b)** Imaging map of *iPS* sample after applying a pulse shear flow obtained by 2D FTIR measurements. The mapping size was 200×100 μm^2 (red rectangle in (a)). **(c)** Infrared spectrum of *iPS* sample at different points in (a) and (b). A) in the center of the shish-kebab-like precursor; B) at the edge of the shish-kebab-like precursor; C) in the amorphous domain.

correlated to the precursor domain in the red rectangle of Fig. 2(a), which suggested the high concentration of long helical bands in the microscale precursor. Three different points were chosen for investigation in more detail; A) in the center of the precursor; B) at the edge of the precursor; C) in the amorphous domain as identified in Figs. 2(a) and 2(b). In the center of the precursor, both long helical bands ($m \geq 16$, $m \geq 10$) and short helical bands ($m \geq 6$, $m \geq 5$) were observed (Fig. 2(c), A). At the edge of the precursor, the intensity of the long helical bands was weaker (Fig. 2(c), B) and in the amorphous domain, almost no long helical bands and only short helical bands were observed (Fig. 2(c), C). It was evident that long helical bands ($m \geq 16$, $m \geq 10$) were detected in the center of the precursor (Fig. 2(c), A) while no long helical bands were detected in the amorphous domain (Fig. 2(c), C).

These precursors were found to disappear during the heating process. Figure 3(a) show micrographs of the shear-induced precursor and imaging maps of long helical bands during the heating process from 250 to 280°C. The region of long helical bands was decreased at 260°C, corresponding to the partial melting of the precursor, while in the center of the precursor, there still was a high concentration of long helical bands. When the temperature reached 270°C, the entire precursor began to melt, and thus the disappearance of the long helical bands was consistent with the results in our previous paper [1]. Finally, almost no long helical bands were observed after the melting of the precursor at 280°C. The disappearance of the long helical bands during the heating process was consistent with the melting of micron-scale precursors. From an intramolecular view, the long helical bands in the precursors may be related to a shear-induced coil-helix transition.

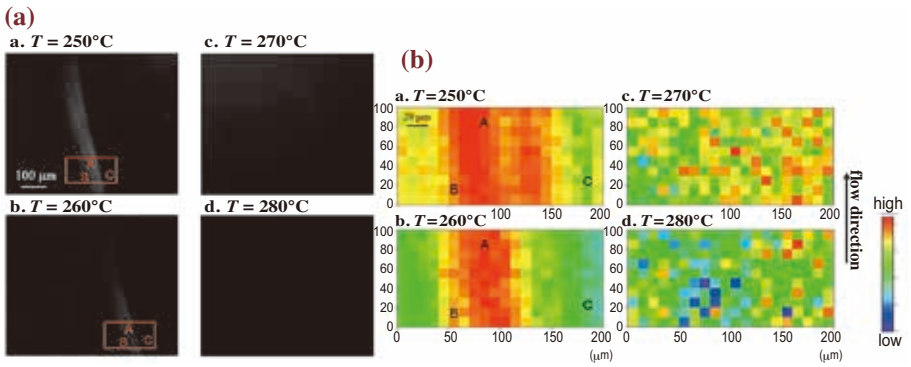

Fig. 3. **(a)** POM observation during the heating process. **(b)** Imaging map of long helical bands during the heating process.

Yunfeng Zhao and Go Matsuba*

Graduate School of Science and Engineering,
Yamagata University

*Email: gmatsuba@yz.yamagata-u.ac.jp

References

[1] Y. Zhao *et al.*: J. Polym. Sci. Part B: Polym. Phys. **49** (2011) 214.
[2] *Y. Zhao, G. Matsuba, T. Moriwaki, Y. Ikemoto, H. Ito: Polymer **53** (2012) 4855.*
[3] Y. Ikemoto *et al.*: Infrared Phys. Tech. **45** (2004) 369.
[4] M. Kobayashi *et al.*: Macromolecules **23** (990) 78.

Nuclear

PHYSICS

The linearly polarized photon beam is produced by backward-Compton scattering of laser photons from 8 GeV electrons at BL33LEP. The current LEPS facility is dedicated to studying photoproduction of hadrons at forward angles, where high linear polarization plays an essential role in the decomposition of various reaction processes.

The beam polarization is high and can be changed easily by changing the laser polarization. The LEPS covers photon energy region from 1.5 GeV to 2.9 GeV, which is suitable for studying the creation of excited baryons containing a strange quark or an anti-strange quark near the production thresholds. The production and decay properties of the excited hadrons shed light on their structure in terms of confined quarks.

The first article reports new results of the penta-quark Q+ study in the $\gamma C \rightarrow K^+K^-$ pn reactions. Firstly, in order to check the validity of the 5-sigma evidence that we obtained by analyzing the data taken in 2002–2003, the same analysis was applied to the new data taken in 2006–2007. A strong narrow peak in the Fermi-motion corrected K^- missing mass was not reproduced in the new data set. Then, we applied an exclusive analysis to both data sets, where background processes due to γp reactions were identified by energy loss information in a plastic counter that was placed just after the liquid-deuterium target. Clear signal enhancements in the γn contributions were seen in the both sets, and the inconsistency turned out to be partly due to fluctuations in the proton contribution of the previous data set. The signal enhancement was also confirmed by a Monte-Carlo-based exclusive analysis.

The second article shows the progress of the LEPS2 project at BL31LEPS, in which we aim to improve both the beam intensity and the detector acceptance. For the experiments at LEPS2, a new type of time-of-flight counter, i.e., the resistive plate chamber (RPC), will be constructed. RPCs will cover a large area of ~10 m^2 with a good time resolution of ~50 ps. The results of a test experiment with a prototype RPC are presented.

Takashi Nakano
Research Center for Nuclear Physics
Osaka University

New results on Θ^+ from LEPS

In 2003, the LEPS (Laser Electron Photon Facility at SPring-8) collaboration reported an evidence of a baryon with the strangeness quantum number S=+1 and charge +1, now called Θ^+, in the $\gamma C \rightarrow K^+K^-X$ reaction [1]. The minimal quark content of Θ^+ is $uudd\bar{s}$. Therefore, Θ^+ is a genuine pentaquark state, which contains four quarks and one antiquark. Θ^+ has attracted attention not only because it is a new type of baryon, but also because it has two features, namely, low mass and narrow width. The mass of Θ^+ is measured to be 1520–1550 MeV/c^2. A naive consideration from the constituent quark model tells us that the sum of the mass of the constituent quark is about 1900 MeV. This is much larger than the measured value. The width of Θ^+ is measured to be at least less than 1 MeV/c^2 from several experiments. This value is too narrow to be explained by current knowledge of hadron physics. Therefore, Θ^+ has the possibility to provide new knowledge of hadron physics.

Since the first report by LEPS, a considerable number of experiments have been performed to confirm the existence of Θ^+. However, its existence is still controversial.

The LEPS collaboration analyzed data with a liquid deuterium target, which were taken in 2002-2003, and reported evidence of Θ^+ in the $\gamma d \rightarrow K^+K^-pn$ reaction [2]. The statistical of the narrow peak in the spectrum of missing mass for the system K^+ and a nucleon, M(NK), was obtained to be 5.1σ.

The CLAS collaboration in the Jefferson Laboratory also searched for the Θ^+ in the same reaction but no narrow peak was observed [3]. However, the two results might be consistent if the differential production cross section has a strong angle dependence, since the detector acceptances of LEPS and CLAS are almost exclusive. To check the LEPS result further and to clarify the controversial situation concerning the existence of Θ^+, the LEPS collaboration performed a new experiment with almost the same setup as in the previous experiment [2] in 2006-2007.

The experiment was carried out at beamline **BL33LEP**. A linearly polarized photon beam was produced by Compton back scattering of the 355 nm laser and 8 GeV electrons circulating in the storage ring of SPring-8. The photon energy range was from 1.5 to 2.4 GeV. For this experiment, we upgraded the laser injection system so that two lasers were simultaneously injected into the storage ring. Figure 1 shows a schematic view of the two-laser injection system. As a result, beam intensity was almost doubled and produced approximately 2.6 times higher statistics.

The reaction of interest is quasi-free production of Θ^+ from a neutron and its decay into nK^+, i.e., $\gamma n \rightarrow K^-\Theta^+ \rightarrow K^-K^+n$. First, we carried out blind analysis to check the previous result. Cut conditions were not changed from those in the previous analysis [2] and detector calibration was performed before opening the box. We detected K^+ and K^- with the LEPS detector. In the previous analysis, the target nucleon was not identified and events from a proton and a neutron were combined. Figure 2(a) shows the M(NK^+) distribution for two data sets. The strong narrow peak structure seen in the previous analysis was not observed.

To determine the reason for the inconsistency in the M(NK^+) distributions between the two data sets, we developed a new analysis method, in which a proton was detected using the energy loss information of the start counter (SC), which is a plastic scintillation counter located just behind the target chamber. When a proton is struck by a photon, it hits the SC and induces a large energy loss on the SC. In contrast, when a neutron is struck by a photon, it does not induce energy loss because the neutron is a neutral particle. The proton tagging efficiency is approximately 60%. Figures 2(b) and 2(c) show the M(pK^+) mass distribution for a proton-tagged sample for each data set. In the previous data, a peak structure is seen in the proton-tagged sample, which cannot be from a single charged Θ^+. While such a structure is not seen in the present data. This suggests that part of the peak structure seen in the previous data comes from statistical fluctuation. It is possible to increase

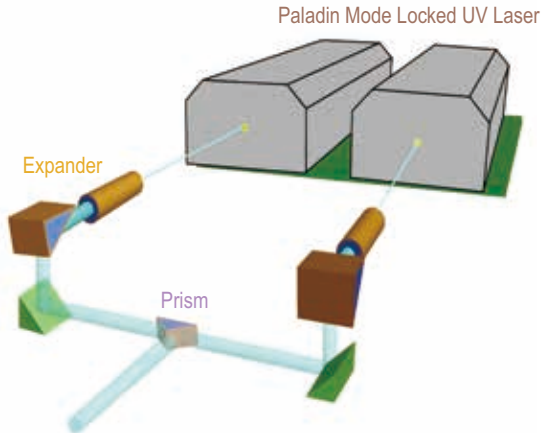

Fig. 1. Schematic view of the two-laser injection system.

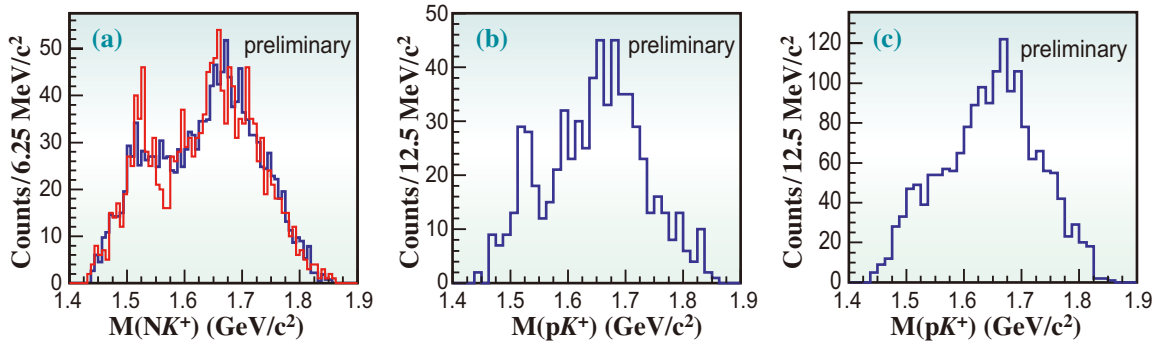

Fig. 2. **(a)** M(NK^+) distributions for previous data (blue) and present data (new). **(b)** M(pK^+) distribution for previous data. **(c)** M(pK^+) distribution for present data.

the proton tagging efficiency by selecting the event with the reaction vertex downstream of the target. The proton tagging efficiency is improved to 90% by selecting approximately one-third of the target volume. Figure 3(a) shows the M(nK^+) mass distribution for a proton-rejected sample after vertex selection. A clear enhancement near the Θ^+ mass region is seen. Because the vertex cut reduced the statistics, we also estimated the proton contributions by fitting a proton-tagged sample with a distribution generated by Monte Carlo simulation and subtracted it from the data sample without the proton rejection cut and the vertex cut.

Figure 3(b) shows the M(NK^+) mass distribution for data and the M(pK^+) mass distribution estimated by Monte Carlo simulation. The blue histogram in Fig. 3(c) shows the difference between the blue histogram and the red histogram in Fig. 3(b). Red points in Fig. 3(c) show the results of the energy loss based exclusive analysis after subtracting proton contributions that miss the SC. The M(nK^+) distributions for the two methods are consistent.

The estimation of the statistical significance and position of the peak is under way. The LEPS collaboration has just started a new experiment with a large SC in October 2012.

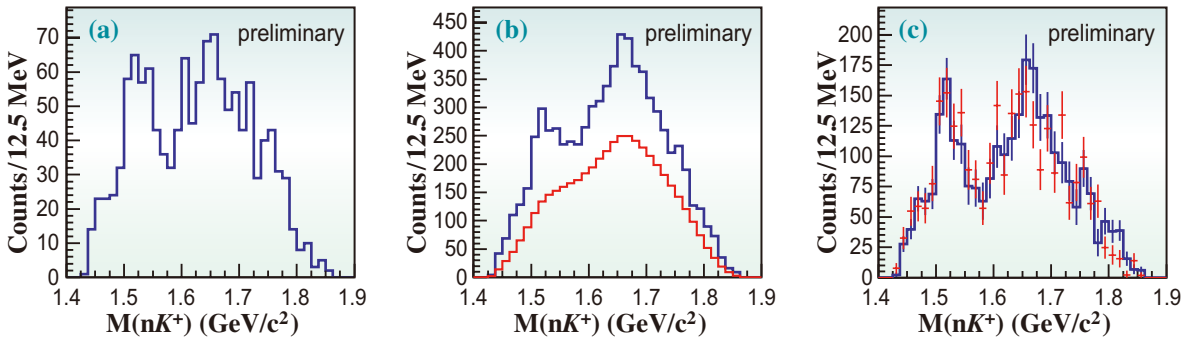

Fig. 3. **(a)** M(nK^+) distribution with vertex cut and proton rejection cut for summed data. **(b)** The blue histogram shows the M(NK^+) distribution without the vertex cut and proton rejection cut for summed data. The red histogram shows the M(pK^+) distribution estimated from MC. **(c)** The blue histogram shows M(nK^+) distribution with MC-based exclusive analysis. Red points show the results of the energy loss based exclusive analysis after subtracting proton contributions that miss the SC, normalized by the area of the blue histogram.

Yuji Kato for the LEPS Collaboration

High Energy Physics Laboratory, Nagoya University

Email: kato@rcnp.osaka-u.ac.jp

References

[1] T. Nakano *et al.*: Phys. Rev. Lett. **91** (2003) 012002.
[2] T. Nakano *et al.*: Phys. Rev. C **79** (2009) 025210.
[3] B. McKinnon *et al.*: Phys. Rev. Lett. **96** (2006) 212001.

High time resolution resistive plate chambers for the LEPS2 experiment

The construction of LEPS2, a new GeV photon beamline, has started at **BL31LEP**. LEPS2 will be used to study subnuclear physics with photoproduction of baryons and mesons from nuclei. A multi-GeV photon beam is produced by backward Compton scattering of laser photons with 8 GeV electrons in the SPring-8 storage ring. The LEPS experiment at BL33LEP has produced various data concerning photo-productions of pentaquarks and ϕ-mesons using laser-electron photons [1,2]. However, the acceptance of LEPS detectors is limited to a forward angle, and a spectrometer covering a full solid angle is long awaited. Figure 1 shows the schematic drawing of the LEPS2 spectrometer. This device consists of a solenoid magnet and covers almost 4π sr. The solenoid magnet was that used for the AGS E787/E949 experiment at the Brookhaven National Laboratory in the U.S. It was transported to SPring-8 in 2012. Detectors that will be used to identify particles and to measure their momenta are now under development. Trackers, particle identification detectors and calorimeters will be placed in the magnet. Particle identification will be performed with time-of-flight (TOF) detectors and aerogel Cherenkov (AC) counters. The TOF detectors will be installed in a barrel region with a radius of 0.9 m and a depth of 2.0 m. The flight length from the target to the TOF detectors will range from 0.9 m to 1.7 m. In order to separate kaons from pions up to 1.1 GeV/c via a TOF measurement with 3σ accuracy, a high time resolution of up to 50 ps is required. No experimental group has achieved such a good time resolution with large-area (~10 m^2) coverage; thus, this is a challenging task.

The start timing of TOF measurements can be determined with a 15 ps resolution using the RF signal from SPring-8 accelerators. We chose resistive plate chambers (RPCs) for the stop counters of TOF measurements. RPCs are gas detectors made of high-resistivity glasses. A typical structure of the detectors is shown in Fig. 2. When a charged particle passes an RPC, gas is ionized and avalanches occur in the gas gap. Avalanches induce signals on the readout strips. Because of the thin gas gaps, the timing fluctuation of avalanches is small and RPCs can achieve an excellent time resolution on the order of 50 ps. RPCs are employed in many experiments as TOF detectors and used with 70–100 ps resolution [3]. Some prototype RPCs achieved better resolution and the world's best RPC achieved a time resolution of 20 ps including the jitter of front-end electronics [4]. In general, RPCs have better time resolutions with an increase in the number of gaps and a reduction in the area of readout strips. The many RPCs used in high-energy experiments employed small (10 – 20 cm^2) readout strips. However, if the readout strip is small, the number of readout channels becomes large. In order to reduce the readout circuit cost, we should reduce the number of readout channels to less than 2000 in the LEPS2 experiment. This indicates that a readout strip read by one channel should be larger than 50 cm^2. Achieving good time resolutions with such a large readout strip is also a difficult challenge.

We have developed many prototype RPCs and performed beam tests at BL33LEP. The setup of the beam test is shown in Fig. 3. Laser-electron photons were irradiated to a lead target and electron-positron pairs were produced via pair-creation. Electrons were bent with a dipole magnet and passed through the RPCs. The stop timing of TOF was measured with

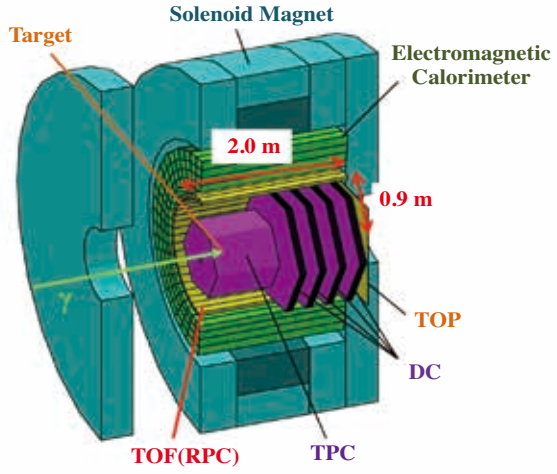

Fig. 1. Schematic drawing of the LEPS2 detector. RPCs cover the barrel region (painted yellow).

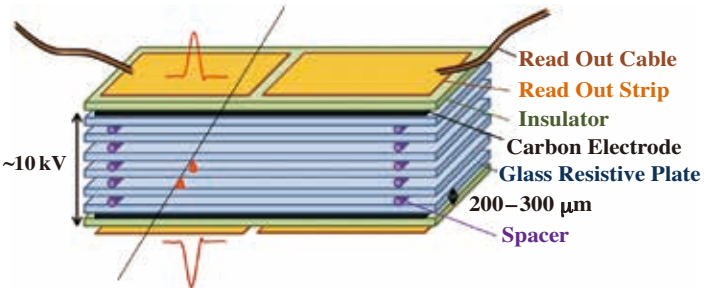

Fig. 2. Schematic drawing of an RPC. A high voltage of about 10 kV/mm is applied to the gas gaps.

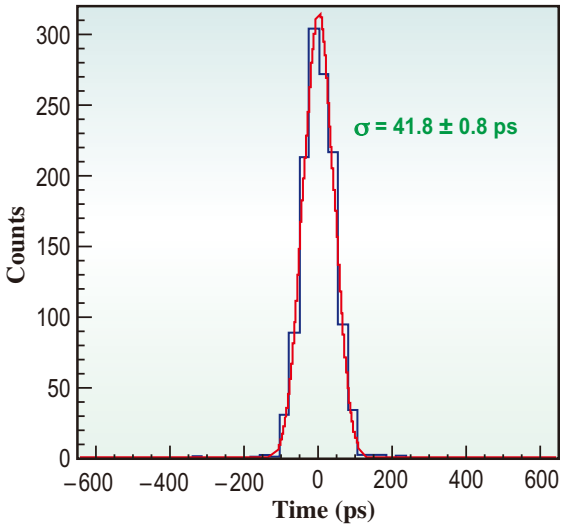

Fig. 4. Time distribution of the 24-gap RPC. The RPC achieved a time resolution of 40 ps.

the RPCs. On the other hand, the start timing was derived from the RF signal. Since both electrons in the storage ring and laser-electron photons fly at the same (light) speed, the time distribution of electrons in the storage ring is conserved in the laser-electron photons at the target position. Thus, the ambiguity of the timing of pair-creation at the target is due only to the bunch width. Owing to the small electron bunch width in the SPring-8 storage ring (~15 ps) and very precise RF signal (<< 10 ps), we can determine the start timing with very good resolution of ~15 ps.

We started with small (8 cm^2) readout strips and examined general features of the RPCs [5]. By increasing the number of gas gaps to 24, we achieved the best resolution of 40 ps including the jitter of front-end electronics (Fig. 4). However, on increasing the readout strip area, the time resolutions became extremely low. The resolution of a 7.4 cm × 10 cm strip (1600 ch at LEPS2) was 150 ps. This was because signals of the large readout strip consist of many signals with different propagation pathways. Then, we attempted to use long [2.5 cm × 40 cm (2000 ch at LEPS2) and 2.5 cm × 100 cm (800 ch at LEPS2)] double-ended strips. With both kinds of strips a 60 ps time resolution was achieved. This was one of the highest resolutions of large-readout-strip RPCs in the world. We found that long strips are suited for high time resolution RPCs. We also examined the position dependence of time resolution and confirmed that there is no big dependence. Long-strips RPCs achieved time resolution of 60 ps even in the gap between strips.

Although the time resolutions of long strip RPCs are slightly lower than the requirement of LEPS2, their performance almost satisfies the requirements of LEPS2. The time resolutions include about 40 ps jitter of front-end electronics and can be improved if we can develop better electronics. We are now developing such electronics and plan to have a beam test at BL33LEP. RPCs will be installed partially at BL31LEP in 2013 and we will start physics experiments.

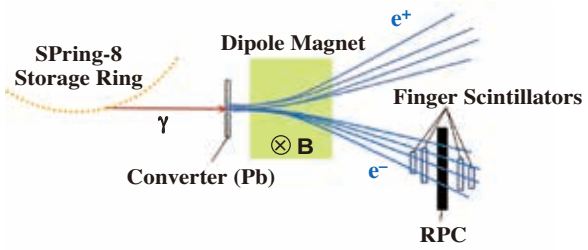

Fig. 3. Experimental setup of beam test at BL33LEP. Gamma rays are converted to electron-positron pairs. Electrons are bent with a dipole magnet and hit the RPC.

Natsuki Tomida for the LEPS2 Collaboration

Department of Physics, Kyoto University

Email: natsuki@scphys.kyoto-u.ac.jp

References

[1] T. Nakano: SPring-8 Research Frontiers 2003 (2004) p.130.
[2] T. Mibe *et al.*: SPring-8 Research Frontiers 2004 (2005) p.147.
[3] A. Alici: JINST **7** (2012) P10024.
[4] S. An *et al.*: Nucl. Instr. and Meth. A **594** (2008) 39.
[5] N. Tomida *et al.*: JINST **7** (2012) P12005.

Accelerators & Beamlines Frontiers

Beam Performance

Developments and Upgrades of Storage Ring

Machine Tuning for Lower Emittance Optics of SPring-8 Storage Ring

To provide higher brilliance and flux density for the hard X-ray region than those of the present, a new optics of the SPring-8 storage ring has been examined. The design emittance of the new optics is reduced from the present emittance of 3.49 to 2.41 nm·rad at 8 GeV (Table 1). It is predicted by SPECTRA [1] that the new optics can provide 1.5 times higher brilliance and 1.25 times higher flux density for 10 keV photons with the SPring-8 standard undulator than those of the present. It is noted that, in the new optics, magnetic positions and polarities are fixed and magnetic fields are optimized within the specifications, so that the shutdown time is not required for switching from the present optics to the new one.

The machine tuning processes for the new optics, such as increase in the injection efficiency and optimization of the bump orbit for the top-up injection, have been carried out during the machine study run. It was confirmed that the top-up injection efficiency and beam lifetime of the new optics are sufficient for adopting the user operation.

The emittance was estimated by measuring the electron beam size using the X-ray beam profile monitor, and by using the lattice functions estimated from the response matrix analysis. The resulting value of the horizontal emittance shows good agreement with the design. The ratio of the vertical emittance to the horizontal emittance of the new optics is about 0.55%, which is almost the same as the present.

The test run of the new optics was demonstrated on Jan. 26, 2013 to check the photon beam performance at some beamlines. The increase in the partial flux (~10%), the increment of the brilliance (25%) and the decrease in the photon beam size at the front-end slit (10%) were observed at insertion device beamlines. After checking the photon beam performance at all beamlines, the new optics will be released to user operation from May 2013.

Table 1. Main parameters of present optics and new optics.

	Present Optics	New Optics
Beam energy	8 GeV	8 GeV
Natural emittance	3.49 nm·rad	2.41 nm·rad
Energy spread σ_E/E	0.11%	0.11%
Tune (Q_x, Q_y)	(40.14, 19.35)	(41.14, 19.35)
Natural chromaticity (ξ_x, ξ_y)	(−88, −42)	(−117, −47)
Effective emittance @ ID center	3.77 nm·rad	2.79 nm·rad
Lattice function (β_x, β_y, D) @ ID center	(22.5 m, 5.6 m, 0.11 m)	(31.2 m, 5.0 m, 0.15 m)

Improvement of Coupling Correction

The vertical beam spread, or the emittance coupling, is one of the most important parameters for the high brilliance light source storage ring. By the precise alignment of the magnets and the proper COD correction, at the commissioning phase of the SPring-8 storage ring, we succeeded in achieving the very small coupling, of ~0.2% without correction. However, the coupling had grown large over the years; thus, at present, we have corrected it and recovered the initial performance.

Recently, although the coupling has been corrected, it has become noticeable that the vertical beam spread becomes large in the magnet array gaps of some insertion devices (ID's) closed. For example, Fig. 1 shows the trend of the vertical beam size measured by the visible light interferometer in the beamline tuning time with the ID10 gap, which implies the clear effect of the ID magnetic field on the coupling. To correct the coupling induced by the ID10, we tune the skew quadrupole magnets, sk_9_3 and sk_10_2, close to the ID. The tuning was done at 10:00 on October 1, whose process is shown in Fig. 2. By adjusting the skew quadrupole magnets, we reduced the vertical beam size from 26 to 23 μm, which is the size with all ID's gaps fully open. For the purpose of independently changing the ID gap without any effect on the user beam operation, we plan to prepare the software for adjusting the strength of the skew quadrupole magnets automatically.

The vertical dispersion, which does not exist in the design and is generated by means of an error

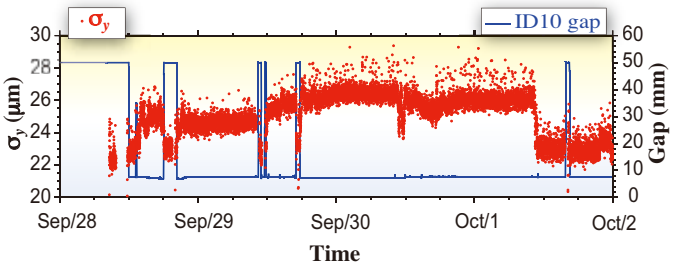

Fig. 1. Trend of vertical beam size and magnet array gap of ID10 during beamline tuning time.

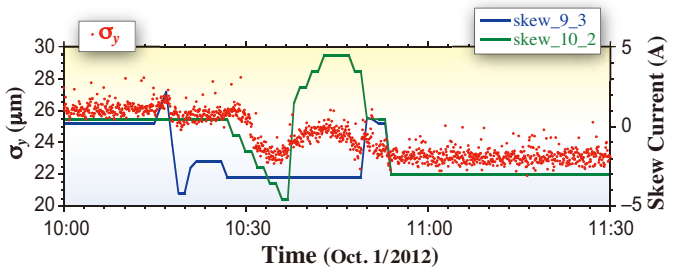

Fig. 2. Vertical beam size and currents of power supplies of skew quadrupole magnets.

magnetic field, also gives rise to the vertical beam spread, and thus is corrected as well as the coupling. To improve the vertical dispersion correction, we replace some of the skew quadrupole magnets with stronger ones and rearrange the removed ones at different locations. Figure 3 shows the vertical dispersions before and after the correction. The r.m.s. vertical dispersions are 5.01 and 0.87 mm. Before introducing the stronger skew quadrupole magnet, we can never reduce the r.m.s. vertical dispersion to sub-millimeter scale.

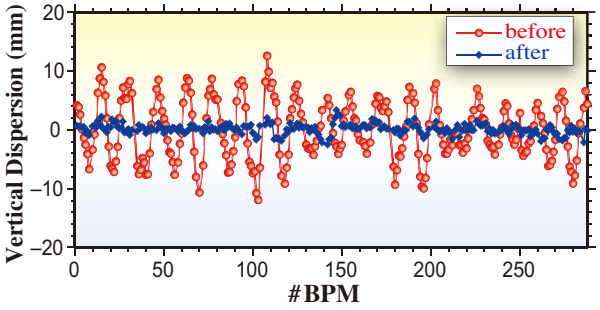

Fig. 3. Vertical dispersion before and after correction.

Design of Low-Vertical Beta Straight Section for Installing Cryoundulator

In one of the normal straight sections of the storage ring, a 1.5-m-long cryoundulator with a short period of 15 mm was installed in March 2013 and beam tests are planned to examine its performance. This cryoundulator is of the in-vacuum type and the minimum gap can be set to as small as 3 mm. At present, such a small gap value is allowed only in machine studies and not acceptable in user time due to the degradation of the beam injection efficiency and lifetime. For the present storage ring optics, the vertical betatron function takes a value of 5.6 m at the center of the normal straight section, and the minimum gap is limited to 5.6 mm to maintain stable top-up operation. To realize a gap of about 3 mm in user time, we need to modify the lattice locally to lower the vertical betatron function at this point to 1.2 m.

Figure 4 shows a design of a new lattice having a low-vertical beta straight section. The vertical betatron function will be lowered from 5.6 to 1.2 m, and this allows us to close the gap of the cryoundulator down to 3 mm. In this design of a new lattice, two families of quadrupole magnets are added to control the betatron functions at the center of the normal straight section, and the cabling of power supplies of adjacent three families of existing quadrupole magnets is changed so that they can be excited independently to fulfill matching conditions. The betatron tunes of the ring are then adjusted globally. Since the lattice functions in the rest of the ring and the emittance are unchanged, the performance of other beamlines will not be affected by this local lattice modification.

From the viewpoint of accelerator operation, however, the dynamic stability of the electron beam becomes slightly worse (the dynamic aperture shrinks by about 10 to 20%), since the symmetry of the lattice for the whole ring is broken and harmful resonances are excited. To recover the dynamic aperture and maintain the operational performance of the ring as high as possible, optimization of sextupole strengths will be carried out.

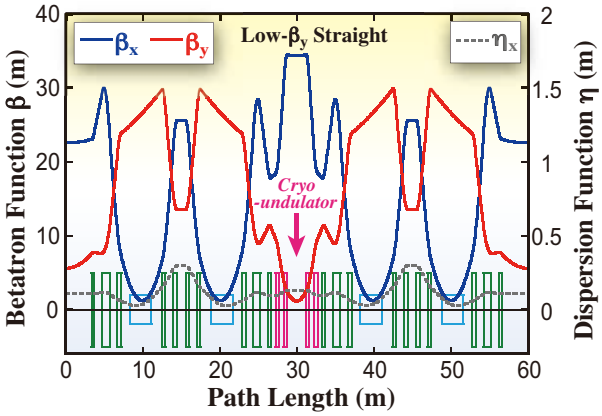

Fig. 4. Lattice functions in modified normal straight section. Also shown in the figure is the magnet arrangement (blue: bending magnets, green: quadrupole magnets, pink: quadrupole doublets to be added).

Development of Bunch-by-Bunch Feedback System

The filling mode of the storage ring named "H-mode", the hybrid filling with a 5 mA/bunch singlet and a 95 mA bunch-train of 11/29-filling with a low

bunch current of 0.1 mA/bunch, was added to the list of the user operation filling mode and was successfully put to user operation in December 2012. This mode fulfills the requests of the users of high-current isolated singlet bunch and those of high average current. The successful suppression of the beam instabilities by the SPring-8 bunch-by-bunch feedback (BBF) system is the key for this filling.

In such filling, the strong single-bunch instability of the high-current singlet and the multi-bunch instability of the bunch train, both in the horizontal and vertical betatron oscillations, have to be suppressed simultaneously by the BBF system. The BBF detects the bunch position with the beam position monitor (BPM) signal and drives the kicker to dump the oscillations. However, the BPM signal is proportional to the bunch current and to the position; hence, the BPM signal of the high-current singlet is too big for the BBF, the gain of which was tuned to the low bunch current of the bunch train. To overcome this problem, the bunch-current-sensitive fast attenuator [2] was developed to attenuate the BPM signal level of the high bunch current as shown in Fig. 5. Also, the high-efficiency horizontal kicker was installed to increase the controllable amplitude range to cover the large oscillation excited at injection.

Several attempts to increase the bunch current from 5 to 10 mA/bunch by suppressing the strong single-bunch beam instabilities are in progress, including the installation of the vertical feedback loop dedicated to the high-current singlet bunches for more flexible tuning than the fast attenuator, and the development of the new digital feedback processor. The new digital feedback processor under development can strengthen the feedback system, to update the devices for the FPGA, ADC and DAC, and to simplify the current system by merging the function of the feedback processor and the fast attenuator. In the fiscal year 2012, the hardware of the new processor composed of a brand-new Xilinx Virtex-7 FPGA board and 508 MS/s ADC/DAC boards was developed. The development of the FPGA program for the feedback operation and the PC program for the control of the FPGA board from PC through Ethernet is scheduled in the fiscal year 2013. The new feedback processor also has the capability to perform the planned new feedback schemes with which the single bunch current is intended to be raised to 10 mA/bunch from 5mA/bunch.

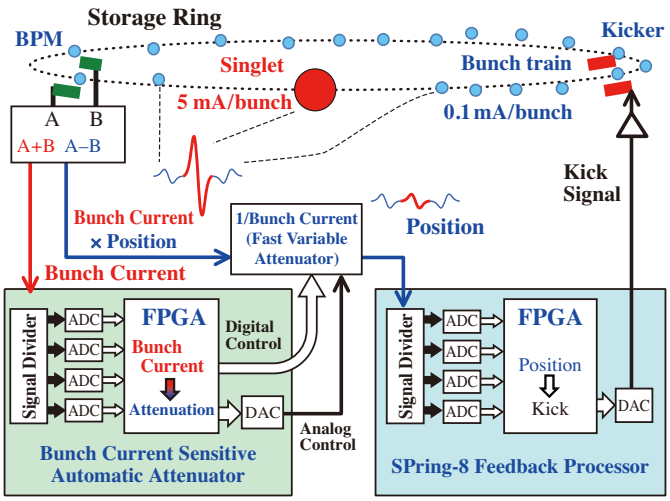

Fig. 5. Bunch current sensitive automatic attenuator (left) and feedback processor (right) for BBF for hybrid filling with high bunch current singlet and low bunch current bunch train.

At the low-energy high-current operation of the SPring-8 storage ring, longitudinal multi-bunch instability driven by high-order modes of the acceleration cavities was observed, and it degraded the beam quality. To suppress this instability, the longitudinal energy kicker (Fig. 6) based on the new concept [4] developed in SPring-8 was fabricated and installed in the storage ring. This new type of kicker has several times higher shunt impedance/length than the widely used overloaded cavity-type kicker. Also, the components of the longitudinal feedback system were prepared for the feedback operation scheduled in the fiscal year 2013.

Fig. 6. New high efficiency longitudinal energy kicker (3 kicker cells inside).

Development of Turn-by-Turn Beam Profile Monitor

The turn-by-turn beam profile monitor (TTPM) [4] observing monochromatic photon beam profiles of the ID has been developed. It enables us to observe fast phenomena, such as oscillations of the stored beam at top-up injections, blowups of transverse size and energy spread of a high-current single bunch caused by beam instabilities. The experimental setup of the TTPM is shown in Fig. 7. It consists of a

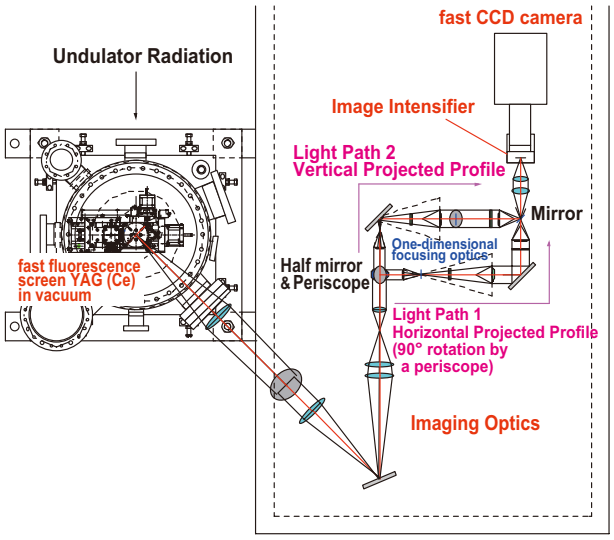

Fig. 7. Experimental setup of turn-by-turn beam profile monitor (TTPM) developed at diagnostics beamline II.

YAG (Ce) screen with decay time of several tens of nanoseconds, imaging optics and a fast CCD camera with an image intensifier (I.I.). The imaging optics of the TTPM transforms the 2D beam profile on the YAG (Ce) screen to the two line profiles projected on the horizontal and vertical axes. The fast gate by the microchannel plates (MCPs) of the I.I. selects the light from specific bunches out of all the stored bunches. The kinetics readout mode of the fast CCD camera (Roper Scientific: ProEM 512B) enables measurements with high repetition rates.

In Fig. 8, we show an example of angular oscillation of the photon beam axis of the ID observed with the TTPM at the top-up beam injection in user time. For injection, four bump magnets are excited by four individual pulsed power supplies to generate a pulsed bump orbit. A residual kick caused by the non-similarity of the temporal shape of the magnetic fields of the four pulsed magnets could excite a horizontal oscillation of the stored beam. Efforts have been made by tuning the fields of the four bump magnets to reduce the residual kick and by applying a counter kick of a fast correction magnet to the residual kick [5,6]. Although the residual kick at the temporal peak of the bump magnetic fields has been successfully suppressed, there still remains a significant kick to the stored beam at the rising part of the fields. Figure 8 shows the profiles of the photon beam of the ID obtained every 5 turns by using the kinetics readout mode of the fast CCD camera, by selecting with the I.I. those bunches suffered residual kick at the rising part of the bump magnetic fields. The maximum oscillation amplitude just after the injection turn corresponds to the angle of 20 μrad, which will hopefully be reduced by further tuning of the fast correction magnet on the basis of the oscillation measurements using the TTPM.

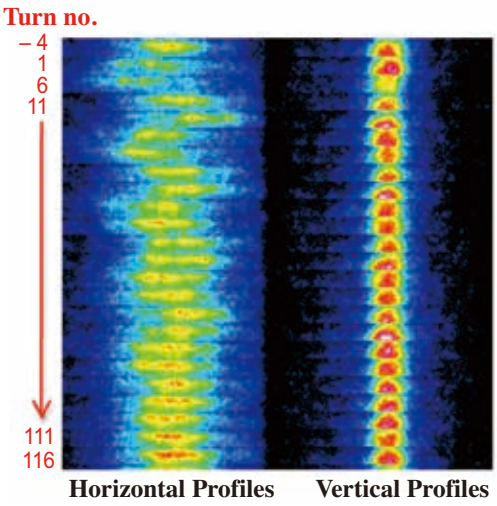

Fig. 8. Example of profiles of photon beam of ID obtained every 5 turns by TTPM. The left and right images are for horizontal and vertical profiles, respectively. The numbers on the left side show the turn numbers after top-up injection of which the turn of the bump orbit excitation is labeled as the zeroth turn (see text).

Development of Compact Fast-Pulsed Power Supply System

We have developed a compact fast-pulsed power supply system to supply the fast kicker magnet system since 2008, with the purposes of generating short-pulsed X-ray in the 1-ps region [7] and suppressing the residual beam oscillation at injection [8].

The location for installation of the kicker magnet had to be selected under the assuming that the existing main accelerator components are left unchanged, and giving the optimum phase advance to maximize the kicker effect. According to the restriction, the space allowed for installation was 30 cm long. To fulfill the required fast rise time with a compact size chassis that fits in the allowed small space, the power supply was divided into two parts: the driving circuit part and the main voltage supply part. The driving part was placed close to the kicker magnet with one turn air coil for reducing the load to the power supply (Fig. 9). In addition to the reduction of the occupied volume, an advantage of separating the power supply by two parts is the easy protection from scattered X-rays of synchrotron radiation because the power supply part

Fig. 9. Setup of power supply system in the accelerator tunnel. The power supply system is placed in the radiation and noise shield box.

is placed outside the accelerator tunnel.

To generate the fast-rise time short pulse with a large output current, a high voltage was supplied to the driving part and switched to the load through Si-MOSFETs (FET). The performance of the power supply largely depends on FET properties, especially the voltage resistance. The voltage resistance increased from 400 V in 2008 to 1200 V as of 2011, and using these 1200-V resistant devices, we have confirmed a 400-ns, 200-A pulsed output with 10-Hz repetition (Fig. 10). We expect the output of 500 A with the output driving module that is now under construction. To increase the output current, FETs were connected in a parallel-series configuration for the output stage. This configuration requires strict synchronization of switching FETs to obtain a short rise time and a large output current without invoking damage overload to the FETs.

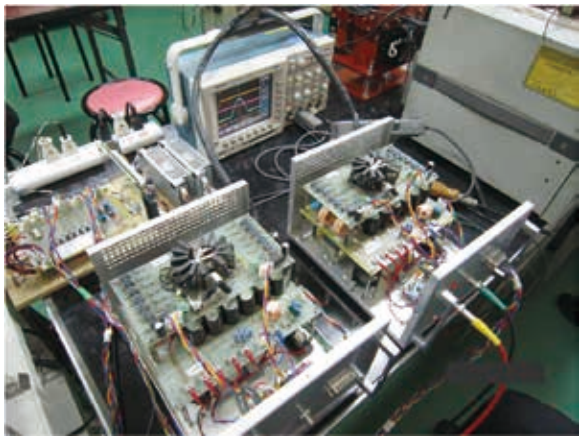

Fig. 10. Photo of improved compact fast-pulsed power supply system using serial-parallel MOSFET connection. With this module, the output of 200 A with a pulse width of 400 ns was achieved in 2012. The case size is 210(W) × 160(H) × 300(D) mm^3.

For practical use, trouble-free operation during user experiment runs is required. However, the power supply failures were caused by the following reasons; 1) high frequency noises caused by the beam wake fields, 2) high voltage induced by the kicked beam on the coil of the kicker magnet, 3) radiation damage from the scattered X-rays, 4) impedance mismatch between the power supply and the coil load that could induce an overvoltage, and 5) FET breakdown with overload caused by the switching of the parallel circuits out of synchronization. To reduce the risk of malfunction, reverse high voltage protection circuits were installed, as well as the radiation and noise shields. With the improvement of the protection circuits and noise and radiation shields, the power supply achieved continuous operation without failure for 40 days.

As the next step, we are planning to improve the power supply by adopting SiC-MOSFET, which has a higher resistance voltage, to reach the 1-kA region in the output current with 200-ns pulse width and 1-kHz repetition.

High Power Test of the Ceramic Window for Sealing WR-1500 Waveguide under Vacuum

We use beam-accelerating cavities resonating at 508.58 MHz in the SPring-8 storage ring and the booster synchrotron. RF input couplers are specific antennae that feed an RF (radio frequency) power into the cavities under vacuum. The power is transmitted from a klystron of RF source to the cavities with a circuit of WR-1500 rectangular waveguides. The coupler transduces the transmission line from the WR-1500 waveguide to a WX-D77 coaxial one terminated with a loop coupling to the cavity. A cylindrical ceramic window was brazed at the coaxial part of the coupler and seals the inside of the cavity in a vacuum. When the window happens to be damaged and leaked, the whole body of the coupler must be replaced with a new one since the brazed window cannot be detached. The replacement procedure is complicated and takes a long time. Therefore, we have developed a compact and replaceable ceramic window bolted to the WR-1500 waveguide to recover from the mechanical failure in a short time.

Figure 11 shows the fabricated window. It is a rectangular plate of low-loss alumina with a purity of 99.8% with a relative permittivity of 9.9 and dimensions of 258.6×80×5 in mm^3. The ceramic was brazed to a rectangular copper frame fitting to the waveguide. The compact body affords us easy

Fig. 11. Fabricated ceramic window for high-power RF input coupler.

assembly in sure vacuum seal and sound RF contact. The window was designed to transmit an RF power of 600 kW CW (continuous wave), which was twice as much as the maximum power in the current cavity operation. The VSWRs of the window were less than 1.1 in a wide frequency range of more than 30 MHz. Figure 12 shows 3D electromagnetic and structural simulations. The maximum electric fields were held down to 0.4 kV/mm in 600 kW operation and smaller than the breakdown limit of 16 kV/mm of the alumina. Two cooling channels with a water flow of 3 *l*/min are arranged on both sides of the ceramic; these channels remove the heat by power loss and reduce the thermal stress in the window to less than the proof stresses of copper and alumina.

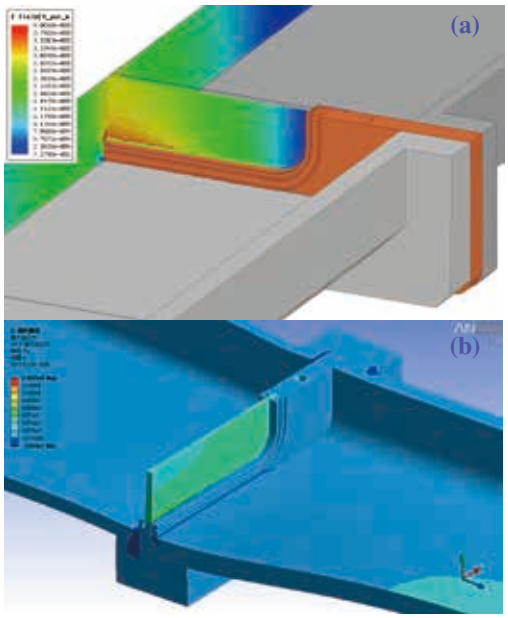

Fig. 12. 3D simulations of **(a)** electric fields and **(b)** stresses in window. The deformation in (b) is depicted exaggeratedly for easy tracing.

We assembled the window and a vacuum waveguide terminated with a short plate and tested it with a standing CW of 150 kW as shown in Fig. 13. The RF and heat loads to the window of the standing wave were almost equivalent to those by a travelling wave of 600 kW. We could successfully and stably transmit the rated RF power without vacuum leakage or damage to the window by RF processing in about 18 h.

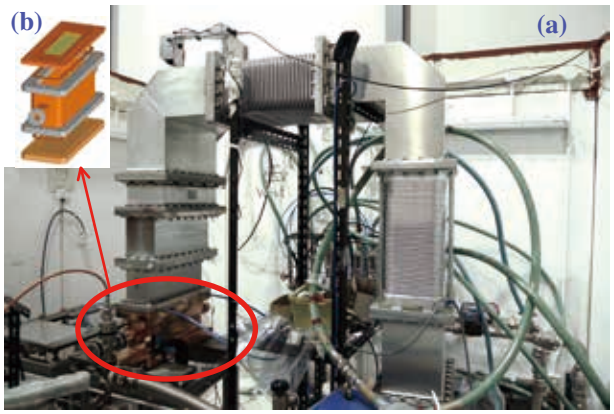

Fig. 13. **(a)** Setup of window for high-power test and **(b)** schematic drawing of window assembly.

Haruo Ohkuma, Shigeki Sasaki

SPring-8/JASRI

*Email: ohkuma@spring8.or.jp

References

[1] T. Tanaka and H. Kitamura: SPECRA code ver. 9.02 (2012).
[2] K. Kobayashi and T. Nakamura: Proc. ICALEPCS 2009, Kobe, Japan, p.659
[3] T. Nakamura: Proc. of IPAC '11, San Sebastian, Spain, p.493
[4] M. Masaki *et al.*: Proc. of IBIC2012, Tsukuba, Japan.
[5] SPring-8 Research Frontiers 2009, p.154.
[6] SPring-8 Research Frontiers 2010, p.152.
[7] C. Mitsuda *et al.*: J. Physics: Conference Series **425** (2013) 042012.
[8] C. Mitsuda *et al.*: Proc. of IPAC'10, Kyoto, Japan, p.2252.

New Apparatus, Upgrades & Methodology

Development of quick-scanning X-ray absorption spectroscopy system with servo-motor-driven channel-cut monochromator

Time-resolved quick-scanning X-ray absorption fine structure (QXAFS) techniques are powerful tools for *in situ* investigations of the dynamics of physical/chemical reactions that occur over time scales of seconds or shorter. Many QXAFS techniques have been developed over the last two decades. Frahm *et al*. acquired extended X-ray absorption fine structure (EXAFS) spectra with a repetition rate of up to about 40 Hz using a cam-driven monochromator at the undulator beamline at DESY [1]. Uruga *et al*. measured EXAFS spectra with a temporal resolution of 50 ms using a compact Si channel-cut crystal and a quasi-monochromatic helical undulator radiation over the energy range 8 – 17 keV [2].

A dedicated beamline **BL33XU** (Toyota beamline) commenced operation in 2009. It is designed to be used to research a wide variety of new materials for sustainable vehicle technologies, such as automobile exhaust catalysts, secondary batteries, and fuel cells. In studies of such functional materials, *in situ* time-resolved measurements are essential for determining the mechanisms that give rise to their functions. To realize this goal, we designed a novel QXAFS system with a temporal resolution of 10 ms [3].

A higher photon flux is required to obtain better quality spectra that can be used for XAFS analysis with a short scanning time. We employed a tapered undulator to obtain a high photon flux and to increase the energy bandwidth of XAFS measurements by tapering the gaps in the undulator magnet array. To realize 10 ms QXAFS measurements using intense undulator radiation, we designed a QXAFS monochromator system that consists of a compact channel-cut Si crystal and a high-speed direct-drive AC servo-motor.

The light source is a tapered in-vacuum undulator, which is the first tapered undulator installed at SPring-8. Figure 1 shows the spectral fluxes of the fundamental harmonic measured on the X-ray beam axis for an average gap width of 14 mm and two different taper ratios. The measured energy widths were 600 and 1700 eV for taper ratios of 0.5 mm/4.5 m and 2.0 mm/4.5 m, which are, respectively, suitable for XANES and EXAFS measurements.

The minimum temporal resolution of QXAFS is limited by the maximum oscillation frequency of the crystal, which depends on the inertia of the crystal and holders and on the torque of the servo motor. The monolithic Si channel-cut crystal was designed to reduce the rotational inertia of high-frequency mechanical oscillations. The crystal has a narrow 3-mm-wide gap between the reflecting planes, which enables the crystal to be downsized to 70×70×70 mm^3. The reflecting planes were fabricated inside the crystal by hollowing out the silicon block. The crystal is almost axially symmetric about the rotation axis of the monochromator. The first and second reflecting planes are arranged to be geometrically equivalent so that they are uniformly cooled, which reduces the throughput loss.

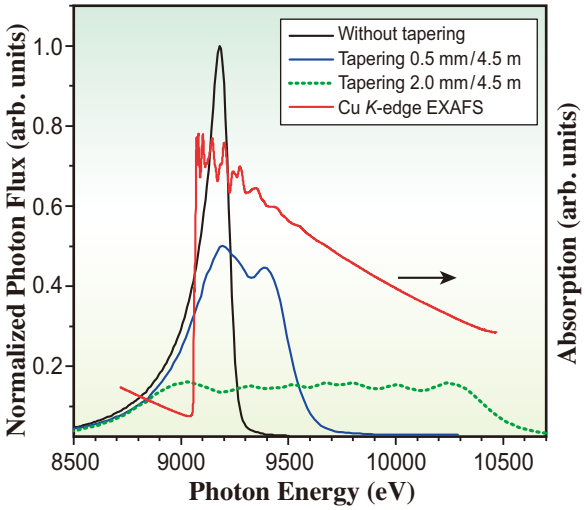

Fig. 1. Measured on-axis spectral flux of the fundamental harmonic of the tapered in-vacuum undulator (average gap width: 14 mm) and a Cu *K*-edge XAFS spectrum of a Cu foil obtained with 2.0 mm/4.5 m tapering.

Figure 2 shows a diagram of the interior of the servo-motor-driven monochromator. The channel-cut crystal is clamped on both sides by liquid-nitrogen-cooled copper blocks. This arrangement enables the crystal to be tightly held by the cooled blocks to withstand high-frequency oscillations, and it reduces deformation of the reflecting plane owing to the clamping force.

The crystal holder is rotated by a high-precision, high-torque AC direct-drive servo motor (Nikki Denso, D250-100-F) installed outside the vacuum vessel. A magnetic fluid rotary feedthrough seal unit (Rigaku Mechatronics) is used to transfer the rotary motion of

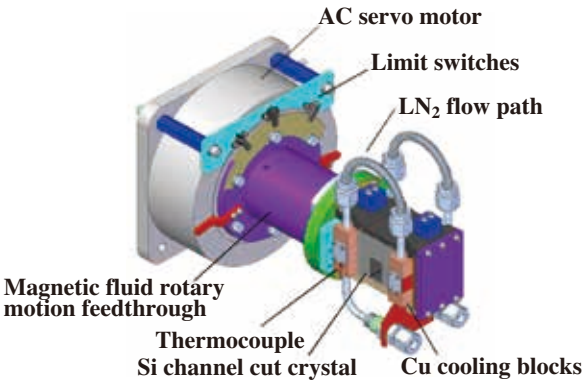

Fig. 2. Schematic of interior of the direct-drive servo-motor-driven monochromator.

the servo motor to the crystal holder inside the vacuum vessel. The angular resolution of the monochromator is 10^{-4} degrees (0.36 arcsec), which is determined by the resolution of the servo-motor internal encoder.

Two monochromators are aligned in tandem in the first experimental hutch of BL33XU. The monochromators with Si(111) or Si(220) crystals cover energy ranges of 4.0 – 28.2 keV and 6.6 – 46.0 keV, respectively. The Si(111) and Si(220) monochromators can be interchanged on the X-ray beam axis by using vertical translation stages without breaking the vacuum in the vessels.

A control system was constructed for three XAFS scanning modes with different temporal resolutions. Table 1 shows the specifications of these three scanning modes. For the continuous scanning mode, the undulator gap is tapered and the angular velocity of the servo motor has a triangular wave. However, for scanning faster than 0.5 Hz (i.e., a temporal resolution of less than 1 s), the servo motor cannot be oscillated with a triangular wave due to the inertia of the crystal and the holder; instead, it is oscillated with a sinusoidal wave (termed the super quick scan mode). For XAFS scans that require long measurement times, the servo motor is rotated incrementally and the undulator gap is not tapered; rather, it is tuned to maximize the photon flux at each measurement point (step scan mode). These three scan modes can be switched in a very short time and the energy ranges of scans, the starting angles of oscillations, and the frequencies can be adjusted instantly. The control and measurement system is fully operated by a PC using user-friendly application software written in LabVIEW.

Table 1. Specifications of three XAFS scanning modes available with the system.

Mode	Super quick scan	Continuous scan	Step scan
Temporal resolution	< 1 s	1 s – 1 min	>1 min
Motion pattern	Sinusoidal wave	Triangular wave	Incremental
Undulator gap	Tapered	Tapered	Non-tapered
Data acquisition	ADC	Counter /ADC	Counter

The QXAFS system was characterized by conducting performance tests in the superquick scan mode. Figure 3 shows XANES spectra of a Cu foil measured at different scan speeds with an angular range of 0.2° using the Si(111) monochromator. The undulator gap had a taper ratio of 0.5 mm/4.5 m. The pre-edge spectrum (around 8980 eV), which represents metallic Cu, is clearly visible even in the 50 Hz oscillation spectra. The signal-to-noise ratio of the 50 Hz oscillation spectra is sufficiently high for analysis owing to the high incident X-ray flux from the tapered undulator and to the low-noise data acquisition system. These results indicate that our QXAFS system (including the light source, beamline optics, and measurement system) operates effectively with a temporal resolution of up to 10 ms.

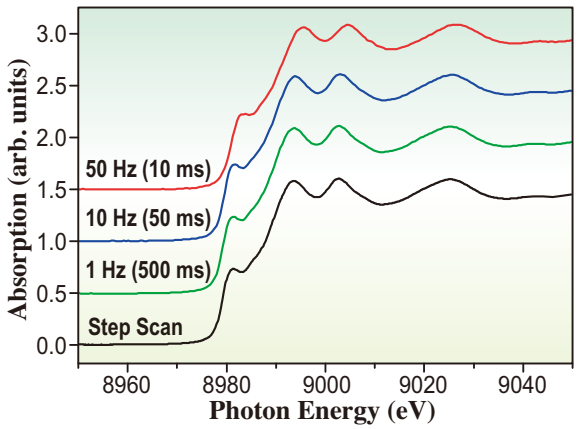

Fig. 3. Cu *K*-edge XANES spectra of 6-μm-thick Cu foil measured in superquick scan mode using the Si(111) channel-cut crystal (undulator gap taper: 0.5 mm/4.5 m). A step scan spectrum is also shown for comparison.

Takamasa Nonaka

Toyota Central R&D Labs., Inc.

Email: nonaka@mosk.tytlabs.co.jp

References

[1] R. Frahm *et al.*: Phys. Scr. **T115** (2005) 974.
[2] T. Uruga *et al.*: AIP Conf. Proc. **882** (2007) 914.
[3] *T. Nonaka, K. Dohmae, T. Araki, Y, Hayashi, Y. Hirose, T. Uruga, H. Yamazaki, T. Mochizuki, H. Tanida and S. Goto: Rev. Sci. Instrum.* ***83*** *(2012) 083112.*

New XAFS beamline BL36XU for catalytic reaction dynamics for fuel cells

Recently, the development of a low carbon society has become a countermeasure against problems of global climate warming or exhaustion of resources. Fuel cells that generate electricity from hydrogen and oxygen are one of the most promising technologies for green energy creation. Crucial issues to be resolved for developing next-generation polymer electrolyte fuel cells (PEFCs) are the improvement of activity, achievement of high durability, and reduction in the cost of Pt/C cathode catalysts. A schematic drawing of PEFC is shown in Fig. 1. To use PEFCs particularly in automobiles, it is necessary to clarify the dynamic aspects of structures and electronic states, the kinetics/dynamics of the cathode catalysts in membrane electrode assemblies (MEAs), and chemical reaction mechanisms at cathode catalyst surfaces under PEFC operating conditions and in deterioration processes.

Temporally and spatially resolved X-ray absorption fine structure (XAFS) techniques are very powerful in the investigation of the structure and chemical states of nanoparticle catalysts under *in situ* working conditions, especially in such complex systems as PEFCs. To investigate the elementary steps in the practical catalytic reaction mechanism and deterioration process of PEFCs in real time, XAFS measurements with time resolutions of 100 μs to 1 s are required. Also, the catalyst layer of MEAs is a microscopically heterogeneous dispersed system consisting of a spatially complex mixture of catalyst, support, ionomer and water, and requires spatial resolutions of 100 nm to 10 μm for XAFS measurements. However, there was no beamline capable of conducting the XAFS measurements with such high time and spatial resolutions.

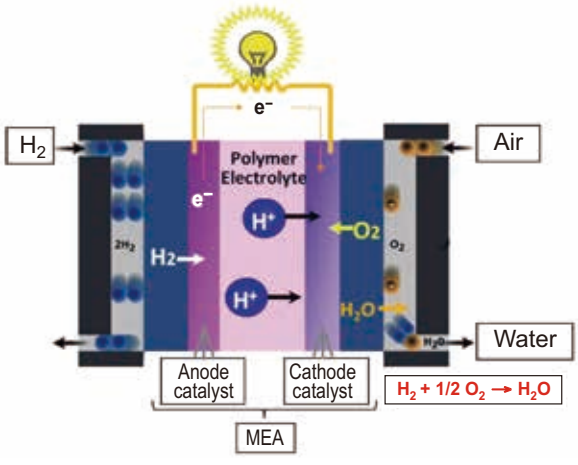

Fig. 1. Schematic drawing of PEFC.

Therefore, we constructed a new XAFS beamline **BL36XU** [1] under a New Energy and Industrial Technology Development Organization (NEDO) program, which provides highly temporally and spatially resolved XAFS methods specialized for the structural and electronic analyses of the dynamic events on the cathode catalysts in PEFC MEAs. The target specifications of BL36XU are as follows: time resolutions of 800 μs by quick XAFS and 100 μs by energy dispersive XAFS (DXAFS), a two-dimensional in-plane spatial resolution of 200 nm, and a 3-dimensional resolution of 1 μm for MEA samples. The energy range is from 4.5 to 35 keV, which covers absorption edges of almost all metal elements used for the PEFC catalysts.

Figures 2 and 3 show the schematic layout and arrangement of the main components of the beamline, respectively. The design of the synchrotron light source and optics is a SPring-8 standard, and results in both quick XAFS measurements with 10 ms time resolution and spatially resolved measurements using 100-nm-order X-ray beams. The light source is an in-vacuum-type tapered undulator for adjusting the energy width of an X-ray suited for quick XAFS and DXAFS measurements. The hutches consist of one optics hutch and one experimental hutch. The experimental hutch is located 77 m from the light source to obtain a high reduction ratio of the focusing mirror.

The main X-ray optics consists of four mirrors and two monochromators. The mirrors are used for two-dimensional focusing of X-rays on the 100 μm level and higher harmonics rejection. Two servo-motor-driven compact monochromators [2] with a channel-cut Si (111) crystal for 4.5 – 28 keV and a Si (220) crystal for 7 – 35 keV are tandemly arranged to realize 10-ms-time-resolved quick XAFS measurements.

For 800-μs-time-resolved quick XAFS measurement, the servo-motor-driven monochromator is removed from the beam axis, and instead, a newly developed galvano scanner motor driven monochromator [3] is set in the experimental hutch. The monochromator has a compact channel-cut Si crystal installed in a He chamber and has no active cooling devices for reducing the rotational inertia for fast angle scanning. The heat load of the undulator radiation on the monochromator crystal can be reduced to less than 5 W by rejecting higher harmonics using the mirrors and by limiting the incident beam size using the front-end slit.

A 100-μs-time-resolved DXAFS method is especially used for model samples of PEFC with

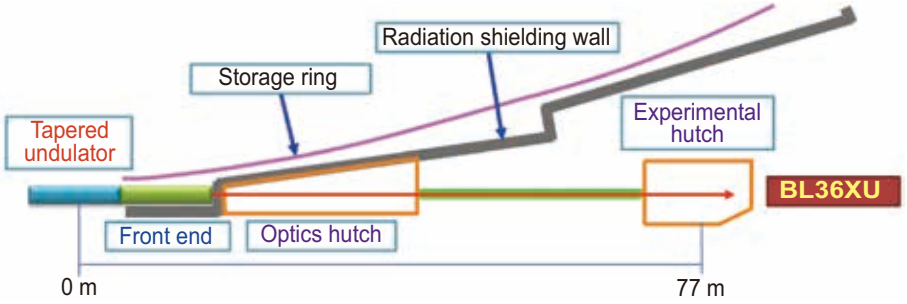

Fig. 2. Layout of BL36XU.

high catalyst concentration to obtain information on the faster elementary steps in a cathode catalytic reaction. To cover a wide energy range, two types of polychromator configuration, i.e., Bragg configuration for 4.5 – 12 keV and Laue configuration for 12-35 keV, are installed.

Two types of 2-dimensional imaging XAFS methods are available in BL36XU depending on the catalyst concentration in MEAs. For high-concentration samples, the transmission microscopic XAFS method is used. X-ray images transmitted through the sample are measured using a 2-dimensional X-ray imaging detector. The field of view and spatial resolution are about 500×500 μm^2 and 1×1 μm^2, respectively. For low-concentration samples, a fast scanning microscopic XAFS system [4] is installed. In this method, 2-dimensional X-ray fluorescence images are measured by fast scanning of a sample at each energy point of the XAFS measurement. The X-ray beam is focused to about 100×100 nm^2 at the sample using a Kirkpatrick-Baez mirror.

A laminography XAFS measurement system based on that developed at BL47XU [5] is installed for measuring a 3D XAFS image of the MEA of PEFCs. X-ray laminography is a 3D image reconstruction method applicable for to membrane samples. The 3D X-ray laminography images are measured at each energy point of the XAFS measurement to obtain a 3D XAFS image. The field of view and spatial resolution are about $500 \times 500 \times 500$ μm^3 and $1 \times 1 \times 1$ μm^3, respectively.

The beamline commissioning was finished at the end of 2012 and BL36XU was opened for user experiments in Jan. 2013.

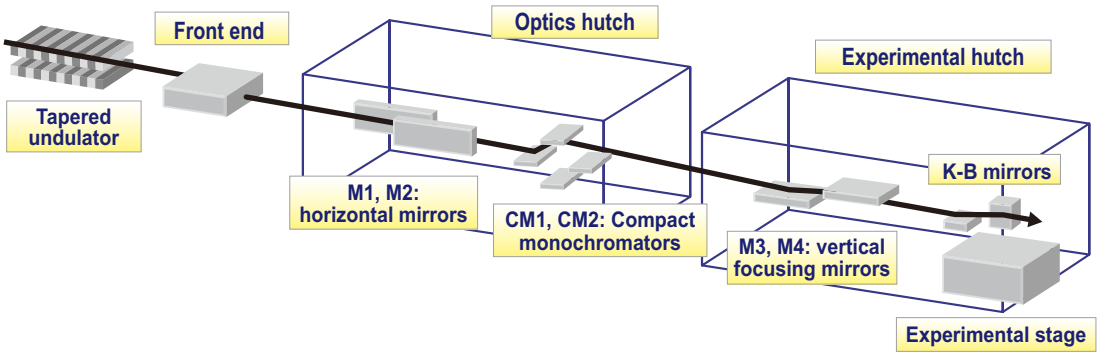

Fig. 3. Arrangement of main components of BL36XU.

Tomoya Uruga[a,b], Mizuki Tada[c] and Yasuhiro Iwasawa[a,*]

[a] Innovation Research Center for Fuel Cells, The University of Electro-Communications
[b] SPring-8/JASRI
[c] Institute for Molecular Science

*Email: iwasawa@pc.uec.ac.jp

References

[1] *O. Sekizawa, T. Uruga, M. Tada, K. Nitta, K. Kato, H. Tanida, K. Takeshita, S. Takahashi, M. Sano, H. Aoyagi, A. Watanabe, N. Nariyama, H. Ohashi, H. Yumoto, T. Koyama, Y. Senba, T. Takeuchi, Y. Furukawa, T. Ohata, T. Matsushita, Y. Ishizawa, T. Kudo, H. Kimura, H. Yamazaki, T. Tanaka, T. Bizen, T. Seike, S. Goto, H. Ohno, M. Takata, H. Kitamura, T. Ishikawa, T. Yokoyama and Y. Iwasawa: J. Phys.: Conf. Ser.* ***430*** *(2013) 012019.*
[2] T. Nonaka *et al.*: Rev. Sci. Instrum. **83** (2012) 083112.
[3] T. Uruga *et al.*: AIP Conf. Proc. **882** (2007) 914.
[4] T. Tsuji *et al.*: J. Phys.: Conf. Ser. **430** (2013) 012020.
[5] T. Saida *et al.*: Angew. Chem. Int. Ed. **51** (2012) 10311.

Facility Status

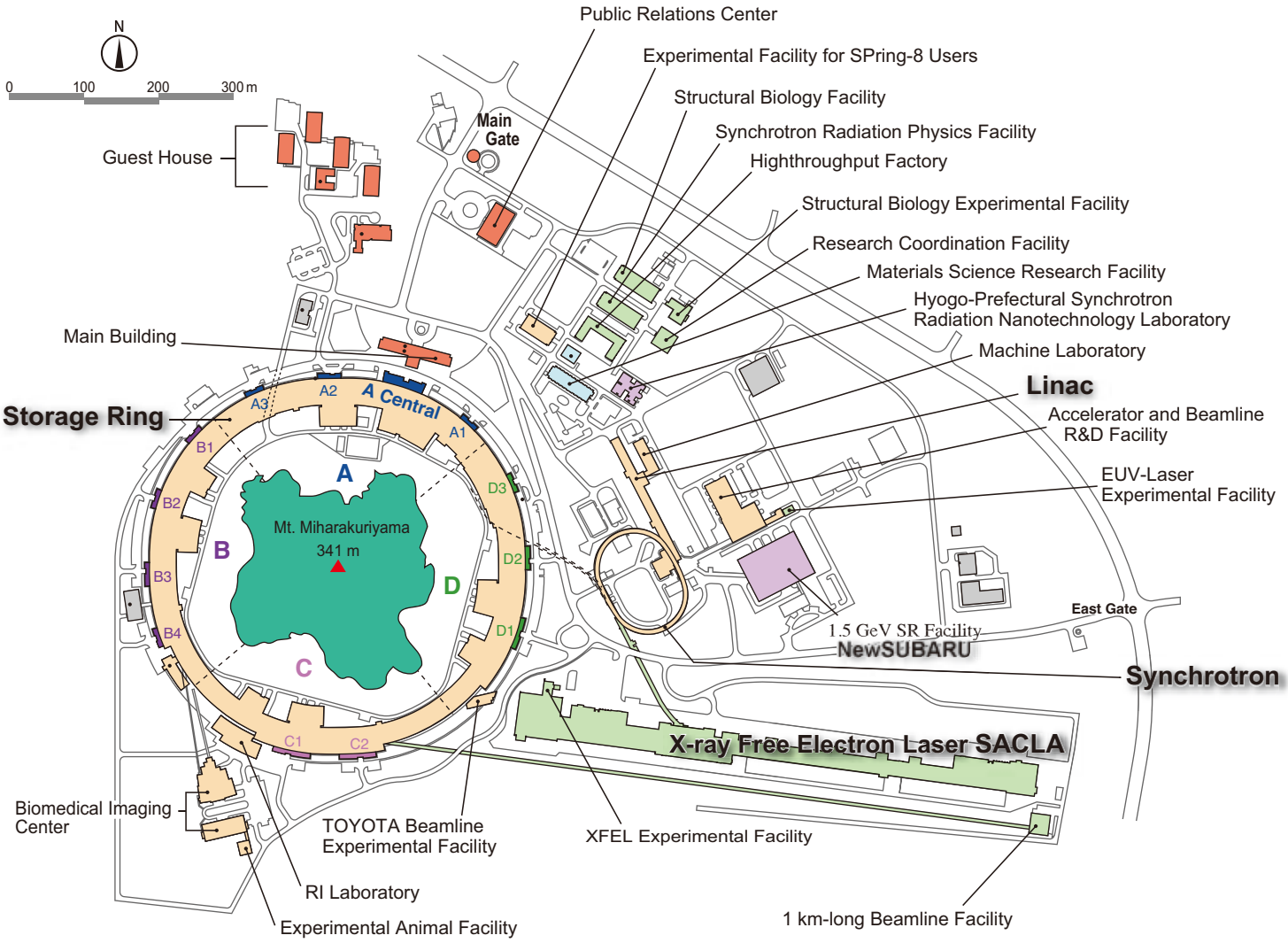

I. Introduction

General

Among the various problems that the Great East Japan Earthquake still continues to cause, the tight electricity situation is one of the central problems. Once deactivated for periodic inspection, none of the nuclear power plants has so far been approved to resume operation under the austere inspection procedure newly implemented, thus making it difficult for electricity companies to stably supply electricity. Hence, the local electricity company requested large-scale power consumers, including SPring-8, to reduce their power consumption by 15% in the summer of 2012 as part of the measures to avoid large-scale blackout.

Consequently, SPring-8 had to halt the use of its X-ray beams in July 2012 and February 2013 to conform with the above request. Under such circumstances, however, SPring-8 endeavored to maximize the user time as much as possible by minimizing the time for studying and maintaining the accelerator complex and the beamlines, and by redesigning the facility logistics. In fact, SPring-8 was able to provide more than 4156 hours with a beam-loss time of only 39 hours.

New Contract Beamlines

SPring-8 continue to dynamically evolve throughout the year of 2012, as it has since its inauguration in 1997. Three new contract beamlines were inaugurated, further diversifying the beamline portfolio of SPring-8. They are the (i) “RISING” beamline at BL28XU of Kyoto University to analyze rechargeable batteries, (ii) “Catalytic Reaction Dynamics for Fuel Cells” beamline at BL36XU of The University of Electro-Communications to conduct research activities indicated by its name, and (iii) “Laser-Electron Photon II” beamline at BL31LEP of Research Center for Nuclear Physics, Osaka University to challenge the frontier of quark-nucleon physics, focusing on pentaquarks.

User Community

It is extremely important for the dynamically advancing SPring-8 to coherently work with a well-organized user community not only to make SPring-8 user-oriented for the present, but also to keep SPring-8 at the forefront for the future as well. At this time, therefore, SPring-8 would like to congratulate and

to express its respect to all its users for successfully establishing their own community, i.e., SPring-8 Users Community (SPRUC), which has more than 10,000 registered members.

Despite still being in the early stage, SPRUC exhibited enthusiastic initiative in organizing SPring-8 Symposium 2012 with Japan Synchrotron Radiation Research Institute (JASRI) and RIKEN, held at Osaka University, August 25-26, where SPRUC proactively discussed the present/future position of SPring-8 among other synchrotron radiation facilities in Japan. For Japan Synchrotron Radiation Research Institute (JASRI), it was fruitful to carry out an attitude survey of SPring-8 users with emphasis on the upgrade/future plan of SPring-8 in collaboration with SPRUC.

"Combinational Utilization" of SPring-8, J-PARC, and K-Computer

Since X-ray and neutron data for the same sample often become much clearer and convincing when complementally combined with each other, it is a natural consequence to attempt to for establish such a utilization framework within which SPring-8 users could employ neutron beams at the Materials and Life Science Experimental Facility (MLF) as J-PARC users, and vice versa. Collectively calling X-ray beams and neutron beams as Quantum Beams, such a utilization scheme could be named the Quantum Beam Platform. It is also clear that it should include K-computer utilization as well in order to accommodate hyper-science consisting of quantum beam science and computer science.

Being the Registered Institutions for Facilities Use Promotion of SPring-8, J-PARC/MLF, and K-computer, respectively, JASRI, Comprehensive Research Organization for Science and Society (CROSS), and Research Organization for Information Science and Technology (RIST) signed a trilateral cooperation agreement June 1, 2012, in order to establish the above-described utilization scheme among the three advanced scientific infrastructures as early as possible. As the first step towards this direction, JASRI started inviting proposals for complementary use with J-PARC/MLF on a trial basis this year, in collaboration with CROSS. Successful proposals were carried out in the period of 2013A.

Industrial Applications

Compared with other synchrotron radiation facilities in the world, it is a particular characteristic of SPring-8 that industrial applications not only account for ~20% of the proposals approved, but also cover a wide spectrum from electronics to health care. Since synchrotron radiation facilities are expected to directly contribute to society through industrial applications, it was a great pleasure for SPring-8 to host the 3rd SPring-8-Diamond Joint Workshop for Industrial Applications of Synchrotron Radiation, which was held on the SPring-8 campus and at Kobe, May 21–23, 2012. In accordance with the guideline indicated by the UK-Japan Joint Commission on Cooperation in Science and Technology held November 28-29, 2011, London, the workshop covered a wide range of industrial applications conducted at SPring-8 and Diamond Light Source with special emphasis on "Energy" in light of the lessons gained from the global energy agenda, and in particular, from the Great East Japan Earthquake.

International Collaborations

As part of its continuous contribution to synchrotron radiation science communities in the Asia-Oceania region, SPring-8 provided a venue for Cheiron School 2012, which was designed to offer useful and basic knowledge and perspectives of synchrotron radiation science and technology to young scientists and engineers in this region.

To facilitate international collaborations in synchrotron radiation science and technology, SPring-8 concluded the Memorandum of Understanding (MoU) with Canadian Light Source (CLS) in Canada, November 2012. On the basis of this fruitful relationship, SPring-8 extended the MoU with Paul Scherrer Institute (PSI) in Switzerland, October 2012, and Deutsches Elektronen-Synchrotron (DESY) in Germany, February 2013, including research collaboration in the field of free electron laser technology.

Reviews

There were two external review committees organized by JASRI: (i) for research activities conducted by JASRI staff mainly using SPring-8 public beamlines, to facilitate its utilization as part of the missions of JASRI as a Registered Institution for Facilities Promotion, and (ii) the Nanotechnology Support Proposal that was designated as one of the Priority Research Programs from 2007 for five years at SPring-8 from the viewpoint of strategic importance in accordance with the Basic Program for Science and Technology decided by the Japanese Government.

II. Machine Operation

The operation statistics for the last five fiscal years are shown in Fig. 1. In FY2012, the total operation time of the accelerator complex was 5078.8 h. The operation time of the storage ring was 5063.1 h, 82.1% of which (4155.6 h) was made available for SR experiments. The downtime resulting from failure accounted for 0.94% (39.2 h) of the total user time. In FY2012, no great loss of user time exceeding several hours occurred. Since FY2004, top-up injection was introduced. Concerning user service operation, a high availability (ratio of net user time to planned user time), e.g., 98.9%, was achieved in FY2012. The total tuning and study time of 884 h was used for machine tuning, for the study of the linac, booster synchrotron and storage ring, and also for the beamline tuning and study.

Operations in two different filling modes were provided for the following user time: 60.6% in the several-bunch mode, such as the mode of 29 equally spaced trains of 11 bunches, and 39.4% in the hybrid filling mode, such as the mode of 1/14-partially filled multi-bunch with 12-isolated bunches. In FY2012, there was no operation in the multi-bunch mode. The several-bunch mode was the dominant filling mode. The 203-bunch mode and the mode of 29 equally spaced trains of 11 bunches reached 29.8% and 30.9% of the total user time, respectively. The new hybrid filling mode of 11/29-partially filled multi-bunch with a 5.0 mA isolated bunch. For the hybrid filling mode, 1.0 mA, 1.6 mA, 3.0 mA, or 5.0 mA is stored in each isolated bunch. An isolated bunch impurity better than 10^{-10} is routinely maintained in the top-up operation. Table I shows a summary of the useful beam parameters of the storage ring. Table II shows a summary of the beam filling patterns.

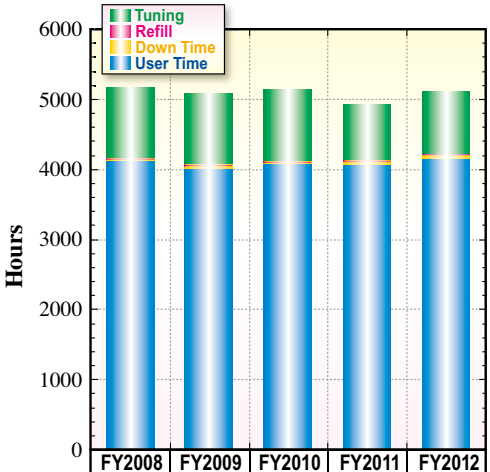

	FY2008	FY2009	FY2010	FY2011	FY2012
Accelerator Operation Time	5150.1	5068.8	5125.6	4918.6	5078.8
Storage Ring Operation Time	5133.3	5035.4	5096.3	4904.2	5063.1
Tuning & Study (Acc. & BL)	1008.2	1019.1	1026.6	803	884
Refill	10.1	6.3	5.0	4.4	5.2
Down Time	31.0	34.8	27.5	57	39.2
Mean Time Between Failures	153.8	122.9	178.4	117.7	107.7
Achieved User Time	4110.9	4014.9	4071.6	4058.5	4155.6
Planning User Time	4152.0	4056.0	4104.0	4120.0	4200.0
Availability (%)	99.0	99.0	99.2	98.5	98.9

Fig. 1. Operation statistics for the last five fiscal years.

Table I. Beam parameters of SPring-8 storage ring

Energy [GeV]	8
Number of buckets	2436
Tunes (ν_x / ν_y)	40.14 / 19.35
Current [mA]:	
single-bunch	12
multi-bunch	100
Bunch length (σ) [psec]	13
Horizontal emittance [nm·rad]	3.5 *
Vertical emittance [pm·rad]	6.9 *
Coupling [%]	0.2
RF Voltage [MV]	16
Momentum acceptance [%]	±3 (±240 MeV)
Beam size (σ_x / σ_y)* [μm]	
Long ID section	297 / 10
ID section	303 / 6
BM1 section	108 / 13
BM2 section	115 / 14
Beam divergence (σ_x' / σ_y')* [μrad]	
Long ID section	13 / 0.7
ID section	12 / 1.1
BM1 section	57 / 0.6
BM2 section	74 / 0.6
Operational chromaticities (ξ_x / ξ_y)	+1 / +1**
Lifetime [h] :	
100 mA (multi-bunch)	~200
1 mA (single-bunch)	~20
Horizontal dispersion [m]:	
Long ID section	0.103
ID section	0.107
BM1 section	0.032
BM2 section	0.070
Fast orbit stability (0.1 – 200 Hz) [μm]:	
horizontal (rms)	~4
vertical (rms)	~1

* Assuming 0.2% coupling
** With bunch-by-bunch feedback

Table II. Filling patterns

	bunch current (mA)	life time (h)
203 bunches	0.5	25 ~ 30
11 bunch-train × 29	0.3	35 ~ 50
11/29 - filling + 1 single bunch	5.0 (single)	40 ~ 50
1/7 - filling + 5 single bunches	3.0 (single)	18 ~ 25
1/14 - filling + 12 single bunches	1.6 (single)	18 ~ 25
4/58 - filling + 53 single bunches	1.0 (single)	18 ~ 25

III. Beamlines

The SPring-8 storage ring can accommodate up to 62 beamlines: 34 insertion devices, 4 long undulators, and 24 bending magnets. At the time of writing, 55 beamlines are in operation, covering a wide variety of research fields of synchrotron radiation science and technology. The beamlines are classified into the following four types.

(1) Public Beamlines
(2) Contract Beamlines
(3) RIKEN Beamlines
(4) Accelerator Diagnostics Beamlines

There are now 26 public beamlines in full operation. The beamlines, that are proposed and constructed by external organizations, such as universities, research institutes, and private companies, are called contract beamlines and exclusively used by the contractors for their own research purposes. At present, 19 contract beamlines are in operation. The contract beamlines include NSRRC BM (BL12B2) and NSRRC ID (BL12XU) beamlines, which were constructed by the National Synchrotron Radiation Research Center in Taiwan. In January 2013, Catalytic Reaction Dynamics for Fuel Cells beamline (BL36XU) constructed by the University of Erectro-Communications has started operation. Laser-Electron Photon II beamline (BL31LEP) will be in operation to users in September 2013. The beamlines constructed by RIKEN are called RIKEN beamlines, and used for RIKEN's own research activities. RIKEN is now operating nine RIKEN beamlines and reconstructing one beamline. In addition, two accelerator diagnostics beamlines are in operation.

To display the beamline portfolio of SPring-8, the beamline map is shown in Fig. 2 together with the beamline classification. The research field of each beamline is presented in Table III.

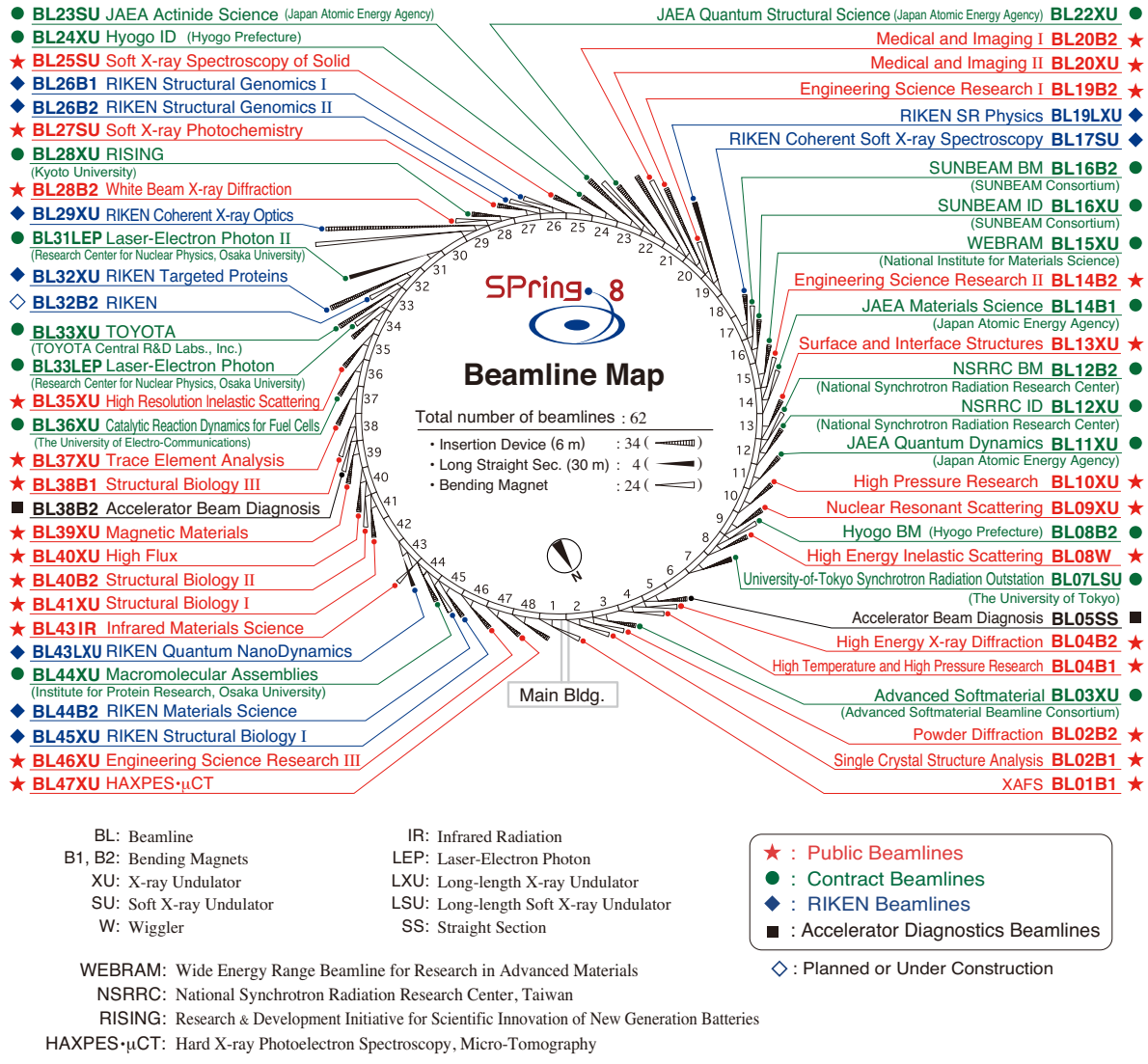

Fig. 2. Beamline map.

Table III. List of beamlines

BL #	Beamline Name	(Public Use) or (First Beam)	Areas of Research
★ Public Beamlines			
BL01B1	XAFS	(Oct. 1997)	XAFS in wide energy region (3.8 to 113 keV). XAFS of dilute systems and thin films. Quick XAFS with a time resolution of seconds to as tenth seconds.
BL02B1	Single Crystal Structure Analysis	(Oct. 1997)	Precise crystal structure analysis using high resolution data of single crystal (X-ray energy: 8–115 keV). Magnetic resonant X-ray scattering.
BL02B2	Powder Diffraction	(Sep. 1999)	Accurate structure analysis of crystalline materials using powder diffraction data by Rietveld refinements and maximum entropy method (MEM).
BL04B1	High Temperature and High Pressure Research	(Oct. 1997)	Mineral physics at high temperature and high pressure. Energy-dispersive X-ray diffraction and X-ray radiography using the large-volume press.
BL04B2	High Energy X-ray Diffraction	(Sep. 1999)	Structural analysis of glass, liquid, and amorphous materials. X-ray diffraction under ultra high-pressure.
BL08W	High Energy Inelastic Scattering	(Oct. 1997)	Magnetic Compton scattering. High-resolution Compton scattering. High-energy Bragg scattering. High-energy fluorescent X-ray analysis.
BL09XU	Nuclear Resonant Scattering	(Oct. 1997)	Lattice dynamics using nuclear inelastic scattering. Time domain Mössbauer spectroscopy, especially under the extreme conditions. Nuclear excitation by electron transition (NEET).
BL10XU	High Pressure Research	(Oct. 1997)	Structure analysis and phase transitions under ultra high pressure (DAC experiment). Earth and planetary science.
BL13XU	Surface and Interface Structures	(Sep. 2001)	Atomic-scale structural analysis of surfaces and interfaces of crystalline materials, ultra-thin films, and nanostructures. Surface X-ray diffraction (SXRD). Microbeam diffraction.
BL14B2	Engineering Science Research II	(Sep. 2007)	XAFS in wide energy region (3.8 to 72 keV). XAFS of dilute systems and thin films.
BL19B2	Engineering Science Research I	(Nov. 2001)	Residual stress measurement. Structural analysis of thin film, surface, interface. Powder diffraction. X-ray imaging, X-ray topography. Ultra-small angle X-ray scattering.
BL20XU	Medical and Imaging II	(Sep. 2001)	Microimaging. Hard X-ray microbeam/scanning microscopy, imaging microscopy, microtomography, phase-contrast microtomography with Bonse-Hart interferometer, X-ray holography, coherent X-ray optics, and other experiments on X-ray optics and developments of optical elements. Medical application. Microangiography, refraction-enhanced imaging, radiation therapy, phase-contrast CT using interferometer. Ultra-small angle scattering.
BL20B2	Medical and Imaging I	(Sep. 1999)	Microimaging: microtomography, phase-contrast microtomography with Bonse-Hart interferometer and grating interferometer for biological specimen and other kinds of specimen. Evaluation and development of various kinds of optical elements for novel imaging techniques. Large field X-ray topography.
BL25SU	Soft X-ray Spectroscopy of Solid	(Apr. 1998)	Observation of electronic structures by photoemission spectroscopy (PES). Observation of electronic band structures by angle resolved photoemission spectroscopy (ARPES). Magnetic state study by magnetic circular dichroism (MCD) of soft X-ray absorption. Element-specific magnetization curve measurements by MCD analysis of atomic arrangements by photoelectron diffraction (PED). Observation of magnetic domains by photoelectron emission microscope (PEEM).
BL27SU	Soft X-ray Photochemistry	(May 1998)	Ambient atmospheric pressure Soft X-ray photoabsorption spectroscopy. Chemical state analysis of light elements in dilute samples (NEXAFS). High resolution atomic and molecular electron spectroscopy. Dissociation dynamics of inner-shell excited molecules. (Molecular science) Photoemission and soft-X-ray emission spectroscopy for solids. (Solid state and surface physics)
BL28B2	White Beam X-ray Diffraction	(Sep. 1999)	White X-ray diffraction and topography. Time-resolved energy-dispersive XAFS (DXAFS) for studies of chemical and/or physical reaction process. Biomedical imaging and radiation biology studies.
BL35XU	High Resolution Inelastic Scattering	(Sep. 2001)	Material dynamics on ~meV energy scales using inelastic X-ray scattering (IXS) and, sometimes, nuclear resonant scattering (NRS).
BL37XU	Trace Element Analysis	(Nov. 2002)	X-ray microbeam spectrochemical analysis. Ultra trace element analysis. High energy X-ray fluorescence analysis.
BL38B1	Structural Biology III	(Oct. 2000)	Structural biology. Macromolecular crystallography. Automatic data collection.
BL39XU	Magnetic Materials	(Oct. 1997)	X-ray magnetic circular dichroism (XMCD) spectroscopy and element-specific magnetometry under multiple-extreme conditions. XMCD/XAS using a sub-micron X-ray beam. X-ray emission spectroscopy. Resonant X-ray magnetic scattering.
BL40XU	High Flux	(Apr. 2000)	Time-resolved diffraction and scattering experiments. Microbeam X-ray diffraction and scattering experiments. X-ray photon correlation spectroscopy. Fluorescence analysis. Quick XAFS.
BL40B2	Structural Biology II	(Sep. 1999)	Noncrystalline small and wide angle X-ray scattering.
BL41XU	Structural Biology I	(Oct. 1997)	Structural biology. Macromolecular crystallography. Data collection from small crystals and large unicell crystals. Ultra-high resolution data collection.
BL43IR	Infrared Materials Science	(Apr. 2000)	Infrared microspectroscopy. Magneto-optical spectroscopy.
BL46XU	Engineering Science Research III	(Nov. 2000)	Structural characterization of thin films by X-ray diffraction and X-ray reflectivity measurement. Residual stress measurement. Time resolved X-ray diffraction measurement. Hard X-ray photoemission spectroscopy.
BL47XU	HAXPES·μCT	(Oct. 1997)	Hard X-ray photoelectron spectroscopy (HAXPES). Depth analysis of angle resolved HAXPES with wide acceptance lens. Projection type microtomography. Imaging type microtomography. Hard X-ray microbeam/scanning microscopy.

BL #	Beamline Name	(Public Use) or (First Beam)	Areas of Research
	● Contract Beamlines		
BL03XU	**Advanced Softmaterial** (Advanced Softmaterial Beamline Consortium)	(Nov. 2009)	Structural characterization of softmaterials using small- and wide-angle X-ray scattering. Grazing-incidence small- and wide-angle X-ray scattering for thin films. X-ray diffraction and reflectivity measurements for softmaterials.
BL07LSU	**University-of-Tokyo Synchrotron Radiation Outstation** (The University of Tokyo)	(Oct.2009)	Time-resolved soft X-ray spectroscopy, nano-beam photoemission spectroscopy, ultra high-resolution soft X-ray emission spectroscopy, and any methods requiring the highly brilliant soft X-ray beam.
BL08B2	**Hyogo BM** (Hyogo Prefecture)	(Jun. 2005)	XAFS in a wide energy region. Small angle X-ray scattering for structural analyses of polymer and nanocomposite materials. X-ray topography. Imaging. Powder diffraction with a high angular-resolution.
BL11XU	**JAEA Quantum Dynamics** (Japan Atomic Energy Agency)	(Oct. 1998)	Nuclear scattering. Surface and interface structure analysis with MBE. Inelastic X-ray scattering. XAFS.
BL12B2	**NSRRC BM** (National Synchrotron Rad. Res. Center, Taiwan)	(Oct. 2000)	X-ray absorption spectroscopy. Powder X-ray diffraction. High resolution X-ray scattering. Protein crystallography.
BL12XU	**NSRRC ID** (National Synchrotron Rad. Res. Center, Taiwan)	(Dec. 2001)	High resolution non-resonant or resonant inelastic X-ray scattering. High resolution near-edge X-ray Raman scattering. Phase transitions under high-pressure, low and high temperatures. High-resolution X-ray absorption and emission spectroscopy. X-ray physics and optics.
BL14B1	**JAEA Materials Science** (Japan Atomic Energy Agency)	(Dec. 1997)	Materials science under high-temperature. *In situ* study on catalysis using dispersive XAFS. X-ray diffraction for structure physics.
BL15XU	**WEBRAM** (National Institute for Materials Science)	(Jan. 2000)	Hard X-ray photoelectron spectroscopy. High-precision X-ray powder diffraction.
BL16B2	**SUNBEAM BM** (Consortium)	(Oct. 1998)	Characterization of secondary battery related materials, semiconductors, fuel cells, catalysts, and several industrial materials by X-ray absorption fine structure measurements, X-ray diffraction (including X-ray reflectivity technique) and X-ray topography.
BL16XU	**SUNBEAM ID** (Consortium)	(Oct. 1998)	Characterization of semiconductor materials, secondary batteries, fuel cells, catalysts, electrical display related materials, and structural materials by X-ray diffraction, X-ray microbeam based evaluation technique (including X-ray magnetic circular dichroism), and fluorescence X-ray analysis.
BL22XU	**JAEA Quantum Structural Science** (Japan Atomic Energy Agency)	(May 2002)	Materials science under high-pressure. Resonant X-ray scattering. Speckle scattering. Residual stress/strain distribution analysis.
BL23SU	**JAEA Actinide Science** (Japan Atomic Energy Agency)	(Feb. 1998)	Surface chemistry with supersonic molecular beam. Biophysical spectroscopy. Photoelectron spectroscopy. Magnetic circular dichroism.
BL24XU	**Hyogo ID** (Hyogo Prefecture)	(May. 1998)	Surface/interface analysis by fluorescent X-ray analysis, strain measurements and grazing incidence X-ray diffraction. Microbeam formation studies for materials and life sciences. Micro-SAXS for local long-range structure analysis.
BL28XU	**Research & Development Initiative for Scientific Innovation of New Generation Batteries (RISING)** (Kyoto University)	(Apr. 2012)	Analysis of rechargeable batteries. Time-resolved X-ray diffraction and XAFS with microbeam. XAFS of dilute systems and thin films. Dispersive XAFS. Hard X-ray photoelectron spectroscopy.
BL31LEP	**Laser-Electron Photon II** (RCNP, Osaka University)	(May 2013)	Production of high intensity GeV photon beam by laser-backward Compton scattering. Hadron physics via photonucleon and photonuclear reactions. Test and calibration of detectors with GeV gamma-ray and converted electrons/positrons.
BL33LEP	**Laser-Electron Photon** (RCNP, Osaka University)	(Jun. 1999)	Meson photoproduction from nucleon and nucleus. Photoexcitation of hyperons, nucleon resonances, and other exotic states. Photonuclear reactions. Beam diagnoses. Test and calibration of detectors with GeV photon beam.
BL33XU	**TOYOTA** (TOYOTA Central R&D Labs., Inc.)	(Apr. 2009)	Time-resolved XAFS. Characterization of industrial materials, such as catalysts, secondary batteries, fuel cells.
BL36XU	**Catalytic Reaction Dynamics for Fuel Cells** (The University of Electro-Communications)	(Jan.2013)	Real time analysis of catalytic reaction dynamics for fuel cells. Time resolved XAFS, 2D spatial resolved XAFS, depth resolved XAFS, 3D laminography XAFS, hard X-ray photoelectron spectroscopy.
BL44XU	**Macromolecular Assemblies** (IPR, Osaka University)	(May 1999)	Crystal structure analysis of biological macromolecular assemblies (e.g. membrane complexes, protein complexes, protein-nucleic acid complexes, and viruses).
	◆ RIKEN Beamlines		
BL17SU	**RIKEN Coherent Soft X-ray Spectroscopy**	(Sep. 2003)	High resolution photoemission spectroscopy. Soft X-ray emission spectroscopy for liquid and biological samples. Soft X-ray diffraction spectroscopy. Surface science.
BL19LXU	**RIKEN SR Physics**	(Oct. 2000)	SR science with highly brilliant X-ray beam.
BL26B1	**RIKEN Structural Genomics I**	(Apr. 2002)	Structural genomics research based on single crystal X-ray diffraction.
BL26B2	**RIKEN Structural Genomics II**	(Apr. 2002)	Structural genomics research based on single crystal X-ray diffraction.
BL29XU	**RIKEN Coherent X-ray Optics**	(Dec. 1998)	X-ray optics, especially coherent X-ray optics.
BL32XU	**RIKEN Targeted Proteins**	(Oct. 2009)	Protein micro-crystallography.
BL43LXU	**RIKEN Quantum NanoDynamics**	(Oct. 2011)	High resolution inelastic X-ray scattering for investigating atomic and electronic dynamics.
BL44B2	**RIKEN Materials Science**	(Feb. 1998)	Structural materials science research using powder X-ray diffraction.
BL45XU	**RIKEN Structural Biology I**	(Jul. 1997)	Time-resolved and static structures of non-crystalline biological materials using small-angle scattering and diffraction techniques.
	■ Accelerator Diagnostics Beamlines		
BL05SS	**Accelerator Beam Diagnosis**	(Mar. 2004)	Accelerator beam diagnosis. R&D of accelerator components.
BL38B2	**Accelerator Beam Diagnosis**	(Sep. 1999)	Accelerator beam diagnosis. R&D of accelerator components.

IV. User Program and Statistics

SPring-8 calls for public use proposals principally twice a year. The submitted proposals are reviewed by the Proposal Review Committee (PRC). As for General Proposals, 466 proposals out of the 694 submitted proposals were approved in the research term 2011B, and 471 out of the 618 submitted proposals were approved in 2012A. Since the start of the Long-term Program in 2000B, 38 Long-term Proposals have been implemented, that is, 15 and 14 proposals were carried out in 2011B and 2012A, which include 3 and 1 proposals newly approved. As for Priority Field Proposals, Nanotechnology Support Proposals, Green/Life Innovation Proposals and Industrial Application Proposals were called for in 2011B, while Green/Life Innovation Proposals and Industry Creation Proposals were called for in 2012A. Out of the 249 submitted proposals, 148 proposals were approved in 2011B, and 44 out of the 72 submitted proposals were approved in 2012A. The proposal statistics are shown in Table IV for the period from 1997B to 2012A; Power User Proposals and JASRI Proposals are excluded. During the period from 2003B to 2012A, 18 user groups were designated as Power User groups (PUs), which include 7 PUs active in 2012A. To date, a total of 4710 shifts have been used by PUs, 588 shifts of which were spent from 2011B to 2012A. In particular, 3 proposals were approved as the "Affected Facilities Support Proposal" in 2011B.

SPring-8 consistently provided 1,927 hours of user beamtime in 2011B and 1,971 hours in 2012A. Since the start of operation in 1997, SPring-8 has succeeded in providing users with a total beamtime of 57,112 hours. In 2011B, 1,049 experiments were conducted by 7,345 users at public and contract beamlines, and 922 experiments by 6,996 users in 2012A. From the start of operation in 1997 to 2012A, a total of 21,411 experiments were conducted by 146,473 users.

The beamtime available to the users, the number of experiments conducted, and the number of user visits at the public and contract beamlines are summarized in Table V and in Fig. 3.

Figure 4 shows the breakdown of the approved proposals sorted by user affiliation and of the number of experiments conducted at the public beamlines from 1997B to 2012A. The percentages of experiments conducted by users from abroad were 5.6% in 2011B and 5.8% in 2012A.

For the promotion of Industrial Application at SPring-8, the Industrial Application Division was established in 2005. With consultation support for industrial users given by the division's coordinators, currently, Industrial Application Proposals account for

Table IV. Numbers of submitted proposals and approved proposals by research term

Research Term	Beamtime (shifts)	Deadline	Submitted proposals	Approved proposals
1997B: 1997.10 - 1998.03	168	1997.1.10	198	134
1998A: 1998.04 - 1998.10	204	1998.1.6	305	229
1999A: 1998.11 - 1999.06	250	1998.7.12	392	258
1999B: 1999.09 - 1999.12	140	1999.6.19	431	246
2000A: 2000.02 - 2000.06	204	1999.10.16	424	326
2000B: 2000.10 - 2001.01	156	2000.6.17	582	380
2001A: 2001.02 - 2001.06	238	2000.10.21	502	409
2001B: 2001.09 - 2002.02	190	2001.5.26	619	457
2002A: 2002.02 - 2002.07	226	2001.10.27	643	520
2002B: 2002.09 - 2003.02	190	2002.6.3	751	472
2003A: 2003.02 - 2003.07	228	2002.10.28	733	563
2003B: 2003.09 - 2004.02	202	2003.6.16	938	621
2004A: 2004.02 - 2004.07	211	2003.11.4	772	595
2004B: 2004.09 - 2004.12	203	2004.6.9	886	562
2005A: 2005.04 - 2005.08	188	2005.1.5	878	547
2005B: 2005.09 - 2005.12	182	2005.6.7	973	624
2006A: 2006.03 - 2006.07	220	2005.11.15	916	699
2006B: 2006.09 - 2006.12	159	2006.5.25	867	555
2007A: 2007.03 - 2007.07	246	2006.11.16	1099	761
2007B: 2007.09 - 2008.02	216	2007.6.7	1007	721
2008A: 2008.04 - 2008.07	225	2007.12.13	1009	749
2008B: 2008.10 - 2009.03	189	2008.6.26	1163	659
2009A: 2009.04 - 2009.07	195	2008.12.11	979	654
2009B: 2009.10 - 2010.02	210	2009.6.25	1076	709
2010A: 2010.04 - 2010.07	201	2009.12.17	919	665
2010B: 2010.10 - 2011.02	210	2010.7.1	1022	728
2011A: 2011.04 - 2011.07	215	2010.12.9	1024	731
2011B: 2011.10 - 2012.02	195	2011.6.30	1077	724
2012A: 2012.04 - 2012.07	201	2011.12.8	816	621

Notes
1997B-2006B: The number of proposals are indicated as of submission deadline.
After 2007A: The total number of proposals are indicated.
The number of longterm proposals are counted by beamline, that is, if the project leader uses 2 beamlines, it is counted as 2 proposals.

Table V. Numbers of experiments and users at public and contract beamlines by research term

Research Term	User time (hours)	Public BL		Contract BL	
		Experiments	Users	Experiments	Users
1997B: 1997.10 - 1998.03	1,286	94	681	–	–
1998A: 1998.04 - 1998.10	1,702	234	1,252	7	–
1999A: 1998.11 - 1999.06	2,585	274	1,542	33	467
1999B: 1999.09 - 1999.12	1,371	242	1,631	65	427
2000A: 2000.02 - 2000.06	2,051	365	2,486	100	794
2000B: 2000.10 - 2001.01	1,522	383	2,370	88	620
2001A: 2001.02 - 2001.06	2,313	474	2,915	102	766
2001B: 2001.09 - 2002.02	1,867	488	3,277	114	977
2002A: 2002.02 - 2002.07	2,093	545	3,246	110	1,043
2002B: 2002.09 - 2003.02	1,867	540	3,508	142	1,046
2003A: 2003.02 - 2003.07	2,246	634	3,777	164	1,347
2003B: 2003.09 - 2004.02	1,844	549	3,428	154	1,264
2004A: 2004.02 - 2004.07	2,095	569	3,756	161	1,269
2004B: 2004.09 - 2004.12	1,971	555	3,546	146	1,154
2005A: 2005.04 - 2005.08	1,880	560	3,741	146	1,185
2005B: 2005.09 - 2005.12	1,818	620	4,032	187	1,379
2006A: 2006.03 - 2006.07	2,202	724	4,809	226	1,831
2006B: 2006.09 - 2006.12	1,587	550	3,513	199	1,487
2007A: 2007.03 - 2007.07	2,448	781	4,999	260	2,282
2007B: 2007.09 - 2008.02	2,140	739	4,814	226	1,938
2008A: 2008.04 - 2008.07	2,231	769	4,840	232	1,891
2008B: 2008.10 - 2009.03	1,879	672	4,325	217	1,630
2009A: 2009.04 - 2009.07	1,927	669	4,240	238	1,761
2009B: 2009.10 - 2010.02	2,087	722	4,793	275	2,144
2010A: 2010.04 - 2010.07	1,977	685	4,329	293	2,483
2010B: 2010.10 - 2011.02	2,094	744	4,872	325	2,812
2011A: 2011.04 - 2011.07	2,131	740	4,640	309	2,773
2011B: 2011.10 - 2012.02	1,927	730	4,576	319	2,769
2012A: 2012.04 - 2012.07	1,971	637	4,304	285	2,692
	57,112	16,288	104,242	5,123	42,231

Notes
The number of longterm proposals are counted by beamline, that is, if two beamlines were used for one experiment, those are counted as two experiments.

approximately 20% of the total number of proposals conducted at the public beamlines. In addition, the Measurement Service has been introduced since 2007B, in which the personnel of the Industrial Application Division carry out XAFS measurements on behalf of users at BL14B2. SPring-8 has also launched the Mail-in Protein Crystallography Data Collection Service at BL38B1 and the Powder X-ray Diffraction Measurement Service at BL19B2 since 2009B.

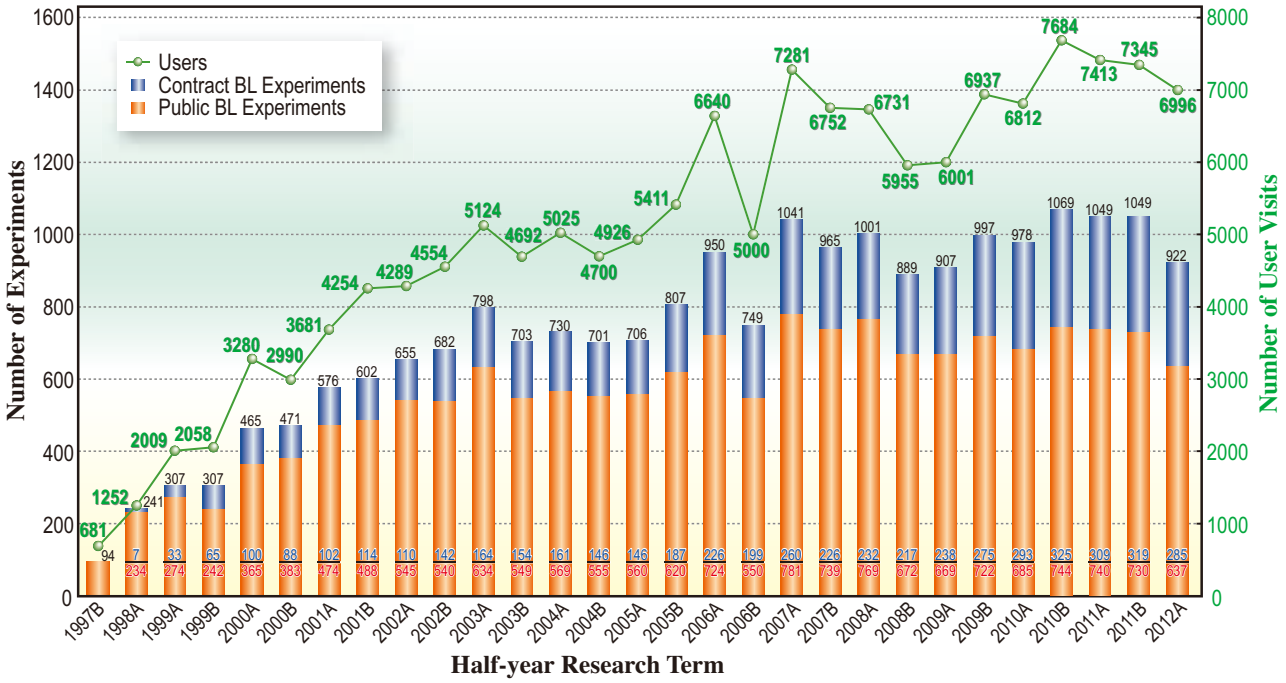

Fig. 3. Numbers of user visits and conducted experiments.

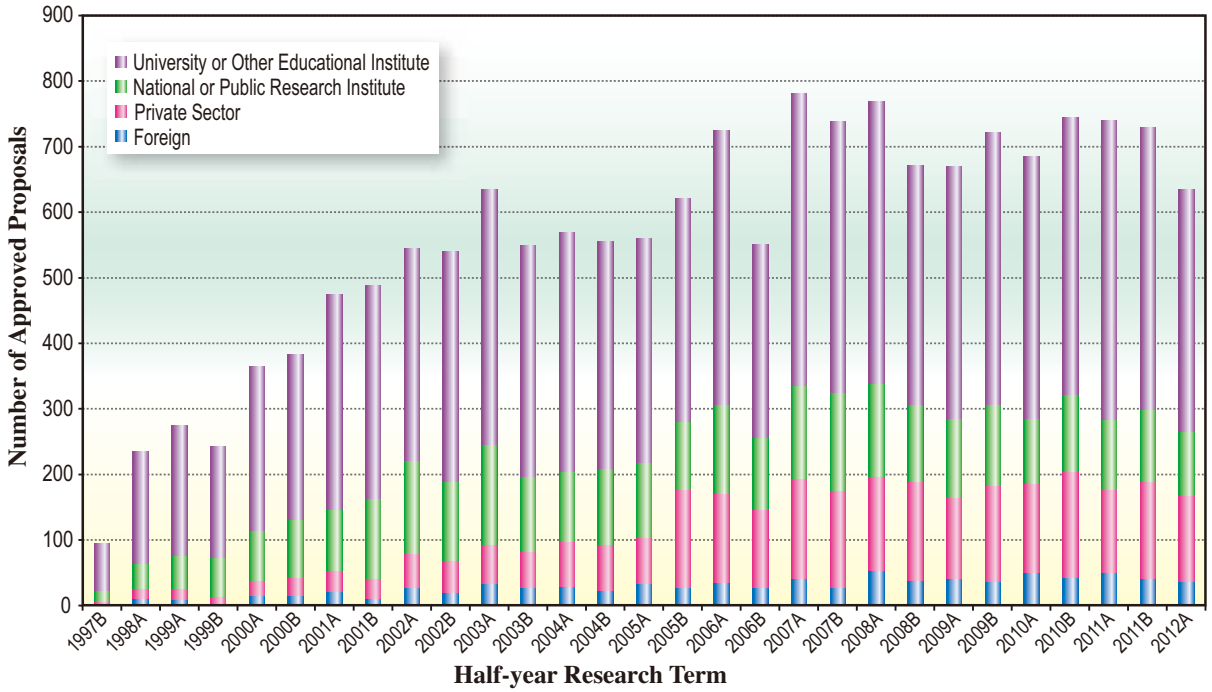

Fig. 4. Number of approved proposals by affiliation of applicants (public beamlines).

V. Research Outcome

From 2011B, the users are strongly required to publish their research results in refereed journals or equivalent, and to register the published works with the Publications Database within three years after the end of the research term. In case of being unable to comply with this requirement, the users are obligated to submit a SPring-8 Research Report refereed by JASRI or, for industrial users, a corporate technical journal article refereed at their home institution. Figure 5 shows the annual statistics of refereed papers. As of March 2013, the number of registered refereed papers is 7,592, out of which 6,584 papers resulted from the use of public beamlines, 1,457 papers from that of contract beamlines, 924 papers from that of RIKEN beamlines, and 436 papers from hardware/software R&D. The papers resulting from the use of two or more beamlines are counted at each beamline.

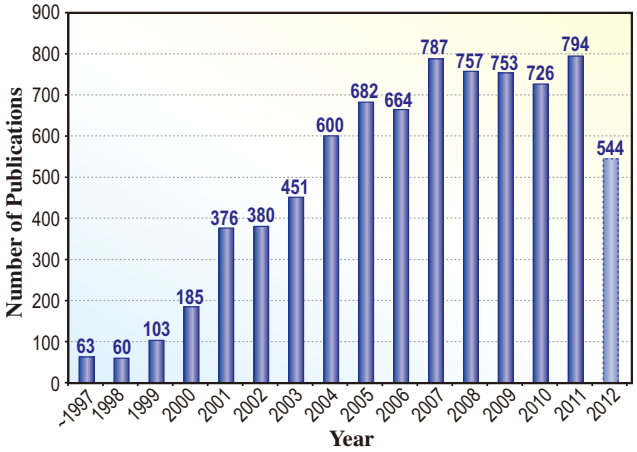

Fig. 5. Number of refereed publications as of March 2013.

VI. Budget and Personnel

Since the start of operation in 1997, SPring-8 had been jointly managed by RIKEN, JAERI (JAEA, as it is known today), and JASRI. Since JAERI withdrew from the management of SPring-8 on September 30, 2005, SPring-8 has been administered by RIKEN and JASRI in a collaborative manner.

Figure 6 shows the annual budget allocated to the operation, maintenance, and promotion of the use of SPring-8 from FY1997 to date. The budget for FY2012 is 8.848 billion yen. The total number of staff members of RIKEN and JASRI is 1,333 as of October 2012, as shown in Fig. 7.

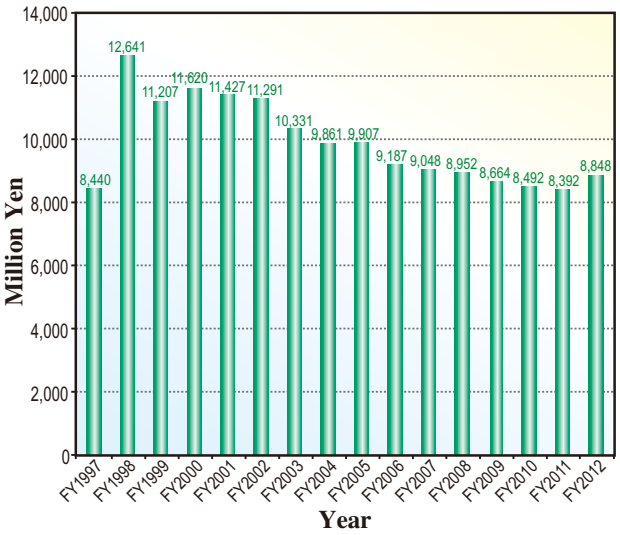

Fig. 6. SPring-8 budget.

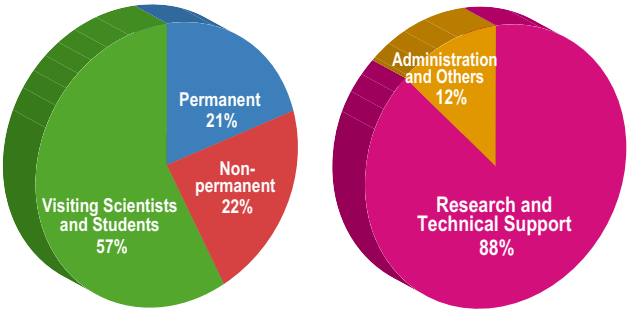

	by Type			by Field	
	Permanent	Non-permanent	Visiting Scientists and Students	Research and Technical Support	Administration and Others
RIKEN	48	171	640	818	41
JASRI	236	128	110	355	119

Including double counts.

Fig. 7. Personnel at SPring-8: JASRI and RIKEN.

VII. Research Complex

The facilities of SPring-8, SACLA, and NewSUBARU form a center of excellence at the SPring-8 campus, where JASRI, public beamline users, contractors of contract beamlines, RIKEN, and the University of Hyogo work in close cooperation to form a research complex by playing their own roles to deliver high-quality results in the field of synchrotron radiation science and technology. Figure 8 shows the SPring-8 research complex and the operation and management of each research facility. The organizational charts of RIKEN and JASRI, which form the kernel of this research complex, are shown in Fig. 9 and Fig. 10, respectively.

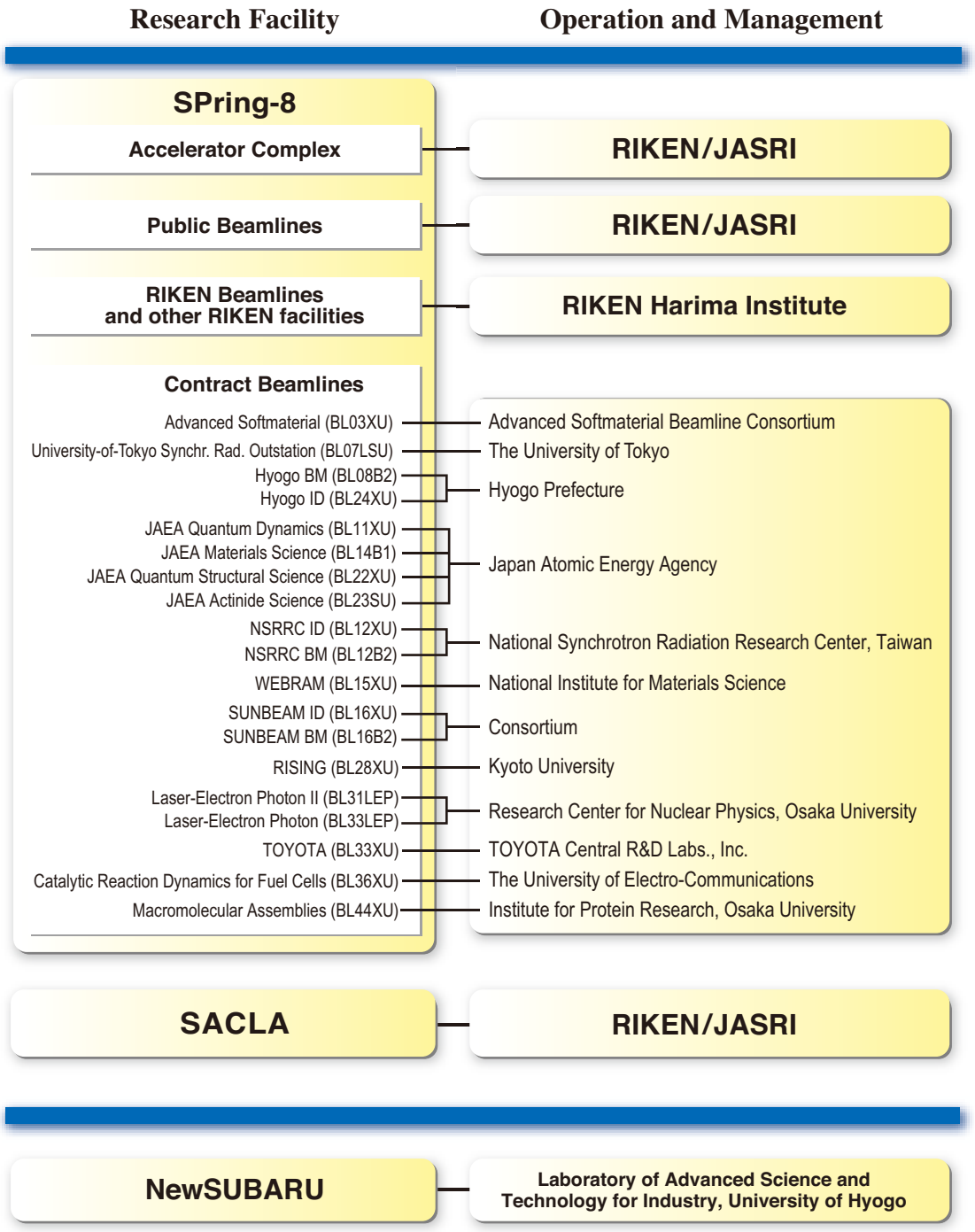

Fig. 8. SPring-8 research complex as of April 2013.

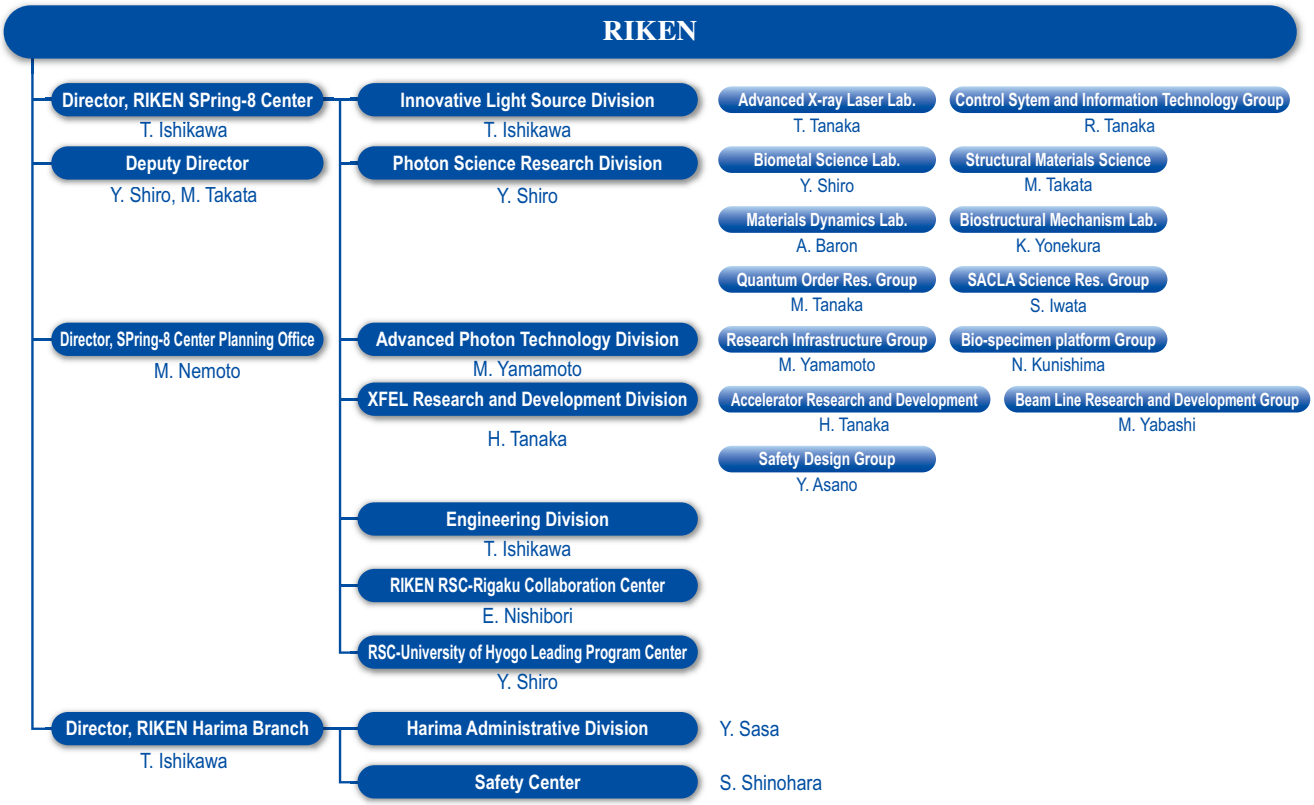

Fig. 9. RIKEN Harima chart as of April 2013.

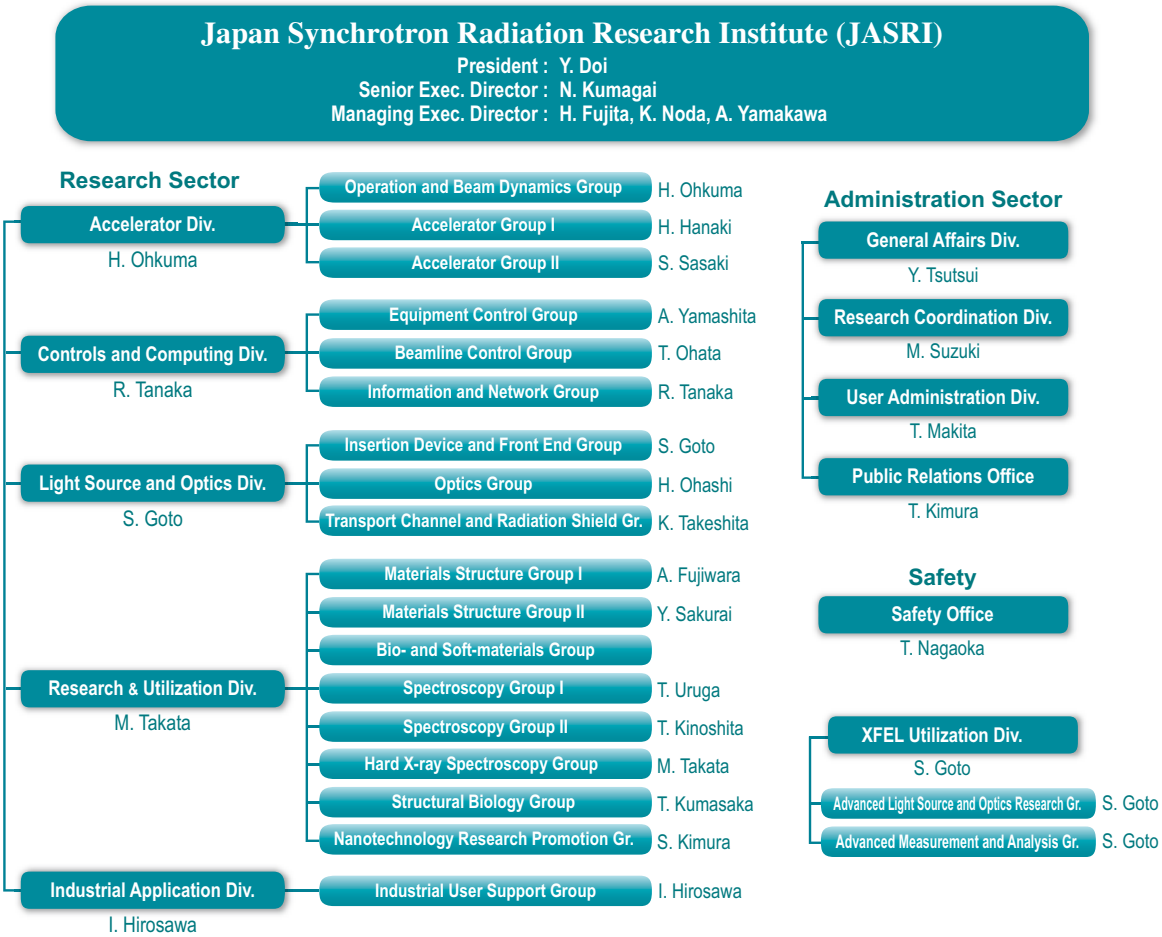

Fig. 10. JASRI chart as of June 2013.

VIII. Users Societies, Conferences, and Other Activities

Users Society

The **SPring-8 Users Society** was organized in May 1993, when SPring-8 still did not exist, to discuss the construction of and the scientific research studies at SPring-8. During the construction and development phases of SPring-8, the SPring-8 Users Society made enormous contributions to the construction of the beamlines and the promotion of the utilization of SPring-8 through discussions among users and between users and facility staff. However, the number of members of the SPring-8 Users Society remained at about 1,200, while the number of SPring-8 users reached more than 10,000. This situation necessitated the reconstruction of the SPring-8 Users Society to enable it to organize all users of SPring-8 and continue to contribute to the promotion of the utilization and upgrade of SPring-8 in the mature phase.

In April of 2012, a new organization, **SPring-8 Users Community** (SPRUC), was formed. It includes not only all users but also potential users who are interested in using SPring-8. In terms of its organization, SPRUC has a remarkable feature: that is, representatives of about thirty institutes (principal universities and national research institutes), to which quite a few users belong, participate in SPRUC to discuss further promotion of the utilization of SPring-8 from strategic and bird's-eye viewpoints. To kick off SPRUC, the SPring-8 Symposium 2012, with the theme of "Science, Technology and Innovation", was held on August 25 and 26, 2012, at Osaka University. At the symposium, the SPRUC2012 Young Scientist Award was conferred to two young scientists (Dr. Xeniya Kozina of JASRI and Dr. Marcus Kitchen of Monash University.) A Panel discussion session on "Ground design of Synchrotron Radiation Research and the Mission of SPRUC" was organized, in which views on the future of Synchrotron Radiation Research were presented by chairs of principal synchrotron radiation facilities in Japan, and hot discussion followed on the basis of the views presented. The SPring-8 Symposium 2013 is scheduled for September at Kyoto University.

Users Meeting

The meeting for users jointly organized by the SPring-8 Users Society and/or the Industrial User Society of SPring-8, and JASRI and RIKEN is listed below.

• The first SPring-8 Symposium by SPRUC
August 25–26, 2012 - Osaka University, Suita, Osaka

• The 9th Activities Report Meeting on SPring-8 Industrial Application
September 6–7, 2012 - Aichi Arts Center, Nagoya, Aichi

Conferences and Workshops

The conferences and workshops organized, sponsored, or hosted by RIKEN, JASRI, or both in 2012 are listed below.

• 25th Annual Meeting of Japanese Society for Synchrotron Radiation Research
January 6–9, 2012 - Civic Cultural Hall Tosu, Saga

• The first JASRI CROSS Joint Workshop Industrial Applications of Synchrotron Radiation
January 16, 2012 - KENKYUSHA EIGO CENTRE, Tokyo

• The 3rd SPring-8 DIAMOND Joint Workshop Industrial Applications of Synchrotron Radiation
May 21–23, 2012 - XFEL Experimental Facility, SACLA and Nichii Gakkan Kobe Port Island Center, Kobe

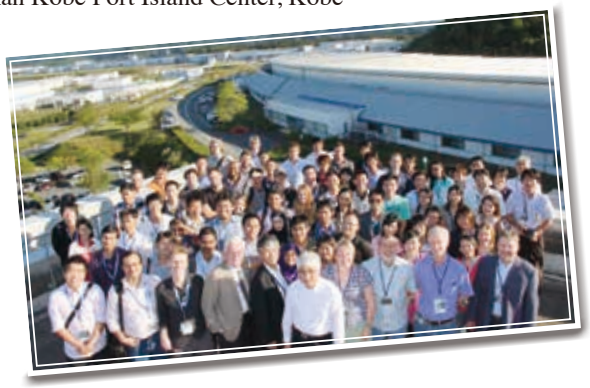

• The 17th Sagamore Conference
July 15–20, 2012 - Daini Meisui Tei, Kitayuzawa, Hokkaido

• The 2st Workshop on the Utilization of SACLA
August 1, 2012 - XFEL Experimental Facility, SACLA

• The 4th Workshop on the Basis of Synchrotron Radiation
August 3–4, 2012 - The University of Tokyo, Tokyo

• The 34th International Free-Electron Laser Conference (FEL2012)
August 26–31, 2012 - Nara Prefectural New Public Hall, Nara

• The 6th International Workshop on Semiconductor Pixel Detectors for Particles and Imaging (PIXEL2012)
September 3–7, 2012 - Hotel Listel Inawashiro, Fukushima

• The Workshop on Science of Cultural Heritage
September 28, 2012 - Kenkyusha Eigo Centre, Tokyo

• The 2st Annual Meeting for Whole-Organism Science Society
Joint Meeting with
The 11th Annual Meeting of Whole Cell Project of *Thermus thermophilus* HB8
September 28–29, 2012 - Public Relations Center, SPring-8 and XFEL Experimental Facility, SACLA

• The first SPring-8 Photon Factory joint Workshop Industrial Applications of Synchrotron Radiation
October 19, 2012 - TKP Tokyo-eki Yaesu Conference Center, Tokyo

• The 5th Workshop on the SPring-8 Budding Researchers Support Program
November 27, 2012 - Campus Innovation Centre, Tokyo

• The 2st SACLA Symposium
December 8, 2012 - Tokyo International Forum, Tokyo

• International Workshop on the Science and Design of Diffraction Limited Storage Rings
December 14–15, 2012 - XFEL Experimental Facility, SACLA

Other Activities

• The 20th SPring-8 Open House
April 30, 2012 - SPring-8, Hyogo

• The 12th SPring-8 Summer School 2012
July 15–18, 2012 - Public Relations Center, SPring-8

• The 6th AOFSRR School - Cheiron School 2012
September 24 – October 3, 2012 - Public Relations Center, SPring-8

SACLA

SACLA launched user operations in March 2012, marking the world's second XFEL facility for users, following LCLS. The inaugural user group was led by Dr. Hideo Ago from RIKEN SPring-8 Center, which started single-shot, damage-free protein structural analysis using conventional X-ray crystallography. The total user time during fiscal year 2012 was 3,150 hours (out of 7,000 hours of total operation time). SACLA plans to steadily increase user time over the next five years to achieve a tentative goal of 4,000 hours of user time (out of 6,000 hours of total operation time). The most exciting SACLA capabilities for users have been its high shot-by-shot stability in the pointing direction, spatial profile, laser wavelength and intensity. Although SACLA started user operations with a single X-ray FEL beamline and one low-energy spontaneous beamline, most users have focused operations on the X-ray FEL since it can deliver higher energy laser photons than LCLS.

Through our experience with user operations, it has become clear that the scientific fields requiring XFEL are much more widespread than what a single facility, or even more than ten facilities, can accommodate. Therefore, it is feasible for SACLA and LCLS to avoid overlapping their respective targeted fields. Even with new facilities coming on-line, such as European, SWISS, and PAL XFELs, it would not be difficult to minimize overlapping of targeted fields if we choose to do so.

Unfortunately, our selection of machine technology does not allow us to achieve very high pulse energy for single pulses, as that would certainly destroy samples and might even deteriorate optical elements. Rather than striving for higher pulse energy, we have decided to develop high-performance focusing systems that can produce much higher power density. A Kirkpatrick-Baez (KB) focusing mirror with elliptically figured mirrors has been working effectively, offering a 1 μm × 1 μm focal spot with a working distance exceeding 1000 mm. A two-stage KB mirror offers a 50 nm × 50 nm focal spot inside the SACLA-SPring-8 Experimental Facility where the SACLA and SPring-8 X-ray beams intersect. The extremely high photon flux density generated by this focusing method has been used to conduct research on nonlinear X-ray optics as well as on high-energy-density science.

Over the past year, SACLA has developed now-standard experimental techniques for XFEL, including Coherent Diffraction Imaging; Ultra-Fast Tracking of gas, liquid, and solid-phase materials; and X-ray Quantum Optics. SACLA has also been developing X-ray image sensors with a fast read-out. The integration of X-ray optics, such as focusing systems, sample manipulation systems, detectors and data analysis systems, is progressing to improve capabilities for user experiments.

After the successful self-seeding at LCLS, SACLA decided to follow the same seeding scheme. A small chicane was prepared by moving one undulator unit after the most downstream one to install transmission crystal optics for seeding. Tests of seeding operations will be conducted in the latter half of 2013. Also, high-efficiency seeding with laser higher harmonics has been demonstrated at the SCSS prototype EUV FEL, which will be relocated to the SACLA undulator hall in a couple of years.

Last, but not least, we are sad to announce the sudden loss of Dr. Mitsuru Nagasono, who was responsible for SCSS experiments. We miss him and wish him and his family peace.

Tetsuya Ishikawa

Machine Operation

Since starting the public user operation at SACLA in March 2012, we have delivered XFEL light in the self-amplified spontaneous emission (SASE) scheme with improved laser performance, especially in terms of intensity and stability.

1. Intensity enhancement

The laser pulse energy, which was only 30 μJ before the summer shutdown in 2011 and reached 120 μJ at the end of the year, was increased to 330 μJ in autumn 2012 by elaborate tuning efforts. Since then, pulse energy higher than 300 μJ has been routinely and constantly supplied to user experiments, as shown in Fig. 1. The following three improvements have contributed to this intensity enhancement. (a) The diameter of the circular collimator, which scrapes the beam halo off an electron beam core at 500 keV, was changed from 5 to 4 mm to improve the beam slice emittance. (b) The maximum undulator K-value and electron beam energy have been increased from 1.8 to 2.1 and from 8.0 to 8.4 GeV, respectively, to enhance the SASE amplification gain over a wide photon energy range from 4.5 to 15 keV. (c) The alignment of electron beam orbit over the accelerating structures has been improved to reduce the projected emittance.

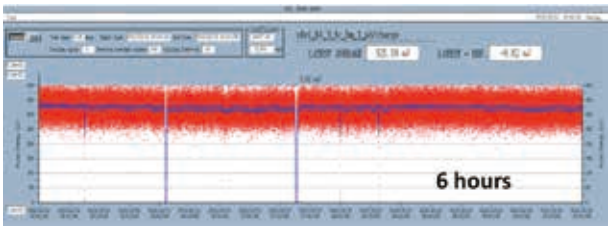

Fig. 1. XFEL intensity variation during the user experiment at a photon energy of 5.5 keV. Laser intensity was measured with the inline monitor at the optical hutch connected to the experimental hutch.

2. Stability improvement

The laser instability was reduced step by step, and the stability has reached a high level, as shown in Table 1 since the summer shutdown in 2012. Figure 2 shows the laser pointing fluctuations before and after the improvement, measured in the optical hutch where the beam size is about 200 μm FWHM. The present center of mass fluctuations are smaller than the beam sizes. The following four improvements at the injector section have contributed to lasing stabilization. On suppressing the drifts caused by RF phase shifts, (a) the precision of the temperature control for Low Level RF (LLRF) system was improved from 0.1 K to 0.01 K PP (peak-to-peak value) by reducing the temperature variation of cooling water and (b) the cavity-type band-pass filters (BPFs) in the LLRF system with high sensitivity against temperature variations were replaced by BPFs with lower temperature sensitivity. On suppressing the fast variations at approximately 0.5 Hz, (c) AC heaters used for the temperature control of RF cavities were replaced by DC ones to remove the magnetic noise causing the fluctuation of the low energy electron beam. (d) Thermometer modules were also replaced by those with fine temperature resolutions of 0.001 K to suppress the cavity temperature variation to less than 0.01 K.

Table 1. Achieved laser stability

Laser property	Normalized variation $\sigma_{\delta x/x}$ (%)
Intensity	≤10
Pointing	3 – 7
Wavelength	≤0.1

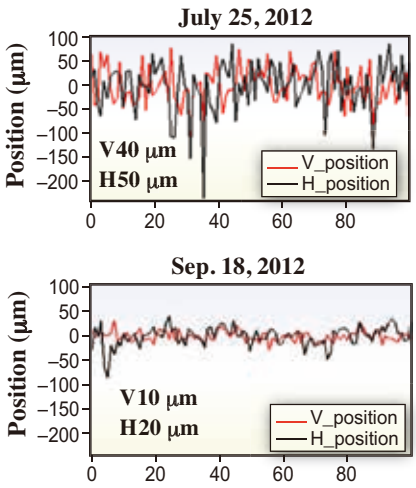

Fig. 2. Laser pointing stability at the optical hutch before and after machine improvement.

3. Short pulse generation

The elaborate efforts on beam tuning have brought about significant improvement of the electron beam brilliance. As a result of this improvement, the gain length denoting the laser amplification efficiency has decreased to 2.3 m as shown in Fig. 3. FEL simulations reproducing the gain curve (Fig. 3) suggest that the peak power is larger than 30 GW and the laser pulse duration is less than 10 fs. This condition

is routinely reproducible and the short-pulsed laser with high peak intensity has been constantly delivered to user experiments.

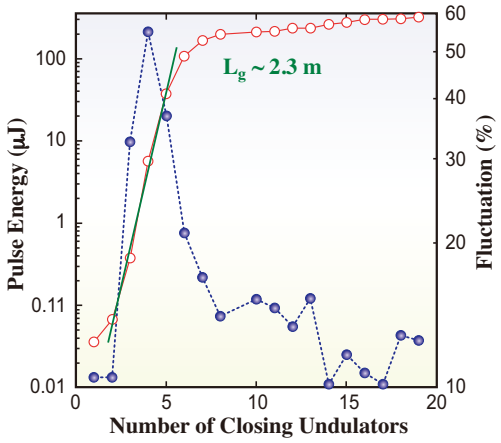

Fig. 3. SASE gain length at 10 keV. Pulse energy (left ordinate) is plotted against the number of closing undulators together with pulse energy fluctuation (right ordinate). Gain length in an exponential gain region is estimated to be 2.3 m. After power saturation, the pulse energy fluctuation is nearly 10%.

4. Two-color SASE generation

In 2012, the two-color XFEL operation was achieved for the first time in hard X-rays [1]. Figure 4 shows a schematic layout of SACLA BL3. A magnetic chicane, which creates a detour for the electron beam and causes a delay, is located in the middle of 18 undulators. For the two-color operation, the magnetic gaps of the undulators are set at different K values before and after the chicane to generate two photon pulses at different wavelengths. Figure 5 shows a spectrum of the two-color XFEL measured by a scanning monochromator. The time delay between two pulses can be finely tuned by adjusting the chicane with attosecond resolution. Since two photon pulses are emitted from the same electron bunch, there is no time jitter between them. In addition, we have a wide tuning range for the wavelengths of two colors. Thus, the two-color XFEL has significant capability for performing X-ray pump X-ray probe experiments, which enables researchers to exploit a novel experimental technique.

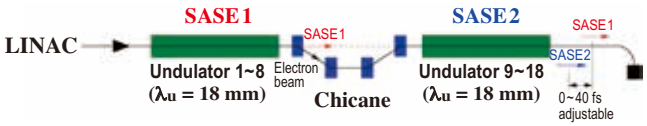

Fig. 4. Schematic layout of the undulator beamline of SACLA BL3.

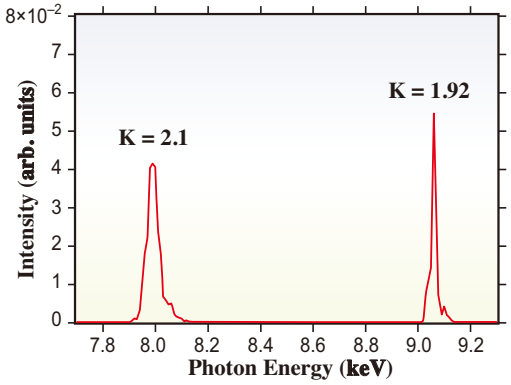

Fig. 5. Measured spectrum of two-color XFEL. K-value was set at K=1.92 for five undulators before the chicane, and at K=2.1 for ten undulators after the chicane. Electron beam energy was 7 GeV.

Beamline and Experimental Stations

As the first compact XFEL facility in the world, SACLA successfully completed its initial commissioning by the end of 2011. Following the commissioning, SACLA started user operation in March 2012. Stable XFEL light has been routinely provided for users without serious downtime. 52 experimental proposals from various fields including biological imaging, femtosecond protein crystallography, ultrafast materials science, high energy density science, nonlinear X-ray optics, and industrial applications, were approved by the JASRI Proposal Review Committee and conducted in the period of 2012A (March to July, 2012) and 2012B (September 2012 to March 2013). In parallel to the user operation, exciting and useful information on radiation properties of XFEL has been obtained by utilizing instruments and methods newly developed for SACLA. In this section, we will introduce methods for the control and characterization of the unique properties of XFEL light, which are important for achieving robust operation of light sources and reliable analysis of experimental data. We also describe the development status of new infrastructures.

1. Control and characterization of XFEL light

A focusing system is a key device for enhancing the high power density of XFEL light. Under close collaboration with the group of Prof. Yamauchi (Osaka University), we have decided to use a reflective focusing system, which has the advantage of a high efficiency close to 100%, as well as high tolerance to intense XFEL light. A combination of two concave mirrors in the Kirkpatrick and Baez geometry was designed for focusing XFEL light down to 1 micron in order to increase the power density to ~10^{18} W/cm^2.

This level is sufficiently high to generate nonlinear X-ray phenomena. We have optimized the focusing profile by a conventional knife-edge scanning method (Fig. 6), proving the high stability of the light source and the beamline optics at SACLA [2]. The system has been used for various types of user experiments including nonlinear X-ray optics, coherent diffraction imaging, and femtosecond protein crystallography.

We applied the system to studies of damage to optical elements under irradiation of intense XFEL light, and obtained important information for all XFEL beamlines, under an international collaboration among XFEL facilities. Damage thresholds for various elements (semiconductor substrates, metal coating, multilayers, etc.) in both normal and grazing incidence geometries have been systematically evaluated using a newly developed dedicated chamber [3].

Among the radiation properties of XFEL, intensity (pulse energy) is one of the most fundamental parameters. Conventional monitoring systems, however, cannot be utilized owing to the high intensity and pulsed nature of XFEL light. For this purpose, SACLA organized an international collaboration program with AIST in Japan, and DESY and PTB in Germany. Absolute intensity evaluated with a gas monitor detector developed by DESY-PTB was compared with that obtained with a calorimeter developed by AIST. We found that the agreement was excellent. The result has been applied to calibrate the foil-based intensity monitor developed by SACLA [4].

We have also evaluated the pulse duration of XFEL light by high-resolution spectral measurement, on the basis of the Fourier transform relationship. For this purpose, we developed a dispersive spectrometer that consists of a concave mirror to increase the beam divergence, a flat crystal analyzer to provide dispersion, and an MPCCD detector to record the spectrum in a single shot. An excellent resolution of 13 meV at 10 keV enabled us to resolve the fine spike structures originating from the SASE mechanism of XFEL generation. By combining the FEL simulation code SIMPLEX, we have evaluated the pulse duration to be from 4.5 to 31 fs [5], which is controlled by the bunch compression parameter (Fig. 7).

The ultrafast pulse duration and moderate spectral bandwidth of SASE XFEL light are promising for performing time-resolved X-ray absorption spectroscopy in a dispersive geometry. We are developing a method that uses both a high-resolution spectrometer and a grating beam splitter. The excellent capability of this method has been proved with a preliminary test.

Fig. 7. Typical spectrum measured with high-resolution spectrometer. From the spike width of ~400 meV, temporal width was evaluated to be ~7 fs.

2. Experimental infrastructures

In 2011, we constructed the beamline for the SACLA-SPring-8 Experimental Facility that enables combinative experiments using SACLA and SPring-8 simultaneously. We also installed a two-stage focusing system into this facility under collaboration with the groups of Prof. Mimura (University of Tokyo) and Prof. Yamauchi (Fig. 8). In 2012, we successfully commissioned this system. We will open the facility to users in 2013A.

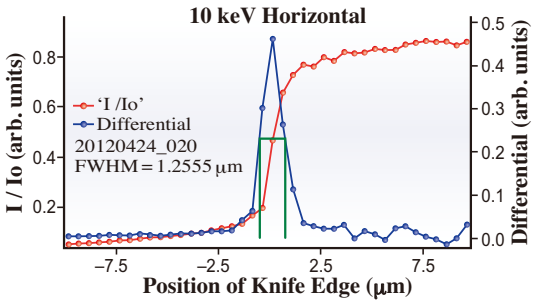

Fig. 6. Horizontal focusing profile with a width of 1.3 um (FWHM) measured by the knife-edge scan method.

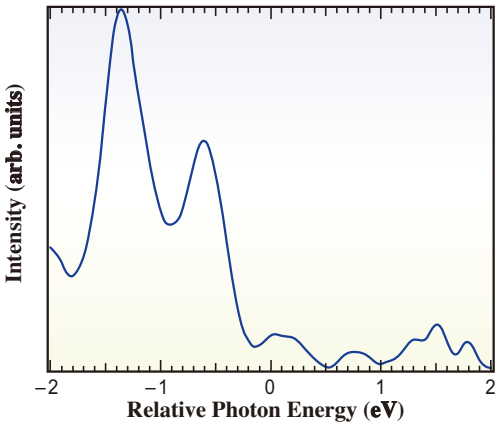

Fig. 8. Beamline components including the two-stage focusing system, installed at EH5 in the SACLA-SPring-8 Experimental Facility.

The SCSS Test Accelerator

In the SASE-FEL scheme, spectra in the longitudinal phase space (i.e., the temporal and frequency domains) are composed of random and uncontrollable spikes. A seeding scheme is required for realizing a fully coherent light source with perfect longitudinal coherence. At the SCSS test accelerator (SCSS), we have chosen to develop a direct seeding system in the EUV region using the high-order harmonic generation (HHG) of Ti:S laser pulses [6,7]. By focusing intense ultrafast laser pulses into a gaseous medium, fully coherent HH radiation in the extreme ultraviolet (EUV) region can be generated.

In 2012, we continued the development of techniques for maintaining the overlap between the electron bunch and the seeding pulse in 6D phase space. One of the most crucial issues is the temporal overlap. For this purpose, we developed a feedback system with an electro-optic sampling (EOS) technique [8], in addition to an OTR monitoring system and a streak camera (Fig. 9). Using the EOS system, we measured the timing of the arrival of an electron bunch with respect to that in case of EO-probing laser pulses, which were optically split from the common laser source used also for HH generation. This system enabled us to compensate for the long-term drift of the timing of arrival. Using these devices, we finally achieved a high hit rate range of 20–30%.

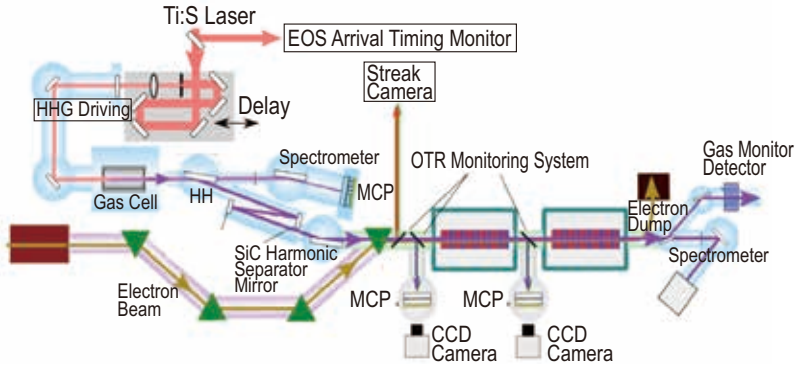

Fig. 9. Layout for HH-seeding system at SCSS.

References

[1] T. Hara *et al.*: submitted.
[2] K. Yumoto *et al.*: Nat. Photon. **7** (2013) 43.
[3] T. Koyama *et al.*: Opt. Exp. (2013) - in press.
[4] M. Kato *et al.*: Appl. Phys. Lett. **101** (2012) 023503.
[5] Y. Inubushi *et al.*: Phys. Rev. Lett. **109** (2012) 144801.
[6] G. Lambert *et al.*: Nat. Phys. **4** (2008) 296.
[7] T. Togashi *et al.*: Opt. Exp. **19** (2011) 317.
[8] M. Yabashi *et al.*: J. Phys. B - in press.

NewSUBARU

The NewSUBARU synchrotron radiation facility is operated by the Laboratory of Advanced Science and Technology for Industry (LASTI), University of Hyogo. This facility consists of an electron storage ring and nine beamlines. Electron injection is supplied from a 1 GeV linac of the SPring-8 facility. The conceptual layout of the NewSUBARU facility is illustrated below.

Topics of the NewSUBARU facility in fiscal year 2012 are as follows.
(1) An LSI mask pattern observation system for extreme ultraviolet lithography using a lensless scatterometry microscope was developed.
(2) The beam current was enhanced from 220 mA to 300 mA. This was achieved by the precise tuning of magnetic optics and improvement of beam lifetime.
(3) A new irradiation hutch for a γ-ray beam was added in collaboration with Konan University. The γ-ray beam of photon energy up to 76.3 MeV was started for the users. The maximum γ-ray power generated was 0.33 mW.
(4) LEENA, a small linear electron accelerator at NewSUBARU, was reconstructed, and the generation of THz Smith-Purcell radiation was started.

Furthermore, all NewSUBARU beamlines are open for industry use. Promotion of user operation and technical assistance for users are supported by the "Open advanced research facility initiative" of MEXT.

Shuji Miyamoto
Director of LASTI, University of Hyogo

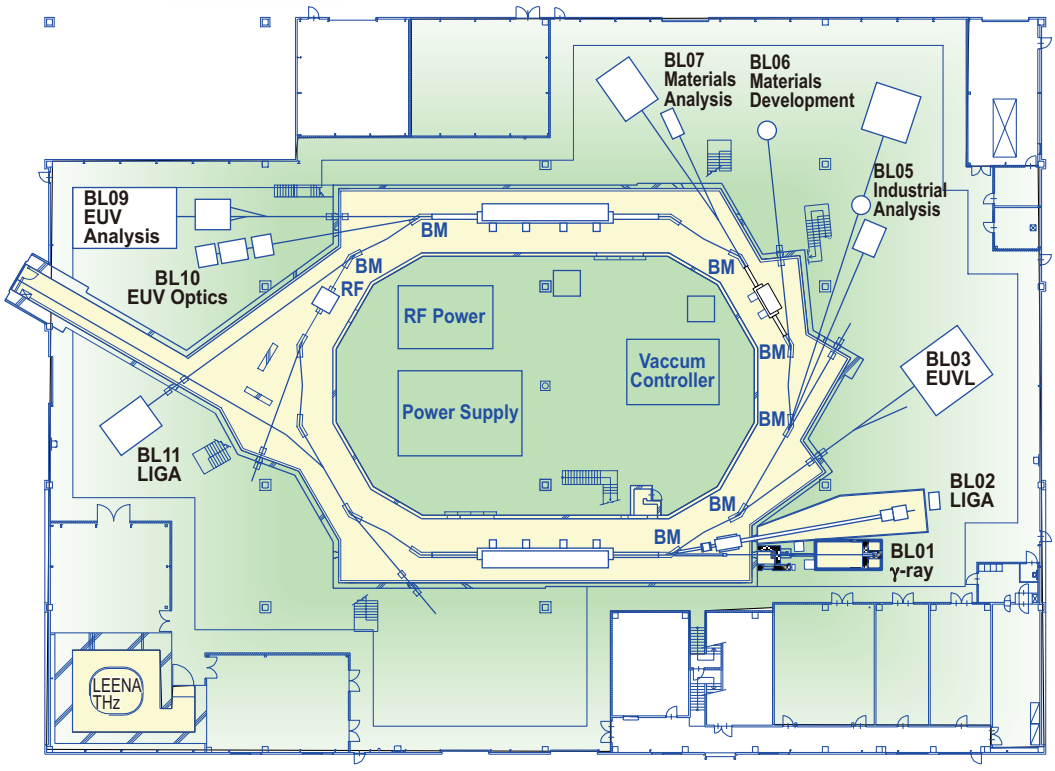

LSI mask pattern observation for EUV lithography using lensless microscope

Extreme ultraviolet (EUV) lithography is a promising technology for the production of semiconductor devices at the 22 nm node and below, where the working wavelength of EUV lithography is 13.5 nm. Recently, a lithography system supplier of ASML has shipped the EUV beta tools to semiconductor companies, which is the preproduction tool for high-volume manufacturing. In the NewSUBARU synchrotron facility, we had developed the world's first full-filed EUV exposure tool [1] for the feasibility study of EUV lithography. Moreover, we have developed EUV resist evaluation tools [2] and EUV mask evaluation tools [3]. In this paper, we introduce the mask evaluation tools.

The mask is a master pattern of the LSI, which is printed on wafers with 1/4 magnification. The critical issue of EUV lithography is the production of a defect-free mask. A defect is not allowed on the mask, which will be printed on all LSI patterns. An EUV mask is of reflective type, which consists of a glass substrate, a reflective Mo/Si multilayer, and an absorber pattern. Thus, the phase structure is printable as a defect, which is a bump or a pit structure on the substrate or a particle in the multilayer. A shallow structure of 1 nm height would be printable because of the EUV short working wavelength of 13.5 nm, which cannot be detected by SEM. To evaluate the phase defect, an EUV actinic microscope is strongly required. We have developed a coherent EUV scatterometry microscope (CSM) based on a coherent diffraction imaging method at the NewSUBARU synchrotron facility, which is a lensless microscope without an objective [4,5].

Figure 1 shows a schematic view of the CSM system, which has a numerical aperture of 0.14 and a field of view of ϕ5 μm. The spatial resolution of the CSM is about 60 nm. The main structures of the CSM system are a coherent EUV source and an EUV CCD camera, which records diffraction from the pattern directly. The incident beam was monochromatized by Mo/Si multilayers. The image-forming optics are replaced by an inverse computation using scattered intensity, which is based on the coherent diffraction imaging method of ptychography. In this iterative calculation, the phase data of frequency space is retrieved. Therefore, aerial image phase data are also retrieved. The CSM thus observes a phase image of the sample EUV pattern.

Figure 2 shows a reconstructed result of the corner structure of the 128-nm line-and-space (L/S) pattern. This figure shows a complex amplitude image with the amplitude represented by brightness and the phase represented by hue. The periodic structure of the L/S pattern and aperiodic structure of the corner structure were well reconstructed. The phase structure was also well reconstructed.

Figure 3 shows a reconstructed result of phase defect squares with 1 μm width, which had a 6.2 nm height evaluated by AFM. The sample mask was an EUV mask that contained programmed bump structures on a glass substrate. Figure 3(a) shows a complex amplitude image with the amplitude

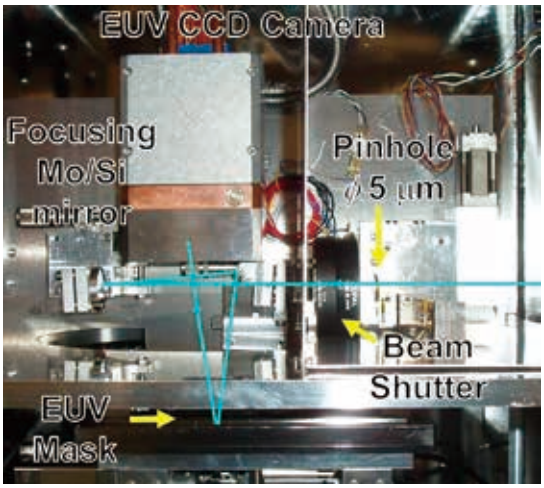

Fig. 1. Photograph of CSM system.

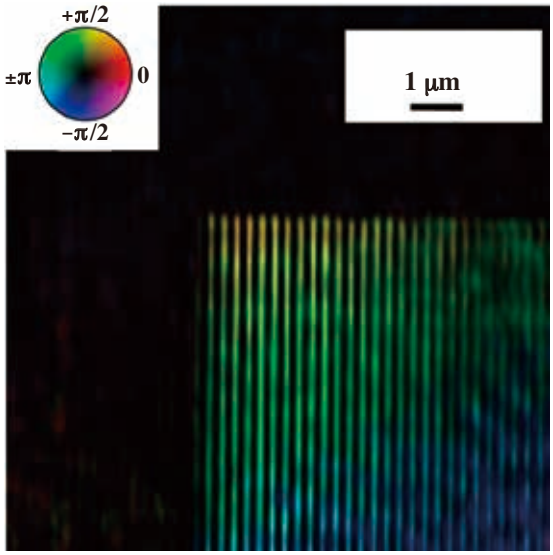

Fig. 2. Reconstructed result of corner structure of the 128 nm L/S pattern.

represented by brightness and the phase represented by hue. The defect edge was reconstructed as black, which is caused by the destructive interference of the phase structure. This edge structure was also observed in the conventional EUV microscope. In addition to the intensity information, using CSM the phase distribution was observed (Fig. 3(a)). Figure 3(b) shows a 3D image of the phase distribution. The defect had a phase angle of –33°, which means 6.1 nm in height. Therefore, the CSM result corresponded well with the AFM results. CSM showed the actinic phase distribution of the phase defect. It is known that the EUV actinic image of the small phase defect was different from the AFM results; the actinic feature of the defect is very important for defect compensation and hiding. In lithography, the mask phase information is also essential for lithography simulators to predict aerial images, which is fundamental imaging information. The actinic phase image captured using the CSM helps with the fabrication of a defect-free mask for the defect compensation and hiding method.

To characterize a smaller phase defect property, we have developed a micro-CSM system that has focusing optics of a Fresnel zone plate. Micro-CSM focuses the illumination EUV to ϕ200 nm on the defect. This layout reduces the background noise signal from the mask roughness, and enlarges the defect signal. The target defect size was less than 30 nm in width and 1 nm in height.

We have developed these lensless EUV microscopes to make the EUV mask evaluation standard with a simple layout and a high capability.

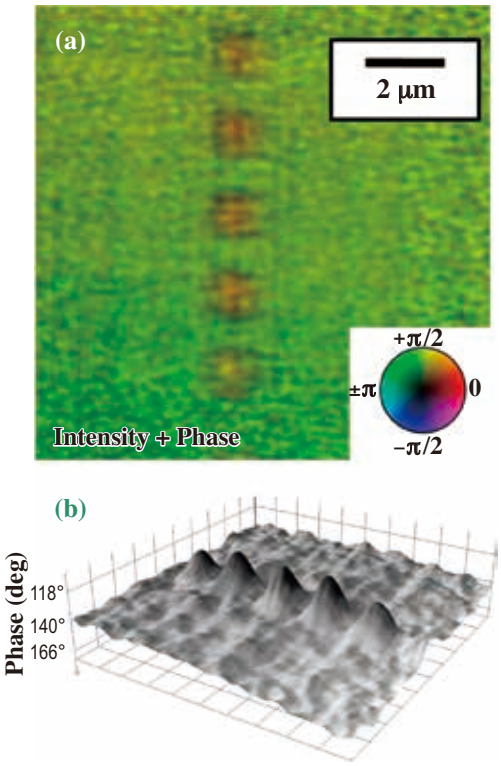

Fig. 3. Reconstructed result of phase defects. **(a)** Intensity and phase image. **(b)** 3D image of phase distribution.

Tetsuo Harada[a,b,*], Takeo Watanabe[a,b], and Hiroo Kinoshita[a,b]

[a] NewSUBARU, LASTI, University of Hyogo
[b] CREST - JST

*Email: harada@lasti.u-hyogo.ac.jp

References

[1] T. Watanabe *et al.*: Jpn. J. Appl. Phys. **41** (2002) 4105.
[2] T. Urayama *et al.*: J. Photopolym. Sci. Technol, **24** (2011) 153.
[3] K. Hamamoto *et al.*: Jpn. J. Appl. Phys. **45** (2006) 5378.
[4] *T. Harada, M. Nakasuji, M. Tada, Y. Nagata, T. Watanabe and H. Kinoshita: Jpn. J. Appl. Phys.* ***50*** *(2011) 06GB03.*
[5] *T. Harada, M. Nakasuji, T. Kimura, T. Watanabe, H. Kinoshita and Y. Nagata: J. Vac. Sci. Technol. B* ***29*** *(2011) 06F503.*

Editor
Hideo Ohno
SPring-8 / JASRI

Editing, Design & Layout
Marcia M. Obuti-Daté
SPring-8 / JASRI

Printing
ROKKO Publishing & Sale Co.

J A S R I
Library and Information
Users Administration Division

1-1-1 Kouto, Sayo-cho, Sayo-gun
Hyogo 679-5198 • JAPAN
Tel. +81-(0)791 58-2797 Fax. +81-(0)791 58-1869

frontiers@spring8.or.jp
http://www.spring8.or.jp/

August 2013

Japan Synchrotron Radiation Research Institute
1-1-1 Kouto, Sayo-cho, Sayo-gun, Hyogo 679-5198 JAPAN
http://www.spring8.or.jp